

**Université du Québec  
INRS – Énergie, Matériaux et Télécommunications**

**Controlled Growth and Positioning of Functional Materials  
By Unconventional Nanoscale Patterning**

**Par**

**Cristian Victor Cojocaru**

**Thèse présentée pour l'obtention  
du grade de Philosophiae doctor (Ph.D.)  
en Science de l'Énergie et des Matériaux**

**Jury d'évaluation**

**Président du Jury  
et examinateur interne**

**Prof. Roberto Morandotti  
INRS-EMT**

**Examineur externe**

**Prof. Peter Grütter  
McGill University**

**Examineur externe**

**Prof. Yves-Alain Peter  
École Polytechnique de Montréal**

**Directeur de recherche**

**Prof. Federico Rosei  
INRS-EMT**

**Co-Directeur de recherche**

**Prof. Alain Pignolet  
INRS-EMT**

*To my family*

## ABSTRACT

The growth of functional nanostructures with controlled size and shape, precisely registered on a substrate of choice, using a minimal number of processing steps, represents a widely discussed, critical issue in Nanotechnology. Furthermore, the fabrication and patterning of novel complex materials with integrated functionality represents an interesting challenge for the development and the application of smart materials. Probing new routes to prepare these materials and understanding the relationship between their fabrication process, their size/structure and their properties is therefore essential. In this context, a variety of conceptually simple forms of lithography - such as molding, stamping, imprinting - are now being revisited for their potential as alternative nanofabrication and patterning techniques. However, there is a common drawback associated with almost all alternatives to traditional lithographic approaches: they still require some type of resist (polymer) processing and consequently numerous chemical, thermal and etch associated steps.

The approach that we have adopted and further built on in this work is *nanostenciling*, i.e. the controlled growth of nanostructures by direct deposition through miniature shadow-masks. The use of a *nanostencil* or tiny mask with nano-apertures opened in ultrathin solid-state membranes, allows for a direct, selective and clean deposition of various materials on almost any type of surface. Nanostenciling is a “resist-free”, parallel fabrication process, very much compatible with high and ultra high vacuum technology and thus a valuable approach to pursue fundamental research in a university environment.

Through the combination of pulsed laser deposition (PLD) with nanostenciling, we have focused on patterning of two representative material-systems: (i) semiconductor germanium-silicon heterostructures and (ii) functional perovskite-type ferroelectric and multiferroic oxides.

The work undertaken on patterning of Ge/Si heterostructures was two-fold. Firstly, using deposition through nanostencils mechanically attached to the substrate, we demonstrate a resist-free and site-selective growth approach of arrays of Ge

nanocrystalline structures, with possible applications in optoelectronics. Secondly, using nanostencils as fabrication and patterning tools, we provide new insights into kinetic phenomena that lead to the growth of crystalline Ge dots during the PLD process.

We further demonstrated the method's high flexibility and its suitability for virtually any deposited material on any substrate, by fabricating ferroelectric oxides (e.g. BaTiO<sub>3</sub>) nanostructures. Their local ferroelectric properties were investigated using piezoresponse force microscopy, a unique method which enables studies of polar properties at the nanoscale and permits to investigate size effects (i.e. suppression of ferroelectricity below a critical size at room temperature) in patterned ferroelectric nanostructures. In the case of multiferroic complex oxides (e.g. BiFeO<sub>3</sub> and Bi<sub>2</sub>FeCrO<sub>6</sub>), stenciling proved to be a valuable tool for enabling investigations into the multifunctionality of individual nanostructures. In the particular case of the newly predicted quaternary Bi<sub>2</sub>FeCrO<sub>6</sub> multiferroic, we obtained for the first time, epitaxial structures which we proved to be both ferroelectric and magnetic at room temperature.

This work demonstrates the generality of nanostenciling and its suitability as an excellent alternative approach to nanofabrication and patterning, since different material systems, ranging from metals to semiconductors to complex oxides, can be treated with the same ease.



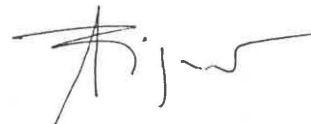
---

Cristian Victor Cojocaru  
Ph.D. Student



---

Prof. Federico Rosei  
Thesis Advisor



---

Prof. Alain Pignolet  
Thesis Co-Advisor

# Acknowledgements

I express my entire gratitude to my thesis advisor Professor Federico Rosei for offering me the opportunity to work in his group, for the freedom given in exploring the “nano-realm” and for his ongoing support, faith and valuable advice. I am also grateful to my thesis co-advisor, Professor Alain Pignolet who guided my endeavors in the fascinating field of “ferroics” and who supervised my work with patience and sound advice.

It was a great pleasure to pursue my studies and research in the environment provided by INRS-EMT Varennes center. During the last four years, I have been member of two groups: Nano Femto Lab and Ferroic Lab. My warmest thoughts and thanks go to their past and present members: Dr. Fulvio Ratto, Jill Miwa, Dr. Catalin Harnagea, Dr. Krishna Nath, Dr. Daria Riabinina, Dr. Fabio Cicoira, Dr. Fiorenzo Vetrone, Fabio Variola, Dr. Josh Lipton-Duffin, Dr. Jennifer Macleod, Dr. Sylvain Clair, Afshin Dadvand, Olivier Gautreau and Riad Nechache. They are great colleagues and I was fortunate to work and collaborate with them.

Many thanks as well for the INRS-EMT technical support offered by Georges Veilleux, Christophe Chabanier, Pierre-Paul Mercier, Etienne Charette, and Christian Dubuc.

I would like to thank Professors Roberto Morandotti, Peter Grütter and Yves-Alain Peter, to have agreed to be members of the evaluation jury for this thesis and to devote their time to evaluate this document.

I am deeply grateful to my parents, Cornelia and Mircea Cojocaru, who offered unconditional support, encouragement and valuable counsel at each moment of my life. Their foresight and values guided me in pursuing my goals.

I wouldn't have gone so far in this endeavor without the immense support, endless patience, trust and love of my wife, Oana. Thank you from the bottom of my heart!

# Table of Contents

Abstract.....	iii
Acknowledgements.....	v
Table of contents.....	vi
List of figures.....	x
List of tables.....	xv
<b>1. Introduction</b>	<b>1</b>
1.1 The “nano-realm”: a brief history.....	1
1.2 What does “nano” bring?.....	3
1.3 Defining the science and technology at the nanoscale.....	6
1.4 Functional nanostructures from functional materials.....	7
1.5 Objective and structure of the thesis.....	8
1.6 References.....	11
<b>2. Fabricating and Patterning at the Nanoscale: Concepts and Strategies</b>	<b>13</b>
2.1 The quest for nanopatterning.....	13
2.2 “Top-down” versus “Bottom-up”.....	16
2.2.1 Generating and replicating patterned features via top-down.....	16
2.2.2 Bottom-up via self-assembly and “assisted” self-organization.....	17
2.3 “Conventional” versus “Unconventional”.....	19
2.3.1 Conventional patterning processes.....	19
2.3.1.1 Patterning with photons and particles.....	20
2.3.2 Unconventional patterning processes.....	27
2.3.2.1 Scanning probe lithography.....	27
2.3.2.2 Patterning with stamps and molds.....	29
2.3.2.3 Patterning via controlled deposition.....	33
2.4 Summary.....	37
2.5 References.....	38

<b>3. Experimental and Characterization Approaches</b>	<b>43</b>
3.1 Introduction.....	43
3.2 Nanostencil fabrication processes.....	44
3.2.1 Wafer flow process (WFP).....	45
3.2.2 Membrane flow process (MFP).....	48
3.2.2.1 FIB drilling of free-standing SiN ultra-thin membranes.....	51
3.3. Pulsed laser deposition (PLD) technique for growth of thin films and structures.....	53
3.3.1 Background.....	53
3.3.2 PLD parameters.....	55
3.3.3 PLD-nanostencil experimental apparatus.....	60
3.4 Characterization Approaches.....	62
3.4.1 Scanning electron microscopy (SEM).....	62
3.4.2 X-ray diffraction (XRD).....	65
3.4.3 Micro-Raman spectroscopy.....	67
3.4.4 Scanning probe microscopy (SPM).....	68
3.4.4.1 Atomic force microscopy (AFM).....	69
3.4.4.2 Piezoresponse force microscopy (PFM).....	71
3.4.4.3 Magnetic force microscopy (MFM).....	74
3.5 References.....	76
<b>4. Nanostenciling of Semiconductor Ge/Si Heterostructures via Pulsed Laser   Deposition</b>	<b>79</b>
4.1 Introduction.....	79
4.2 Ge/Si nanostructures.....	82
4.2.1 Growth mechanisms.....	82
4.2.2 Self-assembled and self-organized Ge/Si nanostructures on pre-patterned substrates.....	84
4.3 Growth and patterning of germanium via PLD.....	87
4.3.1 Ge PLD nanostenciling at room temperature.....	88
4.4 Ge PLD patterning in the high temperature regime.....	93

4.4.1 Ge patterned islands on Si(100): coverage dependence of island morphology.....	94
4.4.2 Micro-Raman analysis of patterned Ge/Si(100) islands.....	98
4.4.3 Ge patterned islands on Si(111).....	100
4.4.4 Effect of the laser repetition rate on Ge QD density.....	101
4.4.5 Micro-Raman characterization of patterned Ge/Si(111) islands.....	105
4.5 Summary.....	107
4.6 References.....	109
<b>5. Nanostenciling of Functional Perovskite-type Complex Oxides via Pulsed Laser Deposition</b>	<b>112</b>
5.1 Introduction.....	112
5.2 Piezoelectricity and Ferroelectricity.....	115
5.3 Ferroelectric nanostructures and size effects.....	119
5.4 Nanostenciling of piezoelectric / ferroelectric materials.....	124
5.4.1 Patterning of barium titanate (BaTiO <sub>3</sub> ).....	125
5.4.1.1 Room-temperature patterning regime.....	126
5.4.1.2 High-temperature patterning regime.....	136
5.5 Nanostenciling of multiferroics.....	145
5.5.1 Patterning of Bismuth Ferrite (BiFeO <sub>3</sub> ).....	146
5.5.2 Patterning of Bi <sub>2</sub> FeCrO <sub>6</sub> .....	151
5.6 Summary.....	159
5.7 References.....	160
<b>6. Conclusions and Outlook</b>	<b>164</b>
6.1 General.....	164
6.2 Summary of findings.....	165
6.3 Outlook.....	168
6.4 References.....	170

<b>List of publications.....</b>	<b>171</b>
<b>Appendix A.....</b>	<b>172</b>
<b>Appendix B.....</b>	<b>173</b>
<b>Résumé en français.....</b>	<b>1-25</b>

## List of figures

Figure 1.1: Iron (Fe) on (111) copper (Cu) “Quantum coral”.....	2
Figure 2.1: Schematics of optical lithography process.....	20
Figure 2.2: Extreme ultraviolet lithography (EUVL) schematics.....	22
Figure 2.3: Laser interference lithography (LIL) technique based on dual-beam interference and Lloyd’s mirror interferometer configuration.....	24
Figure 2.4: Schematics of dip-pen nanolithography (DPN) principle.....	28
Figure 2.5: Schematics of replica molding.....	29
Figure 2.6: Schematics of thermal nanoimprint (T-NIL) and step and flash nanoimprint (S-FIL) processes.....	31
Figure 2.7: Schematics of static nanostenciling approach.....	33
Figure 3.1: Schematic drawings of wafer flow and membrane flow processes used for nanostencil fabrication.....	44
Figure 3.2: Optical images of nano/micro-stencils.....	46
Figure 3.3: SEM micrographs of stencils fabricated by LIL and reactive ion etching (RIE).....	46
Figure 3.4: Patterned architectures milled in silicon carbide (SiC) and silicon nitride (SiN) membranes.....	50
Figure 3.5: Focused ion beam (FIB) images of SiN milled membranes.....	52
Figure 3.6: Schematics of the PLD – nanostencil apparatus.....	60
Figure 3.7: Schematic drawing of stencil deposition.....	61
Figure 3.8: SEM micrographs of bismuth ferrite (BiFeO <sub>3</sub> ) structures on (100) Nb doped strontium titanate (SrTiO <sub>3</sub> ) substrate.....	64
Figure 3.9: X-ray diffraction: schematics and diffraction patterns recorded in grazing incidence mode.....	65
Figure 3.10: Energy diagram for Raman scattering.....	67

Figure 3.11	Schematics of the operation principle of an atomic force microscope (AFM) set-up with an optical detection of the cantilever bend.....	70
Figure 3.12	Schematics of the operation principle for piezoresponse force microscopy (PFM).....	71
Figure 3.13	Ferroelectric domain imaging in (001)-oriented barium titanate (BaTiO <sub>3</sub> ) revealed by PFM.....	72
Figure 3.14	Magnetic force microscopy (MFM) image obtained by scanning an area of patterned BiFeO <sub>3</sub> structures on (100) Nb: SrTiO <sub>3</sub> .....	75
Figure 4.1	Schematics of the three distinct epitaxial growth modes governing hetero-systems growth.....	82
Figure 4.2	Stacking Ge nano-islands on Si(001): cross sectional TEM .....	85
Figure 4.3	SEM micrograph detail of arrays of assorted apertures opened by FIB milling in SiN membranes and Ge patterned structures replicated through the sieves at room temperature.....	89
Figure 4.4	AFM topography of Ge patterned islands.....	91
Figure 4.5	SEM micrographs of patterned arrays of Ge islands after consecutive depositions through the same stencil.....	92
Figure 4.6	Ge patterned areas corresponding to 14 perforated membranes built in the LIL-based stencils.....	94
Figure 4.7	AFM topography and Ge mounds height profile obtained for 250 pulses at 600°C using a stencil with hexagonal arrays of aperture.....	95
Figure 4.8	SEM micrographs of ordered Ge nanostructures replicated on Si (100) by pulsed laser deposition for (a) 250, (b) 750, (c) 1250 and (d) 1500 laser pulses.....	95
Figure 4.9	Stencil-induced structures thickness gradient: schematics and sequence of SEM micrographs.....	97
Figure 4.10	Raman spectra acquired by probing the Ge patterned areas with the 514.5 nm line of an Ar <sup>+</sup> ion laser.....	98

Figure 4.11	The dependency of the integrated intensity of Ge-Ge phonon peak with the number of pulses and phonon frequency shift vs. number of pulses.....	99
Figure 4.12	SEM micrographs of arrays of Ge mounds and dots obtained on Si (111) at 600°C via direct patterning through the nanostencils.....	100
Figure 4.13	SEM micrographs of Ge patterned on Si (111) at 600 °C for 1000 laser pulses and different repetition rates.....	102
Figure 4.14	SEM micrographs of Ge QDs obtained for (a) 1000 and (b) 2000 laser pulses.....	103
Figure 4.15	Statistical distribution of the number of QDs per deposited site for (a) 1000 and (b) 2000 laser pulses; and size distribution (QD major length) for (c) 1000 and (d) 2000 laser pulses	104
Figure 4.16	Micro-Raman spectroscopy on patterned Ge/Si(111) .....	105
Figure 4.17	SEM micrographs of Ge QDs obtained by PLD stenciling for 1000 and 2000 laser pulses respectively and detail of Raman spectra around the Ge-Ge phonon mode at $300\text{ cm}^{-1}$ .....	106
Figure 5.1	The crystal structure of tetragonal barium titanate ( $\text{BaTiO}_3$ ).....	113
Figure 5.2	$\text{ABO}_3$ perovskite crystal structure for: cubic, high temperature, paraelectric phase and tetragonal, room temperature, piezoelectric/ferroelectric phase.....	116
Figure 5.3.	Hysteresis loop of an ideal ferroelectric domain and hysteresis loop of a real ferroelectric material.....	117
Figure 5.4	Ferroelectric nanostructures: $\text{SrBi}_2\text{Ta}_2\text{O}_9$ (SBT) test structures fabricated by FIB milling and e-beam direct writing (EBDW).....	122
Figure 5.5	AFM topography image of an array of ferroelectric PZT cells on Nb doped $\text{SrTiO}_3$ substrate prepared by imprint lithography.....	123
Figure 5.6	$\text{BaTiO}_3$ film deposited at room temperature and in vacuum: AFM profilometry and XRD spectra recorded in grazing-incidence mode after annealing of the film.....	127

Figure 5.7	SEM micrograph of a LS-SiN sieve and of ordered arrays of BaTiO <sub>3</sub> structures obtained by deposition through it.....	128
Figure 5.8	SEM micrograph detail of BaTiO <sub>3</sub> structures patterned through 350 nm wide apertures and AFM section profile of the structures.....	129
Figure 5.9	AFM topography and typical section profiles for BaTiO <sub>3</sub> arrays.....	130
Figure 5.10	SEM micrographs of BaTiO <sub>3</sub> patterned structures obtained with the same stencil used in consecutive depositions.....	131
Figure 5.11	3-D AFM topography and section profiles for BaTiO <sub>3</sub> patterned at room temperature and BaTiO <sub>3</sub> after annealing at 900°C.....	132
Figure 5.12	Grazing incidence X-ray diffraction patterns for BaTiO <sub>3</sub> samples patterned at room temperature and annealed in O <sub>2</sub> above 650 °C.....	133
Figure 5.13	AFM topography and PFM domain image of the BaTiO <sub>3</sub> arrays prepared at room-temperature and post deposition annealed at 900°C...	134
Figure 5.14	AFM topography in contact mode, PFM switching and piezoresponse hysteresis loop recorded from individual structures.....	135
Figure 5.15	SEM micrographs for the ordered BaTiO <sub>3</sub> arrays obtained in conditions described in table 5.1.....	137
Figure 5.16.	AFM topography in tapping mode and section analysis for the structures showed in the SEM micrographs from fig. 5.15.....	138
Figure 5.17	X-ray diffraction spectra ( $\theta$ -2 $\theta$ ) for patterned BaTiO <sub>3</sub> samples listed in table 5.1.....	139
Figure 5.18	X-ray diffraction spectra ( $\theta$ -2 $\theta$ ) detail recorded in the range 20 - 25°.....	140
Figure 5.19	X-ray reciprocal space mapping (RSM) performed for BaTiO <sub>3</sub> film and patterned samples listed in table 5.1.....	141
Figure 5.20	BaTiO <sub>3</sub> (c/a) ratio versus O <sub>2</sub> pressure for the samples given in table 5.2.....	142
Figure 5.21	PFM domain images and local piezoresponse hysteresis loops recorded from samples BTO I and BTO II.....	143
Figure 5.22	The interplay between spontaneous electric polarization (P), spontaneous magnetization (M) and spontaneous strain ( $\epsilon$ ) that might be present in a multiferroic material.....	145

Figure 5.23	SEM micrograph of BiFeO <sub>3</sub> stenciled at RT. AFM topography and PFM domain image of the structures after RTA annealing.....	148
Figure 5.24	SEM micrographs of BiFeO <sub>3</sub> stenciled patterns on (100) SrTiO <sub>3</sub> substrates at high temperature.....	149
Figure 5.25	X-ray diffraction spectra for BiFeO <sub>3</sub> patterned at low-oxygen pressure and reciprocal space maps.....	150
Figure 5.26	Stenciling of multiferroic Bi <sub>2</sub> FeCrO <sub>6</sub> .....	152
Figure 5.27	SEM micrograph showing the elongation along one crystallographic axis and structures down to 150 nm.....	153
Figure 5.28	X-ray diffraction spectra ( $\theta$ -2 $\theta$ ) for the Bi <sub>2</sub> FeCrO <sub>6</sub> structures.....	154
Figure 5.29	High-resolution cross-section TEM image taken along the [010] direction and showing a part from a Bi <sub>2</sub> FeCrO <sub>6</sub> island.....	155
Figure 5.30	Characterization of the ferroelectric behavior of the Bi <sub>2</sub> FeCrO <sub>6</sub> structures via AFM / PFM measurements.....	156
Figure 5.31	MFM measurements performed in magnetic field (~250 Oe) showing the magnetic switching of Bi <sub>2</sub> FeCrO <sub>6</sub> patterned structures.....	157
Figure 5.32	Magnetic hysteresis loops recorded from the Bi <sub>2</sub> FeCrO <sub>6</sub> patterned area via vibrating sample magnetometry.....	158

## List of tables

Table 5.1:	Deposition conditions for BaTiO <sub>3</sub> growth and patterning	136
Table 5.2:	In-plane and out-of plane lattice parameters for BaTiO <sub>3</sub> film and patterned structures	142
Table 5.3:	In-plane and out-of plane lattice parameters for BiFeO <sub>3</sub> film and patterned structures	150

*“We are on the verge of a new scientific and technological era,  
the standard of which is the nanometer”*  
H. Rohrer

# **1. Introduction**

## **1.1 The “nano-realm”: a brief history**

The rise of a new realm, the “*nano-realm*”, was envisioned by Richard Feynman in the seminal talk “*There’s Plenty of Room at the Bottom: an Invitation to Enter a New Field of Physics*” given in 1959 at the annual meeting of the American Physical Society at the California Institute of Technology (Caltech) [1]. At the time, Feynman outlined a number of appealing reasons for which a “general ability” to manipulate matter on an atomic scale would be not only informative for various scientific communities but also valuable for industrial and economic applications. He talked in particular about the prospects of denser information data storage and computer circuitry by “*writing*” and further “*replicating*” at smaller scales. Moreover he discussed the need to develop microscopes that could “*read*” at this scale and eventually “*see*” things much smaller than possible with a scanning electron microscope (SEM)<sup>1</sup>. He also pointed out the tremendous usefulness of precisely “*placing*” atoms at desired locations, for instance for the purpose of advancing synthetic chemistry.

Two decades after Feynman’s remarkable lecture, research scientists from IBM-Zurich advanced his dream and created the scanning tunneling microscope (STM) (G. Binnig and H. Rohrer, 1981) [2], which was followed later by the atomic force microscope (AFM) (G. Binnig, C.F. Quate and G. Gerber, 1986) [3]. Since then, both STM and AFM have become highly valuable tools for “*seeing*” and “*touching*” matter at the atomic scale. In this context, one of the most astonishing performances in

---

<sup>1</sup> Ernst Ruska, invented the first electron microscope in 1933; he was awarded Nobel Prize in Physics 1986 together with G. Binnig and H. Rohrer for the STM.

manipulating, positioning and imaging individual atoms is represented by the work of D. Eigler and E. Schweizer from IBM-Almaden (1990), who used a STM tip to write their company's logo with individual xenon (Xe) atoms [4]. Two years later, Eigler's team demonstrated the manipulation of 48 iron (Fe) atoms on a copper (Cu) surface into a circular ring to "corral" some of the surface electrons (Fig. 1.1) and force them into quantum states determined by the circular corral walls [5].

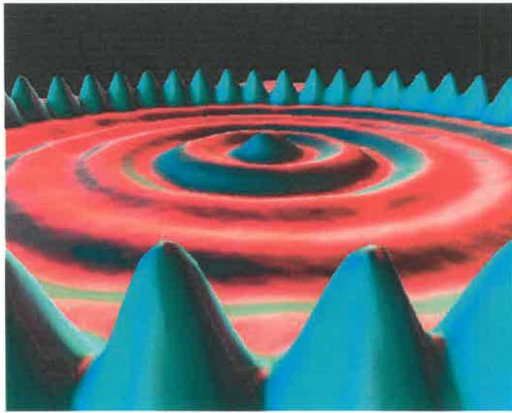


**Figure 1.1** Fe on Cu (111) "Quantum coral"  
The ripples in the ring of atoms are the wave patterns of some of the electrons that were trapped in the corral.

[<http://www.almaden.ibm.com/vis/stm/corral.html>]

The birth of STM and AFM triggered further development of a wealth of new types of instruments and characterization methods, sharing in principle the basic features of STM and AFM, but undergoing modifications suitable for novel applications [6,7]. They are now all broadly referred to as scanning probe microscopes (SPMs) [8] and they have been the enablers of the tremendous advancement of science and technology pursued at the *nano* scale. Concurrently, "elder" techniques such as electron based microscopy (i.e. SEM and TEM), optical spectroscopy (e.g. micro-Raman) or X-ray based techniques have been continuously developed. At present, there is a vast number of complementary tools and techniques capable of revealing the structure, bonding and electronic properties of condensed matter, at increasingly local levels, guiding us in the fascinating realm of "*nano*".

In the same 1959 lecture, Feynman also partially tackled the concept of "*nanotechnology*" (without naming it) proposing the manipulation of matter on an atomic scale with a "top - down" approach. He presented his ideas of micro/nano-manufacturing by imagining "ordinary machine-shop tools" capable of developing and operating sets of "one-fourth" and even "one-sixteenth-scale" smaller machine tools, that eventually will

be operated by “miniaturized hands”. Due to the long term resonance of his lecture on the possibilities of engineering at the atomic and molecular scale, Richard Feynman is generally regarded as one of the founding fathers of today’s *nanotechnology*. However, it was only in 1974 that the term “*nanotechnology*” was first introduced by Norio Taniguchi, professor at Tokyo Science University, when he referred to precision manufacturing at the nanometer scale for traditional silicon machining [9]. Since then, nanotechnology had impacted gradually almost every segment of our society. Currently, developments in nanotechnology are fueling advancements in information technology, chemicals, pharmaceuticals, health care, transportation, energy, defense, environmental sciences, and manufacturing. From manufacturing “nano”-electronic devices to incorporating “nanoparticles” in cosmetics or targeting them to destroy viruses and to “nano-coating” textiles, the spectrum of opportunities is huge.

Developing *nano-materials* turns out to represent much more than just a step further in downsizing; it is about using the knowledge of the atomic realm to produce *novel functionalities* in a reliable and cost-effective way. Finding answers to Feynman’s inquiry “*What would the properties of materials be if we could really arrange the atoms the way we want them?*” represents, even after almost 50 years, the driving force behind the research efforts undertaken today in the various fields of nanoscience and technology.

## 1.2 What does “nano” bring?

The prefix “nano”, derived from the Greek word *nanos*, literally means dwarf. In science (and technology), one nanometer (1 nm) is one-billionth of a meter ( $10^{-9}$ m), and can be imagined as approximately ten hydrogen atoms placed in a row. For a more visual comparison of scale: a human hair is  $\approx 80,000$  nm wide and a red blood cell is  $\approx 7000$  nm wide. The nano-scale is comparable to the associated DeBroglie wavelength of an electron and to the sizes of most biological molecules.

Remarkable properties (e.g. catalytic, mechanical, electronic, magnetic, and optical) are revealed as the dimensions of a bulk crystal - practically an infinite and periodic system - are reduced to a system composed of a relatively small number of atoms [10]. These properties are not present at macro- or micro-scales and therefore

*engineered nanoscale structures*, either by way of a *top-down* or a *bottom-up* approach<sup>2</sup>, go further than just another step towards miniaturization [11].

Two main reasons explain this change in properties: first an increased *surface area to volume (S/V)* ratio for a “nano” entity, and second the appearance and dominance of *quantum effects* due to the reduced dimensionality.

For example, a spherical particle with a radius of 1 nm has a surface to volume ratio equal to  $3 \times 10^9 \text{ (nm}^{-1}\text{)}$ . This increase in surface area (per unit mass) usually leads to increased chemical reactivity (as growth and catalytic chemical reactions occur at surfaces), making the *nanomaterial* an excellent *catalyst* for chemical processes [12].

Another significant example is extended tubes of rolled *graphene* sheets (a few nanometers in diameter and several micrometers to centimeters long) called carbon nanotubes (CNTs). Firstly reported by Iijima in 1991 [13], carbon nanotubes are currently intensively investigated due to their novel chemical and physical properties. They prove mechanically very strong (their Young’s modulus is over 1 terapascal, making CNTs as stiff as diamond), are flexible (about their axis), and conduct electricity extremely well (the *helicity* of the graphene sheet determines whether the CNT is a semiconductor or metallic). All of these outstanding properties give CNTs a range of potential applications: for example in nanoelectronics, reinforced composites, sensors and display devices [14].

As the size of matter is reduced to tens of nanometers new properties may appear. For example, gold and silver nanoparticles less than 100 nm in diameter appear red or blue in color due to a shift in the plasmon resonance frequency [15]. In fact, *size-dependent* properties have been exploited (unknowingly) for centuries. Scrap metals have been used as colored pigments in stained glass and ceramics since ancient times by Egyptians and Romans glassmakers. For instance, the famous Lycurgus Cup (British Museum), has a murky mustard color but glows purple-red to transmitted light and green in reflected light due to tiny gold particles (~70 nm in diameter) embedded in the glass. The challenge for the ancient (*al*)chemists was to make all the particles the same size (and hence exhibiting the same color) - the fabrication of single-size nanoparticles is still a challenge today.

---

<sup>2</sup> In top-down processes, the “bulk” material is progressively structured to obtain ever smaller features; in bottom-up processes the natural tendency of atoms and molecules to assemble and form regular structures is exploited; these concepts are described in detail in Chapter 2

Presently, semiconductor nanoparticles made small enough so as to exhibit quantum effects and called “quantum dots” (QDs) represent an area of research of great interest [16]. The electronic band structure of QDs resembles the discrete energetic levels found in atoms, thus QDs are often referred to as “artificial atoms”. As energy is related to wavelength, and thus to color, the optical properties of the QDs can be finely tuned depending on their size. Thus, QDs can be made to emit or absorb specific wavelengths of light merely by controlling their size, therefore exhibiting certain colors. Recently, QDs have found applications as fluorescent biological labels for cell diagnosis which use both their small particle size and their tunable energy levels. Among other appealing applications for QDs let us mention nanoelectronics and optoelectronics, quantum information storage [17] and quantum computing [18]. In relation to these latter potential applications we present in Chapter 4 the nanostenciling of crystalline germanium dots on silicon surfaces as an alternative method to pattern semiconductor QDs on a substrate.

Nanowires, i.e. one-dimensional (1D) crystalline structures (or linear arrays of dots) that can be practically made from a wide range of materials, represent another huge area of interest [19]. Single crystalline nanowires allow researchers to observe relatively strong 1D confinement effects for both carriers and phonons. Semiconductor nanowires made of silicon, germanium or III-IV compounds have demonstrated significant optical, electronic and magnetic characteristics. Nanowires have potential applications in high-density data storage, either as magnetic read heads or as patterned storage media, as well as for metallic interconnects of quantum devices and nanodevices [20].

Another potential application of nanoparticles, nanotubes and nanowires is in *composites*, materials that combine one or more distinct components and which are designed to exploit particular properties of each component. For instance, carbon fibers are used to reinforce plastic – with applications in aerospace, automotive and small consumer goods. Bundles of multi-walled carbon nanotubes (CNTs) are used in polymers to control or enhance conductivity, with applications such as antistatic packaging. For automotive components, nanoparticles, nanotubes, dispersed within a matrix material offer very promising opportunities [21]; for example, carbon black is used as a filler to reinforce car tires and nanoclays (clays from the smectite family) are used as fillers in polymers for fabrication of new types of nanocomposites.

## 1.3 Defining science and technology at the nanoscale

*“Nano-technology mainly consists of the processing of separation, consolidation, and deformation of materials by one atom or one molecule”* stated Prof. Taniguchi who coined the term in 1974. As previously stated, the main driving force for *miniaturization* came from the electronics industry, which aimed to develop tools to create smaller, faster and more complex electronic devices on silicon chips. The doubling of computing power every eighteen months, known as Moore's Law [22], is one of the more commonly cited examples of such progress.

Today, a primary issue facing nanotechnology is the confusion about its definition. In the inaugural issue [23] of the journal *Nature Nanotechnology* several researchers and scientists attempt to give a definition and from enthusiastic to skeptical, the responses reflect a variety of opinions. Thus naturally appears the question “what exactly is nanotechnology?” Even though there is no standard definition, perhaps one of the most widely accepted definitions of *nanotechnology* appears on the NASA website: *“Nanotechnology is the creation of functional materials, devices and systems through control of matter on the nanometer length scale (1-100 nanometers), and exploitation of novel phenomena and properties (physical, chemical, biological) at that length scale”*<sup>3</sup>.

In the definition above, by the “control of matter” is generally understood the control of the *shape, size and composition* of these entities and for application purposes their precise *positioning* (registration) via a suitable fabrication process. Presently nanostructure fabrication is a formidable challenge and the subject of many studies. Once *nanofabrication* is successfully achieved, we resort to a wide range of techniques to study the phenomena governing these small entities so as to understand if their properties differ significantly from those at a larger scale. Thus, new science is emerging and we may call *nanoscience* the science that deals with nano-entities. It is generally considered nowadays that “nanoscience” deals with understanding the size-dependent effects and their influence on the properties of reduced-size materials whereas “nanotechnology” aims to exploit these effects to create functional materials, devices and systems for next-generation technology.

---

<sup>3</sup> <http://ipt.arc.nasa.gov/nanotechnology.html>

At the laboratory scale and at the level of prototyping, the pursuit of nano-scale engineering has been mostly focused on explorations of individually “crafted” nanostructures [24-27]. Here we define *nanostructures* as architectures which have structured components with at least one dimension less than 100 nm [28]. The investigation of isolated nanostructures and the characterization of single nanodevices are of great importance and, as expected, of strong appeal to researchers. Even more challenging and perhaps of greater potential for novel applications is the collective behavior of nanostructures. Finding ways to manipulate large ensembles of nanostructures and to integrate and pattern them into *functional units* may result in a fundamental change of the systems properties different from the classical or individual-behavior of the latter. Thus, it is both attractive and natural to explore ways to advance both the fabrication capabilities and the scientific investigations. This applies to fabricating, manipulating, measuring and understanding *functional nanostructures*.

## 1.4 Functional nanostructures from functional materials

Functional materials cover a broad range of materials with physical and chemical properties sensitive to a change in their environment such as temperature, pressure, electric or magnetic fields, optical irradiation, etc. and thus able to perform a specific function using their intrinsic properties [29]. Examples include: pyroelectrics, piezoelectrics, ferroelectrics, semiconductors, ionic conductors, superconductors, electro and magneto optic materials, magnetic materials. They are expected to be the building-blocks of the newly emerging “*smart systems*” allowing those to achieve high-performance in sensing, processing, actuating, giving feedback or self-recovering in response to environment change. In this context, in Chapter 5 of this thesis we will elaborate on the functionality of oxide ceramics that exhibit *ferroic* properties.

The key aspect for the development of novel functional materials and their integration into smart systems is the ability to control the *relationship* between their *structure* and *properties* thus improving their response to specific environmental changes and accordingly optimizing their functions. At the nanoscale in particular, as our understanding of physical properties and ability to control features morphology and

positioning via fabrication improves, there is a definite potential to create a range of materials with novel characteristics, functions and applications.

As pointed out previously, the functionality of nanomaterials arises from either surface-area or quantum effects that begin to dominate their properties thus making them excellent candidates for advanced technology. In this context, the controlled fabrication of various types of structures with dimensions in the nanoscale becomes imperative. Advanced lithographic methods that make use of radiation with wavelengths smaller than visible light (e.g. e-beams or x-rays) and apply otherwise the same technological processes known from conventional resist-based lithography are under constant development to accomplish the tasks of fabricating and patterning at the nanoscale. Yet, very often, the preparation of high-quality nanodots, nanotubes or wires relies on *self-assembly* (“natural arrangement” of atoms on surfaces) and *self-organization* (onto pre-patterned substrates) processes, accomplished via various growth techniques such as chemical vapor deposition (CVD), physical vapor deposition (PVD) such as molecular beam epitaxy (MBE), or electrodeposition etc. Technologically much simpler and cost-effective, these approaches have the disadvantage of less control over the resulting structures’ size and shape but mostly very little control on their registration. Alternative techniques to traditional photolithography have recently emerged and are currently being developed, showing great promises mainly due to their low-cost and flexibility. In this context, along this thesis, we will evaluate and show the potential offered by “nanostenciling” in delivering high-quality patterned functional nanostructures.

## 1.5 Objective and structure of the thesis

In this thesis we focus on the *controlled growth, positioning and characterization of nanostructured functional materials* such as semiconductor heterostructures and perovskite-type complex oxides by means of *unconventional patterning* techniques. The main approach investigated and developed in this project is based on *nanostenciling*, i.e. the site-selective growth of nanostructures by deposition through miniature shadow-masks [30-33].

Stenciling (shadow-masking or screen printing) has always been a convenient practice in the patterning of electronic components such as printed circuit boards (PCB). Fabricated either from stainless steel or plastic, stencils are frequently used for the application of solder paste in surface mount technology (SMT) (e.g. soldering the leads) or adhesives in advanced packaging. Metal grids, screens, filters and sieves constitute further types of stencils, commercially available, mainly used in the fabrication of printed circuit boards or in a wide range of vacuum chamber evaporation and sputtering deposition processes. These practical, simple and well established methods for microscale-patterning represent the starting point for new applications in nanotechnology.

The use of a *nanostencil*, a tiny mask with nano-apertures opened in ultrathin solid-state membranes, in close proximity with a substrate allows direct, selective and uncontaminated deposition of many materials on almost any type of surface. Therefore the method is highly suitable for parallel prototyping of various materials and suitable for direct deposition on fragile, functionalized or pre-processed surfaces. It is a resist-free, parallel process highly compatible with high and ultra-high vacuum technology. These attributes designate nanostenciling as the technique of choice for laboratory-environment nanoscale prototyping and as an invaluable tool for studies of novel material-systems.

A common task within these studies is to assess the capability of nanostenciling, as a *general-purpose nanoscale patterning method* that combines high resolution, high purity and flexibility with respect to the choice of deposited material and substrate. To address these issues, using the pulsed laser deposition (PLD) as synthesis technique, we have focused on nanoscale patterning of: (i) semiconductor germanium-silicon heterostructures and, (ii) perovskite-type ferroelectric and multiferroic oxides.

Through detailed studies we aim not only to evaluate the feasibility of nanostenciling as an alternative approach for nanostructure fabrication, but also to gain important insights into kinetic processes associated with the growth of nanostructures (e.g. Ge/Si) and size-effects of novel functional materials (e.g. ferroic and multiferroic materials). The choice of these two major material systems is due to their significant application potential in optoelectronics and high-density data storage media, making them desirable systems from not only a fundamental perspective but from an application one as well.

The main drawbacks associated with deposition through stencils i.e. gradual clogging of apertures and membrane deformation due to the deposition-induced stresses are equally addressed and discussed.

This thesis is organized as follows: In *Chapter 2* we discuss the concepts of “top-down” and “bottom-up” fabrication and offer a selective review on both “conventional” (photo/particle beam lithography) and “unconventional” (molding, imprinting, stenciling) strategies for nanofabrication and surface nanopatterning. The *nanostenciling* approach is introduced in the context of newly emerging and promising techniques able to deliver high-quality structures at the nanoscale. The experimental work undertaken to prepare the nanostencils is presented in *Chapter 3*. Two main routes used to fabricate solid-state miniature show-masks, i.e. via laser interference lithography and focused ion beam techniques are described in detail. The characterization techniques employed for the morphological, structural and compositional analysis of the patterned nanostructures are also discussed. In *Chapter 4* we present the results from Ge/Si nanostenciling via PLD. We show that this is a simple, resist-free approach to pattern arrays of Ge nanocrystalline structures, with possible applications in optoelectronics. We also provide new insight into the kinetic phenomena that lead to the growth of crystalline Ge dots during the laser ablation process, observing a modified Stranski-Krastanov type growth induced by the finite size of the wetting layer under each aperture location. *Chapter 5* deals with the PLD nanostenciling of functional perovskite-type complex oxides. In a first phase we present results on nanostructuring of prototypical piezoelectric and ferroelectric barium titanate ( $\text{BaTiO}_3$ ). The local ferroelectric properties are investigated using piezoresponse force microscopy, a unique ultra-local characterization method which enables studies of possible size effects (i.e. suppression of ferroelectricity below a critical size at room temperature) in patterned ferroelectric nanostructures. Novel system materials such as multiferroic bismuth ferrite ( $\text{BiFeO}_3$ ) and the theoretically predicted but only recently synthesized bismuth iron chromium oxide ( $\text{Bi}_2\text{FeCrO}_6$ ) are investigated and discussed in the second section. *Chapter 6* concludes the thesis with a summary of our findings and perspectives for future work.

## 1.6 References

- [1] R. P. Feynman, Caltech's Engineering and Science XXIII, 22 (1960)
- [2] G. Binnig, H. Rohrer, Ch. Gerber and E. Weibel, Phys. Rev. Lett. 49, 57 (1982)
- [3] G. Binnig, C. F. Quate and Ch. Gerber, Phys. Rev. Lett. 56, 930 (1986)
- [4] D. M. Eigler and E. K. Schweizer, Nature 344, 524 (1990)
- [5] M. F. Crommie, C. P. Lutz and D. M. Eigler, Science 262, 218 (1993)
- [6] P. Grütter, H. J. Mamin and D. Rugar, Springer Series Surf. Sci. 28, 151 (1992)
- [7] R. C. Dunn, Chem. Rev. 99, 2891 (1999)
- [8] A. I. Kingon, P. M. Vilarinho and Y. Rosenwaks, "*Scanning Probe Microscopy: Characterization, Nanofabrication and Device Application of Functional Materials*", Springer, (2005)
- [9] N. Taniguchi, Proc. Intl. Conf. Prod. Eng. Tokyo, Part II, Japan Society of Precision Engineering, (1974)
- [10] F. Rosei, J. Phys.: Condens. Matter. 16, S1373 (2004)
- [11] H. Rohrer, Microelectron. Eng. 27, 3 (1995)
- [12] G. A. Somorjai and R. M. Rioux, Catalysis Today 100, 201 (2005)
- [13] S. Iijima, Nature 354, 56 (1991)
- [14] P. M. Ajayan, J.-C. Charlier and A. G. Rinzler, PNAS 96, 14199 (1999)
- [15] P. K. Jain, X. Huang, I. H. El-Sayed and M. A. El-Sayed, Plasmonics 2, 107 (2007)
- [16] A. P. Alivisatos, Science 271, 933 (1996)
- [17] P. M. Petroff, A. Lorke and A. Imamoglu, Phys. Today 54, 46 (2001)
- [18] C. S. Lent, P. D. Tougaw, W. Porod and G. H. Bernstein, Nanotechnology 4, 49 (1993)
- [19] W. Liu and C. Lieber, J. Phys. D: Appl. Phys. 39, R387 (2006)
- [20] M. Law, J. Goldberger and P. Yang, Annu. Rev. Mater. Res. 34, 83 (2004)
- [21] H. Presting and U. König, Mat. Sc. and Eng. C 23, 737 (2003)
- [22] G. E. Moore, Electronics 38, 1 (1965)
- [23] Feature article, "*nan'o-technol'o-gy n.*", Nature Nanotech. 1, 8 (2006)
- [24] S. J. Tan, A. R. M. Verschueren and C. Dekker, Nature 393, 49 (1998)

- [25] H. W. C. Postma, T. Teepen, Z. Yao, M. Grifoni and C. Dekker, *Science* 293, 76 (2001)
- [26] Y. Huang, X. Duan, Y. Cui, L. J. Lauhon, K. H. Kim and C. M. Lieber, *Science* 294, 1313 (2001)
- [27] X. Duan, Y. Huang, R. Agarwal and C. M. Lieber, *Nature* 421, 241 (2003)
- [28] P. Moriarty, *Rep. Prog. Phys.* 64, 297 (2001)
- [29] Z. L. Wang and Z. C. Kang, “*Functional and Smart Materials: Structural Evolution and Structure Analysis*”, Springer, (1998)
- [30] J. Kohler, M. Albrecht, C. R. Musil and E. Bucher, *Physica E* 4, 1961 (1999)
- [31] M. M. Deshmukh, D. C. Ralph, M. Thomas and J. Silcox, *Appl. Phys. Lett.* 75, 1631 (1999)
- [32] R. Luthi, R. R. Schlittler, J. Brugger, P. Vettiger, M. E. Welland and J. K. Gimzewski, *Appl. Phys. Lett.* 75, 1314 (1999)
- [33] J. Brugger, J. W. Berenschot, S. Kuiper, W. Nijdam, B. Otter and M. Elwenspoek, *Microelectron. Eng.* 53, 403 (2000)

## **2. Fabricating and Patterning at the Nanoscale:** **Concepts and Strategies**

### **2.1 The quest for nanopatterning**

To accomplish its pledge, Nanotechnology must enter decisively into the market, assuring the link to the macroscopic world and endowing end-users with devices that accurately control events at the nanoscale. Therefore, *tailoring nanoscale functional structures* and *patterning* them into desired architectures, using a minimal number of processing steps, are among Nanotechnology's crucial issues. Applications demanding nano-scale patterning of thin films of functional materials extend nowadays from the fabrication of integrated circuits, media for data storage and display units to the creation of micro/nano-electromechanical systems (MEMS/NEMS), miniaturized sensors and actuators, micro-fluidic devices, micro-optical components, photonic band gap crystals, bio-chips and biocompatible nanostructured surfaces. For all these areas, advances in creating *suitable nanoscale fabrication and patterning techniques* [1-3] are the prerequisite for their successful development and subsequent commercialization.

The process of *patterning* is universally linked to that of *lithography*<sup>1</sup>, a practice which involves a flow of information that typically begins with the design of a pattern in the form of a drawing and ends with a patterned array of features on the surface of a material (substrate) of choice. In general, lithographic techniques involve the existence of

---

<sup>1</sup> The word *lithography* comes from the Greek *lithos* (stones) and *graphia* (to write) and it means quite literally writing on stones. Invented by the Bavarian author Aloys Senefelder in 1796, lithography is a printing process in which the image to be printed is rendered on a flat surface and treated to retain ink while the non-image areas are treated to repel ink.

the following key elements: (i) a pre-designed set of patterns in the form of a *mask* or a *master*, (ii) an *approach* to replicate or transfer the patterns, (iii) a *reactive medium* (usually called photoresist) capable of serving as a sacrificial layer for subsequent steps and (iv) *the equipment* that guarantees suitable processing.

The requirements for a lithographic process may vary considerably depending on the application. Materials that are to be processed, the size of the intended patterned area and frequently the minimum size of the projected features and their overlay accuracy are issues that one has to consider before choosing the appropriate lithographic technique. Very often, due to manufacturability throughput and cost considerations, stringent fabrication specifications might be imposed in industrial processes. For instance, in the semiconductor industry, where there is a continuous strive to downsize the features of integrated devices while preserving functionality, the patterning process involves profuse and complex lithographic steps and sophisticated tools that assure high accuracy in feature resolution and overlay and high-throughput of wafer production [4, 5].

Optical (projection) lithography (OPL) has been the main form of lithography used by the semiconductor industry community for several decades and most likely it will be used for another decade [6]. The central fabrication techniques that have emerged from development efforts in microelectronics (e.g. deep-UV (DUV), extreme-UV (EUV) or electron-beam lithography (EBL)) are however dedicated to patterning motifs in photo or electron-beam resists, spin-coated on planar, ultra-flat semiconductor surfaces. Adapting these lithographic methods to other areas of interest that may involve structuring and designing atypical materials or architectures [7] on non-conventional substrates represents a great challenge. Moreover, the well-established lithographic techniques are usually confined to a cleanroom environment that requires ever-increasing capital and operation costs.

Fewer restrictive conditions are imposed in research environments, where yield for production is not an issue. Very often, in a university laboratory, easily accessible, flexible nanofabrication techniques are required for experiments that enable an understanding of the *fundamental science* involved at the *nanometer scale* in fields such as materials science, microscopy, (nano)optics and organic optoelectronics or biological sciences to name a few. It is expected that applications of *functional nanostructures* will

touch areas that have not been demonstrated yet, such as nanoscale electronics, bio-sensing and nano-biomedicine. To aid in this goal, suitable patterning methods need to be explored to create and position nanostructures on non-planar (e.g. previously processed, curved or rough) surfaces or other functionalized and often fragile surfaces (membranes, cantilevers, organic layers). In this context, a variety of other forms of parallel lithography such as molding, stamping, imprinting or stenciling are revisited for their potential as “unconventional” nanofabrication and patterning alternatives that can alleviate “conventional” photolithography limitations and costs [8].

Along with the previously mentioned issues, the quest for controlled growth of nanostructured materials with *novel integrated functionality* represents an intrinsic and great challenge for materials science community. Exploring new routes to prepare multifunctional materials and understanding the relationship between their size/structure and their properties is therefore essential to provide the background knowledge that is needed to sustain the present pace of miniaturization and innovation.

The methods used for fabrication and patterning of nanostructures can be generally addressed from the viewpoint of two main concepts: “*top-down*” and “*bottom-up*”. We address these concepts in section (2.2) of the present chapter.

A further classification is presently made between “*conventional*” (optical based) and “*unconventional*” (non-optical based) patterning methods. In section (2.3) we first provide an overview of “conventional” methods with a proven track record in patterning. This will serve as background for discussions of “unconventional” techniques that show wide potential and flexibility in patterning and we discuss their advantages and disadvantages. Strategies to define surface nanopatterns by photons, particles, replication against masters and molds, scanning probes or even by making use of the intrinsic characteristics of the materials used (e.g. Stranski-Krastanov epitaxial growth and self-organization of semiconductor heterostructures) will be addressed.

In the context of emerging unconventional patterning techniques, our special attention is focused on “*nanostenciling*”, the approach we consider as overcoming several of the challenges faced by current conventional techniques and a valuable tool to pursue fundamental research in a university environment.

## 2.2 “Top-down” versus “Bottom-up”

The main schemes used to generate arrays - ordered or randomly positioned - of micro and nanoscale structures are commonly referred to as “*top-down*” and “*bottom-up*”.

The “top-down” concept is based on various methods of lithography to shape minute structures starting from a bulk material. Very often the bulk material is a continuous thin film, previously deposited by means of chemical or physical deposition on an appropriate substrate [4].

Conversely, a bottom-up technique exploits the intrinsic interactions between atoms, molecules or colloidal particles to assemble discrete nanoscale structures in two and three dimensions. Self-assembly process, identified as the autonomous organization of components into patterns or structures beyond human intervention [9], is the chief example of a bottom-up parallel process that generates arrays of nanostructures.

### 2.2.1 Generating and replicating patterned features via top-down

A top-down approach can use both *serial* and *parallel* techniques for *fabricating de novo* and *replicating* patterned features, typically in two-dimensions (2D), over length scales much larger in linear dimensions than an individual structure. The issue of fabricating patterned nanostructures can be generally partitioned into two main processes: *writing* and *replication*. Both writing and replication relate to the concept of a “master” template that provides or encodes a pattern to be replicated in multiple copies [10].

Generation and replication processes are conceptually different, and thus relate to different stages and aspects of nanopatterning and nanofabrication. For instance a writing process is usually performed with serial techniques that provide maximum resolution but are extremely slow, thus rendering the process practical only for few copies of an original drawing. Top-down approach includes serial techniques such as particle beam maskless lithography – i.e. scanning electron beam or focused ion beam lithography - to “write” masters such as photo-masks, imprinting moulds or stamps. Writing or generating de

novo nanostructures can also be achieved in fundamentally different manners using for instance an “inked” probe tip of an atomic force cantilever (e.g. dip-pen lithography) or controlled add-on processes such as laser induced chemical vapor deposition or electron/ion beam induced deposition.

A replication process is commonly characterized by a parallel and efficient transfer of the features previously written by a serial process, from one material onto another material. Top-down parallel techniques are represented, for instance, by optical or X-ray lithography, nanoimprint or micro contact ( $\mu\text{C}$ ) printing so as to transfer the shapes and patterned architectures from the masters to a *functional material*, in a single step, with high resolution, inexpensively and with high-throughput. The replication of a master represents the most efficient and suitable path to generate numerous copies of nano-scale features. Thus high-precision writing of masters combined with their low-cost replication provides the most practical protocol for advancing Nanotechnology. The high cost of fabrication implied to make the masters from a set of materials often becomes acceptable in light of the numerous copies generated by the low-cost replication process applied to a different set of materials. For example, in semiconductor manufacturing, making use of multiple sophisticated sets of photomasks, advanced photolithographic techniques can define today structures of  $\sim 50$  nm using ArF ( $\lambda=193$  nm) and F<sub>2</sub> ( $\lambda=157$  nm) excimer lasers with a throughput of more than 100 silicon wafers per hour, with a current periodicity (half-pitch) of 65 nm for dynamic random access memories (DRAM) and the minimum feature size achieved of  $\sim 45$  nm (transistor gate length) [11].

### **2.2.2 Bottom-up via self-assembly and “assisted” self-organization**

In addition to the top-down methods mentioned so far, recent efforts have focused on a vastly different way to create nanoscale structures, making use of the bottom-up approach. This approach exploits the natural tendency of atoms and molecules to assemble and form regular structures and “natural” self-assembly represents the principal example of a bottom-up, parallel process [9].

On a surface, the intrinsic characteristics of the substrate and of the deposited materials, as well as the laws of nucleation and growth, can direct billions of nanoscale islands to grow simultaneously. Their features can be tuned by varying kinetic parameters such as substrate temperature, total coverage, and deposition rate or post-deposition thermal treatment. This type of fabrication represents a very attractive approach for applications, both because it is massively parallel and because it takes place without using artificial patterning, thus making it potentially inexpensive. This has prompted a huge experimental and theoretical effort to understand and possibly control such processes [12,13].

Several critical issues still prevent the full exploitation of natural self-assembly. For example, the functionality of a prospective quantum dot (QD) based device relies on the electronic structure of the confined nanostructures. This, in turn, depends on the size, shape, crystallinity, or chemical composition of the QDs [14]. Thus a narrow size and shape distribution is a crucial requirement. Moreover, the positioning of nanostructures by a simple bottom-up approach is an extremely challenging task. In most cases the nucleation process occurs randomly and the subsequent phenomena of ripening or coalescence do not cause a significant change in position. Yet, nanoscale ordering may be attained using the intrinsic character of the materials system employed, for example by exploiting the strain energy within a hetero-epitaxial system. Thus the self-organization of nanostructures [15-17] becomes an exciting approach that deserves further investigation to reach a better understanding of the processes taking place and to eventually be able to control them.

Self-organization may also be successfully obtained by growing nanostructures on artificially patterned substrates. For example, for the purpose of achieving spatial control, top-down high resolution techniques such as photon or particle beams lithography (e.g. LIL, FIB, EBL) or embossing techniques (e.g. NIL) are used to prepare templates on which a bottom-up process is used to direct the organization of functional nanostructures. In chapter 4 we discuss in more detail the Stranski-Krastanow induced growth and self-assembly of Ge / Si nanostructures and further on, the organization of Ge islands on pre-patterned surfaces.

## **2.3 “Conventional” versus “Unconventional”**

“Conventional” techniques for nanofabrication are considered optical or particle beam lithography, i.e. those that already exist commercially and are extensively implemented in manufacturing. These techniques are characterized by high throughput and high resolution, and also by the high price of the tools that generate the patterns. Conventional nanofabrication techniques are mainly oriented towards planar fabrication in semiconductor materials and are often poorly suited for some issues facing non-standard fabrication such as fabrication on non-planar substrates or fragile surfaces. They also expose substrates to high-energy radiation, high-temperature processes and corrosive etchants; alternatives must be found when one aims to pattern fragile materials, such as organic materials (e.g. biological materials) other than photoresists.

The “unconventional” approaches to nanofabrication and nanopatterning emerged and were mainly developed in research environments where the pressure of high-throughput is not a critical issue. These techniques generate opportunities for nanofabrication on non-planar surfaces (e.g. curved surfaces) and over large areas and may offer competition in nanofabrication where cost and materials make photolithography difficult. They are probably the only techniques that are applicable to biological materials and to sensitive organic materials. Unconventional approaches are often easier to use than conventional techniques and thus enable the straightforward exploration of various fields in nanoscience and nanotechnology. Presently unconventional techniques for surface nanopatterning are just at an incipient stage of marketable maturity and are explored mainly for research purposes. Nevertheless, in time, they may offer alternatives to photolithography in manufacturing [18].

### **2.3.1 Conventional patterning processes**

We start our overview with a background section on conventional approaches, addressing the two main dominant industrial techniques currently employed for patterning nanoscale features: optical lithography (photolithography) and particle beam lithography. This section will further set the scene for assessing the potential of the unconventional strategies that have recently been promoted for nanopatterning.

### 2.3.1.1 Patterning with photons and particles

#### Optical lithography

Optical lithography - the mainstream technique used in industry to replicate patterns rapidly and accurately, from photomasks to wafers - makes use of photons in the optical regime (visible and ultraviolet). The wave-like character of light results in diffraction that limits the patterning resolution to a certain fraction of the wavelength used. This constitutes the major limit of the process and the main concern for people involved in the development of lithographic tools and processes. Yet, the ongoing success of advanced optical lithography is undeniably outstanding [19-21].

To generate a desired pattern by optical lithography - usually in a thin layer of photoresist spin-coated on a substrate - a related pattern is formed on a photomask or a reticle (e.g. patterned chromium features on a quartz plate) and a complex imaging system projects the photomask pattern onto the photoresist. The patterns on the reticle can be 2X to 5X (4X is more frequent) the size of the patterns that will be finally obtained on the substrate. This is realized by a projection lens system which assures the proper demagnification ratio (Fig. 2.1). However, some reticle patterns are 1X the substrate pattern.



**Figure 2.1** Schematics of optical lithography process. UV light passes through the glass mask plate (reticle) and projects the image onto the silicon wafer covered with thin photo-sensitive film ([www.ncnanotechnology.com/public/features/TNLC.asp](http://www.ncnanotechnology.com/public/features/TNLC.asp))

There are three types of pattern printing: contact, proximity, and projection printing, and the equipment used for printing is known as steppers or scanners. Contact and proximity techniques used in the early days of optical lithography have been replaced in time by projection techniques.

The light exposure changes the solubility of the photoresist coated on the substrate; after immersion of the exposed sample in a developer solution a positive replica of the mask is achieved if a positive-tone resist has been used or a negative one if a negative-tone photoresist has been employed. The pattern in the photoresist can further be transferred to the substrate (functional layer) by means of wet or dry etching, using the resist layer as an etch-stop mask.

The resolution,  $R$ , in optical lithography is determined by Rayleigh's equation (2.1) and the corresponding depth of focus (DOF) is given by equation (2.2).

$$R = k_1 \times \frac{\lambda}{NA} \quad (2.1)$$

$$DOF = k_2 \times \frac{\lambda}{NA^2} \quad (2.2)$$

In equations (2.1) and (2.2)  $\lambda$  is the exposure wavelength,  $NA$  is the numerical aperture of the projection lens, and  $k_1$  and  $k_2$  are constants that depend mainly on the characteristics of the photoresist material, process technology and image formation technique that are used. The variables in equations (2.1) and (2.2) reveal the directions in which optical lithography had to develop as to keep up with the demand of shrinking critical features: (i) decreasing the exposure wavelength  $\lambda$ , (ii) increasing the numerical aperture, and (iii) decreasing the parameter  $k_1$ . All of these approaches have been investigated at length, reported in countless scientific papers and implemented to a certain extent in practice [6, 19-21].

### **Extreme ultraviolet lithography (EUVL)**

Extreme ultraviolet lithography (EUVL) or "soft X-ray lithography" - the next generation lithography (NGL) technique competing to replace optical lithography in the near future (~2009) - is a strong candidate for achieving critical dimensions of 50 nm and below [22,23]. EUVL uses the same principle of conventional optical-projection

lithography and also complies with Rayleigh's equation. The resolution of this technique is much higher than that of optical lithography since the exposure wavelength is in the range of 13 nm (Eq. 2.1). However, together with the decreased wavelength value some related challenging issues appeared. For instance, as the absorption of light in this short-wavelength regime is very strong, lens-based refractive optics cannot be used in this lithographic system and thus an all-reflective optic system must be employed. EUVL uses an elaborate setup of concave and convex mirrors coated with multiple layers of molybdenum (Mo) / silicon (Si) and a mask made of reflective materials that ultimately focuses the photons on a resist-coated silicon wafer. The coatings produce nearly 70% reflection of EUV light at a wavelength of 13.5 nanometers; the other 30% is absorbed by the mirrors (Fig. 2.2). Nevertheless, without this multilayered coating, the light would be almost totally absorbed before reaching the wafer. The EUV light is reflected several times within the system before touching the wafer; the photon intensity is reduced to 2% of its initial value when the light reaches the target, thus mandating long exposure times.

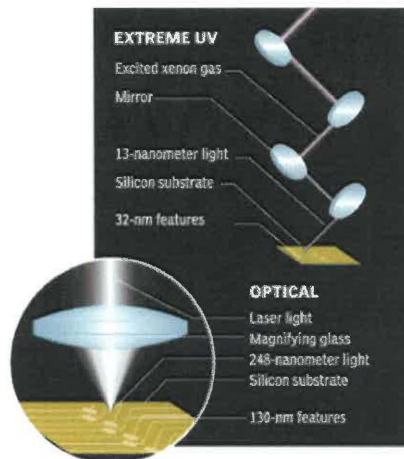


**Figure 2.2** Extreme ultraviolet lithography (EUVL) schematics with an inset showing the comparison with optical projection lithography (www.pcmag.com – July, 2003)

Finding suitable sources for EUV exposures is another challenging issue. Currently, the best candidate source of EUV light is laser-produced plasma of xenon (Xe) gas. However the energy conversion ratio of laser light from a YAG laser to EUV light is rather small, and as a consequence lasers of massive power are required to achieve practical EUV exposure intensities. In this context, different solutions such as the use of electrical discharge lamps are being explored for providing practical light sources for EUV lithography [19].

### **X-ray (proximity) lithography (XRL)**

X-ray lithography (XRL) [24] represents the shortest-wavelength limit of approaches currently being explored for photon-based optical lithography. Two versions have been demonstrated for XRL: soft X-ray or EUVL projection lithography, discussed previously, and X-ray proximity lithography with wavelengths  $\sim 0.2\text{-}2$  nm produced, for instance, at synchrotron radiation facilities. Because it is difficult to use optical diffraction components for imaging in the X-ray regime, X-ray lithography is carried out as a simple 1:1 shadow projection technique with a proximity gap between mask and substrate. Proximity lithography is basically a form of shadow printing i.e. a mask is kept in close proximity to the substrate surface, and the image is produced by exposure of the shadow of the mask on the surface.

In the exposure system for proximity X-ray lithography, X-rays are first collimated using a silicon carbide mirror, and are then passed through a transparent window of beryllium into a chamber containing the mask and wafer. The mask is prepared on a membrane of silicon carbide or diamond, in a layer of tantalum (or other similar high Z material) patterned by direct-write electron-beam lithography, and serves to absorb the X-rays and generate the shadow on the semiconductor wafer. Since wavelengths down to  $\sim 1$  nm are used, resolution is no longer the main concern with proximity printing using X-rays. Instead, the lack of a commercially profitable way to produce the necessary masks, the absence of suitable optics to project or reduce the image of the mask and the difficulty of placing the mask in close proximity ( $\sim 10$  nm) to but not in contact with the substrate has slowed the implementation of X-ray in IC production. X-ray has been used for prototyping and research [25].

### **Laser interference lithography (LIL)**

Laser interference lithography (LIL) is a maskless lithographic technique with great potential for defining periodic patterns, in a parallel manner, over large areas [26-28]. LIL is based on the phenomenon of interference of two coherent beams, obliquely incident on a substrate surface (Fig. 2.3). A pattern of parallel interference pattern is formed and this pattern can be “recorded” in a photo-sensitive material such as

photoresist [29]. The depth-of-focus of this method is dependent on the coherence length of the light and can be of the order of meters or more, compared to microns for conventional optical lithography systems. As a result, the demands on substrate flatness and wafer positioning are not critical. In spite of these advantages, LIL has not been widely used in the semiconductor industry, since it may only be applied for the design of regular patterns and the patterns registration is an challenging issue.

The spatial period of the interference fringes provided by a LIL system, and thus of the patterns exposed in photoresist, is given by the equation:

$$P = \frac{\lambda}{2 \sin \theta} \quad (2.3)$$

where  $\lambda$  is the wavelength of the source, and  $\theta$  is half the interference angle of the two beams. Based on the value of the wavelength used and by changing the angle  $\theta$  the periodicity  $P$  can be easily adjusted from micron to nanometer values.

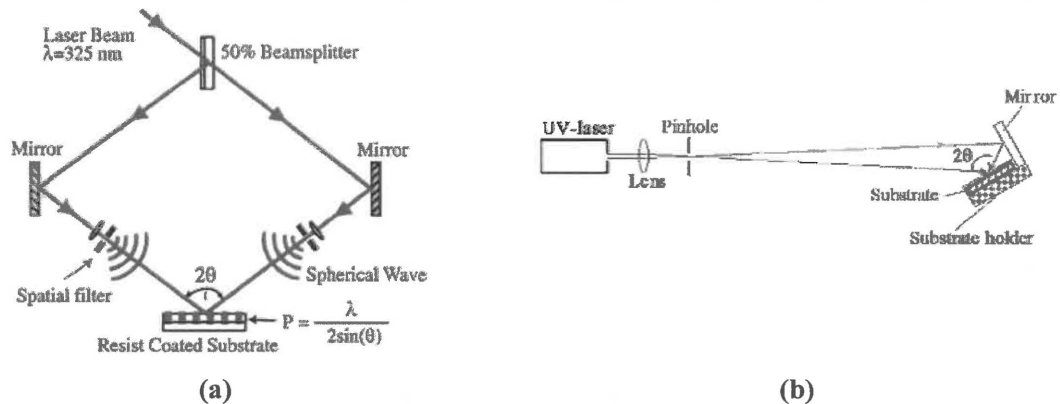


**Figure 2.3** Laser interference lithography (LIL) technique based on (a) dual-beam interference and (b) Lloyd's mirror interferometer configuration [31]

An interference pattern can also be achieved using a primary laser beam while a secondary beam is created by its reflection in a mirror mounted at  $90^\circ$  angle with respect to the substrate – Lloyd's mirror interferometer configuration (Fig.2.3b). In this case, since the second beam is created by the mirror mounted in close proximity to the substrate, the whole setup is less sensitive to vibrations compared with the conventional dual-beam interference setup. If double exposures are performed for instance at  $60^\circ$  or  $90^\circ$ , hexagonal [30] or square architectures of patterns can be obtained and in essence by multiple exposures any shape that can possibly be generated by the intersection of

interference fringes lines can be attained. Another advantage of the Lloyd's-mirror setup is that the periodicity of the exposed patterns can be adjusted from several microns down to hundreds of nm simply by rotating the substrate/mirror assembly about its center point without realigning the optical path.

Equation (2.3) reveals resolution of the method: the spatial-period of such pattern can be theoretically as low as half the wavelength of the interfering beams, thus allowing for structuring in the order of couple of hundreds nm if UV lasers are used while features as small as 30-40 nm are possible using DUV ArF laser. Nevertheless, in the case of smaller periods, the thicknesses of the photoresist and the quality of the subsequent development process have to meet some rigorous requirements because of the viscous character of the development liquid at submicron scale. After exposure and development of the photoresist, the grating is usually transferred to the substrate by a dry etching process (e.g. plasma reactive ion etching).

LIL has been used to fabricate calibration grids, photonic crystals, microsieves for microfiltration and shadow-masks for controlled deposition [31,32], patterned magnetic media [33] and it was often used to prepare templated substrates for further material growth [34]. In chapter 3 (experimental section), we describe in more detail the applicability of this technique for creating hexagonal ordered arrays of circular apertures in free standing SiN membranes that we used extensively along these studies as nanostencils.

### **Electron-beam lithography (EBL)**

As its nomenclature indicates, electron-beam lithography (EBL) employs a beam of electrons rather than photons as the exposure source. EBL has extremely high-resolution capabilities combined with a large depth of focus and is preferred mainly in the production of masks and reticles for optical lithography. The direct writing version – DWEBL - can be used for generating extremely fine patterns; in fact, when combined with etching and deposition processes, fabrication of electronic devices with critical dimension as small as 10 nm has been demonstrated [35]. However, in the context of mass-produced large scale integrated circuitry, the biggest problem of EBL is the low

throughput capability. Although using a finely focused electron beam makes it possible to delineate extraordinarily fine patterns, writing of chip-scale patterns with a single electron beam is a prohibitively slow process. Moreover, as the intricacy and refinement of mask patterns increases, even the use of EBL for mask writing becomes rather slow. This throughput handicap has confined direct writing EBL to a supporting role in the semiconductor industry, where it has applications in several main areas: mask-making, prototyping, small-volume fabrication of special products, and research and development for advanced applications [36]. Besides low speed, another major drawback of EBL is the presence of the proximity effect, which causes pattern-specific line width variations due to electron scattering. This effect can be reduced by working at very high (100 keV) or at very low (500 eV) electron energies in order to minimize, in the first case, backward scattering, or, in the second case, electron depth range.

Low energy e-beam proximity lithography (LEEPL) was recently proposed for integrated circuit lithography for a minimum feature size less than  $0.1\mu\text{m}$  [37]. LEEPL is similar to optical or X-ray proximity lithography except that photons are replaced by low energy electrons ( $\sim 2\text{ keV}$ ). Silicon wafers are used to fabricate 1X patterned masks thus various semiconductor technologies can be applied for fabricating LEEPL masks. The resolution attainable in LEEPL was estimated as 50 nm. Further reduction of the gap between mask and wafers and improved resist process may ultimately bring this value down into the range of 30 nm. Furthermore, the unit cost of this tool is considered to be less than today's advanced optical steppers<sup>2</sup>.

A more promising approach to improve EBL throughput is to use a projection optical system that is geometrically equivalent to that used in optical lithography i.e. the image of an arbitrary LSI circuit to be projected from a mask. Most notable of the attempts to use mask projection are SCALPEL (SCattering Angular-Limited Projection Electron-beam Lithography), developed by Bell Laboratories [38] and PREVAIL (Projection Reduction Exposure with Variable-Axis Immersion Lenses), developed by IBM [39].

---

<sup>2</sup> [http://www.sony.net/Products/SC-HP/cx\\_news/vol29/pdf/mask.pdf](http://www.sony.net/Products/SC-HP/cx_news/vol29/pdf/mask.pdf)

## **Ion beam lithography (IBL)**

Ion beam lithography systems are based on focused ion beams and represent highly attractive tools for writing nanostructures, as they are capable of very high resolution [40]. The best resolution is potentially around 10 nm which is the diameter of latent damage produced by the passage of a single fast ion through sensitive materials where the ion range could be tens of micrometers. However, IBL systems suffer from problems of throughput similar to scanning electron-beam systems. The Focused Ion Beam (FIB) technique will be discussed in more detail in Chapter 3, where its particular application of “milling” patterns in free-standing silicon-nitride membranes is demonstrated in the creation of arbitrary motifs that are further replicated by stenciling.

Ion-projection lithography (IPL) is a technique conceptually related to electron beam lithography, in which the electron beam is replaced by an ion beam [41]. In principle, the much higher mass of the ions should result in imaging capabilities that are less prone to distortions due to back-scattering from the substrates. High-resolution ion-beam systems remain in an incipient state of development compared to that of electron-beam systems.

## **2.3.2 Unconventional patterning processes**

Unconventional patterning approaches have emerged as low-cost, high-resolution alternatives to conventional and advanced lithography and have been explored thus far mainly in academic and research environments. We address in the following several strategies that are showing versatility, high potential and, in some cases, high throughput in generating and replicating surface nanopatterns.

### **2.3.2.1 Scanning probe lithography**

Scanning probe-based lithography (SPL) falls into the category of emerging unconventional alternatives. Nanopatterning via SPL is extremely flexible, yet too sluggish for the demanding semiconductor industry and for this reason it is pursued

mainly in research environments where it has been proven as a valuable tool for elucidating phenomena occurring at the nanoscale. SPL comprises methods that make use of sharp tips that scan in proximity to a sample surface, allowing for the generation of nanometer-scale features with high resolution. Atomic force microscopy (AFM), scanning tunneling microscopy (STM) or near-field scanning optical microscopy (NSOM) have been the most widely used techniques and comprehensive reviews have been written [42-44]. Typical approaches include: the use of an AFM tip to scratch nanostructures in soft materials (mechanical “elimination” of material in a controlled manner), to optically expose (irradiate) thin films of resist via NSOM tips, to induce or enhance oxidation of H-terminated Si(100) (electrical “modification” via STM and AFM tips) or to “write” patterns as for instance in alkanethiols on gold (“addition” of material in a controlled manner).

Dip-pen nanolithography (DPN) is perhaps in the most advanced stage of SPL research and already implemented commercially<sup>3</sup>. This technique has been highlighted in several articles [45,46]. In DPN, AFM tips are “inked” with molecules that are known to self-assemble on solid substrates and brought in contact with the latter. A water meniscus is formed, and the ink coated on the tip is transferred to the substrate when the probe is held in contact or moved along the surface below a certain linear velocity (Fig. 2.4).

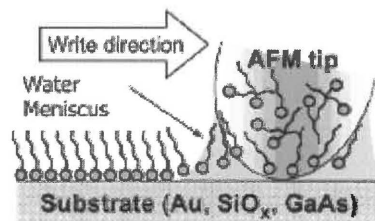


**Figure 2.4** Schematics of dip-pen nanolithography (DPN) principle [44]

DPN can often use commercially available tips, which are not modified prior to the adsorption of the ink. The first report of DPN showed the fabrication of organic patterns of dot arrays or lines (with widths that were less than 100 nm and as narrow as 30 nm) with thiol-based molecular inks on polycrystalline gold and Au(111) [45]. Contact time and humidity play decisive roles in DPN. Longer contact times (e.g., slow scan speeds) lead to larger feature sizes while with increasing humidity, the feature size also increases,

<sup>3</sup> <http://www.nanoink.net>

due to the change in the size of the water meniscus. An attractive feature of DPN is that the structures can be imaged in-situ immediately after the lithography operation to assess the quality of the pattern.

The inherent serial nature of an SPL-based method results in undesirably slow writing thus efforts have been made to demonstrate a more parallel approach to DPN writing, using a linear array of AFM tips [47]. The next advancement in the area of multiple-pen DPN was the development of a MEMS nano-plotter with a high density of probes composed of linear arrays of tips (up to 32) fabricated via photolithography [48].

### 2.3.2.2 Patterning with stamps and molds

Many major developments made in the quest for finding alternatives to optical-lithographic nanostructuring procedures ones are in the area known as “*soft lithography*” [49]. This is a set of methods that makes use of soft elastomeric stamps, molds and conformable photo-masks for patterning two- and three-dimensional structures with feature sizes down to the nanometer regime. The soft lithography approach is broadly divided into two parts: (i) the fabrication of the elastomeric component and (ii) the use of this component to further replicate pattern features with geometries defined by the component’s relief structure. Usually, an established lithographic technique, such as one of those developed for the microelectronics industry, is used to define the master. Many elastomeric elements can be generated from a single master, and each element can be used many times in patterning. (Fig. 2.5) schematically illustrates the steps. Here, photolithography patterns a thin layer of photoresist on a Si wafer.

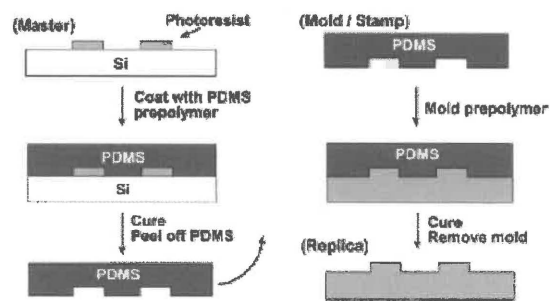


**Figure 2.5** Schematics of replica molding [50]

Elastomeric elements are generated by casting a light- or heat-curable prepolymer against this master. The elastomer poly(dimethylsiloxane) or PDMS (e.g. Sylgard 184, Dow Corning) is commonly used for this purpose. With optimized materials and chemistries, this fabrication sequence has remarkably high fidelity. In fact, recent work shows that relief with nanometer depths [50], and both nanometer depths and widths [51], can be reproduced accurately.

Micro-contact printing ( $\mu$ CP), originally developed by Whitesides' group at Harvard University [52], represents the front-runner of this group of novel patterning techniques, and recent work indicates the possibility of transferring the method out of the laboratory and into manufacturing [18]. In  $\mu$ CP, just as in many conventional printing techniques, the patterned stamp is brought into contact with a substrate to transfer an ink to and thus create an image of the stamp pattern on the substrate surface. In a subsequent processing step this image may be transferred into the substrate material by, for instance, via etching or a material deposition process. In the case of etching, the pattern formed by the ink on the substrate surface can be utilized as an etch resist, whereas in the latter deposition process it may serve as a template for further material growth. The major virtues of  $\mu$ CP are its simplicity and the low cost of the equipment. The main drawbacks are the fact that the technique works only with a limited number of materials and substrates, the impossibility to process the substrate locally and the low capability for three-dimensional structuring. Today  $\mu$ CP finds its main applications in plastic electronics, integrated optics, and MEMS [8,10,18,49].

Significant advances in defining nano-patterns have been made also through *nanoimprint lithography* (NIL), an approach initially introduced by Chou in 1995 [53]. NIL is currently able to deliver features well below 100 nm, rapidly and with high accuracy and throughput at least comparable to advanced optical lithography methods. Either by the hot embossing technique (HET) (known also as thermoplastic T-NIL) [54] or by its related variant, step and flash imprint lithography (S-FIL) [55] (Fig. 2.6.), nanoimprint has great potential for the semiconductor industry and has been already placed on the International Technology Roadmap for Semiconductors (ITRS) at the 32 nm node, which is expected to be reached in a few years [11].

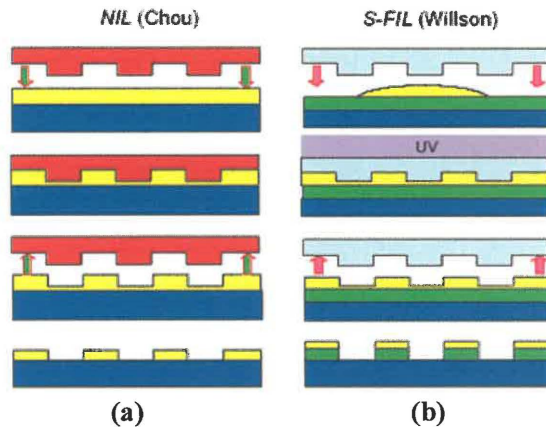


**Figure 2.6** Schematics of: (a) thermal nanoimprint (T-NIL) and (b) step and flash nanoimprint (S-FIL) processes [56]

T-NIL is based on two distinct steps: imprint and pattern transfer, as shown in Fig. 2.6a. In the first step – the imprint - a mold (made of metals, dielectrics, or semiconductors) with nanofabricated patterns on its surface is pressed into a thin polymer spun on a substrate. This step duplicates the nanopatterns from the mold into the polymer film creating a thickness contrast pattern in the latter. During the imprint step, the resist is heated to a temperature typically 50-100 °C above its glass transition temperature ( $T_g$ ). At this temperature, the resist, which is thermoplastic, becomes a viscous liquid and can flow under pressure (about 50–100 bar) and therefore can easily conform to the shape of the mold. The mold is then removed from the imprinted substrate after cooling both the mold and substrate. The second step consists in transferring the pattern by an anisotropic etching process. For example, RIE can be used to remove the residual resist in the embossed area. This step transfers the thickness contrast pattern into the entire thickness of the polymer, which is in turn used as an etching mask for further pattern transfer into the functional layer (substrate). As a first demonstration of the feasibility of this technique, metal dot arrays with a minimum feature size of 25 nm and a period of 70-100 nm were fabricated [57]. It was predicted that with further development NIL would lead to the fabrication of sub-10-nm structures with the potential to become a commercially viable approach for manufacturing integrated circuits and nanodevices [58].

The S-FIL variant is a “step and repeat” nano-replication technique developed by Willson’s group in 1999 [55]. In S-FIL, a low viscosity UV curable liquid resist is

applied to the sample substrate drop-wise, and a mold, usually made of transparent material like fused silica, is pressed against it (Fig. 2.6b). After the mold and the substrate are pressed together, the resist is cured in UV light and becomes solid. Following mold separation, a similar pattern transfer described for the T-NIL process can be used to transfer the pattern formed into the resist onto the underlying material. The use of low viscosity monomers (viscosity of  $< 5$  cps) leads to a low imprint pressure process ( $< 0.25$  psi) resulting in significantly lower defect density. Several challenges need to be addressed if the promise of nanoimprint is to be extended to a larger set of applications. Among them: the ability to print fields with non-uniform pattern density with high throughput, the ability to etch nanostructures with appropriate critical dimension (CD) control, precise alignment and overlay, and the minimization of process-induced defects. S-FIL was initially introduced to address these challenges. In particular, S-FIL uses a bi-layer approach in which the imprinted material is a silicon-containing material that is deposited on an underlying organic layer. This allows the patterning of relatively low aspect ratio features which can then be amplified in aspect ratio by using an  $O_2$  RIE to etch the underlying organic. This low aspect ratio patterning turns out to be the solution in minimizing defects, particularly during the separation of the template from the UV cured material [59,60].

Although NIL was thought initially as a versatile alternative technique for the fabrication of devices for electronics [61] or media for data storage [62], it also found excellent niches in optics, photonics and biology. The imprint lithography techniques discussed by Truskett and Watts in a recent review [63] indicate biotechnology as the most probable area for future imprint applications. Imprinting has already proven to be advantageous in terms of cost and simplicity, for both academic and industrial research, by demonstrating the fabrication of structures less than 100 nm on non-planar surfaces, fabrication of 2D and 3D structures, and patterning and modification of functional materials other than photoresists. Recent work identifies several areas of high-potential interest for NIL, S-FIL and micromolding applications such as microarrays for genomics and proteomics or tissue engineering [64-66].

### 2.3.2.3 Patterning via controlled deposition

#### Nanostenciling

There is a common theme running through the reviews presented so far: the in-plane patterning, on the nanometer scale, of a functional thin film, with accuracy, flexibility, reliability and high throughput is an extremely intricate and challenging task. Very often the costs of tools and their operation are prohibitive, sometimes physical limitations hamper these process or complementary fabrication techniques (e.g. post-patterning selective etching processes) have not yet been developed for certain classes of materials. Even though most of techniques proposed as alternatives to conventional optical lithography are not yet close to meeting the semiconductor industry's stringent requirements, without a doubt they have proven extremely valuable at the laboratory scale, for science and technological advancement. In this context, deposition through the apertures of a miniature shadow-mask (Fig 2.7) has been proposed as a highly flexible approach to control the parallel patterning of clean nanosized structures.

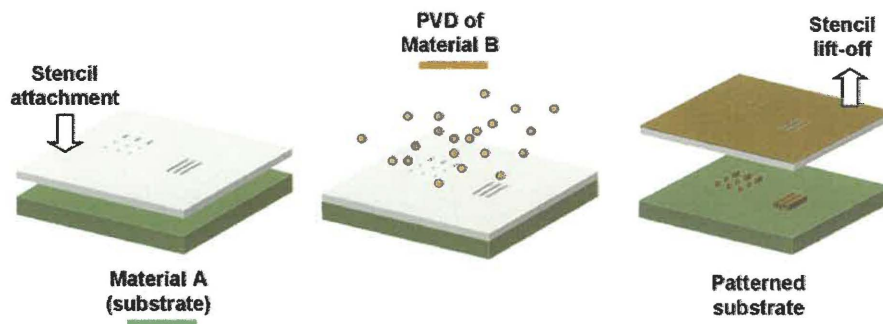


**Figure 2.7** Schematic drawing of static nanostenciling (S-NS) approach: a miniature shadow-mask, with apertures opened in a thin membrane is brought into proximity to the substrate of choice (e.g. material A). Material B can be directly deposited through the apertures using various deposition techniques such as evaporation, sputtering or pulsed laser deposition. The shadow-mask is simply lifted-off at the end of the process. 3D arrays of structures are directly obtained on the substrate and accurately replicate the size and shape of the sieve apertures.

The strategy of stenciling at the nanoscale has been investigated in parallel by several groups and is now considered as a highly suitable method to grow directly patterned nanostructures, in a single step, either in static or dynamic modes [67-72]. Our particular interest in developing and applying nanostenciling as a strategy to generate and

further investigate functional nanostructures has been motivated by several appealing intrinsic features of the method. We outline them as follows:

(i) the process is parallel and applicable to the deposition of various materials directly onto a wide range of substrates. It involves a reduced number of steps compared to any resist (polymer) – based lithography and straightforwardly generates 3-D structures; (ii) the process is compatible with high or ultra-high vacuum technology, making it a reliable option for local deposition of high resolution and high purity nanostructures of functional materials; (iii) the method can be applied at room or high temperature, enables multi- leveling and is highly suitable for parallel prototyping of fragile or functionalized surfaces; (iv) there is unlimited freedom in choosing the vapor deposition technique; the pattern formation using nanostencils does not interfere with the deposited species' growth dynamics and assures a precise and overall positioning control; (v) the stencils – “masters” in this case – produced by various conventional lithographic techniques are re-usable and can be cleaned (e.g. in aqua regia when metals are used), thus allowing for the creation of multiple copies of the features drawn in the originals.

These attributes make nanostenciling a valuable tool for studies of novel system-materials (e.g. multiferroic oxides) as well as the technique of choice for laboratory-environment nanoscale prototyping. Yet there have been essential issues that needed to be addressed for stenciling to be considered as a choice for top-down nanopatterning of surfaces. Among them: what materials should be used for nanostencil fabrication? What architectures should be designed and what deposition techniques should be employed? Will the traditional shadow-masking work at the nanometer scale and if yes, with what throughput? A clogging effect (aperture closure after a number of uses of the masks) was anticipated, thus raising concerns about the stencil's life-time. However, the simplicity and the high flexibility of the technique to deliver ultra-pure and precisely positioned nanostructures were reasons to further develop it beyond these concerns.

In the following we discuss the progress that stenciling has made along the way, from solutions found for stencil fabrication to its application nowadays in various areas of nanoscience and nanotechnology.

The idea of using a shadow-mask for deposition on selected areas was demonstrated two decades ago at HP Laboratories in Palo Alto. Using a silicon wafer

drilled with rectangular windows on top of a GaAs substrate, Dohler and co-workers [73] fabricated selected contacts to doped GaAs superlattices (named n-i-p-i crystals) that resulted in greatly improved electrical and optical characteristics. With the development of various technologies, new equipment became available (e.g. EBL, RIE, FIB) and stencil fabrication has been greatly improved in terms of minimum size and aspect ratios of the apertures. For instance, Ralls and co-workers [74] presented a method for the fabrication of metal nano-bridges by depositing metals through suspended SiN membranes that were previously processed by EBL and RIE. Later on, stenciling via microfabricated solid-state membranes was applied on the micrometer scale to pattern materials in deep holes and non-planar surfaces by Burger et al. [75]. Gribov and co-workers reported a new process for creating metallic point contacts making use of Si-membranes with tapered shape apertures that could be further fine-tuned in lateral size by thermal oxidation [76].

Along the way, other demonstrations of stenciling included the use of elastomeric stencils for micro-patterning cell cultures [77], self-aligning shadow-masks for patterning deeply recessed surfaces of MEMS devices [78], photoplastic microstencils with self-alignment for multi-layer surface patterning [79], microstencils for evaporated, sputtered and chemical vapor deposited metals, insulators and semiconductors [80], stencil-masks for ion implantation [81] or silicon-on-insulator (SOI)-based stencils for ion-beam patterning of magnetic films [82]. Design and fabrication ranged from stencils with mechanical alignment structures for depositions in isolated areas [83] to active nanostencils with integrated micro-shutters [84].

In terms of surface nanopatterning, the “boom” in selected-area nanoscale stenciling for the generation of highly ordered arrays of structures occurred in the period 1999-2000 when both static nanostenciling (S-NS) and dynamic nanostenciling (D-NS) were reported concurrently by several groups. Applying S-NS, Kohler and co-workers [67] used Si<sub>3</sub>N<sub>4</sub> membranes, with arrays of small holes drilled by FIB, to replicate shapes by depositing chromium structures directly onto germanium crystals. Brugger and co-workers [68] made use of microfabricated thin silicon nitride membranes with 2-dimensional arrays of perforated apertures realized by laser interference lithography (LIL) and RIE to pattern Cr/Au dots on free standing micromechanical beams and

recessed surfaces. D-NS was introduced by Luthi and co-workers [69] from IBM Zurich, who, using a combination of scanning probe and shadow mask techniques, fabricated structures with widths below 0.1  $\mu\text{m}$  by local deposition through FIB-ed pinhole-like apertures situated in the proximity of an AFM cantilever tip. The technique, compatible with metal, semiconductor, oxide and molecular deposition, was shown to allow direct and sequential patterning of complex heterostructures and their *in situ* inspection.

From that period onwards, stenciling at nanoscale has raised continuous interest in the materials science community and work focused mainly on metals patterning by evaporation and more recently by pulsed laser deposition has been consistently reported [85-88]. Prototyping using the nanostencil-based technique has been proposed by Champagne and co-workers [70] who deposited single dots of Co-Cr alloy, with diameter ranging from 140 to 25 nm, at the end of sharp commercially available AFM tips. The reason for such endeavors is the development of advanced forms of scanning-probe microscopy (SPM) [89] that employ nanofabricated structures that serve as scanning sensors or functional probes. More recently, Egger and coworkers [90] demonstrated that the working principle of dynamic stenciling (D-NS) is compatible with the basic principles of the combinatorial approach: parallelization and variation. The target is to incorporate organic thin film materials into devices with high potential in electronics and optoelectronics. Compared to a static mask, the ability to precisely control the motion of the shadow mask (embedded in an UHV-chamber-AFM-evaporator setup) gives a significant increase in the number of possible geometries.

To probe different system materials and deposition methods, we have carried out experiments to investigate the pulsed laser deposition (PLD) of semiconductors (Ge/Si) and complex oxides ( $\text{ABO}_3$ -perovskite type) through nanostencils [91-93].

To promote nanostencil-based lithography as a reliable, ultra-high resolution patterning alternative, several issues remain to be improved. Among them, the control of the deposited material with the membrane apertures, the investigations of cleaning methods that will render stencils re-usable and alignment methods (down to several tens nm precision) that will enable the reliable fabrication of multilayer structures.

## 2.4 Summary

Since the 1990s, optical lithography started patterning at sub-wavelength dimensions and in the near future, it will pattern at one-third wavelength, and possibly even one-fifth wavelength dimensions. A combination of short wavelength, high-index immersion fluids, and improved RETs, sustained also by development of much performant photoresists, will be suitable to meet the expected industry needs until at least the year 2013 (the 32 nm node). For serial, small scale patterning, electron-beam lithography represents the technique of choice capable to provide the best feature resolution. This, in turn, increases the costs for surface patterning in the nanometer range.

As optical (advanced) lithography becomes more and more expensive and complex, unconventional techniques for nanofabrication can alleviate the costs and limitations of the former. The more mature technique of NIL is already able to deliver features below 100 nm, rapidly and with accuracy and throughput (4 and 6-inch wafer scale) comparable to advanced optical lithography methods. Thus, nanoimprinting shows great potential for the semiconductor industry and has been already placed on the International Technology Roadmap for Semiconductors (ITRS) in the near future (for 32-nm node). Offering the advantages of high throughput and reproducibility at low cost, and the capability of creating nanopatterns for a broad range of applications (spinning from optical devices to biosensors and molecular electronics) NIL is envisioned to play a major role in the coming years of nanotechnology.

The nanostenciling approach, either in the *static* or the *dynamic* mode, shows attractive assets, proved so far only at the laboratory scale. NS has emerged as a highly-flexible approach to control the parallel patterning of clean nanosized structures, providing thus convenient ways for their further investigations. Resolution below 100nm has been achieved in both static and dynamic modes. Nanostenciling offers a solution for local nanometer scale patterning on “unconventional” surfaces (fragile, functionalized), non-planar surfaces such as MEMS or CMOS chips or mechanically unstable such as cantilevers and membranes. Further developments of this approach will lead to the realization of novel architectures and devices, also providing solutions for critical patterning issues not yet solved.

## 2.5 References

- [1] D. R. Walt, *Nature Mat.* 1, 17 (2002)
- [2] M. Geissler and Y. Xia, *Adv. Mater.* 16, 1249 (2004)
- [3] B. D. Gates, Q. Xu, M. Stewart, D. Ryan, C. G. Wilson and G. M. Whitesides, *Chem.Rev.* 105, 1171 (2005)
- [4] M. J. Madou, “*Fundamentals of Microfabrication: The science of miniaturization*”, 2nd ed., CRC Press, USA (2001)
- [5] S. M. Sze, “*Semiconductor devices: Physics and technology*”, John Wiley, New York (1985)
- [6] M. Rothschild, *Mat. Today* 2, 18 (2005)
- [7] F. Cacialli, P. Samori and C. Silva, *Mat. Today* 7, 24 (2004)
- [8] Y. Xia and G. M. Whitesides, *Angew. Chem. Int. Ed.* 37, 550 (1998)
- [9] G. M. Whitesides and B. Grzybowski, *Science* 295, 2419 (2002)
- [10] Y. Xia, J. A. Rogers, K. E. Paul and G. M. Whitesides, *Chem. Rev.* 99, 1823 (1999)
- [11] ITRS, *Report-up-date* (2006)
- [12] D. L. Feldheim and C. D. Keating, *Chem. Soc. Rev.* 27, 1 (1998)
- [13] J. Stangl, V. Holý and G. Bauer, *Rev. Mod. Phys.* 76, 725 (2004)
- [14] J. M. Baribeau, X. Wu, N. L. Rowell and D. J. Lockwood, *J. Phys.: Condens. Matter* 18, R139 (2006)
- [15] R. Notzel, J. Temmyo and T. Tamamura, *Nature* 369,131 (1994)
- [16] G. Springholz, V. Holy, M. Pinczolits and G. Bauer, *Science* 282, 734 (1998)
- [17] M. Antonietti, *Nat. Materials* 2, 9 (2003)
- [18] J. A. Rogers and R. G. Nuzzo, *Mat. Today* 2, 50 (2005)
- [19] T. Ito and S. Okazaki, *Nature*, 406, 1027 (2000)
- [20] B. Fay, *Microelectron. Eng.* 61-62, 11 (2002)
- [21] D. Bratton, Da Yang, J. Dai and C. K. Ober, *Polym. Adv. Technol.* 17, 94 (2006)
- [22] J. E. Bjorkholm, *Intel Technology Journal* Q3, (1998)
- [23] R. Stulen and D. Sweeney, *IEEE J. Quantum Electron.* 35, 694 (1999)
- [24] S. Hector, *Microelectron. Eng.* 41-42, 25 (1998)

- [25] F. Romanato, L. Businaro, E. Di Fabrizio, A. Passaseo, M. De Vittorio, R. Cingolani, M. Patrini, M. Galli, D. Bajoni, L. C. Andreani, F. Giacometti, M. Gentili, D. Peyrade and Y. Chen, *Nanotechnology* 13, 644 (2002)
- [26] A. Yen, E. H. Anderson, R. A. Ghanbari, M. L. Schattenburg and H. I. Smith, *Appl. Opt.* 31, 4540 (1992)
- [27] S. R. J. Brueck, *Proc. of the IEEE* 93, 1704 (2005)
- [28] C. J. M. van Rijn, *J. Microlith., Microfab., Microsyst.* 5, 011012 (2006)
- [29] M. J. Beesley and J. G. Castledine, *Appl. Opt.* 9, 2720 (1970)
- [30] S. C. Kitson, W. L. Barnes and J. R. Sambles, *IEEE Photonics Technol. Lett.* 8, 1662 (1996)
- [31] C. J. M. van Rijn, G. J. Veldhuis and S. Kuiper, *Nanotechnology* 9, 343 (1998)
- [32] C. J. M. van Rijn, W. Nijdam, S. Kuiper, G. J. Veldhuis, H. van Wolferen and M. Elwenspoek, *J. of Micromech. Microeng.* 9, 170 (1999)
- [33] R. Murillo, H. A. van Wolferen, L. Abelmann, J. C. Lodder, *Microelectron. Eng.* 78-79, 260 (2005)
- [34] M. Schildenberger, Y. Bonetti, J. Gobrecht and R. Prins, *Topics in catalysis* 13, 109 (2000)
- [35] S. Matsui, *Proc. of the IEEE* 85, 629 (1997)
- [36] T.R. Groves, D. Pickard, B. Rafferty, N. Crosland, D. Adam, and G. Schubert, *Microelectron. Eng.* 61–62, 285 (2002)
- [37] T. Utsumi, *Microelectron. Eng.* 83, 738 (2006)
- [38] L. R. Harriott, *J. Vac. Sci. Technol. B* 15, 2130 (1997)
- [39] H. C. Pfeiffer and W. Stikel, *Microelectron. Eng.* 27, 143 (1995)
- [40] R. Kaesmaier, A. Ehrmann, H. Loschner, *Microelectron. Eng.* 57–58, 145 (2001)
- [41] J. Melngailis, A. A. Mondelli, I. L. Berry, R. Mohondro, *J. Vac. Sci. Technol. B* 16, 927 (1998)
- [42] C.F. Quate, *Jpn. J. Appl. Phys.* 1, 4777 (2003)
- [43] R. M. Nyffenegger, R. M. Penner, *Chem. Rev.* 97, 1195 (1997)
- [44] S. Kramer, R. R. Fuierer and C. B. Gorman, *Chem. Rev.* 103, 4367 (2003)
- [45] R. D. Piner, J. Zhou., F. Xu, S. Hong and C. A. Mirkin, *Science* 283, 661 (1999)
- [46] S. H. Hong, J. Zhu and C. A. Mirkin, *Science* 286, 523 (1999)

- [47] S. Hong and C. A. Mirkin, *Science* 288, 1808 (2000)
- [48] M. Zhang, D. Bullen, S. W. Chung, S. Hong, K. S. Ryu, Z. F. Fan, C. A. Mirkin and C. Liu, *Nanotechnology* 13, 212 (2002)
- [49] Y. Xia and G. M. Whitesides, *Annu. Rev. Mater. Sci.* 28, 153 (1998)
- [50] B. D. Gates and G. M. Whitesides, *J. Am. Chem. Soc.* 125, 14986 (2003)
- [51] F. Hua, Y. Sun, A. Gaur, M. A. Meitl, L. Bilhaut, L. Rotkina, J. Wang, P. Geil, M. Shim, J. A. Rogers and A. Shim, *Nano Lett.* 4, 2467 (2004)
- [52] A. Kumar and G. M. Whitesides, *Appl. Phys. Lett.* 63, 2002 (1993)
- [53] S. Y. Chou, P. R. Krauss and P. J. Renstrom, *Appl. Phys. Lett.* 67, 3114 (1995)
- [54] C. M. Sotomayor Torres, S. Zankovych, J. Seekamp, A. P. Kam, C. C. Cedeno, T. Hoffmann, J. Ahopelto, F. Reuther, K. Pfeiffer, G. Bleidiessel, G. Gruetzner, M. V. Maximov and B. Heidari, *Mat. Sci. Eng. C* 23, 23 (2003)
- [55] D. J. Resnick, S. V. Sreenivasan and C. G. Willson, *Mat. Today* 2, 34 (2005)
- [56] L. J. Gou, *J. Phys. D. : Appl. Phys.* 37, R123 (2004)
- [57] S. Y. Chou, P. R. Krauss and P. J. Renstrom, *Science* 272, 85 (1996)
- [58] S. Y. Chou, P. R. Krauss and P. J. Renstrom, *J. Vac. Sci. Technol. B* 14, 4129 (1996)
- [59] S. V. Sreenivasan, C. G. Willson, N. E. Schumaker and D. J. Resnick, *Proc. SPIE* 4608, 187 (2002)
- [60] M. Colburn, T. Bailey, B. J. Choi, G. Eckerdt, S. V. Sreenivasan and C. G. Willson, *Solid State Technology*, July (2001)
- [61] W. Zhang and S. Y. Chou, *Appl. Phys. Lett.* 79, 845 (2001)
- [62] C. Harnagea, M. Alexe, J. Schilling, J. Choi, R.B. Wehrspohn, D. Hesse and U. Gosele, *Appl. Phys. Lett.* 83, 1827 (2003)
- [63] V. N. Truskett and M. P. C. Watts, *Trends in Biotechnology* 24, 312 (2006)
- [64] T. Ohtake, K. Nakamatsu, S. Matsui, H. Tabata and T. Kawai, *J. Vac. Sci. Technol. B* 22, 3275 (2004)
- [65] J. D. Hoff, L. Cheng, E. Meyhöfer, L. Jay Guo and Alan J. Hunt, *Nano Lett.* 4, 853 (2004)
- [66] D. Falconnet, D. Pasqui, S. Park, R. Eckert, H. Schiff, J. Gobrecht, R. Barbucci and M. Textor, *Nano Lett.* 4, 1909 (2004)

- [67] J. Kohler, M. Albrecht, C. R. Musil and E. Bucher, *Physica E* 4, 1961 (1999)
- [68] J. Brugger, J. W. Berenschot, S. Kuiper, W. Nijdam, B. Otter and M. Elwenspoek, *Microelectron. Eng.* 53, 403 (2000)
- [69] R. Luthi, R. R. Schlittler, J. Brugger, P. Vettiger, M. E. Welland and J. K. Gimzewski, *Appl. Phys. Lett.* 75, 1314 (1999)
- [70] A. R. Champagne, A. J. Couture, F. Kuemmeth and D. C. Ralph, *Appl. Phys. Lett.* 82, 111 (2003)
- [71] S. Egger, A. Ilie, Y. Fu, J. Chongsathien, D-J. Kang and M. Welland, *Nano Lett.* 5, 15 (2005)
- [72] C. V. Cojocaru, C. Harnagea, F. Rosei, A. Pignolet, M. A. F. van den Boogaart, and J. Brugger, *Appl. Phys. Lett.* 86, 183107 (2005)
- [73] G. H. Döhler, G. Hasnain and J. N. Miller, *Appl. Phys. Lett.* 49, 704 (1986)
- [74] K. S. Ralls, R. A. Buhram and R. C. Tiberio, *Appl. Phys. Lett.* 55, 2459 (1989)
- [75] G. J. Burger, E. J. T. Smulders, J. W. Berenschot, T. S. J. Lammerink, J. H. J. Fluitman and S. Imai, *Sens. Actuators A* 54, 669 (1996)
- [76] N. N. Gribov, S. J. C. H. Theeuwes, J. Caro and S. Radelaar, *Microelectron. Eng.* 35, 317 (1997)
- [77] A. Folch, B.-H. Jo, O. Hurtado, D. J. Beebe and M. Toner, *J. Biomed. Mater. Res.* 52, 346 (2000)
- [78] J. Brugger, C. Andreoli, M. Despont, U. Drechsler, H. Rothuizen and P. Vettiger, *Sens. Actuators A* 76, 329 (1999)
- [79] G. Kim, B. Kim and J. Brugger, *Sens. Actuators A* 107, 132 (2003)
- [80] M. Graff, S. K. Mohanty, E. Moss and A. B. Frazier, *J. of Microelectromech. Syst.* 13, 956 (2004)
- [81] T. Shibata, K. Suguro, K. Sugihara, H. Mizumo, A. Yagaishita, T. Saito and K. Okumura, *IEEE Trans. Semicond. Manufact.* 15, 183 (2002)
- [82] B. D. Terris, L. Folks, D. Weller, J. E. E. Baglin and A. J. Kellock, *Appl. Phys. Lett.* 75, 403 (1999)
- [83] A. Tixier, Y. Mita, J. P. Gouy and H. Fujita, *J. Micromech. Microeng.* 10, 157 (2000)

- [84] R. W. Tjerkstra, P. Ekkels, G. Krijnen, S. Egger, E. Berenschot, K. C. Ma and J. Brugger, IEEE Conf. proc. Transducers vol. 2, 1651 (2003)
- [85] F. Vroegindeweyj, E. A. Speets, J. A. J. Steen, J. Brugger and D. H. A. Blank, Appl. Phys. A 79, 743 (2004)
- [86] E.A. Speets, B. J. Ravoo, F. J. G. Roesthuis, F. Vroegindeweyj, D. H. A. Blank and D. N. Reinhoudt, Nano Lett. 4, 841 (2004)
- [87] M. A. F. van den Boogaart, G. M. Kim, R. Pellens, J. P. van den Heuvel and J. Brugger, J. Vac. Sci. Technol. B 22, 3174 (2004)
- [88] X. M. Yan, A. M. Contreras, M.M. Koebel, J.A. Liddle and G. A. Somorjai, Nano Lett. 5, 1129 (2005)
- [89] K. Wilder and C. F. Quate, J. Vac. Sci. Technol. B 17, 3256 (1999)
- [90] S. Egger, S. Higuchi and T. Nakayama, J. of Comb. Chemistry 8, 275 (2006)
- [91] C. V. Cojocaru, F. Ratto, C. Harnagea, A. Pignolet and F. Rosei, Microelectron. Eng. 80, 448 (2005)
- [92] C. V. Cojocaru, C. Harnagea, A. Pignolet and F. Rosei, IEEE Trans. on Nanotechnology 5, 470 (2006)
- [93] C. V. Cojocaru, A. Bernardi, J. S. Reparaz, M. I. Alonso, J. M. MacLeod, C. Harnagea and F. Rosei, Appl. Phys. Lett. 91, 113112 (2007)

*In theory, there is no difference between theory and practice,  
but in practice there is a great deal of difference  
..... a thought of a PhD candidate*

## **3. Experimental and Characterization Approaches**

### **3.1 Introduction**

Prior to accomplishing the goals concerning the control of the size, shape and site-selective growth of nanoscale functional structures via *stenciling*, miniature shadow-masks must first be fabricated. Once made, these tiny masks can be used in combination with any physical vapor deposition technique (e.g. thermal evaporation, sputtering, laser ablation) to fabricate patterned structures. In the studies presented here, Pulsed Laser Deposition (PLD) was the preferred growth method. A variety of techniques for characterizing the surface were then employed to acquire information regarding the structural and functional properties of the individual structures. The morphology, structure and composition of the nanostructures were characterized by scanning electron microscopy (SEM), atomic force microscopy (AFM), X-ray diffraction (XRD) and Micro-Raman spectroscopy (e.g. for the Ge/Si materials system). Piezoresponse force microscopy (PFM) and magnetic force microscopy (MFM) were used to study the functionality of the ferroelectric and multiferroic patterned complex oxide structures.

In this chapter, approaches and essential steps undertaken to fabricate the nanostencils will be presented in section (3.2), along with background information about the PLD technique in section (3.3), including its advantages and challenges in providing high-quality thin films and structures. We further discuss in section (3.4) the characteristic features and benefits brought by each of the techniques we considered relevant and that were used for nanoscale characterization of the obtained ordered arrays of structures.

## 3.2 Nanostencil fabrication processes

For the design and fabrication of a stencil mask consisting of a supporting-frame and a thin, free-standing perforated membrane, two main approaches can be applied: the *Wafer flow process* (WFP) and the *Membrane flow process* (MFP) [1] (Fig. 3.1).

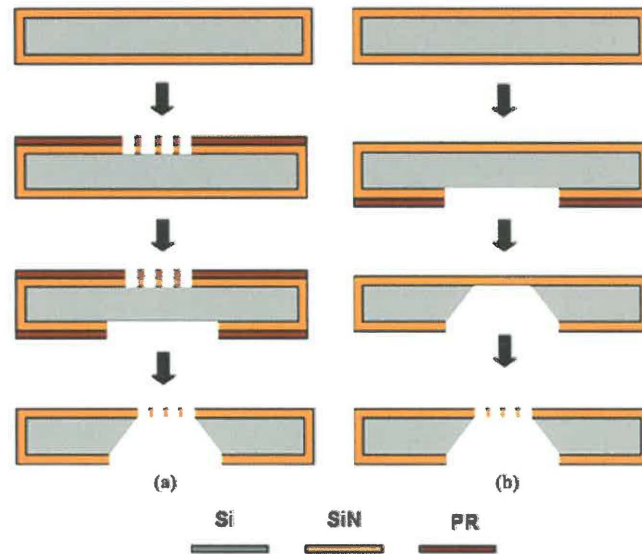


**Figure 3.1** Schematic drawings of WFP (a) and MFP (b) sequences used for nanostencil fabrication. Colors chart: grey- silicon wafer; orange- low-stress LPCVD SiN; brown- photoresist. Description of the processes involved in each approach is provided in sections (3.2.1) and (3.2.2) respectively

Following the WFP scheme, all cycles for pattern definition can be performed with typical processing tools for Si microfabrication (e.g. optical lithography patterning and plasma reactive ion etching (RIE)) on the solid wafer, leaving as the final step the release of the perforated membrane. Choosing the MFP scheme, the free-standing membrane is first formed by lithography and etching processes, then the entire pattern definition process (e.g. electron beam lithography (EBL), or focused ion beam (FIB) milling) takes place directly on the membrane. There is a distinct separation between the *pattern definition* aspect and the *membrane etching and releasing* aspect and for both WFP and MFP schemes, efforts are directed towards the minimization of the risks of contamination of the end product. Process flows that mix steps from both methods have been also reported [2].

### 3.2.1 Wafer flow process (WFP)

In this section, key steps involved in the common WFP (depicted in Fig. 3.1a) are described. The WFP route for nanostencil fabrication has been extensively employed by several groups and diverse descriptions of the processes can be found in [2-5].

As a generic and initial step, an insulating layer such as low-stress silicon nitride (e.g. 500 nm thick  $\text{Si}_x\text{N}_y$  non-stoichiometric) is deposited by low-pressure chemical vapor deposition (LPCVD) on both sides of a (100) silicon wafer. The internal tensile stress of the  $\text{Si}_x\text{N}_y$  layer is kept in the range 100-200 MPa so that the membrane will not break or collapse during subsequent processing steps. Silicon nitride is generally chosen for its very good chemical, thermal and hardness properties, high etch selectivity with respect to Si (for instance during KOH etching, the etching rate is 100  $\mu\text{m}/\text{h}$  for silicon and 0.02  $\mu\text{m}/\text{h}$  for nitride resulting in a selectivity ratio of 5000 to 1) and its compatibility with well-established Si micromachining processes.

In the second step, a photoresist is spun on the wafer's top-side and patterns are defined by means of conventional optical lithography (e.g. advanced deep-UV lithography). After development, the patterns made in the resist are transferred into the  $\text{Si}_x\text{N}_y$  layer by anisotropic etching (e.g. RIE). The lithography and RIE processes are then repeated on the bottom-side silicon nitride layer to define large rectangular openings.

Next the silicon between the patterned membrane layer and the back side of the stencil chip is removed with an anisotropic etch along the (111) planes with a KOH solution until the membrane layer is reached and the perforated membrane is released. Due to large differences in etching rates for the [100] and [111] directions (approximately 100 times faster in the [100] direction), windows are formed under an angle of  $54.74^\circ$  [2].

Besides optical lithography, several methods have been conceived to pattern efficiently the top-side membrane while simultaneously providing high-resolution and well defined shapes into the mask. Among them laser interference lithography (LIL) is a relatively inexpensive technique that can pattern submicron periodic structures over large areas (e.g.  $\text{mm}^2$ ). Multiple-exposure interferometric lithography was first introduced in 1993 by Zaidi and Brueck [6] with the aim of creating periodic structures in two dimensions. By combining LIL with standard silicon micromachining, van Rijn and co-

workers created nanosieves with uniform pore size and pore spacing less than 500 nm for filtration applications [7]. The main advantage of this approach is brought by the fact that using LIL there are no other masks needed to pattern the top-side layer of the stencil.

The stencils can be diced into square pieces, e.g. stencil chips  $5 \times 5 \text{ mm}^2$  in size like those we used during our experiments (Fig. 3.2a), or tentatively used as full wafer-size shadow masks (Fig. 3.2b).

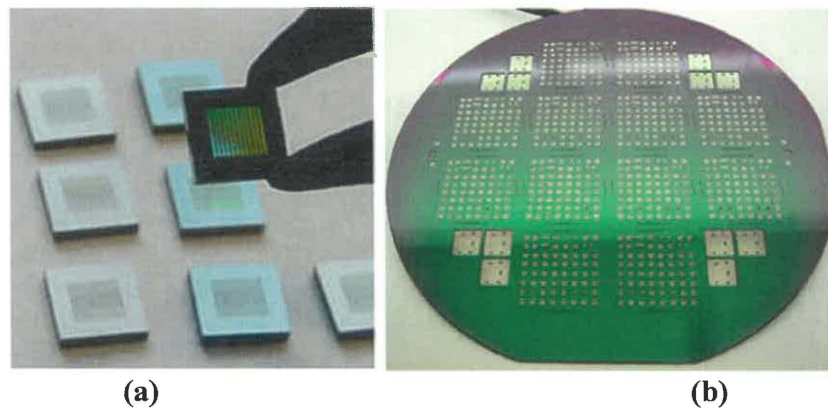


**Figure. 3.2** Optical images of nano/micro-stencils courtesy of Dr. Cees Van Rijn, Aquamarijn Filtration, The Netherlands (a) and Prof. J. Brugger's group, EPFL, Lausanne, Switzerland (b)

In our studies, Si/SiN chips with several built-in nanosieve membranes, each containing hexagonal arrays of nano-apertures, and fabricated by the combination of LIL and RIE [7] (see Fig. 3.3) were extensively used. For this reason the processes involved in their design and fabrication is outlined in the following paragraphs.

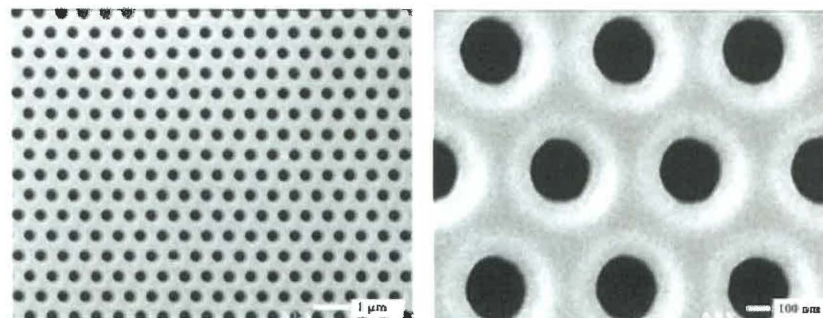


**Figure 3.3** SEM micrographs of stencils fabricated by LIL and RIE; the architectures used during our experiments were: 350 nm wide apertures spaced at 700 nm and respectively 1.6 µm (stencils fabricated at Aquamarijn Filtration, The Netherlands)

The process starts by defining the membrane window areas, thus the backside of a single crystalline (100) silicon wafer, is pre-etched to a determined thickness (e.g. 15  $\mu\text{m}$ ) using optical lithography and conventional KOH wet etching.

On the front side of the pre-etched support a layer of amorphous silicon nitride with a thickness of about 100 nm is deposited by means of LPCVD by reaction of dichloresilane ( $\text{SiH}_2\text{Cl}$ ) and ammonia ( $\text{NH}_3$ ) at a temperature of 850  $^\circ\text{C}$ . An etch mask layer of sputtered chromium with a thickness of about 30 nm is deposited on the stencil's top-side, except on the area where the nanosieve pattern will later be formed. A layer of positive resist is spun on top of the latter and patterned using LIL. The interference pattern obtained on the resist is transferred into the silicon nitride membrane layer by means of reactive ion etching (e.g.  $\text{CHF}_3/\text{O}_2$  at 10 mTorr and 75 W for 2 min) forming the required perforations. Subsequently, the silicon underneath the membrane layer is isotropically etched away (e.g.  $\text{SF}_6/\text{O}_2$  at 100 mTorr and 100 W for 10 min) to form the macroscopic openings in the support.

The LIL exposure set up used is known as "Lloyd's mirror configuration" that was presented in detail in Chapter 2. A part of an incoming plane wave is reflected by the mirror and forms an interference pattern on the substrate with the part that reaches the substrate undisturbed. The period of the generated interference pattern is defined by the relation  $\Lambda = \lambda/2 \sin\theta$ , where the angle  $2\theta$  between the interfering beams can be changed by rotating the mirror/substrate configuration. The main drawback of LIL is that the technique is limited only to patterning of periodic structures without great flexibility in defining shapes.

Another interesting procedure for high volume fabrication of nano-pore membrane chips was proposed by Heyderman and coworkers [8]. They combined the techniques of hot embossing (HET) for replicating the nano-pore arrays and photolithography with silicon micromachining to produce alignment marks, break lines and free-standing membranes. Chips ( $10 \times 10 \text{ mm}^2$ ) containing four nano-pore membranes were fabricated and some of the membranes were structured with arrays of pores with three different diameters.

The use of an electron beam writing (serial) rather than laser interference (parallel) for the formation of structures carries the flexibility to produce each membrane

with a customized nanostructured design. This ‘mix and match’ technique opens the way for batch processing of nanostructured membranes, facilitating new avenues for research and technology.

### 3.2.2 Membrane flow process (MFP)

We preferred to follow the MFP scheme for stencil fabrication (Fig. 3.1(b)). In the early stages of the project we took advantage of the existing expertise at our institute in growing amorphous thin films of silicon carbide (SiC), via plasma-enhanced chemical vapor deposition (PECVD) [9]. Thus we could straightforwardly prepare blank, free-standing SiC membranes. PECVD SiC is a material that represents a very good candidate for replacing the widely used LPCVD grown  $\text{Si}_x\text{N}_y$ , because it has excellent intrinsic structural, mechanical, and optical properties (e.g. a high Young’s modulus, good optical and x-ray transparencies, and they show high tolerance to x-ray radiation) and a lower fabrication temperature than  $\text{Si}_x\text{N}_y$ .

An MFP sequence starts like the WFP one with the deposition of a nitride or carbide coating layer, (e.g. in this case the PECVD deposition of amorphous-hydrogenated SiC layers) on both sides of a (100) silicon wafer. Thermal treatments were performed after each side coating to maintain a low tensile stress within the layer. Backside masking and selective removal of SiC and further Si frame etching in aqueous KOH solution (30%, at 70 °C) were used to remove selected regions of the Si to leave square suspended blank membranes. At this stage either EBL or FIB milling can be employed to “write” the desired patterns (e.g. array of holes, electrodes, etc) directly on the membrane. However, if EBL were used, after pattern development, an additional etching process (e.g.  $\text{CFH}_3/\text{O}_2$  plasma RIE) would be required to realize the perforations through the membrane.

To keep the number of steps involved in the stencil preparation to a minimum, we decided to take advantage of the direct focused ion beam (FIB) milling technique. An FIB tool has a working principle similar to that of a scanning electron microscope, but instead of electrons, ions (e.g.  $\text{Ga}^+$ ) are rastered across the substrate [10,11]. Being much heavier than photons or electrons, ions can strike with a much greater energy density thus

“writing” or more precisely “milling away” features (patterns) directly on various hard materials, such as metals, semiconductors or ceramics. In general, the interaction of an energetic ion with a target-sample, depending on the ion energy, can produce various results: implantation, swelling, deposition, sputtering, re-deposition, backscattering etc. Most of the interactions are not completely separable and may lead to redundant side effects that need to be avoided for specific applications. Sputtering is the major effect in FIB milling, and the sputtering yield, defined as the number of atoms ejected per incident impacting ion, is a measure of the efficiency of material removal. During sputtering, ejected atoms or molecules are frequently redeposited onto the sputtered region and this redeposition makes it difficult to precisely control the amount of material removed by sputtering. The essence of FIB milling is to carefully control both the material sputtering and the redeposition, so that a precise amount of material can be removed. The proper energy of the impinging ions for sputtering away the target material is ranging between 10 and 100 keV for most of the ion species used for milling.

Photons and electrons, due to their low mass, can efficiently expose or write only soft materials such as photoresists or e-beam resists i.e. the media that is usually used to transfer the patterns to the substrates in procedures normally used in photolithographic or e-beam lithographic process. Therefore the choice of FIB milling could represent a more beneficial option with respect to advanced lithography or EBL, since PMMA-coating, exposure and development steps as well as the pattern transfer by means of plasma etching are eliminated (thus not only making the process simpler and quicker but also further reducing the risks of contamination).

Nevertheless, ion milling processes carry their own challenges. In particular, drilling the membrane apertures directly by FIB has limitations imposed by the ion beam diameter, surface charging and, in particular, by the thickness of the insulating membrane layer (easily realized apertures are usually greater than 50 nm in diameter). To reduce charging effects and beam drifting caused by the  $\text{Ga}^+$  ions implantation process into the nitride or carbide layer, a thin metallic layer (e.g. Au/Pd, 5-10 nm thick) is very often, initially sputtered on both-sides of the membrane.

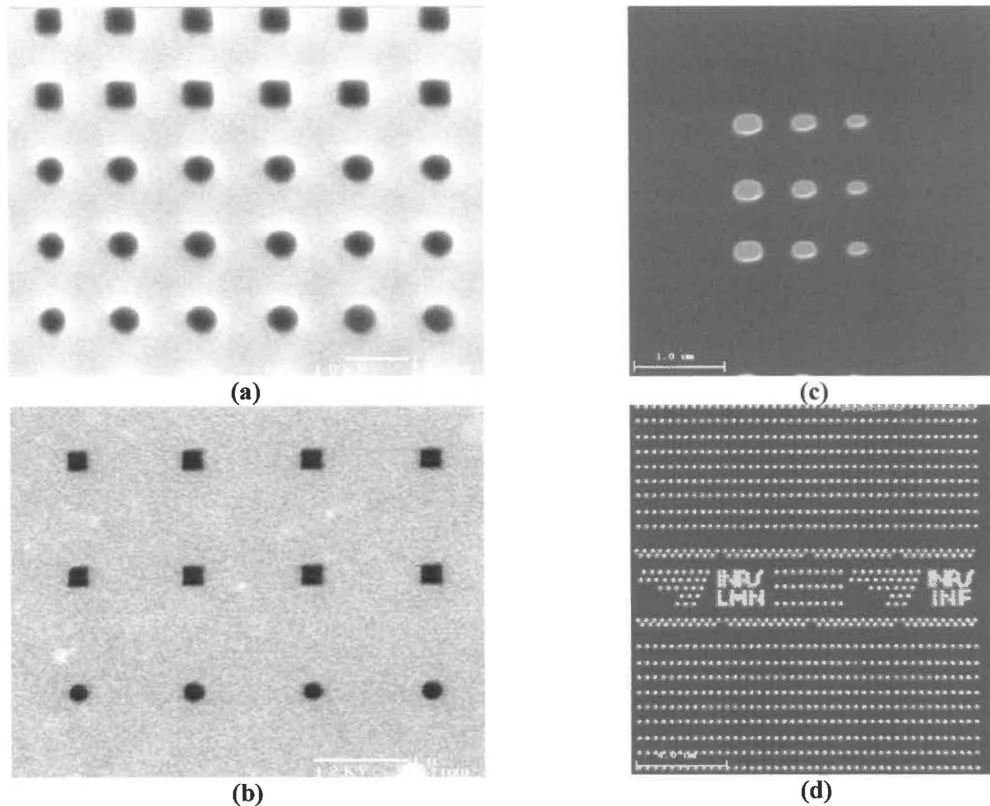


**Figure 3.4** SEM micrographs of patterned architectures realized in 1.2  $\mu\text{m}$  thick SiC membranes (a) and (b); FIB images of milled patterns in 200 nm thick SiN membranes (c) and (d)

A very important aspect in the fabrication of the nanostencils is the aspect ratio (i.e.  $A_r \sim \text{width} / \text{depth}$ ) of the apertures made in the membrane. On one hand thin free-standing membranes are fragile, thus the membrane should be made thick enough to survive processing, handling and usage. On the other hand, fairly thick membranes make it difficult to open up small apertures because of the intricacy of etching features with high aspect ratios. In this respect a 100 nm thick membrane, with an opening of 1-2  $\mu\text{m}^2$ , has yet reliable values for processing and leads easily to apertures with a 1:1 aspect ratio. Since the initial SiC films we used had thicknesses above 1  $\mu\text{m}$ , we decided to use and pattern commercially available ultra-thin SiN membranes<sup>1</sup> to achieve the best possible aspect ratio values for the apertures arrays drawn directly by FIB.

<sup>1</sup> We were using commercially available low-stress  $\text{Si}_x\text{N}_y$  membranes (www.silson.com); chip size 5 x 5 mm; membrane window (active area) from 0.5 x 0.5 to 1.5 x 1.5 mm, membrane thickness between 50 to 200 nm.

### 3.2.2.1 FIB drilling of free-standing SiN ultra-thin membranes

The basic components of a FIB system are an ion source, an ion optics column, a beam deflector and a substrate stage. Liquid metal ion sources (LMIS) are widely used and provide reliable and steady ion beams for a variety of ion species (e.g. Al, As, Be, Ga, etc). LMIS typically consists of a capillary tube with a metallic needle through it heated close to the melting point, an extraction electrode, and shielding elements<sup>2</sup>.

The FIB system we employed in our experiments was a Hitachi FB2000A system operating with a gallium ( $\text{Ga}^+$ ) ion beam at a 30 keV acceleration voltage and an image resolution of about 10 nm. Different sets of beams (e.g. M0-6, M0-50, M0-100) defining the variable aperture widths of the beam in the micron range can be chosen during operation. A limitation of this particular system is that the sample holders can not accommodate samples larger than  $5 \times 5$  mm, these dimensions being typical for thin TEM sample preparation; so the stencil chip frames can not be any larger. Other systems can provide a higher flexibility in terms of sample size processing.

The system is controlled by dedicated software and once the *design* is realized in a form of a *drawing* (e.g. ordered arrays of squares, circles or lines) the drawing is transferred via the “*vector scan controller*” *feature* to the milling system such that *milling* takes place only in the *designated areas*. Once the sample is inside the processing chamber and the alignment and beam focusing are fine tuned the first position for *transferring the drawing* onto the membrane is realized through a *stage controller*. From there, the rest of the patterns will be “stitched” with the desired distance in between.

A further drawback of this system is that one can not spend too much time adjusting the alignment of the membrane, milling and imaging taking place simultaneously.

The FIB 2000A system can work only at fixed pre-defined area magnifications such as  $256 \times 256 \mu\text{m}$ ,  $128 \times 128 \mu\text{m}$ ,  $64 \times 64 \mu\text{m}$  and down to  $1 \times 1 \mu\text{m}$ . In other words for this particular system the maximum area that can be raster by the ion beam and milled in one shot is  $256 \times 256 \mu\text{m}^2$ . Because the *bitmap drawing* must be  $512 \times 512$  pixels, for a magnification of  $256 \times 256 \mu\text{m}$ , the minimum feature size that can be obtained is thus

---

<sup>2</sup> It is to be noted that the backscattered ions can be used to provide an image of the surface, exactly the way electrons do in a scanning electron microscope, usually with a lower resolution.

500 nm (the value corresponding to one pixel). We chose to define our motifs working at magnifications ranging from  $32 \times 32 \mu\text{m}^2$  down to  $8 \times 8 \mu\text{m}^2$  corresponding to minimum aperture widths from 62.5 nm down to 15.625 nm.

In practice, we could not obtain apertures smaller than  $\sim 85$  nm; the main reason being the beams drift on the SiN surface during the milling process; this causes an elongation (deformation) of the initial pattern (Fig. 3.5 (a) and (b)).

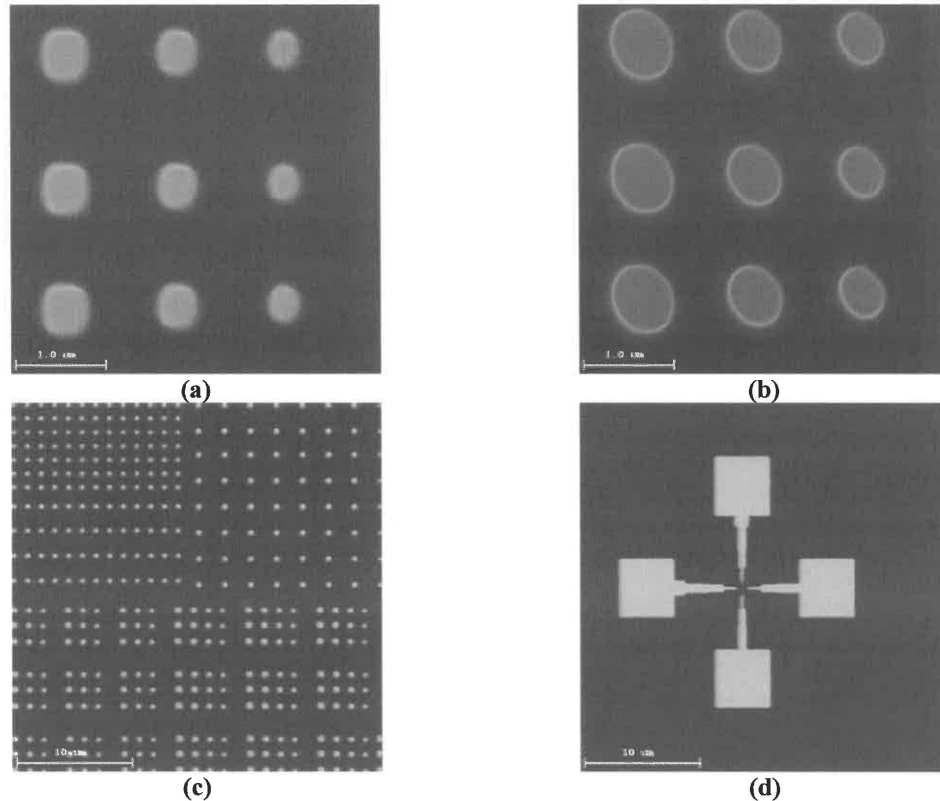


**Figure 3.5** FIB-images of SiN milled membranes. The drift of the  $(\text{Ga}^+)$  ion beam on the membrane surface induces a shape distortion of the desired patterns (a) and (b); various designs milled in 100 nm thick SiN membranes (c) and (d)

We were mostly interested in milling periodic apertures (fig. 3.5 (c)), nevertheless the process is highly flexible to create various designs like for instance the 4-point probe electrodes architecture depicted in fig. 3.5 (d)).

To minimize both charging effects and induced beam drifting induced by the  $\text{Ga}^+$  ions, a thin Au/Pd layer (5-10 nm) was deposited by sputtering on both sides of the membrane. Even though this process helps a lot in the beginning of the milling process leading to better results in terms of pattern reproducibility the non-uniformity of the Au/Pd layer thickness itself induces imperfections in the definition of the apertures.

A whole set of parameters such as beam diameter (e.g. M0-20, M0-50, etc), dwell time, number of scanning frames for the whole process, direction of the beam scanning (up-down, left-right or combination) are absolutely critical for high-definition of the motifs and highly depend on the system that is used. As a general remark, very good feature resolution is obtained at low values for the ion beam current intensity (e.g. few pA) but the time of milling is much longer and surface charging can appear with time. We found a good compromise for “feature resolution vs. speed” in realizing larger drilled areas at around 50 pA. Best resolution is obtained at only couple of pA where the ion spot size is minimum.

### **3.3 Pulsed laser deposition (PLD) technique for growth of thin films and structures**

#### **3.3.1 Background**

The discovery of high- $T_c$  superconductivity in 1986 [12] opened a new era in research of complex thin films. The new challenges associated with the growth of high-quality films of complex materials (often composed from several different elements and having unit cells comprising up to 100 atoms [13]) stirred the exploration of several novel thin-film synthesis approaches. For instance, thin-film deposition methods at or close to the thermodynamic equilibrium, such as chemical vapor deposition (CVD) [14], were basically unable to synthesize high-quality epitaxial, single-phase, complex materials such as cuprate-based superconductors (e.g.  $\text{YBa}_2\text{Cu}_3\text{O}_{7-x}$ ). Chemical vapor deposition is typically used for forming high-throughput coatings on silicon wafers, where the requirements regarding growth and interfacial control are of the order of a few hundred nanometers. On the other hand, the progress in monitoring growth at sub-monolayer resolution using reflection high-energy electron-diffraction (RHEED) demonstrated that complex metal oxides thin-films can be synthesized using molecular beam epitaxy (MBE) [15]. However, in the case of complex materials, the MBE growth turned out to be a laborious and long process demanding dedicated equipment which usually is very

expensive and complicated to operate. Currently, molecular beam epitaxy is used extensively in the production of III–V semiconductor for optical devices, where the dimensions and interfaces need to be controlled on an atomic scale.

At the time of the discovery of the cuprate superconductors, only sputter deposition (SD) showed any promise as a technique to “easily” produce them as thin films [16], due to the non-equilibrium nature of the process. Sputtering became increasingly popular in the early eighties with the appearance of so-called “magnetron” sputtering sources that magnetically confine electrons in a plasma, which in turn increases the degree of ionization, and therefore also the deposition rate. Yet, more versatile alternative methods need to be discovered.

The pioneering work of Venkatesan and co-workers in 1987 [17] brought the relatively unknown technique of pulsed laser deposition (PLD) to researchers attention and demonstrated that the method is both versatile and simple and gives very good results for complex materials. The attractiveness of PLD as a research tool has since increased even more spectacularly than sputtering did in the early 80s.

The leading feature of PLD is its unrivaled ability to preserve the chemical composition of the bulk solid-source materials used to form the resulting thin films, and, providing the right deposition parameters (e.g. low deposition rate and adequate substrates heated at high temperature), to provide a very good control of the crystalline structure and of the quality of the films (sufficient to get epitaxy and flat interfaces for instance). Among numerous successful experimental endeavors, let us mention colossal magnetoresistance, reported in 1994 by Jin et al. [18] for thin films of doped manganite  $\text{La}_{1-x}\text{Ca}_x\text{MnO}_3$  grown by PLD. The unique property of PLD to transfer material congruently (i.e. stoichiometric transfer) from bulk target to the film in a single step, was even more remarkably demonstrated more recently, with the hetero-epitaxial growth of the Nd and Cr co-doped lasing garnet  $\text{Gd}_6\text{Sc}_2\text{Ga}_6\text{O}_{12}$  (Nd,Cr:GSGG) on Si(001) [13]. It is worth noting that Nd,Cr:GSGG contains 160 atoms per unit cell and six different elements, thus it seems quite intricate to synthesize such thin-films using other method .

In the last two decades, along with increased complexity, there has been an associated outburst in the diversity of materials that are being designed, engineered and investigated for their potential technological applications (e.g. piezoelectric, ferroelectric,

ferromagnetic, or combination of thereof). Nevertheless, “traditional” materials such as elemental Si or Ge and the compound semiconductors GaAs, SiGe alloys, etc. also continue to be investigated and to play a fundamental role in micro and nanotechnology today. The flexibility of PLD in conjunction either with nanostenciling or assisted self-assembly mechanisms to fabricate, was therefore ideally suited to *synthesize and investigate patterned nanoscale-sized structures* from two main classes of functional materials, namely Ge/Si semiconductor heterostructures and ABO<sub>3</sub> perovskite-type ferroelectric and multiferroic complex oxides.

### 3.3.2 PLD parameters

In general, for PLD as for any deposition technique, there is a set of fundamental parameters which need to be controlled in order to provide the proper conditions for achieving high-quality thin-films in terms of their morphology and crystallinity. The most important of these parameters are (a) the energy of the particle flux impinging on the substrate, (b) the ambient gas nature and pressure in the deposition chamber, (c) the substrate temperature and (d) the deposition rate. Nonetheless, in the case of PLD, other parameters such as the laser wavelength, target composition and density, substrate crystallinity, orientation, lattice constants or its chemical composition influence strongly the thin-film growth process [19-22].

PLD shows several attractive features such as: the generation of energetic species, stoichiometric transfer of material from the target in certain deposition conditions (including thermal-controlled conditions of the substrate, reaction between the ablated cations and molecular oxygen in the plasma of the ablation plume) and compatibility with a large range of background pressures ranging from UHV to 100 Pa; these features will be discussed in detailed in the following sections.

#### *Energetic character of PLD*

A high power pulsed-laser beam focused onto a target of material to be deposited, vaporizes or ablates a small amount of the target material for each laser pulse if the laser has an adequate *energy density* (i.e. *fluence* on the target) above a critical ablation

threshold. The ablated material is ejected from the target and forms a plasma above the target surface. The plasma expands adiabatically at the end of the laser pulse and is responsible for the strongly forward-directed plume that provides the material flux for film growth. The ideal range of energies for depositing species while promoting surface diffusion on the growing film is between 10 and 50 eV [22]. While PLD usually produces a deposition flux just in this energy region, time-resolved spectroscopy studies of the ablation plume expansion has demonstrated that the ablated species can reach kinetic energies values on the order of several hundred eVs. This can result in species implantation into the substrate and can further produce major disturbances in the crystallinity of the film. In addition, it has been shown that particles with energies above about 50 eV can cause material to be re-sputtered from the film surface. This latter side-effect reduces the effective deposition rate and moreover, in the case of multielemental films can lead to a difference between the film's and the target's stoichiometry since certain elements are more susceptible to re-sputtering than others.

#### *Effects of the ambient gas nature and pressure*

A background gas is often introduced into the deposition chamber with the aim of serving two purposes (simultaneously). Firstly, by introducing a background gas in the PLD deposition chamber, the entire kinetic energy distribution is shifted to lower values until the fraction of particles with energies above the optimum regime became negligible. This in turn will result in a decrease in the deposition rate due to the plume being strongly scattered by the ambient gas and becoming less directed [19,22]. For instance a background gas can be used to moderate the plume energies to less than 1 eV leading to thin-films with fine morphologies. Secondly, in general, the formation of an epitaxial oxide film requires an oxidizing species (typically molecular oxygen) as a component of the flux. The amount of oxygen required for phase formation will depend on the thermodynamic stability of the desired oxide phase. Interaction of ablated species with the background gas often produces sub-oxide species in the ablation plume that can facilitate oxide phase formation.

### ***Substrate temperature***

The role of the substrate temperature in controlling the crystal structure and orientation and further the composition of the film is crucial. For instance, a minimum temperature is usually required to grow *crystalline* rather than *amorphous* films or epitaxial films rather than polycrystalline ones. To keep the desired composition, this temperature should be below the temperature at which excessive vaporization of the volatile film components occurs. The thermal energy that the condensing species possess when reaching the substrate increases surface mobility and provides part of the energy for nucleation and growth of the film. At a particular temperature (generally quite elevated) necessary for these processes to successfully take place, however, some volatile components may not stick to the substrate and/or some may re-evaporate after incorporation into the film.

Several research groups prepared for instance ferroelectric oxide thin films at near room temperature (conditions typically required for stoichiometric, but amorphous materials) followed by post deposition annealing at high temperature to crystallize the material and so that it acquire ferroelectricity. The mostly polycrystalline films that result from post-deposition treatments may not be fully crystallized and are typically neither oriented nor very dense. In-situ deposition, positioning the substrate onto a heated stage, is the preferable approach to achieve high quality film growth and can yield dense and epitaxial films. Usually a temperature window for optimum film growth is frequently given in terms of the temperature of the heater. Each ferroelectric material appears to have a distinct substrate temperature range that is optimum for epitaxial film growth, falling roughly within a 550 °C to 800 °C window or even higher.

### ***Deposition rate***

Epitaxial thin films of complex oxide materials can be produced using ceramic, dense, stoichiometric targets of the material of interest. The film thickness distribution from a stationary plume is rather non-uniform due to the highly forward-directional nature of the ablation plume. To first order, the distribution of material deposited from the ablation plume is symmetric with respect to the target surface normal, and can be

described in terms of a  $\cos^n(\theta)$  distribution, where  $n$  can vary from 4 to 30 [19,22]. The deposit from the ablation plume can also become asymmetric due to texturing of the ablated target surface, spatial inhomogeneities in the spot of the pulsed laser beam on the target surface, and laser absorption by the plasma [22]. However, raster scanning of the ablation beam over the target and/or rotating the substrate can produce uniform film coverage over large areas. As with evaporation, the film-growth process can be controlled at the atomic level using PLD, and epitaxial growth with deposition rates on the order of  $100 \text{ \AA} / \text{s}$  has been demonstrated with this technique.

A major aspect in the use of PLD for applications in industry is the improvement of schemes by which large area substrates can be effectively coated within a reasonable time. The dynamics of the laser ablation process results in a highly focused plume of material ejected from the target as pointed out earlier. While this leads to a congruent deposition with efficiency of about 70% of the ablated material, it also results in a significant variation in deposition rate over distances on the order of a few centimeters. For uniform film thickness over large areas, a special handling of the plume-substrate positioning is necessary and one solution suggested to overcome this limitation was the combination of substrate rotation with laser beam rastering over a large target.

### ***Other considerations***

Especially for the deposition of an oxide material, the selection of the *target* can have a major impact on film growth and the final film properties, including particulate density (droplets), epitaxy, foreign phase formation, and deposition rate [19]. As rule of thumb, ablation of non-metallic materials requires a target material with a high optical absorption coefficient for the selected laser wavelength. Undoubtedly the most used compounds for ablation targets are polycrystalline ceramics. The biggest advantage of ceramic targets is the ease of target fabrication for multi-cation species. In general, the phase of the target does not necessarily need to be that of the projected thin- film. In the case of complex oxides, it could be a mixture of several oxides with the correct global composition. The *cation* stoichiometry especially need be identical to that of the films, assuming the stoichiometric transfer from the target and a negligible evaporation from the film surface, some oxygen deficiency can be corrected by the presence of a reactive

oxygen atmosphere. For ceramic oxide targets, one prefers target that are highly dense, since this will reduce particulate formation during the ablation process. As an alternative to polycrystalline ceramics, the use of single crystals as ablation targets has been investigated, and has shown to be effective in further reducing the density of droplets [19,20,22].

Another important issue to consider is the *laser wavelength* used for ablation. The efficient ablation of the target material requires the non-equilibrium excitation of the ablated volume to temperatures well above that required for evaporation. This generally requires the laser pulse to be short in duration, to have a high energy density, and highly absorbed by the target materials. For ceramic oxide targets, this is most easily achieved via the use of short wavelength lasers operating in the ultraviolet. The most attractive laser sources are excimer lasers operating at 193, 248, or 308 nm wavelength. These lasers exhibit a pulse width on the order of tens of nanoseconds and laser pulse energy of several hundred milli joules.

While having many advantages in particular for the growth complex oxides films, PLD also has limitations that can not be neglected and thus should be addressed. One major potential drawback of PLD is the ejection of micron-size particles (*droplets*) in the ablation process. If these droplets are deposited onto the substrate, they alter the quality of the growing surface and may hinder the formation of multilayer device structures. The use of highly dense ablation targets tends to reduce particle formation but does not eliminate this problem completely. Several techniques have been developed to further reduce particle density. Approaches that focus on preventing the particles from reaching the substrate surface include off-axis laser deposition, velocity filters and line-of-sight shadow masks [23-25]. Another interesting approach suggested for eliminating particles is cross-beam PLD which involves the use of two laser beams focused on separate targets situated perpendicular to each other. The two ablation plumes collide and form a new stream containing light plume components and almost no droplets [26].

### 3.3.3 PLD-nanostencil experimental apparatus

The pulsed laser deposition unit we employed in the present studies is schematically shown in Fig. 3.6 (a). This unit consists of a GSI Lumonics KrF excimer laser ( $\lambda = 248 \text{ nm}$ ,  $\tau=15.4 \text{ ns}$  FWHM of the pulse) and a vacuum deposition chamber. The laser beam is directed onto the target by an optical system of lenses. The lens and window materials are chosen to minimize the absorption of laser light and thus to ensure a maximum possible laser energy on the target. The laser beam is focused at an angle of  $45^\circ$  onto the solid target (e.g. Ge, BaTiO<sub>3</sub>, BiFeO<sub>3</sub>) located in the vacuum chamber.

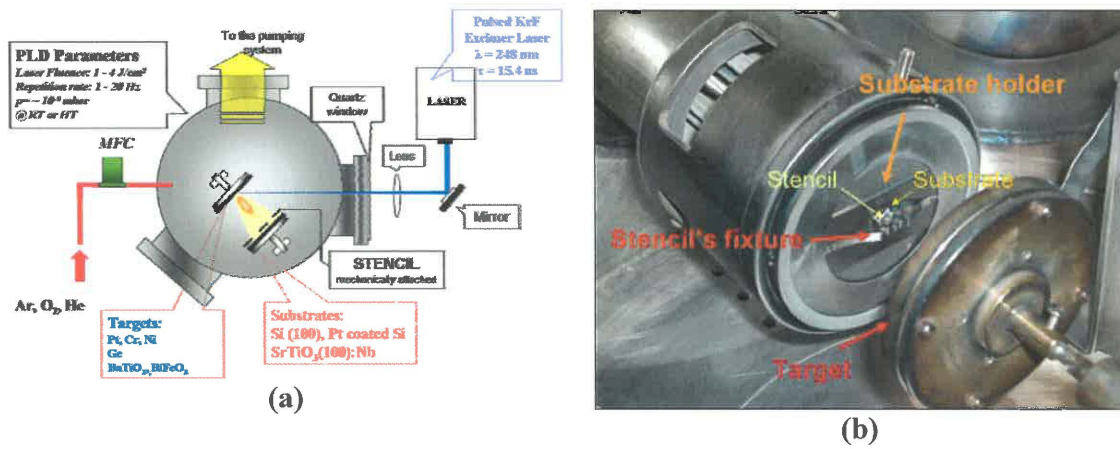


**Figure 3.6** Schematics of the PLD – nanostencil apparatus. (a) PLD principle and (b) optical image of the assembly target – stencil - substrate inside the deposition chamber.

The distance between the sample holder and the target holder is manually adjustable, and the entire deposition process – e.g. selection of the laser energy, laser repetition rate and number of pulses for ablation - is controlled via a computerized console. The substrate temperature is measured on the heater block with a K-type thermocouple and the maximum temperature achievable is about 800 °C. The power of the laser beam, behind the focusing lens and before entering the chamber, is measured as an average over multiple pulses to calculate the laser fluence. Laser fluences between 1-4 J/cm<sup>2</sup> have been attained for laser output energies of 100-250 mJ/pulse.

The stencils described in the previous sections and used as shadow-masks were mechanically clamped and temporarily fixed onto substrates (Fig. 3.6 (b)); the assembly substrate-stencil is mounted in front of the rotating target and this setup was employed in

both room-temperature and high-temperature deposition processes. To stabilize the target's surface, each deposition run was typically preceded by a target "cleaning" (while a shutter protects the substrate), during which the target was irradiated by several laser shots prior to using it for the film deposition. The purpose of this process was to expose fresh material, and maintain a steady-state composition at the target surface. This "cleaning" procedure was repeated whenever the ambient gas conditions were changed because the segregation process at target's surface is highly sensitive to the ambient atmosphere.

### Stencil deposition geometry

The most favorable geometry for deposition through a stencil implies a "punctual" source (S), large distance source-substrate (D) and minimum gap between the mask and substrate (G). These are the basic conditions that will minimize "blurring" effects (enlargement of the deposits) always present during the direct growth through a shadow-mask. PLD satisfies to a large extent most of these conditions. While in our PLD experiments the laser beam was focused via a system of lenses so as to produce a minimum laser spot of 1mm in diameter on the surface target (i.e. reaching the "punctual source (S)" requirement), the gap (G) control was not a trivial issue though since stencils were handled and fixed each time manually. To a good approximation, and if lateral surface diffusion-like processes are excluded, the widths ( $w_B$ -bottom width and  $w_T$ -top width) of a structure realized in this way are given by the geometric equation depicted in Fig. 3.7, where  $w_A$  is the initial aperture size opened in the membrane.

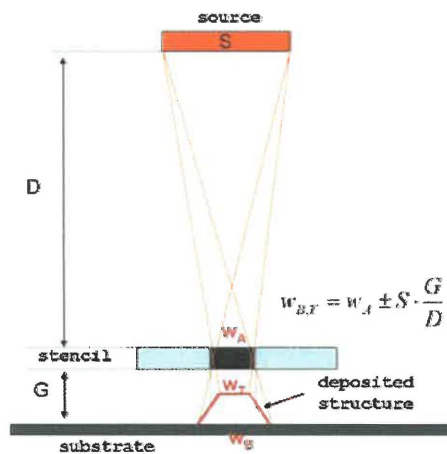


**Figure 3.7:** Schematic drawing of stencil deposition (not to scale); the enlargement of the deposited structure  $w_B$  is highly dependent on the 3 main geometric parameters: the source dimension (S); distance source-stencil (D) and the gap (G) between the stencil and the substrate

$$w_{B,T} = w_A \pm S \cdot \frac{G}{D} \quad (3.1)$$

As a general rule, the gap between stencil and substrate should be as small as possible (ideally 100 nm or less) and must be kept uniform over the whole shadowed area. Nevertheless, the stencil-substrate spacing usually varies due to substrate surface irregularities, foreign particulates, roughness or bending of the membrane layer. Analysis of numerous SEM micrographs showing various patterned structures indicates an average broadening of about 10-15%, value which can be minimized in principle by a more firm fixture stencil-substrate. However, if the stencil is pressed too hard against the substrate, the membrane may bend and breaking can occur.

The enlargement ( $w_B$ ) of the deposited structures with respect to the initial aperture size ( $w_A$ ) might be also caused by a diffusion process of the evaporated species on the substrate. The diffusion length depends primarily on the deposited material and on the substrate surface (temperature, preparation, deposition rate). Lowering the substrate temperature (e.g. experiments carried out at room-temperature) the length diffusion is mostly reduced.

## **3.4 Characterisation Approaches**

### **3.4.1 Scanning electron microscopy (SEM)**

For the investigation of the morphology of any given sample, scanning electron microscopy (SEM) is certainly one of the most suitable and convenient techniques. Specimens of various natures (metallic, semiconducting, insulating or organic) and various sizes (from  $\text{mm}^2$  to full wafers) can be easily accommodated in the multi-purpose observation chamber which is usually maintained under high-vacuum and is equipped with a motorized (automated) stage.

When a focused electron beam (e.g. energy of 1 – 20 keV and spot size 1 – 10 nm) hits the sample's surface several processes occur [27]. The most important ones are as follows: elastic and inelastic backscattering of primary electrons, emission of secondary electrons, as well as Auger electrons and element-specific characteristic X-ray emissions. Different detectors are used which are sensitive to electrons of different energies or photons in the latter case, thus, SEM-images do not only carry a

morphological and topographical information but also information that could be specific to special properties, such as the chemical composition, of the specimen.

The SEM tool functions by scanning the surface of the sample with an electron focused beam collimated by a series of electromagnetic lenses that are situated inside the SEM column. The smaller the focus (i.e. beam spot size on the sample's surface) the better the spatial resolution achieved. The primary electrons in the focused beam penetrate up to 1  $\mu\text{m}$  in depth (depending on their energy) into the sample, various collision and energy dissipation processes creating emission of electrons or photons in a volume having a diameter of the same order as the penetration depth around the focal spot. Both backscattered electrons and characteristic X-rays emitted from this whole volume are detected and thus the resolution of backscattered electron images or x-ray images can not have a resolution better than 1  $\mu\text{m}$ .

To obtain a topographical image of a sample under investigation, secondary electrons are used and captured by a detector. The secondary electrons are mostly emitted from a very limited area of the sample's surface; the area that is very close to the focal spot. However, there are secondary electrons produced at the surface by the backscattered electrons and this effect may deteriorate the resolution. As for the Auger electrons, they are produced and only emitted straight from the surface (energies range from 100 eV to 1 keV) being highly element specific.

The contrast between two areas of a SEM image is a function of the number of the secondary electrons which are collected by the detector when the focused beam of primary electrons hits the sample. The most important contrast is the edge contrast. If an edge is present in the focal spot much more secondary electrons are emitted compared to a smooth surface. The emission of the secondary electrons also depends on the angle of the incident beam with respect to the sample surface (tilting contrast). On the other hand, if the illuminated area is not in direct sight of the detector, fewer electrons contribute to the signal and the spot is dark. Chemical contrast images can be obtained by the examination of the inelastic backscattering or Auger electrons. When very low energy electrons are detected even a potential contrast is seen since differently charged areas of the sample exhibit different electrical fields which may enhance or reduce the detection efficacy of the emitted secondary electrons.

Within the framework of these studies, we used two types of microscopes: (i) a conventional high resolution field-emission SEM (JEOL JSM 6300F) with a nominal resolution (beam spot size) of about 1.5 nm at 30 kV and magnification exceeding 250'000 and (ii) a cold cathode field emission SEM (JSM-7001F) with a nominal resolution of 1.5 nm at 1 kV and 0.8 nm at 30 kV and a magnification going up to 1'000'000 (Examples of images taken with these two microscopes are shown on Fig. 3.8). Cold cathode field emission SEMs provide the highest resolution, beam current stability and produces the finest spot size as well as they generate higher x-ray fluxes for chemical analysis at high resolution conditions.

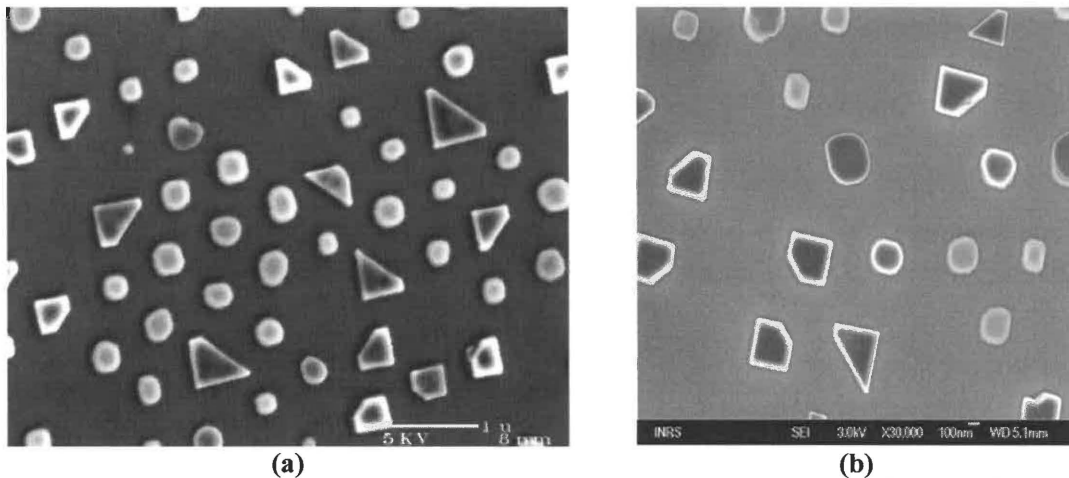


**Figure 3.8** SEM micrographs of bismuth ferrite ( $\text{BiFeO}_3$ ) structures on Nb doped (100) strontium titanate ( $\text{SrTiO}_3$ ) substrate, after room-temperature stenciling and rapid thermal annealing. (a) image taken with JSM6300F and (b) image taken with JSM 7001F

SEM enabled us to examine the morphology of the thin films (mainly the topography) and to assess the sizes and periodicities of patterned nanostructures that were generated within the frame of this work on various surfaces. Since electrons are used to irradiate the sample and electrons are also detected from the sample, major difficulties arise when the investigated samples like semiconductors or insulators that we were examining became charged. Therefore, the energy of the primary electrons has to be adapted and we used low accelerating voltages between 1 – 5 kV. Investigations of the samples were necessary at different stages of the fabrication and patterning processes (e.g. room-temperature deposition and/or after annealing treatments) thus we examined

all the samples without a conventional conductive coating of gold or carbon commonly used to prevent charging effects, since they would irreversibly modify the sample. If the accelerating voltage energy chosen to avoid excessive charging is too low, however, very few secondary electrons are emitted and the sample also becomes negatively charged which can in turn affect the clarity and sharpness of the image.

### 3.4.2 X-ray diffraction (XRD)

When X-ray photons from a beam of monochromatic radiation collide with atoms of a substance that has some degree of order or periodicity in the arrangement of these atoms, coherent scattering of the X-ray occurs. The scattering from these periodic arrays of atoms (Fig 3.9 (a)) leads to diffraction, i.e. to a diffracted intensity maximum if the scattered photons interfere with each other constructively [28,29].

The straightforward relationship that gives the dependence between the diffraction angle ( $\theta$ ), the wavelength of the radiation ( $\lambda$ ) and the spacing between the periodically arranged planes of atoms ( $d$ ), is known as Bragg's law ( $n\lambda = 2d \sin\theta$ ) where  $n$  is an integer. Since the distances between the atomic planes are dependent on the size and distribution of atoms i.e. the structure of the material, in the first place, XRD is extremely useful for qualitative (crystalline) phase identification.

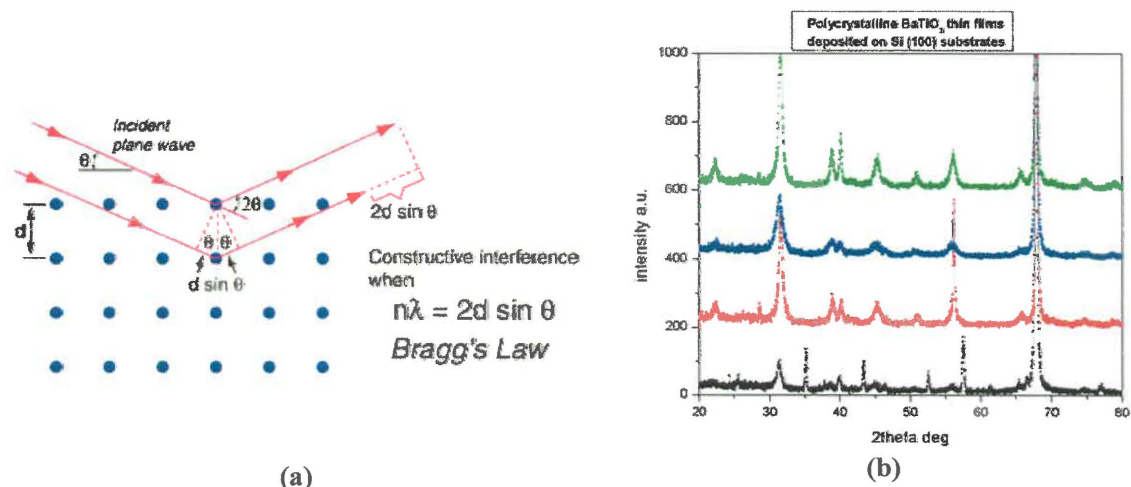


**Figure 3.9** (a) Schematics of the x-ray coherent scattering phenomenon (diffraction) when a beam of monochromatic radiation collide with atoms periodically arranged in a crystalline structure [xray0.princeton.edu/.../XrayDataCollection.html]; (b) diffraction pattern recorded in grazing incidence showing the typical spectra of a polycrystalline BaTiO<sub>3</sub> test thin films deposited on Si (100) substrates, obtained at room-temperature and subsequently post-deposition annealed.

A diffraction pattern is typically recorded in the form of a graph of diffraction angle (actually twice the diffraction angle  $2\Theta$ , or interplanar spacing) versus diffracted line intensity (Fig. 3.9 (b)). In principle, one diffracted line will occur for each unique set of planes of the specimen's lattice with their specific interplanar distance. Each of these distinctive patterns therefore represent an experimental "fingerprint" for any given crystalline materials (having a specific crystallographic structure and specific interplanar distances). This enables the detection of the various crystalline phases present in the investigated film, the specific pattern identification being based on a library of standard patterns of single-phase polycrystalline materials, (*PDFiles ICDD*). When a mixture of different phases is present in the sample, the resultant "diffractogram" is formed by the superposition of the individual patterns.

A diffraction pattern offers a wealth of information if three sets of parameters are recorded accurately: (i) the position of the diffraction maxima, (ii) the peak intensities and (iii) the peak width as a function of diffraction angle. These three pieces of information can, in principle, be used to identify the crystallographic structure and quantify the composition of the sample, as well as to calculate the material's lattice parameters (and further the stress or strain) as well as the crystallite size and distribution.

In our studies we have employed a PANalytical X'Pert Pro MRD 4-circle diffractometer system that has multi-modular incident optics (line and point focus) and that can be configured for: conventional phase analysis in  $\theta - 2\theta$  (Bragg – Brentano) and grazing incidence configurations, in-plane diffraction, texture analysis, high-resolution reciprocal space mapping of epitaxial layer, high-resolution rocking curve measurement of epitaxial layer and residual stress analysis. In addition, we can use the X-ray source and detection system of the diffractometer to perform X-ray reflectivity and thin film thickness analysis.

In the case of complex oxides we used extensively both  $\theta-2\theta$  and grazing incidence ( $\omega = 0.5 - 1$  deg) techniques to assess the structure and quality of our thin films as well as of the patterned arrays of structures (Chapter5). For the latter, due to the very small amount of material deposited, long time integration/scanned step were required in order to record reliable diffraction spectra. To determine the in-plane and out-plane lattice parameters of the deposits reciprocal space mapping (RSM) has been used.

### 3.4.3 Micro-Raman spectroscopy

Raman spectroscopy is a form of vibrational spectroscopy based on the scattering of monochromatic light (usually from a laser) upon interaction with a sample. The photons of the laser light are absorbed by the sample and subsequently reemitted. Most of these scattered photons have exactly the same wavelength as the incident photons (elastic scattering) and are known as Rayleigh scatter; however there is a small amount (approximately 1 in  $10^7$  photons) of the scattered radiation that is shifted to a different wavelength due to the inelastic scattering (Stokes and Anti-Stokes Raman scattering) (fig. 3.10). The change in wavelength of the scattered photon provides the chemical and structural information. The difference in energy between the incident photon and the Raman scattered photon is equal to the energy of a vibration of the scattering sample. A plot of intensity of scattered light versus energy difference is a Raman spectrum.

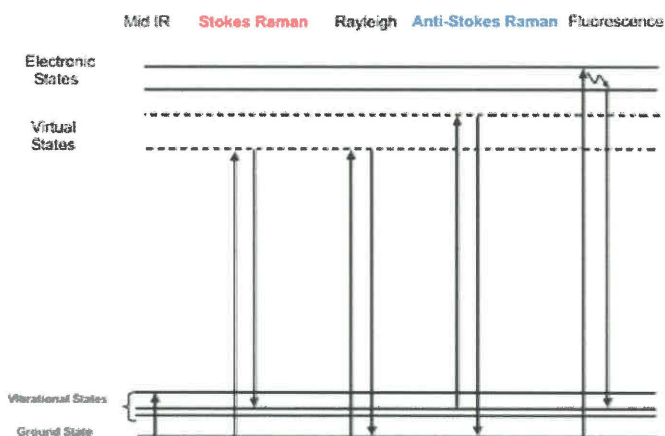


**Figure 3.10** Energy diagram for Raman scattering ([www.jobinyvon.com](http://www.jobinyvon.com))

Frequency of the reemitted photons is shifted up or down in comparison with the original monochromatic frequency, which is known as the Raman *effect*. The Raman shift provides information about vibrational, rotational, electronic level transitions and other molecular modes. Raman spectroscopy can be used to study solid, liquid, and gaseous samples and is extremely useful for chemical identification, characterization of molecular structures, effects of bonding, environment and stress on a sample.

The Raman system typically consists of four main components: (i) an excitation source (laser), (ii) an illumination system and light collection optics, (iii) a wavelength selector (filter or spectrophotometer) and (iv) a detector (photo diode array, CCD or photomultiplier). A sample is normally illuminated with a laser beam in the ultraviolet (UV), visible (Vis) or near-infrared (NIR) range. Scattered light is collected with a lens and sent through an interference filter or spectrophotometer to separate desired Raman modes or to obtain the Raman spectrum of a sample.

Micro-Raman spectroscopy has been demonstrated to be a surface-sensitive technique that is useful for extracting information about the composition and strain inside semiconductor quantum dots [30]. In Chapter 4 we present the structural characterization of patterned germanium nanostructures via micro-Raman spectroscopy; measurements were performed at ICMAB Barcelona, Spain.

The Raman system used is a Jobin-Yvone LabRam HR800 microscope and the optical measurements were carried out by probing the patterned areas with the 514.5 nm line of an Ar<sup>+</sup> ion laser focused with a spot size of about 1  $\mu\text{m}$ .

### **3.4.4 Scanning probe microscopy (SPM)**

The operation of a scanning probe microscope (SPM) consists in imaging surface features through an analysis and mapping of the interaction between a micro-probe with a sharp tip and the sample's surface [31]. One main criterion that differentiates the usage of different types of scanning probe microscopes is whether the sample surface being investigated is conductive or non-conductive. Therefore, scanning tunneling microscopes (STM) [32] are employed only for conductive surfaces whereas scanning force microscopes (SFM) can be used for non-conductive surfaces as well [33].

A further way to differentiate the various types of SFM techniques used relates to the "tip-sample" interaction detected as well as the probes employed. Various *probes* (e.g. magnetic, conductive) attached to a basic tool configuration (i.e. atomic force microscope (AFM)) and the suitable electronics enable the detection of a range of phenomena as for example in magnetic force microscopy (MFM) or piezoresponse force

microscopy (PFM). The resolution achievable depends both on the tip architecture and on the accuracy with which the tip follows the sample surface.

Piezoelectric transducer tubes control the motion of the probes while they are scanned across the area of interest. The tubes holding the piezo element are capable of positioning the tip and specimen with a lateral precision of a few Angstroms or less. A critical issue is how accurate the vertical position in the case of topography (or the amplitude of the interaction probed in other cases) is determined. This and the nature of the interaction probed (atomic attractive or repulsive forces, friction, electric charge distribution or magnetism) is what differentiates different SFM techniques.

In addition, there are different scanning modes classified by the range and the sign of the forces that they monitor (repulsive forces in contact or at very short range, attractive forces at larger distance) or the distance between the tip and the sample surface over which the forces operate. There are three possible operational modes for SFMs: contact, intermittent contact or tapping and true non-contact modes. Whenever possible, contact mode is avoided because of the inherent dangers of damaging the sensitive probe tip or even the sample surface itself. However, certain measurements such as friction, compliance, adhesion, piezoelectric properties, and thermal characteristics require direct contact with the sample.

#### **3.4.4.1 Atomic force microscopy (AFM)**

In atomic force microscopy (AFM) a fine tip at the end of a flexible cantilever is brought in contact with, or very close to, the surface to be imaged. Forces acting between the tip and the surface will cause a bending of the cantilever proportional to the interaction probed [33,34]. The interaction force between the tip and surface is then maintained constant or controlled using a feedback loop, which adjusts the z-position of the cantilever. By scanning the tip above the surface and recording the z-position of the cantilever, a map of the sample topography can be obtained. The deflection of the cantilever can be monitored in different ways but the most common technique is the so-called “optical lever” i.e. a laser beam is reflected by the end of the cantilever into a segmented light photodetector, which detects the deflection of the laser spot and thus

monitors the forces acting on the tip (Fig. 3.11 (a)). The amplitude of the bending is proportional to the force probed, a suitable calibration thus enabling a quantitative measurement of the force.

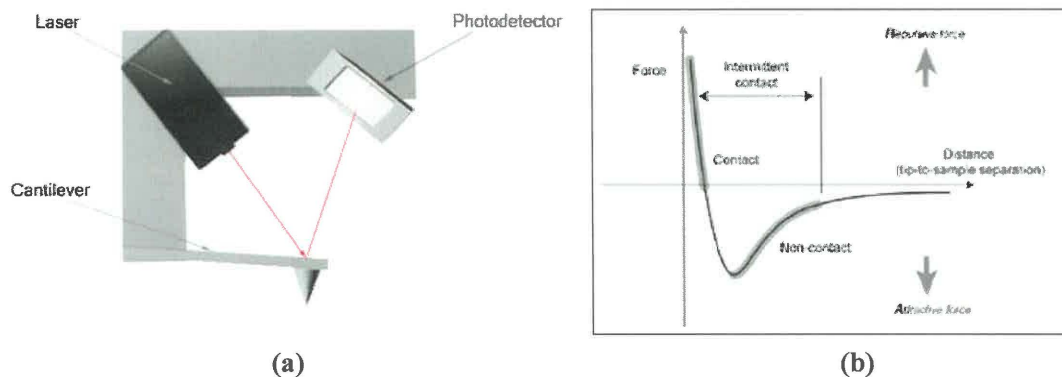


**Figure 3.11** (a) Schematics of the operation principle of an AFM set-up with an optical detection of the cantilever bend; (b) Force-response curve, the superposition of the attractive and repulsive forces acting between tip and sample plotted as functions of distance from the sample surface

The force measured by the AFM is resulting from all the attractive and repulsive forces acting between the tip and the sample, which are very difficult to de-convolute and which critically depend on the material of the tip and of the sample, respectively. Generally speaking the forces can be divided into *long range* and *short range* forces. Figure 3.11 (b) shows a representation of the long range (attractive) and short range (repulsive) forces acting between tip and sample as a function of the separation distance, together with a force response curve which is the superposition of these forces. When scanning in contact with the sample surface, short-range repulsive forces dominate. At larger distance from the surface mostly attractive long range forces will dominate, e.g. van der Waals forces, capillary forces (due to the water layer always coating all surfaces in air), magnetic forces or electrostatic forces.

When scanning is performed in contact mode, the tip elevation is adjusted via the feedback loop in order to follow the surface height using the deflection signal (this is in fact the cantilever bending caused by repulsive forces). When “tapping” mode is used for scanning, the cantilever with the tip is oscillated at its resonance frequency and the height is adjusted so that the tip touches the sample surface only for a short period of time. If the tip encounters a protuberance on surface, the oscillation amplitude will decrease and the feedback control raises the cantilever until the oscillation amplitude reaches the set value.

Using a Digital Instrument (Veeco) DI-EnviroScope tool, we performed AFM measurements in contact mode using for instance Veeco Nanoprobe, general purpose NP cantilevers ( $\text{Si}_3\text{N}_4$ , tip apex radius 20 nm) and in tapping mode using  $\mu\text{Masch}$  NSC15 cantilevers (Si, radius less than 10 nm). To investigate the patterned structures, the “tapping” mode is preferred since the tip-surface interaction is minimized and the tip is preserved sharp thus a better resolution of the image is obtained.

### 3.4.4.2 Piezoresponse force microscopy (PFM)

#### General background

Piezoresponse force microscopy (PFM), also called voltage-modulated scanning force microscopy (VM-SFM), is a method which allows the detection and switching of ferroelectric domains at the nanoscale based on the converse piezoelectric effect [35].

In this method, an ac-test voltage is applied between the bottom electrode of the sample and a conductive AFM tip to induce a local piezoelectric response (fig. 3.12). This local deformation is then retrieved from the deflection signal of the cantilever, and used to construct an image of the surface piezoelectric properties of the sample, and if the material is ferroelectric, to create an image of the ferroelectric domains.

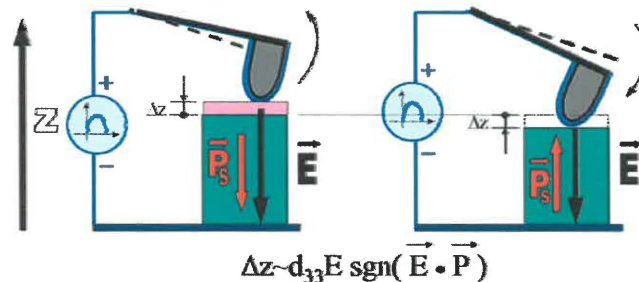


**Figure 3.12** Schematics of the operation principle for piezoresponse force microscopy [36]

In the beginning it was suggested that the surface of a ferroelectric sample is oscillating due to only the *converse piezoelectric effect*<sup>3</sup>, and that these oscillations are directly transmitted to the cantilever [37]. Since then it has been shown that the electrostatic interaction between the tip/cantilever and the bottom electrode of the sample may also play a significant role in the formation of the PFM contrast [38,39]. Recently,

<sup>3</sup> This notion is detailed in Chapter 5, section 5.2.

the contrast in PFM has been thoroughly analyzed and the limits for different contrast mechanisms have been defined [40]. It was found that, for high contact force between the SFM-tip and sample surface named “strong indentation regime”, the piezoelectric contribution is indeed dominant and the electrostatic contribution can be neglected. For low contact force (lower than 100nN) between the tip and the sample surface called “weak indentation regime” [40], the electrostatic contribution has, however, to be taken into account and both the piezoelectric and the electrostatic contributions are significant in the PFM signal. The PFM contrast is therefore strongly dependent on the experimental conditions.

In our experiments, we used medium to stiff cantilevers ( $k > 2 \text{ N /m}$ ) thus we worked in the strong indentation regime where the piezoelectric coefficient  $d_{33}$  can be calculated (in a given point) as follows:

$$v_{\omega} = \delta d_{33} A_{\omega} \quad (3.2)$$

where  $v_{\omega}$  is the amplitude of the piezoresponse signal,  $A_{\omega}$  the amplitude of the testing ac voltage, and  $\delta$  the sensitivity of the optical detector, which is in fact the conversion factor between the mechanical displacement of the tip and the electric deflection signal [35].

PFM is capable of detecting “out-of-plane domains,” where the spontaneous polarization direction is normal to the film plane, and which induces vertical vibrations of the sample surface and therefore of the cantilever, but also “in-plane domains,” where the spontaneous polarization lies within the plane of the film, and whose shear strain induces lateral oscillations of the sample surface, detected via friction and through a measurement of the torsion of the cantilever [41]. An example of ferroelectric domain imaging in (001)-oriented barium titanate single crystal performed using PFM is shown in Fig. 3.13.

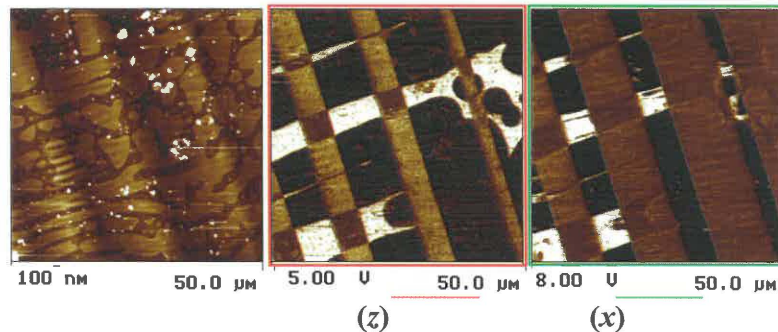


**Figure 3.13** Ferroelectric domain imaging in (001)-oriented barium titanate ( $\text{BaTiO}_3$ ). PFM images showing both z (out-of-plane) and x (in-plane) component simultaneously with the sample topography; image courtesy of Dr. C. Harnagea, INRS-EMT, Varennes, QC, Canada

The ferroelectric domain structure which forms in (001)-oriented BaTiO<sub>3</sub> crystals is well known [42] and may therefore be regarded as a “standard” sample for PFM. The two piezoresponse images were acquired simultaneously with the sample topography. The colors in images Fig. 3.13 (z) and (x) display the piezoresponse out-of-plane and the in-plane image for the same region. The complementarity of these two images is striking: regions with high contrast in the out-of-plane image (e.g. black or white color in image (z)) exhibit zero contrast in the in-plane image (e.g. “gray” color or intermediate contrast in image (x)). Thus, a certain point of the surface can have a polarization either perpendicular or parallel to the surface, in complete agreement with the known ferroelectric domain structure and crystallographic orientation of barium titanate. However, since piezoelectricity is a tensorial property, to determine all three components of polarization, additional information is needed. If for a BaTiO<sub>3</sub> single crystal, it is sufficient to know the crystallographic (001)-orientation of the sample, this may not be the case for materials with a lower symmetry [43].

#### ***PFM set-up used in our experiments***

We performed PFM measurements using a modified DI-EnviroScope (Veeco) AFM, and a computer-controlled lock-in amplifier (*Signal Recovery* Model 7265) connected to the AFM via a Signal Access Module. In a standard PFM experiment two lock-in amplifiers can be used to detect both components accessible together and simultaneously with the sample topography (schematics of the entire setup is shown in Appendix B).

To apply the voltage to the sample, we used conductive cantilevers from *Micromasch* either coated with semiconductor W<sub>2</sub>C or magnetic CoCr, or Applied Nanoscience cantilevers made from high-doped silicon (spring constant of 2 - 40 N/m). A small AC testing voltage of 0.25 - 0.5 V (typical frequency 29 KHz) is applied between the tip and the conductive substrate on which the structures were deposited.

In the experiments presented here, the in-plane domains are imaged with the x-axis horizontal. Also, white contrast stand for the positive direction (upward for z-PFM or left-to-right for x-PFM images) while black contrast in PFM images show a negative

component of polarization (towards the bottom electrode for z-PFM and right-to-left for x-PFM images). Hysteresis measurements were obtained using an auxiliary digital to analog converter of the lock-in amplifier, by applying a DC voltage that is swept between the chosen maximum and minimum values (e.g. -10 V to +10 V).

### **3.4.4.3 Magnetic force microscopy (MFM)**

In Magnetic force microscopy an AFM-tip coated with a magnetic material is used, making it possible to detect magnetic stray fields generated by a magnetic sample [44,45]. The magnetic force felt by the tip causes a shift of the resonance frequency of the cantilever, and tracking this shift while scanning across the surface results in an image of the magnetic field gradient. Alternately, if the cantilever is excited at constant frequency, the magnetic field gradient can be obtained from the phase lag between the mechanical excitation and the cantilever response.

It is necessary to keep the tip at a distance from the sample so that the long range magnetic forces are larger, or at least as large, as the short range contact forces normally used in atomic force microscopy. MFM tips are usually coated with a magnetic material such as CoCr. The material used for coating the tip has to be optimized for the sample under investigation; normally a material with high coercivity is chosen to avoid perturbations of the magnetic state of the tip during scanning. Simultaneously, the stray field from the tip has to be small enough not to affect the magnetic state of the sample under investigation. A simple model for MFM can be considered as follows: the tip and cantilever system is seen as a magnet attached at the end of a spring and the forces between the tip (magnet) and the magnetic surface attract or repulse the tip. The tip is usually magnetized perpendicularly to the sample surface, giving larger forces at the tip where the stray field from the sample is perpendicular to the surface.

The magnetic interaction cannot be easily controlled during an MFM scan. Such a control could be useful, for instance, to study magnetic switching phenomena at the nanoscale or when imaging soft magnetic materials, in order to not modify the magnetic state of the sample. Despite these difficulties, in some particular cases magnetic

switching of distinct nanostructures has been achieved by applying an external magnetic field having a carefully chosen magnitude [46].

Typical magnetic materials studied by MFM are metals or metal alloys. In contrast with metals, multiferroic materials are mostly insulators, meaning that the surface could exhibit localized charges (e.g. present on a dielectric surface or possibly due to ferroelectric domains) i.e. a non-constant electric field emerging from the surface. Since usually the MFM tip/cantilever is also conductive, an electrostatic interaction exists between the tip/cantilever and the sample, and this interaction is superimposed to the magnetic interaction. In consequence, the resulting image is not a pure MFM contrast, but reflects a convolution of the electrostatic and magnetic interactions. One solution to estimate the magnitudes of the two contributions, and therefore to overcome the problem to some extent, would be investigating the surface twice, with two different cantilevers: first with a non-magnetic conductive cantilever, and second with a magnetic cantilever. There is, however, the practical problem remaining of retrieving the same field of investigation after changing the AFM tip.

In a first phase, we have investigated CoNi dots prepared by PLD nanostenciling, performing MFM in the lift-mode (i.e. above the sample of about 50-100 nm). In this mode the lateral resolution induced is increased and is coarser than the ultimate resolution in tapping mode (~10 nm). We further used MFM to probe the magnetic behavior of multiferroic nanostructures as for instance bismuth ferrite (BiFeO<sub>3</sub>) depicted in Fig. 3.14.

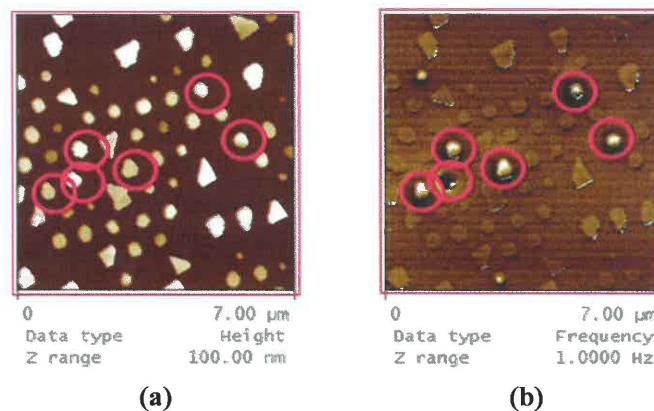


**Figure 3.14** Magnetic force microscopy image obtained by scanning an area of patterned BiFeO<sub>3</sub> nanostructures on (100) Nb doped SrTiO<sub>3</sub> substrate; **(a)** topography and **(b)** magnetic contrast

### 3.5 References

- [1] J. Butschke, A. Ehrmann, B. Höfflinger, M. Irmscher, R. Käismaier and F. Letzkus, *Microelectron. Eng.* 46, 473, (1999)
- [2] C. J. M. van Rijn, “*Nano and micro engineered membrane technology*”, Elsevier Amsterdam, ISBN 0444-51489 9 (2004)
- [3] M. Kölbel, R. W. Tjerkstra, J. Brugger, C.J.M. van Rijn, W. Nijdam, J. Huskens and D.N. Reinhoudt, *Nano Lett.* 2, 1339 (2002)
- [4] G. M. Kim, M. A. F. van den Boogaart and J. Brugger, *Microelectron. Eng.* 67-68, 609 (2003)
- [5] M. A. F. van den Boogaart, G. M. Kim, R. Pellens, J. P. van den Heuvel and J. Brugger, *J. Vac. Sci. Technol. B* 22, 3174 (2004)
- [6] S. H. Zaidi and S. R. J. Brueck, *J. Vac. Sci. Technol. B* 13, 658 (1993)
- [7] C. J. M. van Rijn, G. J. Veldhuis and S. Kuiper, *Nanotechnology* 9, 343 (1998)
- [8] L. J. Heyderman, B. Ketterer, D. Bachle, F. Glaus, B. Haas, H. Schiff, K. Vogelsang, J. Gobrecht, L. Tiefenauer, O. Dubochet, P. Surbled and T. Hessler, *Microelectron. Eng.* 67–68, 208 (2003)
- [9] M. A. El Khakani, M. Chaker, A. Jean, S. Boily, H. Pepin, J. C. Kieffer and S. C. Gujrathi, *J. Appl. Phys.* 74, 2834 (1993)
- [10] L. Frey, C. Lehrer and H. Ryssel, *Appl. Phys. A* 76, 1017 (2003)
- [11] A. A. Tseng, *J. Micromech. Microeng.* 14, R15 (2004)
- [12] J. G. Bednorz and K. A. Muller, *Z. Phys. B* 64, 189 (1986)
- [13] P. R. Willmott, P. Manoravi and K. Holliday, *Appl. Phys. A* 70, 425 (2000)
- [14] J. E. Crowell, *J. Vac. Sci. Technol. A* 21, S88 (2003)
- [15] Z. I. Alferov, *Rev. Mod. Phys.* 73, 767 (2001)
- [16] R. M. Silver, J. Talvacchio and A. L. de Lozanne, *Appl. Phys. Lett.* 51, 2149 (1987)
- [17] D. Dijkkamp, T. Venkatesan, X. D. Wu, S. A. Shaheen, N. Jisrawi, Y. H. Min-Lee, W. L. McLean, M. Croft, *Appl. Phys. Lett.* 51, 619 (1987)
- [18] S. Jin, T. H. Tiefel, M. McCormack, R. A. Fastnacht, R. Ramesh and L. H. Chen, *Science* 264, 413 (1994)

- [19] D. B. Chrisey and G. K. Hubler, “Pulsed Laser Deposition of Thin Films”, John Wiley & Sons Canada, Ltd. (1994)
- [20] Robert Eason, “Pulsed Laser Deposition of Thin Films: Applications-Led Growth of Functional Materials”, John Wiley & Sons Canada, Ltd. (2006)
- [21] P. R. Willmott and J. R. Huber, *Rev. Mod. Phys.* 72, 315 (2000)
- [22] P. R. Willmott, *Prog. in Surf. Sci.* 76, 163 (2004)
- [23] B. Holzapfel, B. Roas, L. Schultz, P. Bauer and G. Saemann-Ischenko, *Appl. Phys. Lett.* 61, 3178 (1992)
- [24] E. V. Pechen, A. V. Varlashkin, S. I. Krasnosvobodtsev, B. Brunner and K. F. Renk, *Appl. Phys. Lett.* 66, 2292 (1995)
- [25] A. Marcu, C. Grigoriu, W. Jiang and K. Yatsui, *Thin Solid Films* 360, 166 (2000)
- [26] M. D. Strikovsky, E. B. Klyuenkov, S. V. Gapanov, J. Schubert and C. A. Coppetti, *Appl. Phys. Lett.* 63, 1146 (1993)
- [27] Oliver H. Seeck, Chapter 11 in *Nanoelectronics and Information technology – Advanced Electronic Materials and Novel Devices*, Edited by R. Waser, Wiley-VCH Verlag GmbH & C. KGaA, Weinheim (2005)
- [28] B. E. Warren, “*X-Ray Diffraction*”, Dover Publications Inc. New York, 1990
- [29] B. D. Cullity and S. R. Stock, “*Elements of X-Ray Diffraction*”, Prentice Hall, 3rd edition, ISBN-10: 0201610914 (2001)
- [30] M. I. Alonso, M. de la Calle, J. O. Ossó, M. Garriga and A. R. Goñi, *J. Appl. Phys.* 98, 033530 (2005)
- [31] G. Binnig and H. Rohrer, *Rev. of Mod. Phys.* 71, S324 (1999)
- [32] G. Binnig and H. Rohrer, *Angew. Chem. Int. Ed.* 26, 606 (1987)
- [33] G. Binnig, C. F. Quate and C. Gerber, *Phys. Rev. Lett.* 56, 930 (1986)
- [34] C. F. Quate, *Surf. Sci.* 299, 980 (1994)
- [35] C. Harnagea, A. Pignolet, M. Alexe, D. Hesse and U. Gösele, *Appl. Phys. A: Mater. Sci. Process.* 70, 261 (2000)
- [36] C. Harnagea, PhD thesis, Max Planck Institute, Halle, Germany, (2001)
- [37] P. Güthner and K. Dransfeld, *Appl. Phys. Lett.* 61, 1137 (1992)
- [38] K. Franke and M. Weihnacht, *Ferroel. Lett.* 19, 25 (1995)

- [39] S. Hong, J. Woo, H. Shin, J. U. Jeon, Y. E. Pak, E. L. Colla, N. Setter, E. Kim and K. No, *J. Appl. Phys.* 89, 1377 (2001)
- [40] S. V. Kalinin and D. A. Bonnell, *Phys. Rev. B* 65, 125408 (2002)
- [41] M. Abplanalp, L. M. Eng and P. Günter, *Appl. Phys. A: Mater. Sci. Process.* 66, S231 (1998)
- [42] J. A. Hooton and W. J. Merz, *Phys. Rev.* 98, 409 (1955)
- [43] C. Harnagea, A. Pignolet, M. Alexe and D. Hesse, *Integr. Ferroel.* 44, 113 (2002)
- [44] P. Grütter, H. J. Mamin and D. Rugar, *Springer Series Surf. Sci.* 28, 151 (1992)
- [45] U. Hartmann, *Annu. Rev. Mater. Sci.* 29, 53 (1999)
- [46] X. B. Zhu and P. Grütter, *MRS Bull.* 29, 457 (2004)

*"Nanotechnology has given us the tools . . .  
. . . the possibilities to create new things appear limitless."  
Horst Stormer*

## **4. Nanostenciling of semiconductor Ge/Si heterostructures via Pulsed Laser Deposition**

### **4.1 Introduction**

The *germanium-silicon (Ge/Si) system* is currently of paramount importance among the various semiconductor heterostructure systems, due to device application significance and fundamental research importance vis-à-vis the understanding of the system's growth processes. In microelectronics for instance,  $\text{Si}_{1-x}\text{Ge}_x$  thin film alloys provide a solution to increasing the speed and decreasing the power of integrated heterojunction-based CMOS transistor components<sup>1</sup> mostly due to the possibility of tailoring the band gap of such heterostructures [1].

At the same time, the desire for monolithic integration of electronics and optics on the same substrate provides the motivation for Si-based optoelectronics research and development [2,3]. The main obstacle is the existence of an indirect band-gap<sup>2</sup> in both the Si and Ge electronic band structures, a characteristic that makes Si and Ge inept light-emitters. New approaches such as *nanostructuring* and *controlled island (quantum dots - QDs) growth* could offer alternatives for the improvement of light emission efficiency due to the three-dimensional confinement and localization of the charge carriers. This represents definite advantages for the evolution of a new generation of devices such as light-emitting QDs-based diodes, lasers [4] or QD infrared photodectors [5].

---

<sup>1</sup> The main application-areas of impact comprise bipolar CMOS (BiCMOS) technology (i.e. SiGe heterojunction bipolar transistors (HBT)), strained silicon CMOS (SS-CMOS))

<sup>2</sup> In indirect band-gap semiconductors, the bottom of the conduction band does not occur at the same wavevector,  $k$ , as the top of the valence band. Radiative recombination across the band gap requires the participation of a phonon, making it an inefficient, second-order process.

The interest in QD research can be traced back to Arakawa and Sakaki [6] who in 1982 suggested that the performance of semiconductor lasers could be improved by reducing the dimensionality of the active regions of these devices. Initial efforts at reducing the dimensionality of the active regions focused on using lithography combined with wet or dry chemical etching to build 3-D structures. It was soon realized, however, that this approach introduces defects that greatly limit the performance of such QDs.

Almost 50 years after Stranski and Krastanow reported island formation in heteroepitaxial ionic crystals [7], Goldstein and co-workers, studying InAs/GaAs superlattices, observed for the first time island formation in a semiconductor system [8]. Initially, this growth instability leading to *islanding* was considered unfavorable for the growth of the so-called “quantum well” systems in strained heteroepitaxy and efforts were undertaken to avoid it. However, in early 1990, it was experimentally observed that under certain growth conditions, when the thickness of the film with the larger lattice constant exceeds a certain critical thickness, the compressive strain within the film is relieved by the formation of *coherent islands* [9-11]. From then onwards, this topic has gained considerable attention, as it was realized that such islands may represent zero-dimensional, or “quantum dot” (QD), semiconductor nanostructures and their quantum confinement effects may be tailored. Later on, it was also observed experimentally that, for appropriate growth conditions, the height and lateral size distribution could be substantially narrowed and thus optical properties of QDs made much more reliable [12].

The possibility to form the energy-quantized islands by a self-assembly process without any artificial masking and patterning triggered abundant research efforts dedicated to the exploration of “dot-like” structures obtained via a Stranski-Krastanov (SK) growth mode. For the Ge/Si system in particular, various features of the system’s morphological evolution such as shape and size, as well as related aspects such as the islands’ composition, strain, density and location entered numerous analyses and debates. The most widely investigated aspects so far dealt with whether the diverse morphologies occur kinetically or thermodynamically [13-16] and with the elucidation of the phenomena that trigger and govern SiGe alloying [17-20].

In most cases, self-assembled and self-organized islands exhibit a certain *size distribution*, however since island nucleation is statistical in nature, the lateral ordering is

typically absent. Even though an *ordered spatial registration* of the structures is required mostly for electronic applications and is not as stringent for optical applications a broad size distribution of the self-assembled Ge QDs leads for instance to non-homogeneous luminescence from dots, thus affecting the efficiency of such prospective devices. The growth of high-quality crystalline arrays of Ge structures, homogeneously shaped and sized, and precisely registered on the substrate of choice turned out to be a highly-intricate issue and beyond a mere self-assembled growth induced process. A thorough literature overview shows that much work remains to be done towards the realization of complex and unequivocally registered “*dot architectures*” like those necessary, for instance, in nanoelectronics, quantum information storage [21] or for quantum computing purposes as suggested in a quantum cellular automata (QCA) device [22].

In this chapter we describe our approach for the fabrication and patterning of Ge/Si semiconductor heterostructures through the combination of nanostenciling and pulsed laser deposition (PLD). An overview of epitaxial growth modes and several unconventional methods reported for the patterning of Ge/Si nanoscale structures is offered in section (4.2). We present results for the PLD-based growth and patterning of Ge on Si substrates for room temperature regime and high temperature regime in sections (4.3) and (4.4) and summarize our main findings in section (4.5).

The work presented in the following represents the first study on nanopatterning of Ge/Si heterostructures via re-usable nanostencils (i.e. ultrathin solid-state membranes) and pulsed laser deposition, performed both at room temperature and directly at high temperature. The purpose of the study is two-fold: firstly, using deposition through nanostencils mechanically attached to the substrate, we demonstrate a resist-free, site-selective growth approach of patterned arrays of Ge nanocrystalline structures, with possible applications in opto-electronics. Secondly, using nanostencils as fabrication and patterning tools, we provide new insight into the kinetic phenomena that lead to the growth of crystalline Ge dots during the laser ablation process.

## 4.2 Ge/Si nanostructures

We discuss in the following the epitaxial growth modes governing the hetero-systems and the growth characteristics of the Ge/Si system. The shape evolution of the Ge islands is discussed in the context of the deposition techniques used to prepare the films. An overview on Ge/Si self-organization process on prepatterned substrates is also presented.

### 4.2.1 Growth mechanisms

For heteroepitaxial growth, three fundamental modes have been observed experimentally: Frank-van der Merwe (FvdM) [23], where growth proceeds in a layer-by-layer mode (2D), Stranski-Krastanov (SK) [7], which proceeds initially as layer-by-layer, followed by islanding after a critical thickness has been exceeded, and Volmer-Weber (VW) [24], where island growth (3D) occurs from the incipient stages of growth (Fig. 4.1).

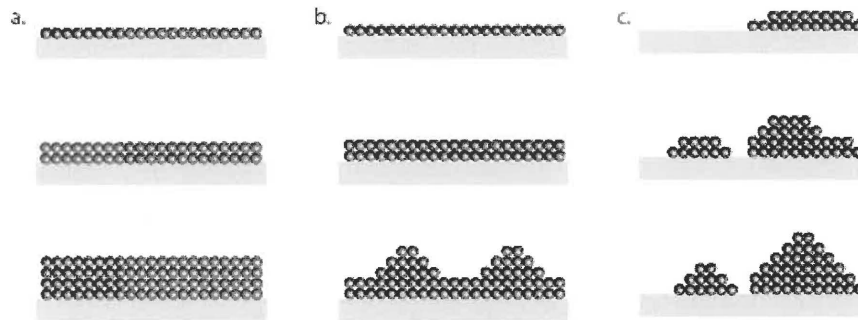


**Figure 4.1** Schematics of the three distinct epitaxial growth modes governing hetero-systems growth: **(a)** Frank-van der Merwe (FvdM), **(b)** Stranski-Krastanov (SK), **(c)** Volmer-Weber (VW) [25]

Based on surface free energy models, in the absence of any strain in the *epilayer*, the growth mode is determined by the surface free energies (per unit area) of the substrate,  $\gamma_s$ , and epilayer,  $\gamma_{epl}$ , and by the interface free energy,  $\gamma_i$ . If  $\gamma_s > \gamma_{epl} + \gamma_i$  then FvdM growth occurs, i.e., the epilayer wets the substrate, whereas if  $\gamma_s < \gamma_{epl} + \gamma_i$  VW growth takes place, i.e., the epilayer does not wets the layer.

It was found that FvdM growth governs materials systems with small lattice mismatch for which the atoms of the epilayer adhere stronger with the substrates' atoms than to one another. In contrast, VW growth occurs for material systems with large lattice mismatch for which also the atoms of the epilayer adhere stronger one to the other, rather than to the substrate.

The most common growth mode is certainly Stranski-Krastanov, the one that governs almost any heterostructure with a certain lattice mismatch between the material constituents. In this case, the growth proceeds as layer-by-layer for few atomic layers (generating thus a flat “*wetting layer*”); however, the accumulation of strain energy due to the lattice mismatch generates islanding after a critical thickness of epilayer is exceeded. To accommodate (relieve) the strain, the epilayer breaks and the growth continues as in a VW mode generating 3-D structures.

The lattice mismatch of 4.2% between the Ge ( $a = 5.65 \text{ \AA}$ ) film and Si ( $a = 5.43 \text{ \AA}$ ) substrate places this materials system in the SK growth mode scenario. When the thickness of the Ge wetting layer reaches a critical value (estimated at 3-6 monolayers (ML)), the film relieves its internal strain by 3D nucleation and island formation [26].

The interplay between reduction of strain energy and increase of surface energy accompanying island formation leads to different shapes within the Ge structures during the growth process. For instance, during the SK growth of Ge (or even SiGe with large content of Ge) on Si(100), island formation starts as  $\{105\}$ -faceted “hut” or “pyramid” shaped structures. As the film coverage increases, multifaceted “domes” with  $\{113\}$  and  $\{102\}$  facets develop on the expense of the hut clusters. With further increase in film coverage (thickness), large clusters or “superdomes” start to form [26].

The growth of Ge on Si (111) looks relatively less complicated in terms of structures morphology. After the completion of the wetting layer, 3D structures with  $\{113\}$  facets and a flat top  $\{111\}$ , are formed. For larger islands a transition from coherent to dislocated islands is observed while the shape remains the same [26].

Most of the experimental work studying growth modes has been pursued on films grown either by molecular beam epitaxy (MBE) or chemical vapor deposition (CVD). Consequently, the growth dynamics of Ge islands (QDs) on Si obtained by these methods has been thoroughly analyzed. The shape of the initial islands was found to depend on the

deposition technique as well as the deposition conditions. When, for instance, liquid phase epitaxy (LPE) was used, the Ge island growth was observed to proceed as {115}-faceted islands instead of {105}-faceted ones, and as on the coverage increased {111}-faceted pyramids were formed [27]. Moreover, if a surfactant<sup>3</sup> like for instance antimony (Sb) was used in the MBE growth of Ge/Si(100) the initial {105}-faceted shape changes to {117}-faceted [28].

While CVD and MBE have been exhaustively used to prepare Ge thin films and dots, pulsed laser deposition (PLD) recently emerged [29,30] as a versatile deposition technique to study the structural [31,32] and functional (electrical and optical) [33] properties of self-assembled Ge QDs on Si substrates. Investigating the growth dynamics of Ge on Si(100) via pulsed laser deposition (PLD), Hegazy et al. reported that like in MBE or CVD, depending on the film thickness, the Ge clusters are exhibiting three shapes: huts, pyramids and domes. They found that huts dominate at low film thicknesses and well-developed huts were observed as being faceted by {305} planes whereas large elongated pyramids were observed when thickness was increased. For these pyramids the main faceting planes was reported as being also {305}, fact that differs entirely from the previous observations in the case of MBE, CVD or LPE. With further deposition, the large pyramids are transformed into domes with smooth edges. These scarce results are yet prompting for further detailed analysis of the PLD parameter influence on the dots morphology, keeping in mind that different PLD set-ups (e.g. laser wavelength, pulse duration) can influence significantly the morphology of the deposits.

#### **4.2.2 Self-assembled and self-organized Ge/Si nanostructures on pre-patterned substrates**

Once SK growth of Ge/Si islands has been reported in early 1990', it became gradually accepted, that a "rough-growing" surface may be considered as a surface containing nanostructures which in turn can play the quantum-dots role [12].

---

<sup>3</sup> A third element introduced in heteroepitaxial growth processes to alleviate the islanding of the epilayer right after the completion of the wetting layer thus providing a smoother interface substrate-epilayer that is desirable for device applications.

Consequently, the concept of “*bottom-up*” fabrication based on SK *self-assembly* has been proposed as a viable path towards a parallel, inexpensive realization of Ge/Si “quantum-dot” like structures. Indeed, SK growth may be regarded as a straightforward path for the bottom up fabrication of nanostructures and quantum dots, representing a very attractive approach for applications, both because it is highly parallel and because it takes place without additional external intervention, thus making it economically advantageous. However, without additional means, the nucleation sites of the 3D islands are random. Moreover, the size evolution of a 3D nucleus generally depends on its local environment, i.e. on its relative position with respect to the surrounding islands and their interactions. The positioning of “naturally” obtained nanostructures by a simple bottom up approach is thus practically not achievable.

However, nanoscale ordering may be attained by exploiting the strain energy within a heteroepitaxial system. One remarkable example was demonstrated by burying an initially random array of 3D Ge islands on Si(001) and subsequently overgrowing Si buffer layers and then new layers with islands on top of them [34]. The tensile strain field prompts nucleation above buried islands, while progressively improving their order and their size uniformity (Fig. 4.2).

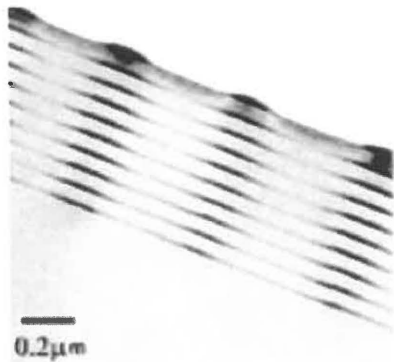


**Figure 4.2** Stacking Ge nano-islands on Si(001): cross sectional TEM of a typical template; Ge/Si heterostructures were deposited at 750 °C. [Capellini et al, ref.34]

For application purposes, besides a narrow size distribution, the *ordering* of islands is generally desired; *self-ordering* of islands generated via a SK growth mode exhibits only a short-range order. Thus island *assisted-nucleation* on *prepatterned* substrates has been proposed with the aim of achieving a certain degree of lateral ordering. A wealth of elegant strategies combining lithography-based approaches (*top down*) and spontaneous self-assembly approaches (*bottom up*) have been pursued to

accomplish accurate control over size and density, but mostly over the *spatial positioning* of Ge islands. Most of the work made use of the assisted-organization of Ge dots grown on pre-patterned Si or SiO<sub>2</sub> substrates either by means of CVD [35-38] or MBE [39-43], and aims to understand and possibly control such processes [44].

On pre-patterned surfaces, similar to non-patterned ones, the nucleation of islands is affected by the surface curvature and the surface stress. On these surfaces the growth of Ge follows a modified SK growth mode, since atomic diffusion is affected by the local arrangement of “artificial” defects. Depending on feature dimensions and growth kinetics, 3D islands preferentially nucleate on top of plateaus, on their edges or within trenches. For instances, it was observed that *self-assembled* Ge QDs were *organizing* along the edges of selectively grown Si-raised regions in pre-patterned SiO<sub>2</sub> layers [37, 41] whereas they preferred the sidewalls of stripe-like vias when unoxidized Si was used [47]. Moreover it was found that when Ge/Si buffer layers were deposited prior to the Ge deposition, the dots preferentially grew and organized on the terrace tops, while when a purely Si buffer layer was employed they accumulated at the sidewalls of the trenches pre-patterned into the Si substrates. In some cases it was shown that even the density of the dots can be adjusted by the width and depth of patterned windows in SiO<sub>2</sub>-covered Si substrates [39].

Without doubt there are many ingenious preparation routes proposed to organize the SK self-assembled Ge QDs and is practically impossible to keep a record of all the ideas reported. An underlying theme runs through all the references mentioned: these phenomena are addressed from the point of view of either the influence of *strain fields* on the island nucleation or the *kinetics* of the growth process. Pre-patterned surfaces are used to influence diffusion processes so as to cause a predefined arrangement of preferential nucleation sites, thus dictating (to a certain extent) island size and ordering. Despite all this progress, Ge/Si self-organization on artificially patterned substrates is not ready yet to offer a practical and reliable route towards the realization of complex and unequivocally registered dot architectures for applications.

The nanostenciling approach that we are applying, though still based on controlled deposition, relies however on a completely different and novel paradigm. We do not intervene on the Si substrate, but rather selectively deposit Ge directly on the sites

where we would like the 3D islands to nucleate, in a regime where otherwise a pure SK growth would take place. This in turn is expected to yield individual structures of optimum crystal quality having thus the best properties.

Our present studies are the first experiments aimed towards assessing the feasibility of simultaneously controlling the Ge nanostructure morphology and positioning via a direct PLD-based patterning process.

### 4.3 Growth and patterning of germanium via PLD

A well-established deposition method developed mainly to grow high-quality epitaxial films of complex materials, PLD also offers the possibility of fine-tuning and controlling deposition parameters rather easily in the case of elemental materials. PLD is highly attractive because delivers stoichiometric films and is also suitable to grow multilayered films by changing targets using a carousel-like target holder unit. For the particular case of Ge/Si system, in principle  $\text{Si}_x\text{Ge}_{1-x}$  films of different compositions can be in principle grown using targets with specific compositions and doping, eliminating thus the need of additional doping sources or residual gases. Nevertheless, to employ PLD as to design efficient Ge QD-based devices, there is a need to understand how to control both the physical properties<sup>4</sup> and the registration of Ge QDs through controlling the deposition parameters.

Certainly, there are distinctive and fundamental differences between the MBE and PLD techniques, the two vapor deposition methods that are perhaps being the most extensively employed (mainly in research environment) in growing high-quality epitaxial thin films. One main difference for instance is that in PLD, the target material ablated by a pulsed laser beam is deposited in pulses on a substrate so that many atoms arrive at the surface simultaneously. Each pulse lasts for tens of nanoseconds, and the time between two pulses is of the order of seconds allowing for surface relaxation and thus differing from MBE where atoms are deposited continuously at a much lower rate. The kinetic energy of ablated species (atoms, clusters, or even droplets) and further incident on the

---

<sup>4</sup> The physical properties of QDs depend strongly on their shape and size distribution, while the device quantum efficiency is affected by the density and spatial distribution of the QDs.

substrate can reach several hundred eV, in contrast to the typical thermal evaporation energies of less than 1 eV as in MBE. The kinetic energy of the ejected species can be basically tuned by choosing the output laser energy, laser fluence on the target and the gas pressure in the deposition chamber thus making PLD an excellent and versatile deposition technique for researchers.

In the case of PLD, it was shown by kinetic Monte Carlo simulations that density and size distribution of deposited QDs are mostly controlled by both the deposition rate and adatoms' kinetic energy, which affects surface diffusion [48]. The deposition rate is primarily controlled by the laser fluence and the laser repetition rate, while adatom surface diffusion is controlled by both the substrate temperature and the laser fluence.

The experimental studies are however very sensitive to the deposition conditions such as: laser parameters, substrate preparation, substrate temperature calibration, etc. In the particular case of Ge grown via PLD the studies are at a rather early stage. The dependence of the shape, of the self-assembled Ge islands on Si (100) on deposition parameters, has been only recently explored using an Nd-YAG laser with a wavelength of  $\lambda = 1064$  nm and pulse duration of  $\tau = 40$  ns [31-32]. These parameters are different from the laser parameters of our PLD unit (KrF excimer laser,  $\lambda = 248$  nm,  $\tau = 15$  ns) thus it is intricate to make a direct comparison and to relate our results on the morphology of the deposited islands, to these reports. Using stenciling and PLD, we investigated simultaneously the morphology and the positioning of Ge nanostructures, achieving highly-organized Ge crystalline islands and thus providing a general strategy for organizing nanostructures on a suitable surface.

### **4.3.1 Ge PLD nanostenciling at room temperature**

The capability of stenciling Ge via PLD has first been assessed at room - temperature (RT). Germanium films and structures were grown in vacuum ( $\sim 10^{-5}$  mbar), using the GSI Lumonics KrF excimer laser unit described in the experimental chapter. The stencils were gently pressed against the substrates by two metallic clips and the substrate-stencil assembly mounted in front of a rotating Ge solid target (99.9% purity). These experiments at RT served as tests to adjust both the geometrical (distance target-

substrate, stencil attachment) and deposition parameters (laser fluence, repetition rate); they can be regarded in principle as a reference process for the RT-PLD growth of other materials (e.g. metals, oxides) on various substrates.

In these trials, we used several types of nanostencils as well as different substrates. As an example Fig. 4.3 (a) shows a detail from a FIB-based stencil<sup>5</sup> used in close contact with a Si substrate on which Ge structures were further replicated (b).

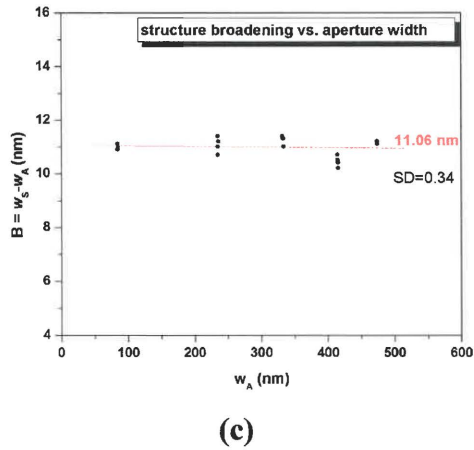
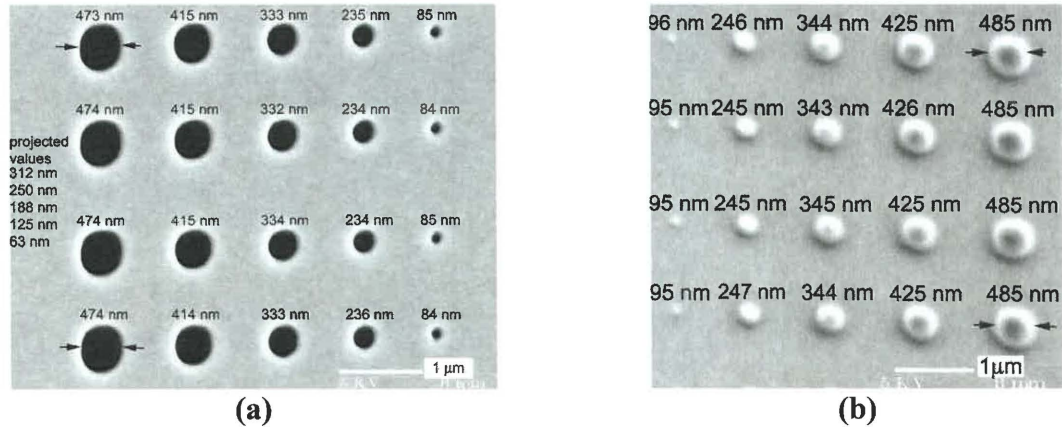


**Figure 4.3** (a) SEM micrographs detail of arrays of assorted apertures opened by FIB milling in SiN membranes (here 200 nm thick) and (b) Ge patterned structures replicated through the sieves with estimates on their lateral sizes (values measured horizontally; SEM resolution  $\sim 1.5$  nm); (c) Plot of broadening ( $B$ ) versus aperture width ( $w_A$ ) using the values showed in the SEM micrographs. The average value for  $B$  is centered at 11.06 nm with a  $SD=0.34$ .

As previously mentioned in the Chapter 3, the milling process of insulating membranes suffers from both charging effects and induced ion beam drifting and the shapes of the milled apertures we obtained were always larger than the projected values (see fig. 4.3 (a)). The stencil's apertures were replicated on the substrate and well ordered arrays of 3D Ge islands were obtained, in a parallel, single deposition step (fig. 4.3 (b)). The deposited structures are retaining the motifs' periodicity for the entire patterned area.

<sup>5</sup> Commercially available SiN membrane windows ( $1 \times 1 \text{ mm}^2$ ) were FIB-drilled on several areas of  $32 \times 32 \text{ } \mu\text{m}^2$  for a minimal projected aperture of 62.5 nm.

The stencil-to-substrate gap turns out to be one of the significant parameters since leads to the enlargement of the deposits (Fig. 4.3 (b)); the smallest islands were growing to about 95-100 nm in lateral size, when deposited through ~85 nm apertures. Analysis of several SEM micrographs indicates a broadening effect up to 15% which can be minimized in principle by a more firm fixture stencil-substrate. However, if the stencil is pressed too hard against the substrate, the membrane may bend and even break.

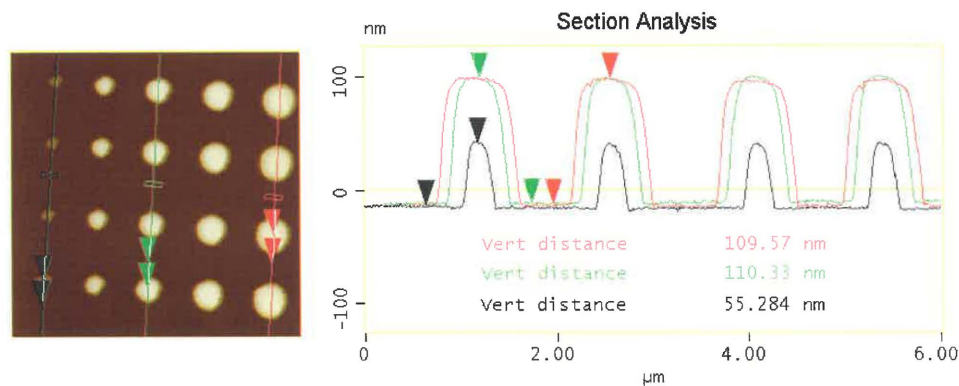
In Chapter 3 (section 3.3.3) we showed that the enlargement (broadening B) of a structure is given with good approximation by the equation:  $B = w_S - w_A \sim S \times (G/D)$ , where  $w_S$  and  $w_A$  are the lateral size of the deposited structure and respectively aperture, (S) is the dimension of the source, (G) is the gap stencil-substrate and D is the distance to the source. While in our experiments the laser beam was focused via a system of lenses so as to produce a minimum laser spot of 1 mm in diameter on the surface target (i.e. S), and the distance target-substrate could be set at a fixed value (e.g. 6cm for the structures in fig. 4.3), the gap control was not a trivial issue since stencils were handled manually.

In general, the enlargement of the deposited structures with respect to the initial aperture size might be caused by two processes: the diffusion of the evaporated species on the substrate or, as already mentioned, due to the geometry setup. The diffusion length depends primarily on the deposited material and on the substrate surface (temperature, preparation, deposition rate). Lowering the substrate temperature (e.g. in these experiments RT) the diffusion length is mostly reduced. Yet, even at RT, since the ablated species have high kinetic energy on arrival at the substrate, the material tends to diffuse under the stencil due to the mobility of the particles.

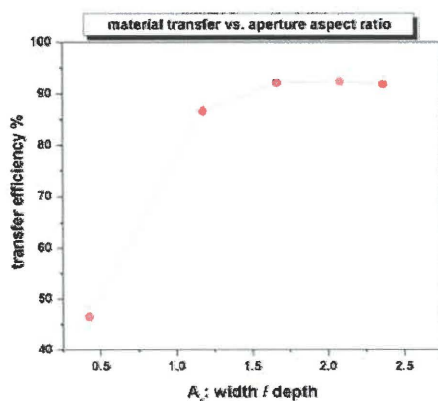
Further assessments on transfer efficiency and the projected “life-time” of a stencil after consecutive depositions performed at RT were made along these preliminary experiments and are discussed in then following. FM analysis performed both in contact and tapping mode<sup>6</sup> onto the RT Ge deposits (Fig. 4.4) served to asses the transfer efficiency through the apertures with different aspect ratios.

---

<sup>6</sup> AFM measurements were performed in contact mode using Veeco Nanoprobe, general purpose NP cantilevers (Si<sub>3</sub>N<sub>4</sub>, tip apex radius 20 nm) and in tapping mode using  $\mu$ Masch NSC15 cantilevers (Si, radius ~10 nm).



(a)



(b)

**Figure 4.4 (a)** AFM topography showing the Ge islands height profile after the first deposition and **(b)** stencil’s transfer efficiency when apertures with different aspect ratios are opened in the same membrane (the values used for aperture widths are from fig. 4.3; the error bars are calculated around the mean value of maximum and minimum from each set of height measurements given by AFM section profiles from (a)).

For the particular stencil architecture presented in Fig. 4.3 we found that up-to an aspect ratio (width /depth) of 1:1 the material transfer is above 90% from the equivalent thickness of a continuous film (e.g.. 120 nm for 4000 pulses at 0.3 Å/pls) whereas the transfer efficiency decreases to 45-50% for apertures with an aspect ratio (width / depth) of 1:2.5 due to a faster clogging of the latter.

During the deposition, material is gradually filling the apertures and is deposited on top of the membrane window as well. The stencil shown in Fig. 4.3(a) was used in 3 consecutive depositions (~ 100 nm thick each) and once an equivalent film thickness of about 3 times the diameter of the initial smallest apertures was reached, the latter clogged completely and the fifth row of structures was missing (see fig. 4.5). The clogging depends though on the deposited material due to different stiction coefficients but also on the membrane surface. It was reported that SiN membranes can be readily treated with an antistiction siloxane self-assembled monolayer to reduce the attachment of the deposited

material to the mask [49]. Such treatment if further developed might increase the “life-time” of the stencils and improve the pattern transfer in terms of definition and resolution of the structures.

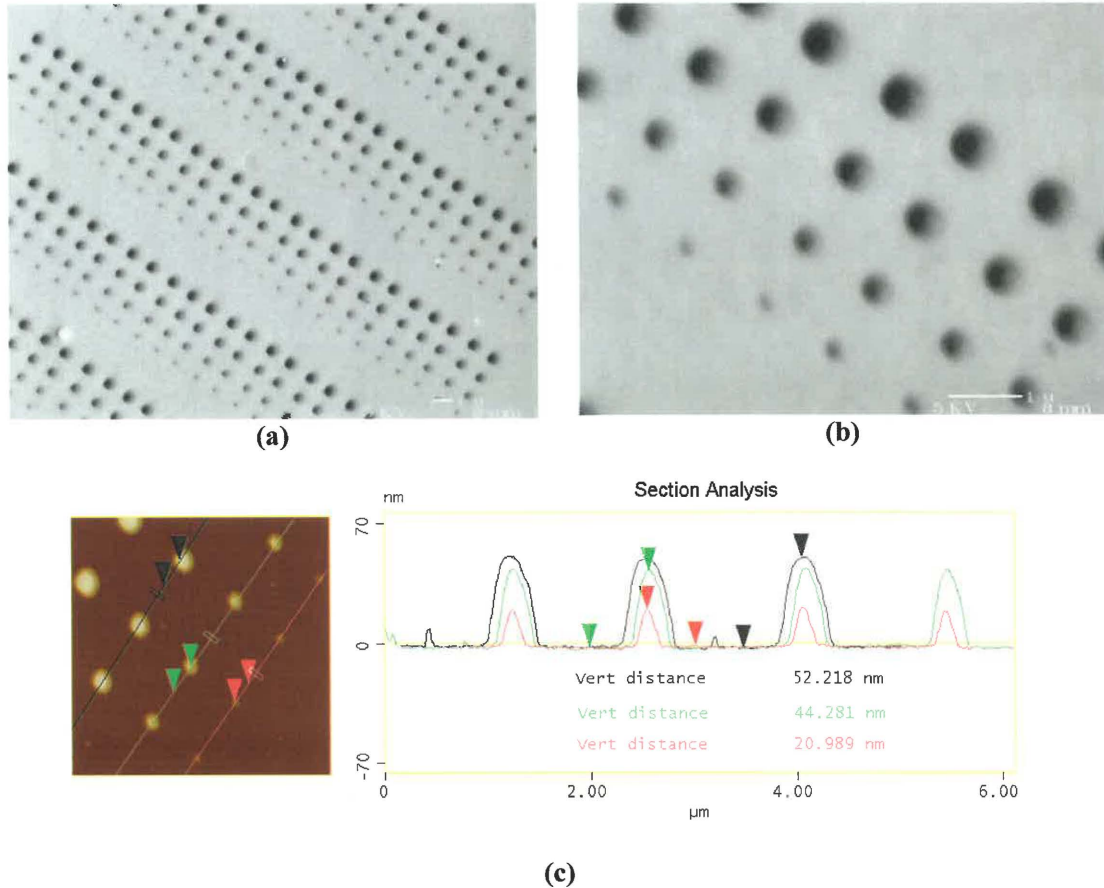


**Figure. 4.5** SEM micrographs of patterned arrays of Ge islands: (a) large scale and (b) detail, after 3 consecutive depositions through the stencils with architecture shown in Fig. 4.3(a); (c) AFM profile height shows a reduction in both lateral size and height of Ge islands due to the gradual filling of the aperture

Besides the clogging, at some point, the deposited layer on the top of the free-standing membrane causes its visible bending due to tensile stress. A deformed membrane has both an increased gap and an aperture deformation and these results in a distorted pattern formation. This effect is amplified on stencil architectures that are having a very small membrane thickness (100-200 nm) and large opened window areas (over  $1 \times 1 \text{ mm}^2$ ) like the ones discussed above and prompts for finding alternatives to improve the stencil masks design and thus its reliability for larger areas patterning [50].

The RT “as-deposited” Ge islands are amorphous and an annealing treatment is required to crystallize the structures. The annealing treatment was performed at 450 °C for 30 min. in a N<sub>2</sub> environment. However for the islands obtained via FIB-based stencils, due to the reduced size of the patterned areas (several squares 32 x 32 μm<sup>2</sup> or even 16 x 16 μm<sup>2</sup>) and the small amount of deposited Ge, the assessment of the crystallinity of the annealed deposits by XRD was not possible.

LIL-based stencils (described in Chapter 3) with hexagonal arrays of circular apertures opened in free-standing low-stress SiN membranes (500 nm thick), turned out to be much more robust and were extensively used in further experiments especially during high temperature depositions. These stencil chips (shown in fig. 3. 2(a) in chapter 3) have the free-standing membranes suspended between silicon reinforcement walls, thus providing an increased mechanical strength. Due to limitations again imposed by fabrication conditions, the apertures of these stencils were not smaller than 350 nm in diameter. However, the LIL-based stencils represented extremely useful “tools” to organize Ge islands and to investigate their growth kinetics when deposition and patterning were performed directly at high temperature.

## 4.4 Ge PLD patterning in the high temperature regime

We used the same PLD unit described in section (4.3.1) and LIL-based stencils with arrays of hexagonal apertures (350 nm in diameter) to investigate the stencil-based patterning of Ge on Si(100) and Si(111) substrates<sup>7</sup>, *directly at high temperature*. Prior to deposition, substrates were degreased and cleaned in ultrasound solvent baths.

To passivate the surface, the native SiO<sub>2</sub> oxide layer was chemically removed in a strong HF (5%) solution, rinsed in de-ionized water and rapidly mounted in the chamber. Ge deposition was performed in vacuum (~10<sup>-5</sup> mbar), at a repetition rate of 10 Hz and laser fluence on the target set of 4 J/cm<sup>2</sup>. The substrate temperature was set at 600 °C and measured with a K-type thermocouple on the heating block that sustains the assembly stencil-substrate. The same stencil was further used in consecutive depositions for various numbers of ablation pulses.

---

<sup>7</sup> Si(100) - (n-type, Sb-doped, resistivity of 0.015 Ωcm); Si(111) – (n-type, As-doped, 0.001-0.005 Ωcm)

In Fig. 4.6 the Ge patterned areas corresponding to 14 perforated membranes built in the stencil are depicted. The structures are clearly reproducing the periodicity of the apertures and analysis of detailed SEM micrographs is revealing that very few structures are missing after first usage. Evidently, a clogging effect is becoming present after several usages, this phenomenon being accentuated in the case of PLD by the presence of droplets in the plume.

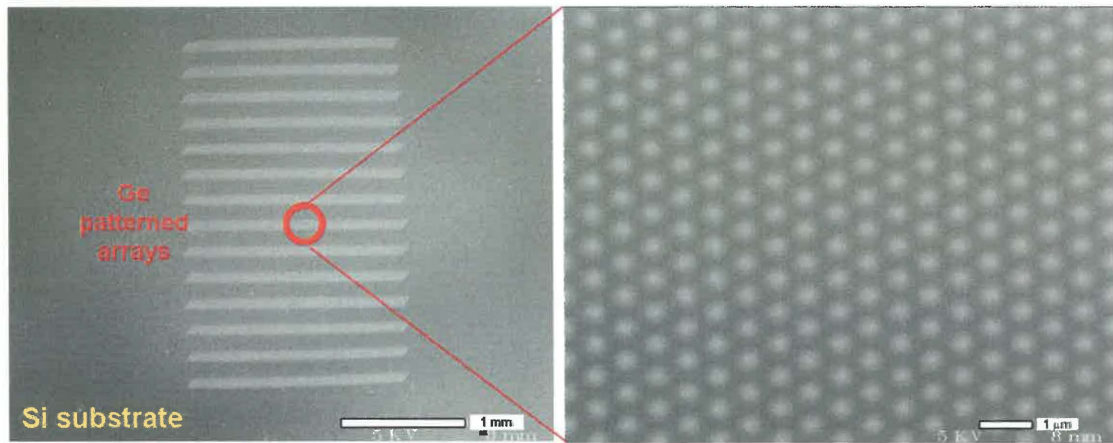


**Figure 4.6** Ge patterned areas corresponding to 14 perforated membranes built in the LIL-based stencils. Stenciled regions are 2 mm in length and 100 microns in width each; the deposits replicated through the apertures are 350 nm in diameter with a pitch of 700 nm.

#### 4.4.1 Ge patterned islands on Si(100): coverage dependence of island morphology

The equivalent film thickness (coverage) can be easily controlled during PLD by varying the number of laser pulses for a certain target-substrate distance, provided that diffusion or desorption from the substrate are negligible. Several samples with Ge patterned islands were obtained on Si(100) by varying the number of laser pulses between 250 and 1500 (in this experiment with an estimated deposition rate of  $\sim 0.28 \text{ \AA/pulse}$  for a distance target-substrate of 6.5 cm).

In the initial stages of growth (i.e. up to 250 laser ablation pulses that leads to an equivalent thickness of 6 nm tall structures) ordered arrays of Ge structures are formed as flat circular mounds, 350 nm in diameter and with a 700 nm periodicity (Fig. 4.7) i.e. the replica of the design defined by the sieve's apertures.

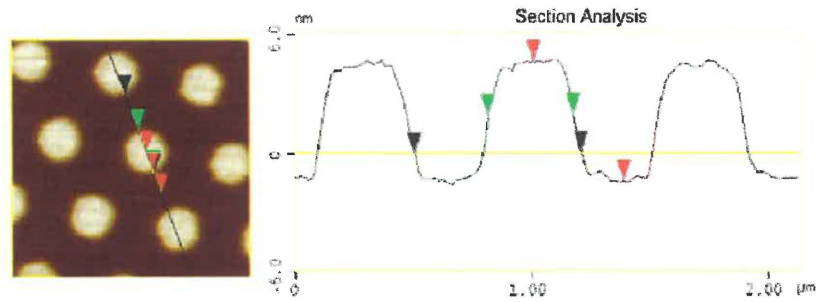


**Figure 4.7** AFM topography (tapping mode) and Ge mounds height profile obtained for 250 pulses at 600°C using a stencil with hexagonal arrays of aperture, with 350 nm nominal diameter.

SEM micrographs show that with increasing Ge thickness the shapes of the obtained structures evolve from the flat “2D-mound” type (Fig. 4.8(a)) to 3D nanocrystalline agglomerations (10-100 nm in lateral size) formed on top of these mounds (Fig. 4.8. (b)), undergoing further a transition to a “coffee-bean” like grained structure (Fig. 4.8. (c)) and finally coalescing into single nanocrystals (Fig. 4.8. (d)).

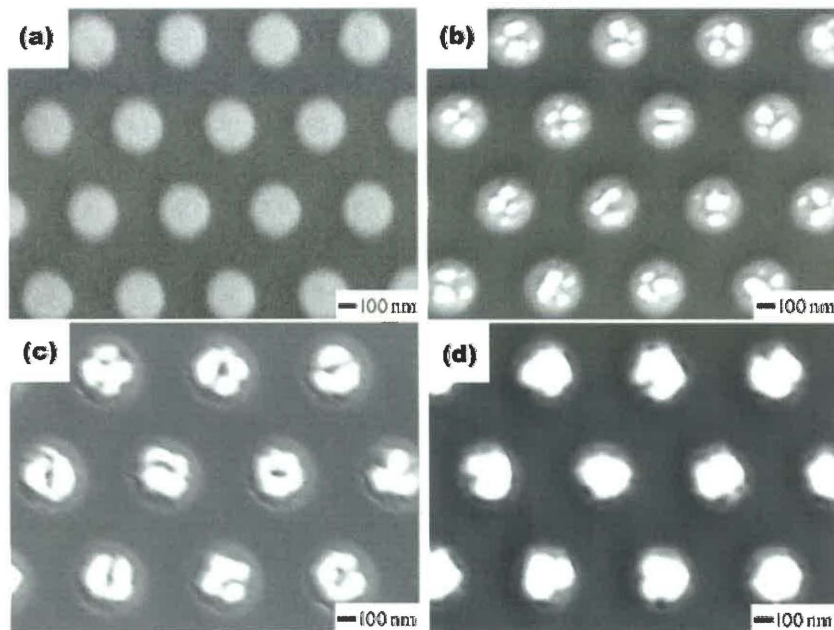


**Figure 4.8** SEM micrographs of ordered Ge nanostructures replicated on Si (100) by pulsed laser deposition for (a) 250, (b) 750, (c) 1250 and (d) 1500 laser pulses with a fluence of 4 J/cm<sup>2</sup>, for a target-substrate distance of 6.5 cm

AFM and SEM images from (Fig. 4.7) and (Fig. 4.8) show that all islands are perfectly separated and well-defined. The lateral extent of the deposits is always restricted to the range of the aperture areas defined in the stencil. The local confinement

of material practically represents a minimal interference with the structures' growth dynamics, thus we assume that the process is mainly driven by a phenomenon resembling the SK growth mode, this time taking place only in areas defined by the mask.

The “2D-mounds” are reminiscent of the thin “wetting layer” (WL) which normally precedes the islanding in classical SK growth. According to AFM topographies the “2D-mounds” grow up to 6 – 7 nm in height, which is roughly ten times thicker than the classical critical value for a conventional WL<sup>8</sup>. This anomalous critical thickness for the onset of 3D nucleation can be explained invoking the finite size of the deposited areas: the “2D-mounds” acting as a WL, have the possibility to relieve strain at their periphery, delaying the strain-induced 3D nucleation of islands. A similar phenomenology was discussed in the case of self-organized Ge islands on lithography-patterned windows opened in ultrathin silicon oxide layers [52].

The morphological evolution of PLD-patterned Ge islands can be intuitively explained based on island coarsening and shape-transition driven by strain-relief, phenomena well observed in other deposition techniques such as MBE or CVD.

The dots that initially nucleate on top of the 2D-mounds (Fig. 4.8 (b)) are round shaped and their aspect ratios (defined as the dot's height divided by the square root of the base area) range from ~0.16 to ~0.20. These dots are reminiscent of the dome-shaped islands observed in Ge/Si(001) heteroepitaxy [53]. The average aspect ratio of the dots increases with coverage to allow for more efficient strain relaxation. Above coverages of 500 pulses, we observe a shape-transition from rounded to a “coffee-bean” like grained structure (Fig. 4.8 (c)). At this stage of growth we detect both coalescence of grains and the formation of a depletion region at the center of the underlying 2D-mounds, where we expect higher elastic compression. This new morphological arrangement with more material accumulated closer to relaxed periphery of the “2D-mounds”, corresponds to a configuration which minimize the elastic energy.

These “coffee bean” clusters resemble the SiGe “quantum rings” grown on Si(001) by molecular beam epitaxy and whose mechanism of formation was explained invoking strain energy relief and Ge segregation [54]. Finally, at higher Ge coverage

---

<sup>8</sup> Typically 0.6-0.7 nm-thick for Ge on Si(001)

(above 1000 ablation pulses), the depletion region disappears and clusters are coalescing into single (rounded) nanocrystals.

A very interesting feature of the stenciling process is the possibility of exploiting the “shadow-effect” induced by the characteristic design of the chip and the aspect ratio of the apertures opened in the membrane as suggested in (Fig. 4.9 a).

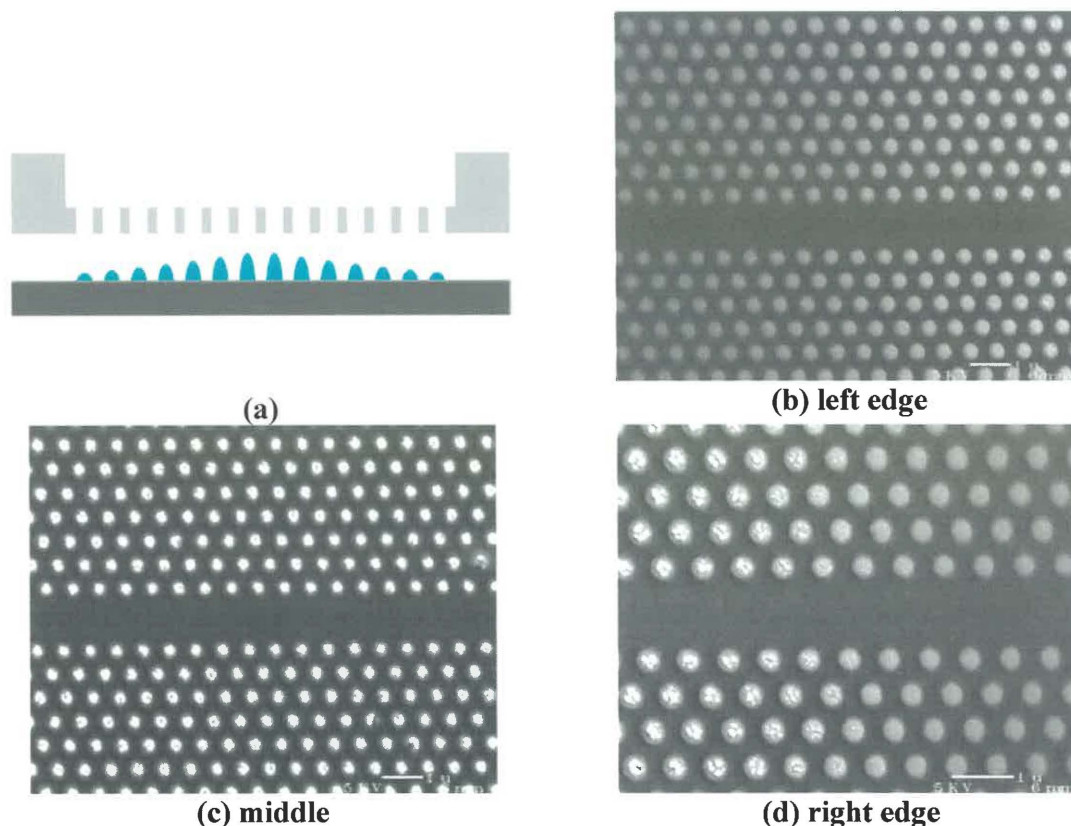


**Figure 4.9** Stencil-induced structures thickness gradient: **(a)** schematic drawing suggesting the shadow-effect and **(b-d)** sequence of SEM micrographs showing the structures thickness gradients within a patterned stripe (100 $\mu\text{m}$  in width) from one edge to the other one. The sample was obtained for a number of 1250 laser ablation pulses, when using LIL-based stencils (scale bars 1  $\mu\text{m}$ ).

Due to the particular architecture of the LIL-based stencils employed in this study<sup>9</sup> we obtained a thickness gradient for the structures patterned within the 100  $\mu\text{m}$ -wide stripe, i.e. lower-coverage structures towards each edge of the patterned stripe area. In fact, this gradient permitted us to seize the 2D $\rightarrow$ 3D transition from flat 2D-mounds to the nucleation of 3D islands on top of them (Fig. 4.9), for *each* patterned sample thus also confirming the islands morphology evolution from sample to sample.

<sup>9</sup> Narrow trenches with about 4:1 (depth/width) aspect ratio etched in the silicon supporting frame are preceding the perforated membrane areas leading to a shadow effect noticed at the edges of each patterned stripe.

The density of Ge dots per deposited location was estimated to couple of tens for the samples deposited from 250 up to 500 pls. For samples deposited up to 1000 pls the enlarged dot size leads to a smaller number of dots (e.g. 3-5 dots as shown in fig 4.8.b). This indicates a feasible control of the number of dots per nominal location and thus their density in the whole patterned area. The dots density can in principle be further tuned by using stencils with smaller or larger apertures or different spacing.

#### 4.4.2 Micro-Raman analysis of patterned Ge/Si(100) islands

The structural characterization of the Ge clusters was addressed by micro-Raman spectroscopy<sup>10</sup>, a surface sensitive technique particularly suitable to extract information about composition and strain inside Ge nanostructures [55,56].

The optical measurements were carried out at room temperature, by probing the patterned area with the 514.5 nm line of an Ar<sup>+</sup> ion laser focused with a spot size of about 1  $\mu\text{m}$ , i.e. each Raman spectrum (fig. 4.10.) is collected from few Ge deposited sites.

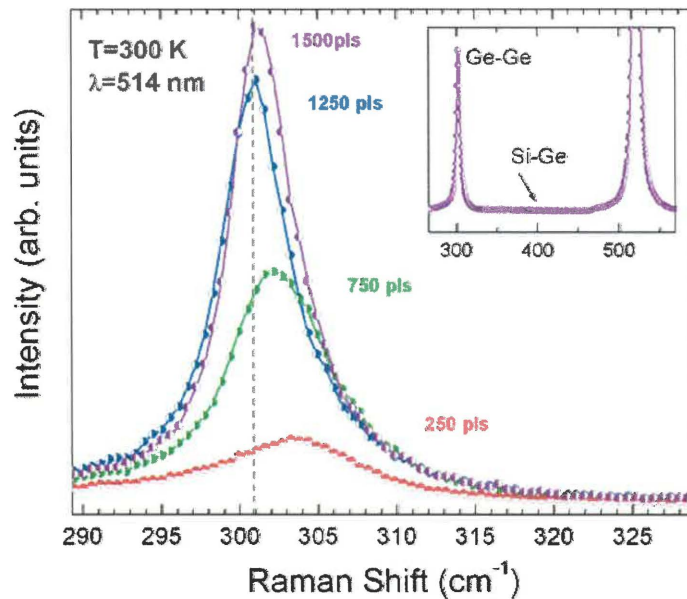


**Figure 4.10.** Raman spectra acquired by probing the Ge patterned areas with the 514.5 nm line of an Ar<sup>+</sup> ion laser. The absence of the Si-Ge phonon band around  $\sim 400 \text{ cm}^{-1}$  (see inset) indicates no trace of Si intermixing; dashed line corresponds to the Ge-Ge bulk phonon frequency ( $300.8 \text{ cm}^{-1}$ )

<sup>10</sup> Measurements performed at ICMAB, Barcelona, Spain.

In Fig. 4.10, the spectral position and shape of the Ge-Ge phonon mode reveals that the Ge structures are crystalline and the absence of the Si-Ge phonon band around  $\sim 400 \text{ cm}^{-1}$  (inset in Fig. 4.10) clearly suggests that there is no trace of Si intermixing. This shows in fact that the intermixing phenomenon is kinetically limited by the high growth rate induced by a 10 Hz laser pulse repetition rate.

Further, for higher number of ablation pulses (i.e. increased deposition coverage) the Ge-Ge phonon peak gets progressively more intense consistently with the increase of Ge coverage. This is shown by the linear dependency of the integrated intensity of Ge-Ge phonon peaks with the number of pulses, which is depicted in Fig. 4.11 a.

Spectra recorded on samples at the first stages of growth exhibit a blue-shifted Ge-Ge phonon frequency ( $\sim 303 \text{ cm}^{-1}$ ) attributed to compressive strain at the island-substrate interface. The strain is progressively relieved for taller clusters (i.e. higher number of laser pulses) whose phonon frequency approaches the value expected for Ge bulk ( $300.8 \text{ cm}^{-1}$ ) (see dashed line in Fig. 4.11 b). The presence of a built in strain indicates that the Ge nanostructures are matching the Si substrate and they also retain this crystallographic orientation.

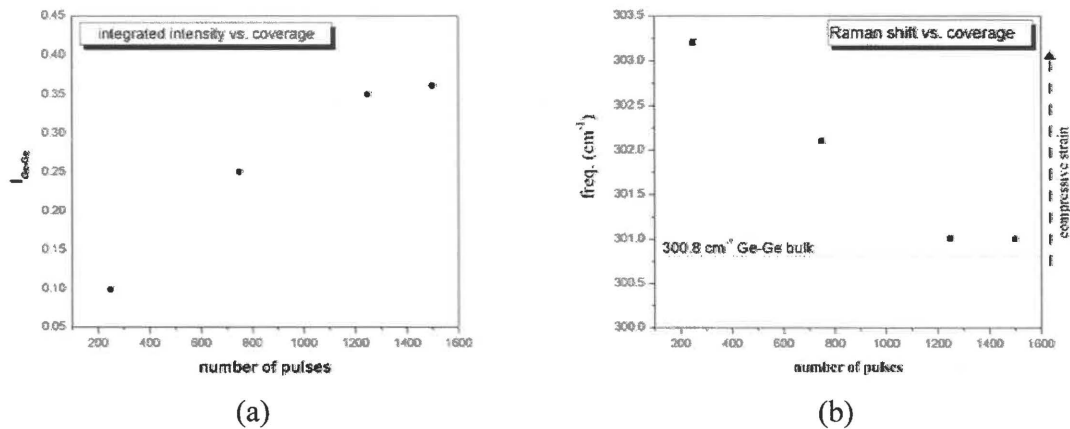


**Figure 4.11.** (a) The dependency of the integrated intensity (values calculated from Fig. 4.6) of the Ge-Ge phonon peak with the number of pulses and (b) phonon frequency shift vs. number of pulses indicating a higher compressive strain for the smaller islands which exhibit a bigger frequency shift

### 4.4.3 Ge patterned islands on Si (111)

We pursued the investigation of the influence of the substrate orientation on the Ge patterned islands and prepared a set of samples by stenciling Ge on Si(111) substrates. The patterning process has been carried out using the same stencil as in the first batch of depositions on Si(100), a further purpose of the experiment being to verify stencil's endurance and if possible its clogging threshold. A modified Shiraki cleaning method ( $\text{H}_2\text{SO}_4 : \text{H}_2\text{O}_2 = 4 : 1$  by volume) has been applied before the oxide stripping in a HF solution 5%. Three samples were grown for a laser repetition rate of at 10Hz,  $4\text{J}/\text{cm}^2$  laser fluence and substrate temperature  $600^\circ\text{C}$ , for 250, 500 and 1000 laser ablation pulses. Interestingly, at 250 laser ablation pulses the replicated ordered arrays of Ge structures were formed again as flat circular mounds, similar to those found on Si(100) substrates and thus prompting no visible influence of the substrate orientation (Fig. 4.12 a). Increasing the Ge coverage, the initial 2D mounds are playing again the role of the anomalously thick “wetting layer” (5-6 nm thick revealed by AFM) and rounded dots are formed once more on top of the mounds (Fig 4.12 b).

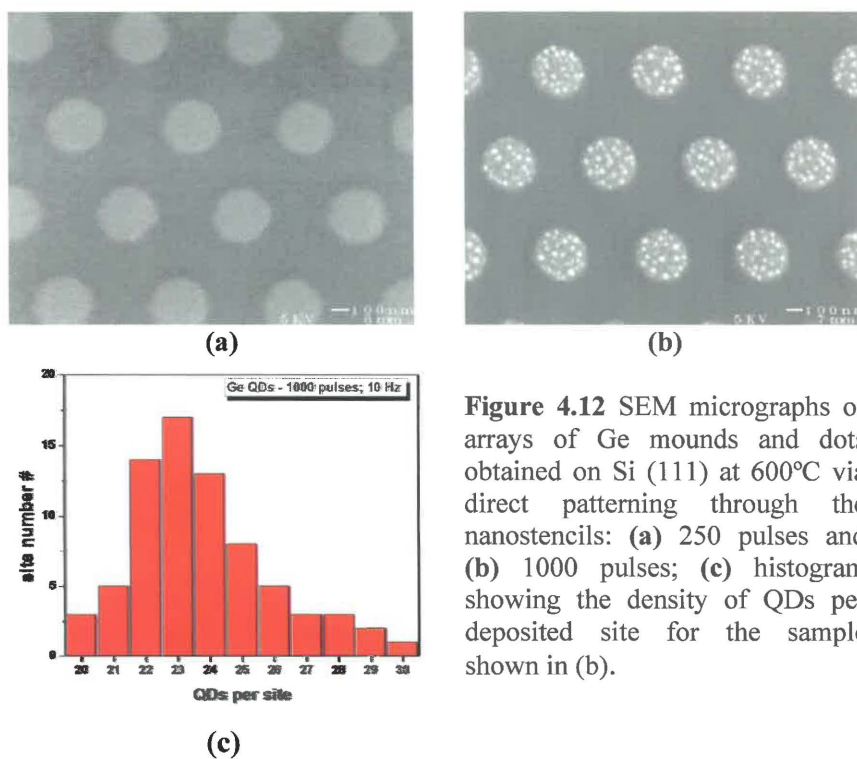


**Figure 4.12** SEM micrographs of arrays of Ge mounds and dots obtained on Si (111) at  $600^\circ\text{C}$  via direct patterning through the nanostencils: (a) 250 pulses and (b) 1000 pulses; (c) histogram showing the density of QDs per deposited site for the sample shown in (b).

The circular shape of the Ge 2D-mounds obtained in both cases might be linked to a combination of effects: (i) a strong and brisk confinement of the instant high flux of impinging species generated by PLD through the stencil's circular openings and (ii) an increased mound "corner diffusion" that has been observed to take place when highly energetic species are arriving on the substrate [57].

The registration of the deposited sites is very well preserved and SEM micrographs show that the QDs prefer to remain only on the top of the mounds, without indications of lateral diffusion between the sites. We do not detect well defined facets for the dots but mostly rounded features which could be due to the highly energetic character of PLD and a high growth rate.

The dots density per site increases with the coverage (Fig. 4.12 b) showing a density of QDs centered at twenty-three (Fig. 4.12 c) and a fairly narrow size distribution of the dots. We further evaluated the variation of dots density in the context of variation of laser repetition rate in subsequent experiments and this issue will be discussed in the following section (4.4.4).

The evaluation of "clogging effect" shows that after 10 recurring depositions using the same stencil (including the first usages on Si(100) for different number of pulses) and a total equivalent film thickness of about 300 nm, the lateral size of the deposited sites gets down to about 330 nm (see Fig. 4.13 a and b) thus indicating just a shallow reduction in the aperture size (~10%) and an efficient transfer of the Ge deposited through the stencils' apertures<sup>11</sup>.

#### **4.4.4 Effect of the laser repetition rate on Ge QDs density**

For a high efficiency, a QD-based device needs a high-density of QDs along with their uniform spatial distribution. Thus we were interested to find if the density and size of the Ge QDs obtained on top of the 2D-mounds can be in fact controlled by adjusting the growth conditions (laser parameters). In a subsequent experiment, we choose to grow

---

<sup>11</sup> As a cleaning process, Ge can be easily removed from the membrane by dipping the stencil in a heated solution of peroxide (H<sub>2</sub>O<sub>2</sub>) and rinsing the stencil in DI water.

a series of samples with a lower deposition rate, making use of lower pulses repetition rates of laser on the target (1 Hz instead of 10 Hz) while keeping the silicon substrates at the same temperature i.e. 600 °C (Fig. 4.13). A lower pulse repetition rate implicitly means a longer deposition time that in turn leads to a longer period of time spent by the substrate at elevated temperature (e.g. 600 °C). This favors desorption of the adatoms impinging on the surface and ultimately can enhance lateral surface diffusion.

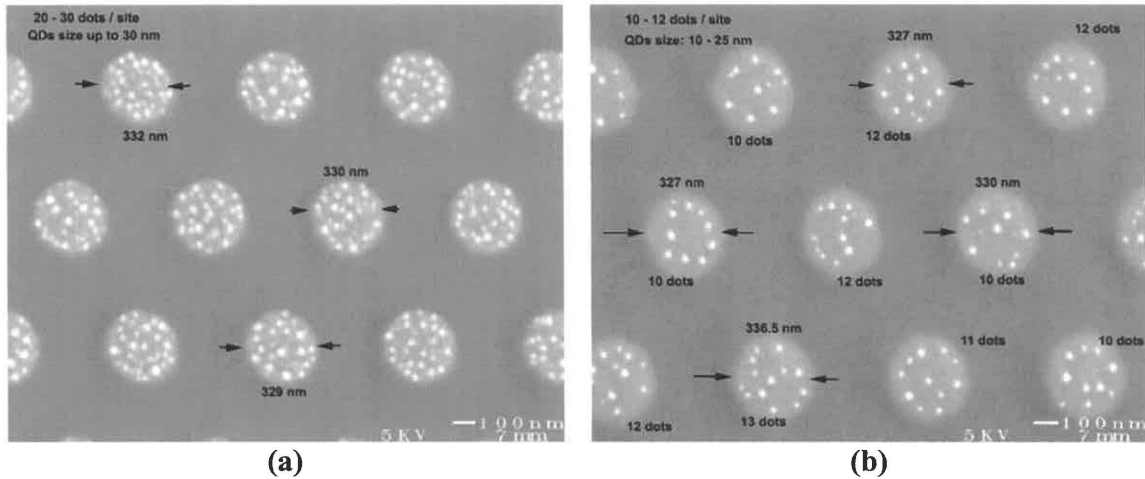


**Figure 4.13.** SEM micrographs of Ge patterned on Si (111) at 600 °C for 1000 laser pulses and different repetition rates: (a) 10 Hz and (b) 1 Hz.

As shown in Fig. 4.13 (b), for a laser repetition rate of only 1 Hz, the density of Ge QDs per deposited site shows values centered at about 10-12 dots, value that is only half from the density of QDs obtained when deposition was carried out at 10 Hz (20-30 QDs / site) (fig. 4.13 (a)). Since no structures were detected between the deposited sites the reduction of QDs density is caused mainly by the Ge desorption from the surface kept a longer time at 600 °C (16 min and 40 sec at 1 Hz instead of 1 min and 40 sec at 10 Hz). The laser fluence was set for 4 J/cm<sup>2</sup> in both cases<sup>12</sup>, thus there is a similar size distribution of the dots prepared in these two particular cases.

The particular architecture of the stencils used in our experiments (i.e. nominal apertures of 350 nm and 700 nm pitches within a stripe area of 2 mm × 100 μm), generates a density of deposited sites of about 2.35 × 10<sup>6</sup> mm<sup>-2</sup>. Following the deposition

<sup>12</sup> A change in laser fluence is expected to influence simultaneously the morphology, size and spatial distribution of deposits leading to extreme complex effects that prompt thorough investigations which are not subject of this study and are envisioned for further experiments.

conditions characterized by a high growth rate (induced by high pulses repetition rates) we estimate approximately 20-30 dots/site, thus the density of the dots can reach values of at least  $4.7 \times 10^9 \text{ cm}^{-2}$ . In this case we obtain a density value that is one order of magnitude smaller than that reported in a mere self-organization of Ge QDs (e.g.  $2.5 \times 10^{10} \text{ cm}^{-2}$ ) via other deposition techniques [57,58].

To observe the coverage dependence of morphology of the Ge QDs while preserving the low growth rate, a subsequent sample was grown for 2000 pulses assuming a linear dependence of the deposited mass with the number of ablation pulses. Once more, Ge QDs were formed only on top of the always-present 2D mounds that are keeping the pattern provided by the stencil's aperture.

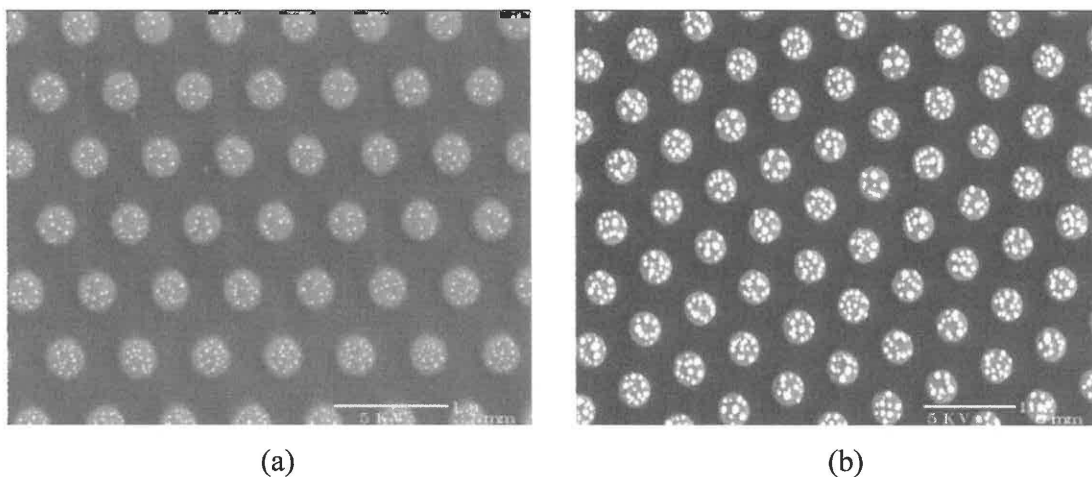


**Figure 4.14** SEM micrographs of Ge QDs obtained for (a) 1000 and (b) 2000 laser pulses;

The size of the dots increased with the number of pulses however for this highest coverage we did not detect coalescence leading to a singular island like in the case of Ge deposited on Si (100). We attribute this to a smaller volume of deposited Ge due to the gradual aperture clogging.

The statistical distribution of the number of QDs per deposited site (Fig. 4.15 (a) and (b)) has been assessed from various SEM micrographs taken on different stripes and as well as on different places of the same stripe. The histograms are showing the QDs density /site centered on close values in spite of the differences in lateral size for the QDs. This indicates that after reaching a critical density within the area defined by the

stencil's aperture, the Ge QDs are growing by expanding their lateral size in a natural attempt of releasing the strain that otherwise is governing the dots with smaller size.

Evaluation of the QDs size distribution for the same samples (fig 4.15 (c) and (d)) shows a fairly narrow distribution in the case of the sample prepared for 1000 pulses with a value centered at 30nm (major length) whereas a value of 50 nm (major length) and a wider distribution is found for the QDs grown for 2000 pulses.

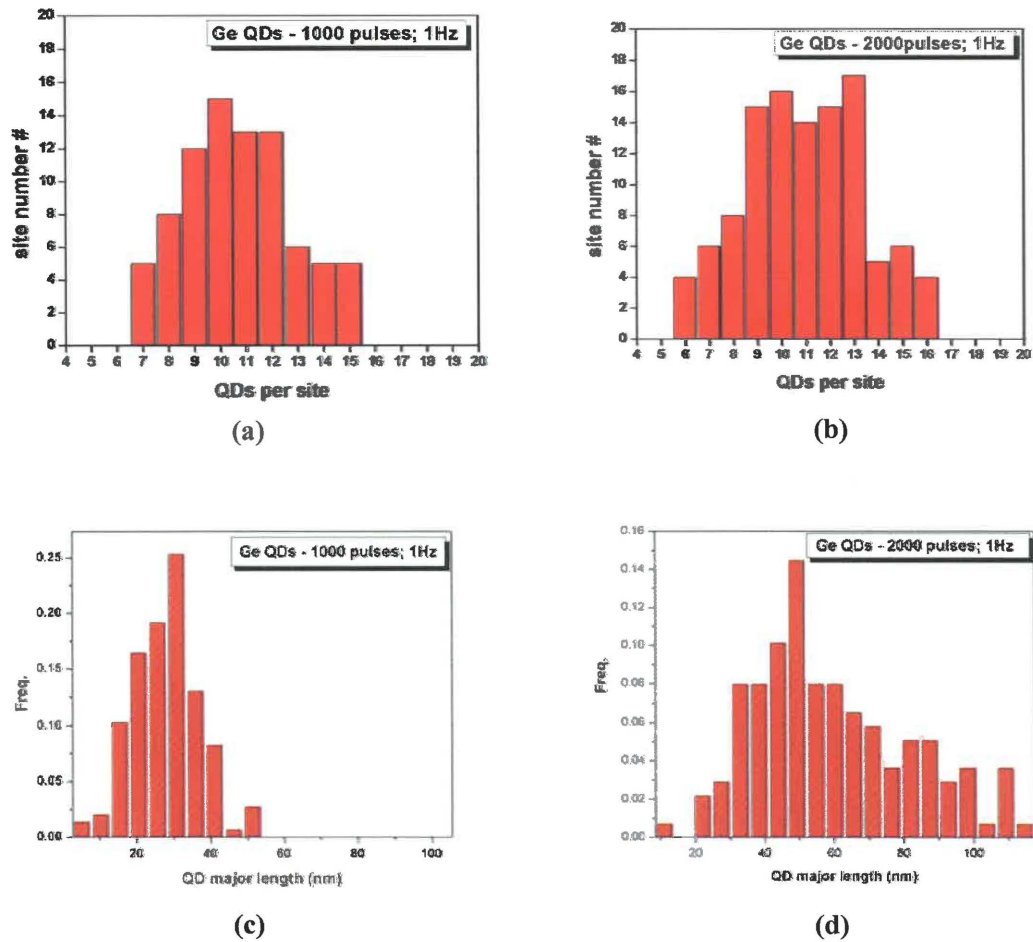


**Figure 4.15** Statistical distribution of the number of QDs per deposited site for (a) 1000 and (b) 2000 laser pulses; and size distribution (QD major length) for (c) 1000 and (d) 2000 laser pulses

#### 4.4.5 Micro-Raman characterization of patterned Ge/Si(111) islands

The structural properties, strain and composition of the Ge patterned islands on Si(111) were investigated once more by micro-Raman spectroscopy (Fig. 4.16) using the set-up with the configuration described in section 4.4.2 (i.e. a 514.5 nm line of an Ar<sup>+</sup> ion laser focused with a spot size of about 1 μm).

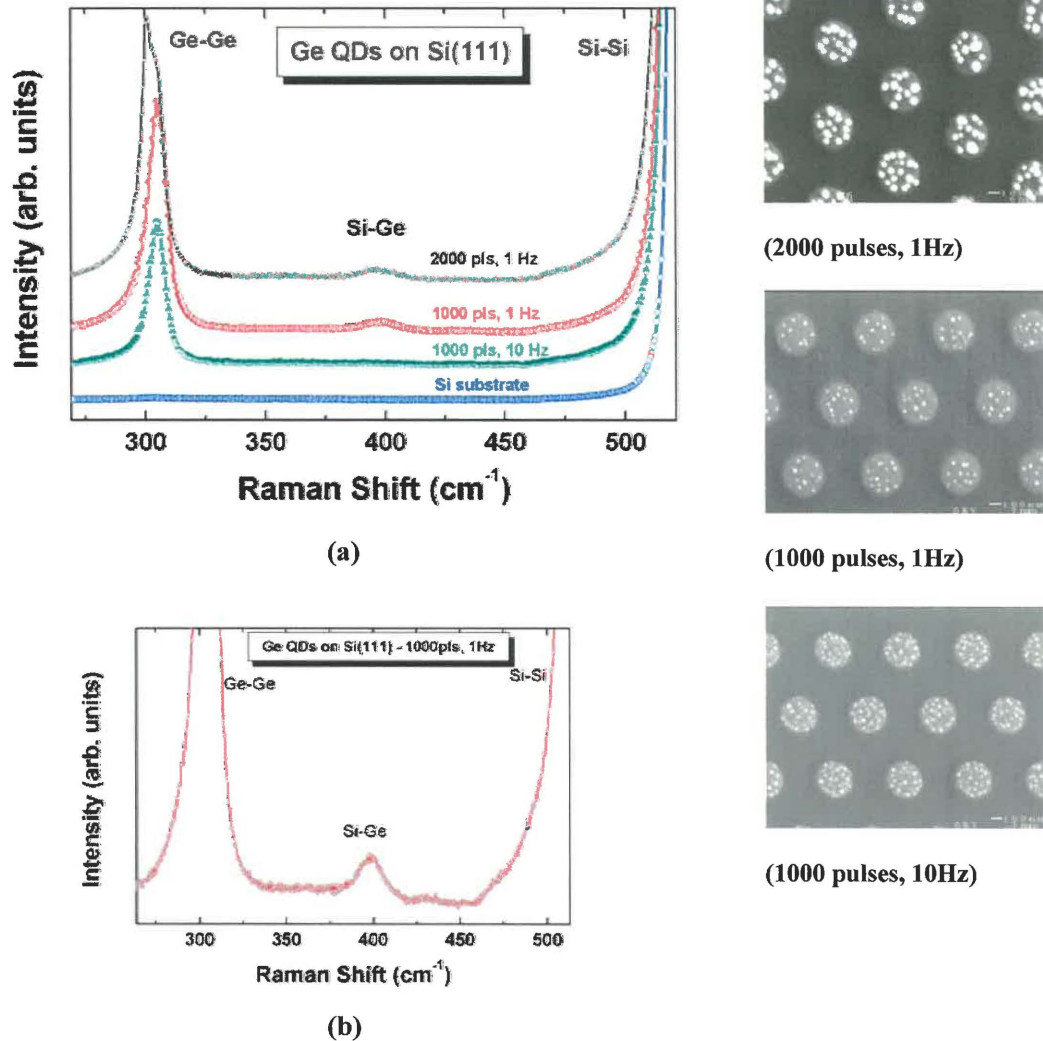


**Figure 4.16** Micro-Raman spectroscopy on patterned Ge/Si(111): (a) obtained for different rate growths and different numbers of laser pulses on the target (samples from SEM micrographs); (b) zoom-in showing the intermixing Si-Ge at  $\sim 400 \text{ cm}^{-1}$

The spectral shape and position of Ge-Ge phonon mode ( $\sim 300 \text{ cm}^{-1}$ ) indicates that all patterned structures are crystalline. Another important feature of the recorded spectra

is the Si-Ge peak ( $\sim 400\text{ cm}^{-1}$ ) observed in the samples grown at low repetition rates (1 Hz) of the pulsed laser. This peak reveals that Si *intermixing* occurs (Fig. 4.16 (b)) in the samples grown at a lower growth rate; whereas for a repetition rate of 10 Hz (i.e. 10 times higher growth rate) the Si-Ge intermixing is kinetically limited.

The spectra recorded for the samples obtained for 1000 pulses exhibit a blue shifted Ge-Ge phonon frequency which is consistent with the small size of the Ge dots grown on top of the mounds, dots that are expected in this case to experience a higher compressive strain due to their reduced size (Fig. 4.17 a).

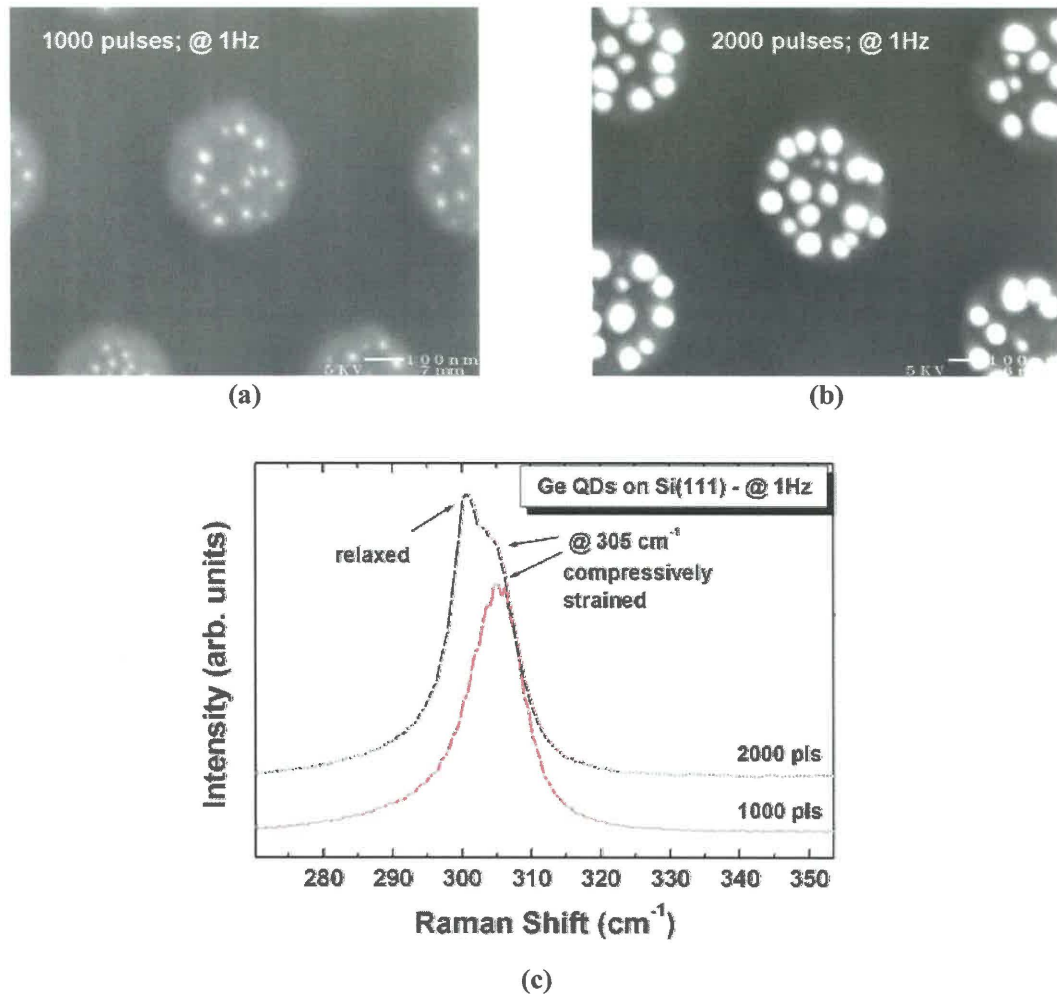


**Figure 4.17** SEM micrographs of Ge QDs obtained by PLD stenciling for (a) 1000 and (b) 2000 laser pulses respectively; (c) detail of Raman spectra around the Ge-Ge phonon mode at  $300\text{ cm}^{-1}$ .

On the other hand, the spectra recorded for the sample deposited for 2000 pulses exhibits a convoluted peak, which again is consistent with the size distribution of the dots per deposited site (i.e. smaller and larger dots) thus indicating that part of the dots are compressively strained (peak spectra at  $\sim 305 \text{ cm}^{-1}$ ) whereas the larger ones are relaxed suggested by the sharp peak at  $\sim 300 \text{ cm}^{-1}$  (Fig. 4.17 b).

Further more, the spectral positions (in  $\text{cm}^{-1}$ ) of the Ge-Ge and Si-Ge peaks allow us to extract the composition ( $x$ ) of the  $\text{Si}_{1-x}\text{Ge}_x$  alloy and the in-plane strain ( $\varepsilon_{\parallel}$ ) applying the empirical relations from [54]:

$$\omega_{\text{Ge-Ge}} = 284 + 5x + 12x^2 + b_{\text{Ge-Ge}} \varepsilon_{\parallel} \quad (4.1)$$

$$\omega_{\text{Si-Ge}} = 400 + 29x - 95x^2 + 213x^3 - 170x^4 + b_{\text{Si-Ge}} \varepsilon_{\parallel} \quad (4.2)$$

Using the following values for the phonon strain-shift coefficients:  $b_{\text{Ge-Ge}} = -400 \text{ cm}^{-1}$  and  $b_{\text{Si-Ge}} = -575 \text{ cm}^{-1}$  determined by Tan et al. [59] for Ge-rich self-assembled QDs, we obtain from the eq. (4.1) and (4.2) for the sample deposited at 1Hz and 1000 pulses a Ge composition of  $x_{\text{Ge}} = 92 \pm 3$  and a compressive strain  $\varepsilon_{\parallel} = -1.3 \pm 0.4 \%$ .<sup>13</sup>

For the sample deposited at 1Hz and 2000 pulses, the first peak at  $300.4 \text{ cm}^{-1}$  is fully relaxed and originating from big relaxed islands on top of the mounds - corresponds to almost pure Ge: composition  $x_{\text{Ge}} = 98 \pm 3$ . For the second peak identified at  $305 \text{ cm}^{-1}$  (strained mound and small Ge dots) composition is  $x_{\text{Ge}} = 93 \pm 3$  and the compressive strain  $\varepsilon_{\parallel} = -1.2 \pm 0.3 \%$ . For the sample deposited at 10Hz the Si-Ge peak is not visible thus indicating a pure germanium composition.

## 4.5 Summary

Within a top-down framework, direct selective deposition of Ge on finite-size locations constitutes a promising path for integrating and using the Ge islands Stranski-Krastanov self-organization phenomena.

We showed that this task can be achieved combining stenciling with PLD which provides a flexible approach to grow and pattern crystalline Ge/Si nanostructures.

---

<sup>13</sup> Errors are estimated considering the dispersion of strain-shift coefficients found in literature

We found that the morphological evolution of the structures with coverage follows a modified Stranski-Krastanov growth mode, due to the finite size of the WL in each aperture location. The locations where the Ge islands nucleate is preserved by the aperture pattern drawn in the nanostencil.

Micro-Raman spectroscopy indicates that the nanostructures are crystalline Ge and that they follow the substrate's crystallographic orientation. A high growth rate increases the QDs density per deposited site and the Si-Ge intermixing is kinetically limited. Furthermore, the density and physical dimensions of the dots can be adjusted by varying the laser repetition rate. Future work might focus onto the correlation between other deposition parameters such as laser fluence and the Ge dots' morphology and their density per deposited site.

We conclude that nanostenciling, combined with any vapor deposition technique such as thermal evaporation, e-beam or MBE, represents an attractive approach to deposit semiconductor heterostructures, since it is parallel and does not require resist-based lithography. This approach can for instance be developed and applied to fabricate QD array architectures of semiconductor nanostructures for optoelectronic applications.

## 4.6 References

- [1] D. J. Paul, *Semicond. Sci. Technol.* 19, R75 (2004)
- [2] P. M. Fauchet, *Mat. Today* 8, 26 (2005)
- [3] L. Pavesi, *Mat. Today* 8, 18 (2005)
- [4] J. Konle, H. Presting and H. Kibbel, *Phys. E* 16, 596 (2003)
- [5] A. Rogalski, *Prog. in Quant. Elec.* 27, 59 (2003)
- [6] Y. Arakawa and H. Sakaki, *Appl. Phys. Lett.* 40, 939 (1982)
- [7] I. N. Stranski and L. Krastanow, *Ber. Akad. Wiss. Wien* 146, 797 (1938)
- [8] L. Goldstein, F. Glas, J. Y. Marczin, M. N. Charasse and G. Le Roux, *Appl. Phys. Lett.* 47, 1099 (1985)
- [9] D. J. Eaglesham and M. Cerullo, *Phys. Rev. Lett.* 64, 1943 (1990)
- [10] Y. M. Mo, D. E. Savage, B. S. Swartzentruber and M. G. Lagally, *Phys. Rev. Lett.* 65, 1020 (1990)
- [11] D. Leonard, M. Krishnamurthy, C.M. Reaves, S.P. Denbaars and P.M. Petroff, *Appl. Phys. Lett.* 63, 3203 (1993)
- [12] J. Stangl, V. Holy and G. Bauer, *Rev. of Mod. Phys.* 76, 725 (2004)
- [13] R. S. Williams, G. Medeiros-Ribeiro, T. I. Kamins and D. A. A. Ohlberg, *Acc. Chem. Res.* 32, 425 (1999)
- [14] G. Medeiros-Ribeiro, A. M. Bratkovski, T. I. Kamins, D. A. A. Ohlberg and R. S. Williams, *Science* 279, 353 (1998)
- [15] F. M. Ross, J. Tersoff and R. M. Tromp, *Phys. Rev. Lett.* 80, 984 (1998)
- [16] F. Rosei and R. Rosei, *Surf. Sci.*, 500, 395 (2002)
- [17] F. Boscherini, G. Capellini, L. Di Gaspare, F. Rosei, N. Motta and S. Mobilio, *Appl. Phys. Lett.* 76, 682 (2000)
- [18] F. Boscherini, G. Capellini, L. Di Gaspare, M. De Seta, F. Rosei, A. Sgarlata, N. Motta and S. Mobilio, *Thin Solid Films* 380, 173 (2000)
- [19] F. Ratto, F. Rosei, A. Locatelli, S. Cherifi, S. Fontana, S. Heun, P-D. Szkutnik, A. Sgarlata, M. De Crescenzi and N. Motta, *Appl. Phys. Lett.* 84, 4526 (2004)
- [20] F. Ratto, G. Constantini, A. Rastelli, O.G. Schmidt, K. Kern and F. Rosei, *J. of Exp. Nanosci.* 1, 279, (2006)

- [21] P. M. Petroff, A. Lorke and A. Imamoglu, *Phys. Today* 54, 46 (2001)
- [22] C. S. Lent, P. D. Tougaw, W. Porod and G. H. Bernstein, *Nanotechnology* 4, 49 (1993)
- [23] F. C. Frank and J. van der Merwe, *Proc. Roy. Soc.(London) A* 198, 216 (1949)
- [24] M. Volmer and A. Weber, *Z. Physik. Chem* 119, 277 (1926)
- [25] J. Macleod, Ph.D. Thesis, Queens Univ. Kingston, ON, Canada, 2006
- [26] B. Voigtlander, *Surf. Sci. Rep.* 43, 127 (2001)
- [27] M. Schmidbauer, T. Wiebach, H. Raidt, M. Hanke, R. Köhler and H. Wawre, *Phys. Rev. B* 58, 10523 (1998)
- [28] M. Horn-von Hoegen, B. H. Müller, A. Al Falou and M. Henzler, *Phys. Rev. Lett.* 71, 3170 (1993)
- [29] K.M. Hassan, A. K. Sharma, J. Narayan, J. F. Muth, C. W. Teng and R. M. Kolbas, *Appl. Phys. Lett.* 75, 1222 (1999)
- [30] B. Shin, J. P. Leonard, J. W. McCamy and M. J. Aziz, *Appl. Phys. Lett.* 87, 181916 (2005)
- [31] M. S. Hegazy and H. E. Elsayed-Ali, *Appl. Phys. Lett.* 86, 23104 (2005)
- [32] M. S. Hegazy and H. E. Elsayed-Ali, *J. Appl. Phys.* 99, 054308 (2006)
- [33] X. Ma, Z. Yan, B. Yuan and B. Li, *Nanotechnology.* 16, 832 (2005)
- [34] G. Cappellini, M. de Seta, C. Spinella and F. Evangelisti, *Appl. Phys. Lett.* 82, 1772 (2003)
- [35] J. R. Heath, R. S. Williams, J. J. Shiang, S. J. Wind, J. Chu, C. D' Emeric, W. Chen, C. L. Stanis and J. J. Bucchignano, *J. Phys. Chem.* 100, 3144 (1996)
- [36] T. I. Kamins and R.S. Williams, *Appl. Phys. Lett.* 71, 1201 (1997)
- [37] T.I. Kamins, D.A.A. Ohlberg, R.S. Williams, W. Zhang and S.Y. Chou, *Appl. Phys. Lett.* 74, 1773 (1999)
- [38] L. Vescan, *Mat. Sci. Eng. A.* 302, 6 (2001)
- [39] E. S. Kim, N. Usami and Y. Shiraki, *Appl. Phys. Lett.* 72, 1617 (1998)
- [40] G. Jin, J. L. Liu, S. G. Thomas, Y. H. Luo and K. L. Wang , *Appl. Phys. Lett.* 75, 2752 (1999)
- [41] G. Jin, J. L. Liu and K. L. Wang, *Appl. Phys. Lett.* 76, 3591 (2000)

- [42] Z. Zhong, A. Halilovic, M. Mühlberger, F. Schäffler and G. Bauer, *J. Appl. Phys.* 93, 6258 (2003)
- [43] O. G. Schmidt, N. Y. Jin-Phillip, C. Lange, U. Denker, K. Eberl, R. Schreiner, H. Grabeldinger and H. Schweizer, *Appl. Phys. Lett.* 77, 4139 (2000)
- [44] L. Vescan, *J. Phys.: Cond. Matt.* 14, 8235 (2002)
- [45] A. Karmous, A. Cuenat, A. Ronda, I. Berbezier, S. Atha and R. Hull, *Appl. Phys. Lett.* 85, 6401 (2004)
- [46] A. Bernardi, M. I. Alonso, A. R. Goñi, J. O. Ossó and M. Garriga, *Appl. Phys. Lett.* 89, 101921 (2006)
- [47] Z. Zhong, A. Halilovic, M. Mühlberger, F. Schäffler and G. Bauer, *Appl. Phys. Lett.* 82, 445 (2003)
- [48] B. Hinnemann, H. Hinrichsen and D. E. Wolf, *Phys. Rev. Lett.* 87, 135701 (2001)
- [49] M. Koelbel, R. W. Tjerkstra, J. Brugger, C. J. M. van Rijn, W. Nijdam, J. Huskens and D. N. Reinhoudt, *Nano Lett.* 2, 1339 (2002)
- [50] M. A. F. Boogaart, L. Doeswijk and J. Brugger, *J. of MEMS*, 15, 1663 (2006)
- [51] L. Vescan, T. Stoica, B. Holländer, A. Nassiopoulou, A. Olzierski, I. Raptis and E. Sutter, *Appl. Phys. Lett.* 82, 3517 (2003)
- [52] A. Rastelli, M. Stoffel, J. Tersoff, G.S. Kar and O.G. Schmidt, *Phys. Rev. Lett.* 95, 026103 (2005)
- [53] J. Cui, Q. He, X.M. Jiang, Y. L. Fan, X. J. Yang, F. Xue and Z. M. Jiang, *Appl. Phys. Lett.* 83, 2907 (2003)
- [54] M. I. Alonso, M. de la Calle, J. O. Ossó, M. Garriga and A. R. Goñi, *J. Appl. Phys.* 98, 033530, (2005)
- [55] A. Bernardi, J. O. Ossó, M. I. Alonso, A. R. Goñi and M. Garriga, *Nanotechnology* 17, 2602 (2006)
- [56] J. G. Amar, *Phys. Rev. B.* 60, R11317 (1999)
- [57] A. Alguno, N. Usami, T. Ujihara, K. Fujiwara, G. Sazaki, K. Nakajima and Y. Shiraki, *Appl. Phys. Lett.* 83, 1258 (2003)
- [58] P. S. Chen, Z. Pei, Y. H. Peng, S. W. Lee and M.-J. Tsai, *Mat. Sci. Eng. B* 108, 213, (2004)
- [59] P. H. Tan, K. Brunner, D. Bougeard, G. Abstreiter, *Phys. Rev. B* 68, 125302 (2003)

## **5. Nanostenciling of Functional Perovskite-type Complex Oxides via Pulsed Laser Deposition**

### **5.1 Introduction**

Ceramic materials comprise inorganic, non-metallic, crystalline compounds. *Electroceramic materials* cover the family of ceramics that are used for their specific mechanical, electrical, magnetic, or optical properties or a combination thereof. *Oxide ceramics* in particular exhibit a vast area of functionalities seen in almost no other class of materials (metals, semiconductors, polymers) and offer a broad variety of properties which can be exploited. Often due to a specific crystal structure, such oxides exhibit various interesting properties such as piezoelectricity, pyroelectricity, ferroelectricity, or magnetic properties like giant magnetoresistance. They could be insulators and dielectrics, or conducting and serve as electrodes or they could even be superconductors (HTSC), thus providing a large number of material-options suitable for realizing electrical and electronic components, sensors and actuators, or micro-electromechanical systems (MEMS) [1].

Among the electroceramic oxides, *piezoelectric* and *ferroelectric ceramics* with a *perovskite-type*<sup>1</sup> crystalline structure - often termed ABO<sub>3</sub>-type oxides<sup>2</sup> (fig. 5.1) - exhibit a wide spectrum of useful functional properties, including high-dielectric permittivity, good electromechanical coupling, high piezoelectric and pyroelectric

---

<sup>1</sup> Named after the mineral calcium titanate (CaTiO<sub>3</sub>) that is found in the Earth's crust

<sup>2</sup> In the general formula ABO<sub>3</sub> for the perovskite structure, A is a metal ion with a +2 valence and B is a metal ion with a +4 valence. The A<sup>2+</sup> and O<sup>2-</sup> ions form a FCC unit cell with the A<sup>2+</sup> ions at the corners of the unit cell and the O<sup>2-</sup> ions in the center of the faces of the unit cell. The B<sup>4+</sup> ion is located at the octahedral interstitial site at the center of the unit cell and is coordinated to six O<sup>2-</sup>.

coefficients, switchable spontaneous polarization, non-linear dielectric behavior or non-linear optical activity [2,3].

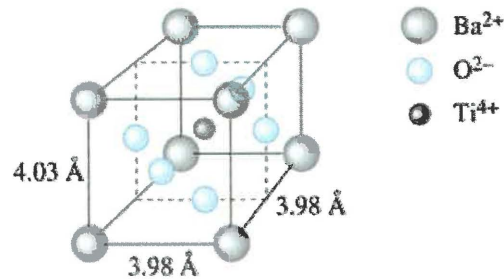


**Figure 5.1** The crystal structure of tetragonal barium titanate (BaTiO<sub>3</sub>) often regarded as the prototypical structure of a perovskite-type complex oxide [4].

Materials integration, required for miniaturized systems, increased in importance in the last decades. Besides their usefulness in the bulk form, electroceramic materials in the *thin films* form can bring a wealth of additional *functionalities* to integrated semiconductor-based chips, opening new avenue for the realization of advanced *multifunctional* and *smart* devices. One of the reasons for developing electroceramic thin films is that the processing temperature is usually much lower than that of the sintering processes needed for bulk ceramic preparation. Another important aspect is that in thin film form, oxide ceramics can be grown in a definite crystal orientation, or *epitaxially*, therefore, the anisotropy of their intrinsic properties can be readily exploited (e.g. pyroelectricity, piezoelectricity, and ferroelectricity).

In contrast to the bulk form, (oxide ceramic) thin films are always part of a combined system (i.e. substrate-film) and their properties are very sensitive to the processing conditions. Moreover, since most of the ceramic oxides are inert and quite resistant to corrosion they are difficult to etch and thus their *integration* onto silicon and other substrates, as well as their *patterning* into *functional elements*, represent complex issues to be solved and well mastered.

Following the trend of the semiconductor industry with respect to the continuing miniaturization of integrated devices, functional oxide ceramic thin films are experiencing a similar evolution from *microtechnology* towards *nanotechnology*. Constant efforts are currently undertaken to *nano-structure* and *nano-pattern* thin films of functional oxides grown by either physical deposition techniques (e.g. magnetron sputtering, pulsed laser deposition, thermal vapor deposition) or chemical deposition

methods (e.g. metal-organic-chemical vapor deposition or chemical solution deposition). Some recent reviews have debated the advantages and difficulties associated with either the top-down or the bottom-up approaches to pattern electroceramic thin films [5-7].

Although some of the alternative patterning techniques to photolithography have already demonstrated the potential to deliver structures with their smallest features close to 100 nm, they are difficult to integrate within a more general and complex fabrication scheme. The requirement of perfect registration is unavoidable for a process to be used in future micro- or nano-electronics. For instance, the integration of ferroelectric oxides for application in memories technology such as for e.g. a prospective 10 Gbit non-volatile ferroelectric random access memory (NV-FeRAM), ferroelectric/piezoelectric hybrid hetero-structures for MEMS/NEMS devices or potential tunable multifunctional devices all require such a stringent registration.

As structure dimensions become smaller, the new functional materials being envisioned exhibit a pronounced *size effect* which manifests itself in a significant deviation of the properties of low-dimensional structures with respect to their bulk properties [8]. Fundamental studies of patterned functional oxide ceramics are therefore further required for these new materials, especially in the nanoscale regime [9]. These studies are crucial to establish experimentally the useful *critical size* for each material, i.e. the smallest size at which it would still provide the desired functionality.

In this chapter we present studies on parallel nanostructuring and patterning of ferroic oxides, mainly piezoelectrics/ferroelectrics, as well as multiferroic oxides via *nanostenciling* and their subsequent characterization. Their functionality is investigated by piezoresponse force microscopy (for ferroelectricity) and magnetic force microscopy (for magnetic properties). In section (5.2) we outline the fundamental aspects of piezoelectric/ferroelectric materials and in section (5.3) we offer a brief overview of the methods used to fabricate ferroelectric nanostructures. In section (5.4) we elaborate on and analyze the performances of the nanostenciling approach for the barium titanate ( $\text{BaTiO}_3$ ) / strontium titanate  $\text{SrTiO}_3$  (100) materials system. Patterning of multiferroics bismuth ferrite ( $\text{BiFeO}_3$ ) and double-perovskite  $\text{Bi}_2\text{FeCrO}_6$  is presented in section (5.5). Finally, a summary of our major findings and the perspectives for future work are outlined in section (5.6).

## 5.2 Piezoelectricity and ferroelectricity

Piezoelectric<sup>3</sup> materials are a class of ceramic materials that exhibit the property of becoming electrically polarized when mechanically stressed and of becoming mechanically strained when an electric field is applied. The *direct piezoelectric effect* is the generation of charges when an external mechanical stress is applied to the material [10]. This phenomenon is mathematically represented by the linear relation that links the electric displacement  $D_i$  with the elastic stress  $X_{jk}$  applied to the piezoelectric material (using the Einstein summation convention) via the *piezoelectric coefficient*  $d_{ijk}$  which is a third-order tensor expressed in [C/N]:

$$D_i = d_{ijk}^{\text{direct}} X_{jk} \quad (5.1)$$

The *converse effect* is the apparition of a strain when the piezoelectric material is subject to an external electric field. The corresponding relation is also mathematically described by a linear equation which relates the strain  $x_{ij}$  developed in a piezoelectric material and the external electric field:

$$x_{ij} = d_{kij}^{\text{converse}} E_k \quad (5.2)$$

The converse piezoelectric coefficient is expressed in [m/V]. Thermodynamics shows that the piezoelectric coefficients for the direct and converse piezoelectric effects are identical i.e.  $d^{\text{converse}} = d^{\text{direct}}$ .

The piezoelectric coefficient measured in the direction of the applied stress is usually called the *longitudinal* coefficient, and that measured in the direction perpendicular to the field is known as the *transverse* coefficient. Other piezoelectric coefficients are denominated *shear* coefficients.

In a “standard” *dielectric*, positive and negative bound-charges are displaced from their original position by the application of an external electric field. This induced dipole is called the dielectric *polarization* ( $\mathbf{P}$ ). However, this polarization will vanish, if the electric field is removed. There are, however, piezoelectrics that possess, within a certain

---

<sup>3</sup> The word “piezo” is derived from the Greek word “piezin” which means “to press” or “to squeeze”

range of temperatures and pressures, an intrinsic *spontaneous polarization* ( $\mathbf{P}_s$ ) even in the absence of an external electric field. In such materials, at the equilibrium the center of gravity of the negative and positive charges within their structural unit cells is not the same thus forming a *permanent* electric dipole. The ability of a crystal to exhibit a spontaneous polarization  $\mathbf{P}_s$  is strongly related to its symmetry. To exhibit a spontaneous polarization (which is a vector), the material has to possess at least one specific direction, called the polar axis, two points of which cannot be related by any symmetry element of the material. As a consequence it can be immediately understood that centrosymmetric crystalline systems (characterized by an inversion center) can not have such polar properties. They are called *paraelectric* systems.

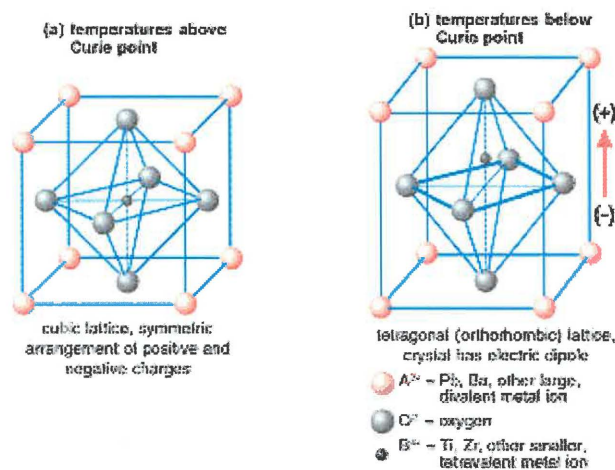


**Figure 5.2.**  $ABO_3$  perovskite crystal structure for: (a) cubic, high temperature, paraelectric phase and (b) tetragonal, room temperature, piezoelectric/ferroelectric phase. Most ferroelectrics exist in a paraelectric form at higher temperatures and transform into a non-centrosymmetric phase on cooling below a characteristic temperature, the so-called *Curie Temperature*,  $T_c$ .

For instance, that is the case for barium titanate ( $BaTiO_3$ ): in the high temperature paraelectric *cubic phase*, the central Ti atom serves as an inversion center. However, at a temperature lower than a critical temperature (called Curie Temperature), the material transforms into a *tetragonal phase*, where positively charged  $Ba^{2+}$  and  $Ti^{4+}$  ions are displaced with respect to the negatively charged  $O^{2-}$  network and define a polar axis. Hence, the tetragonal deformation determines the direction of the spontaneous polarization. The magnitude of the spontaneous polarization ( $\mathbf{P}_s$ ) is related with the surface charge density ( $\sigma$ ) present on the polar surfaces (perpendicular to the polar axis).

A temperature change induces a change in the distribution of the surface charges and thus of the resulting spontaneous polarization. This effect is called *pyroelectric effect*<sup>4</sup>.

It is not only the existence of spontaneous polarization alone (which is the signature of a *pyroelectric* material), but the fact that it can be switched, i.e. inverted or re-oriented by an external electric field that defines a *ferroelectric* material. Indeed, the main feature that defines and distinguishes ferroelectrics is the “*switchability*” of their polarization, i.e. the fact that in *ferroelectrics* the direction of the polarization can be reversed or re-oriented by the application of an external electric field. The orientation of the spontaneous polarization remains in that state, which is stable, as long as no other external electric field is applied to change it again. As a result, the polarization of ferroelectrics shows a *hysteretic* behavior or a *hysteresis* when the applied electric field is cycled from negative to positive and back (as shown in fig. 5.3) and its value in any point will be given by:

$$P(E) = P_s(E) + \epsilon_0(\epsilon-1)E \quad (5.3)$$

with  $\epsilon$  the relative dielectric permittivity. As it can be seen on Fig. 5.3(a), the total polarization in the absence of an external electric field within a single ferroelectric domain equals thus the spontaneous polarization  $P_s$ .

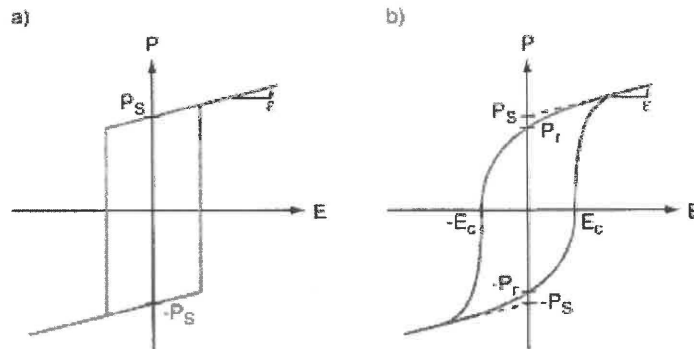


**Figure 5.3** (a) Hysteresis loop of an ideal ferroelectric domain. (b) Hysteresis loop of a real ferroelectric material [11].

In a more realistic case of a ferroelectric with several domains having slightly different behavior, the loop is less square. This is due to the presence of nucleation centers in each domain, which induce an earlier or later switching of this particular domain (as shown in

<sup>4</sup> From the Greek word “*pyros*” which literally means fire

figure 5.3.b). In this case, the spontaneous polarization is obtained by extrapolating the polarization at high electric field linearly down to zero fields<sup>5</sup>.

The polarization remaining after the disappearance of the external electric field is called *remanent polarization* ( $\mathbf{P}_r$ ). It is worth mentioning that the remanent polarization is not a material parameter, as it would be for the spontaneous polarization.  $\mathbf{P}_r$  depends on the history of the sample, e.g., on the strength of the last electric field used for poling. The electric field at which the polarization changes sign (at which the switching occurs in an ideal single ferroelectric domain) is called *coercive field* ( $\mathbf{E}_C$ ).

The electric displacement  $\mathbf{D}_i$  for a ferroelectric takes the form:

$$\mathbf{D}_i = \varepsilon_0 \varepsilon_{ij} \mathbf{E}_j + \mathbf{P}_S \quad (5.4)$$

In practice, it is useful to relate the piezoelectric coefficients to the local spontaneous polarization ( $\mathbf{P}_S$ ). For most ferroelectric materials, the paraelectric phase is centrosymmetric, which leads to the disappearance of the linear piezoelectric coefficients. For the ferroelectric phase which is nonlinear, the piezoelectric coefficients are third-rank tensors given by:

$$d_{im} = \varepsilon_{ij} Q_{mjk} P_{S k} \quad (5.5)$$

where  $Q_{ijk}$  are the polarization-related *electrostrictive coefficients* and  $\varepsilon_{ij}$  the linear dielectric tensors. Detailed explanations and the calculation formalism used for defining these coefficients are given in [12].

For the particular case of a tetragonal symmetry where the axis “3” is the polar axis, the 18 independent components of the piezoelectric tensor significantly reduce and only three different components remain:

$$\circ \text{ the parallel component } d_{33} = 2\varepsilon_{33} Q_{33} P_{S 33} \quad (5.6 \text{ a})$$

$$\circ \text{ the perpendicular component } d_{31} = 2\varepsilon_{33} Q_{13} P_{S 33} \quad (5.6 \text{ b})$$

$$\circ \text{ the shear component } d_{15} = 2\varepsilon_{11} Q_{44} P_{S 33} \quad (5.6 \text{ c})$$

Since the spontaneous polarization  $\mathbf{P}_S$  and the piezoelectric coefficient  $\mathbf{d}$  are related (equation 5.5 above), when *piezoresponse force microscopy* measurements are performed, the existence of a hysteresis for piezoelectricity is equivalent to the existence of a polarization hysteresis.

---

<sup>5</sup> This is valid if the crystal is in a monodomain state at high fields; more precisely the extrapolated value is referred to as saturation polarization ( $P_{sat}$ )

Therefore, a local piezoresponse hysteresis loop is a clear proof that the spontaneous polarization has indeed been switched. In the “z-mode” of piezoresponse force microscopy, the coefficient  $d_{zz}$  is evaluated, i.e.  $d_{33}$ , if the film is oriented with its axis “3” normal to the surface. The absolute value of the polarization can be estimated if the *electrostrictive* coefficient  $Q_{33}$  and the dielectric constant  $\epsilon_{33}$  are known. While it was deduced for a single crystal, this relationship may be considered a good approximation for the *effective* values of the quantities involved [13]

### 5.3 Ferroelectric nanostructures and size effects

The synthesis of thin-films and structures of novel complex oxides is currently advancing in two main directions: (i) an increase in the complexity of the functional materials being deposited and investigated, resulting from expanding the search for materials with better functionality to more complex materials, and (ii) the reduction of the structures typical dimensions - including the films thickness, but also and mostly, the lateral dimensions - while trying to preserve their functionality, or determining critical dimensions under which the properties of interest are drastically changing, either disappearing (i.e. “size effects”) or leading to new interesting phenomena at the nanoscale (i.e. “nano” aspect of nanomaterials and nano-structured materials).

Ongoing advances in science and technology of perovskite-type oxides showing piezoelectricity and ferroelectricity [14] have resulted in the development of structures and devices with the length scales of several hundred nanometers [15-17]. In the particular case of ferroelectric materials, theoretical predictions suggest that, due to an increasing role of the depolarization field and the weakening of long range cooperative interactions, which are the driving force for ferroelectricity, the latter is supposed to disappear below a critical size and these calculations suggest a material-dependent critical thickness and correlation volume (e.g. 2.4 nm for a  $\text{BaTiO}_3$  thin film between two metallic  $\text{SrRuO}_3$  electrodes) [18]. Experimental studies proved that ferroelectricity exists in ultrathin (4nm)  $\text{Pb}(\text{Zr},\text{Ti})\text{O}_3$  (PZT) epitaxial films [19] and ferroelectricity was observed in  $\text{BaTiO}_3$  films of about 5 nm thick [20]. Other, theoretical studies on size effects estimated the minimum volume at which the polarization and the ferroelectric

properties should vanish (critical volume) to be about  $1000 \text{ nm}^3$  [21]. Scaling the structures dimensions down to the range where ferroelectric materials start to show a pronounced size effect has brought along the necessity to study their ferroelectric properties very locally, at the nanoscale. The “size effect” in ferroelectrics, induced by the reduction in the sample geometrical dimensions, can result for instance in a decrease of the remanent polarization value, of the dielectric permittivity or in the phase transition temperature, in an increase in the coercive field, or in changes in the domain structure, among other phenomena [9].

The development of material processing techniques that allowed fabrication of various nanoscale ferroelectric structures, such as ultrathin epitaxial films [22], nanoscale capacitors [23], nanotubes [24] or nanorods [25] has been tremendously important for investigating the scaling behavior of ferroelectrics. Once the techniques to fabricate such nanostructures are established, the nanostructures obtained can be used for studying the intrinsic size effects in ferroelectrics as well as for addressing technologically important issues such as processing damage, effects of the grain size, of the aspect ratio, the edge effects, or the effects of interfacial strain, of domain pinning and of imprint [9]. In this context the development of scanning probe microscopy - especially of piezoresponse force microscopy (PFM) - into a powerful tool for high-resolution ultra-local characterization of ferroelectrics, offered an unprecedented and unrivaled opportunity for imaging the ferroelectric domain structures at the nanoscale [26]. SPM has also opened new avenues in nanoscale domain patterning, for instance in ferroelectric lithography [27] or applications as high-density data storage [28].

Along the way, various methods including both top-down and bottom-up approaches have been tested and employed to produce nanoscale ferroelectric structures. The ultimate goal of all these novel processing approaches is to deliver high-resolution, large-scale arrays of functional structures, precisely registered on the substrate of choice, with comparable (or even exceeding) performances and cost-effectiveness than the standard photolithographic processes used nowadays.

A conventional patterning process, based on usual resist lithography followed by etching of the oxide film is fraught with severe problems, especially for ferroelectric thin films. Contamination and side-wall redeposition are altering the polarization switching

(even for features as large as in the micrometer range), and constitute challenging issues to be overcome in the patterning of complex ferroelectric thin films. Structuring piezoelectric/ferroelectric ceramic thin films for application in micro-sensors, -actuators or MEMS is presently the subject of an extensive research, as for instance the improvement of the standard micromachining processes used to fabricate lead zirconate titanate PZT piezoelectric thin film devices [29]. The top-down methods that are currently used in nanotechnology provide high-precision positioning and size control but are often limited in resolution. For instance considering a prospective 1 Gbit FeRAM memory architecture, a “memory cell” can not be larger than  $150 \times 150 \text{ nm}^2$  and its ferroelectric capacitor active area will thus probably have a lateral dimension of about 100 nm [30]. Such features are challenging to realize even with today’s advanced lithography, especially since thin-films are prone to processing damages induced by the often time-consuming sequential nature of the many process involved.

Alternatively, the bottom-up strategies, either by physical or chemical self-patterning of complex oxides [31,32] promise the fabrication of much smaller features than those achievable with top-down techniques. Self-assembling processes, governed by growth processes similar to those found for Ge islanding on Si (001) surfaces, overcome the low throughput and processing damage of the conventional patterning methods [33]. Nevertheless, they suffer from poor registration, and to achieve a certain organization requires a prior substrate patterning, which in turn involves an additional top-down processing [34]. Appealing for scientific purposes, bottom-up approaches are therefore presently still ineffective and unreliable and not yet ripe to be implemented for new technologies.

In the following, we briefly review some of the top-down processing methods used to realize ferroelectric nano-cells and arrays thereof that we consider representative of the state of the art as well as relevant to the subject of our studies.

Focused ion beam (FIB) [35] and maskless electron beam direct writing (EBDW) [30] have been reportedly used for fabrication and patterning of ferroelectric structures. Ganpule et al. using a focused beam of Ga ions (FIB), produced nanoscale ferroelectric capacitors by “cutting out” an isolated island from a Pt-coated  $\text{SrBi}_2\text{Ta}_2\text{O}_9$  (SBT) [23] and from a Pt-coated Nb-doped PZT [36] ferroelectric thin film. Optimizing the process,

it was possible to reach lateral dimensions as small as  $70 \times 70 \text{ nm}^2$ . The ferroelectric properties of as-processed capacitors showed very weak hysteresis behavior right after processing, apparently due to the Ga-induced damages, and an annealing process at  $600^\circ\text{C}$  was necessary to recover its properties. Still, the presence of a permanently damaged 10 nm thick layer has been reported.

The nano-capacitors obtained were used to study the intrinsic size effect in SBT and PZT:Nb. Nagarajan and co-workers reported that the FIB-fabricated capacitors milled down to the bottom electrode exhibited a higher piezoelectric response than the nano-capacitors where only the top electrode was milled [37]. This result was attributed to the reduction in the in-plane constraints in the isolated cells compared with the continuous film, and thus could not be considered as the intrinsic size effect.

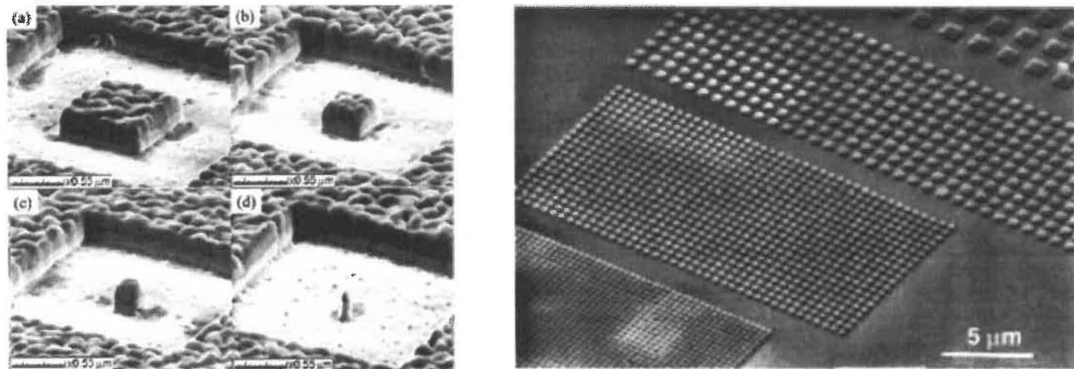


**Figure 5.4** Ferroelectric nanostructures: (*left*) Pt-coated  $\text{SrBi}_2\text{Ta}_2\text{O}_9$  (SBT) test structures fabricated by FIB milling in the size range  $1\mu\text{m} \times 1\mu\text{m} - 0.25\mu\text{m} \times 0.25\mu\text{m}$ ; in (d)  $70 \text{ nm} \times 70 \text{ nm}$  cell [ref 23]; (*right*) Test patterns of (SBT) cells with lateral dimension between  $1 \mu\text{m}$  and  $0.125 \mu\text{m}$  prepared in the corresponding metalorganic film by e-beam direct writing [ref 30]

An increase in the piezoelectric constants of the nano-size PZT single crystals was also reported by Buhlmann and co-workers [38]. The processes, consisting in e-beam lithography of a PMMA coated PZT epitaxial layer to first fabricate a Cr hard mask by lift-off, and then use reactive ion etching (RIE) to pattern the PZT, lead to cells with lateral size from  $1\mu\text{m}$  down to  $100\text{nm}$ . The piezoelectric response of the islands showed a sudden increase for structures with lateral size below  $300 \text{ nm}$ . The phenomenon was explained by a decrease in the fraction of “*a*-domains” (with polarization ‘in plane’) with respect to the *c*-domains (with polarization ‘out-of-plane’) upon scaling the structure size, resulting again in reduced mechanical constraint, hence not an intrinsic size-effect. The coercive field was found to be size-independent.

E-beam direct writing (EBDW) used by Alexe and co-workers [7,30] for fabrication of ferroelectric nano-cells, eliminates the drawback of  $\text{Ga}^+$ -induced damaging produced during FIB patterning while allowing for patterning structures with similar dimensions but on a much larger scale. In this approach, a metalorganic film deposited on a conductive substrate is irradiated locally with an electron beam (direct writing). The metalorganic precursor film is subsequently developed and the unexposed areas dissolved. Annealing and crystallization transforms the produced metalorganic mesas into crystalline ferroelectric cells of well-defined shape and dimensions. Using this method, arrays of  $100 \times 100 \text{ nm}^2$  cells of PZT and SBT have been successfully fabricated [39].

Although being slow, ion and electron beam-assisted fabrication, proved to be useful in producing nanoscale ferroelectric structures, suitable for studying the intrinsic size effects in ferroelectrics. Although the realizations of nanostructures were successful, one of the biggest challenges was to distinguish between the intrinsic and extrinsic size effects and the damage effects caused by the fabrication process.

Another approach has been investigated by Harnagea and co-workers [40] who prepared ferroelectric PZT cell arrays using a combination of chemical solution deposition and nanoimprint lithography (NIL). A precursor film chemically spin-coated on a conductive substrate was patterned by pressing a nanostructured mold into it. The molds consisted of either electrochemically prepared macroporous silicon or of  $\text{SiO}_2$ -covered silicon wafers with stamp motifs patterned by photolithography and RIE. After removing the mold, the precursor was crystallized into a ferroelectric oxide by drying and annealing. Arrays of ferroelectric cells with lateral sizes down to 250 nm were successfully prepared and their functionality was demonstrated by PFM (fig. 5.5).

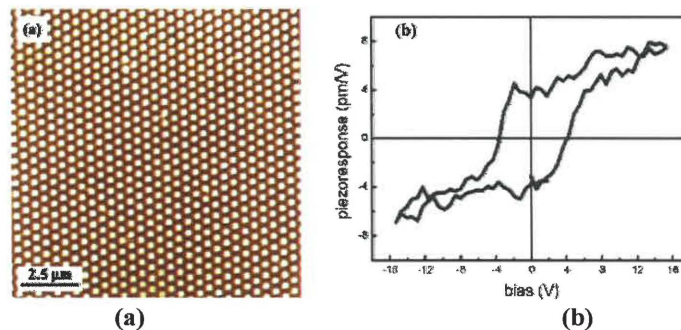


**Figure 5.5** AFM topography image of an array of ferroelectric PZT cells on Nb doped  $\text{SrTiO}_3$  substrate prepared by imprint lithography. (b) Piezoelectric hysteresis loop of a single ferroelectric cell proving its functionality.

More recently, parallel patterning of ferroelectric nanostructures, via a reduced number of processing steps compared with the conventional photolithography or other alternatives techniques has been reported. Attempts to deposit perovskite-type oxide materials through masks made from monolayers of latex spheres [41], “gold nanotube-membranes” [42] and, in our group, through silicon nitride, solid-state, reusable stencils [43] have been undertaken using pulsed laser deposition at room temperature and subsequent annealing. The ferroelectric properties of those structures have been confirmed in all cases by PFM studies.

The latter technique has been deemed to be extremely promising and has been selected for further study and development. In the following sections we describe in detail the work undertaken in our group to fabricate and pattern nanostructures of ferroelectric and multiferroic complex oxides via PLD nanostenciling, both for room temperature and for high temperature growth regimes. The challenges related with the characterization of the ordered arrays of functional oxide nanostructures obtained will be equally addressed.

## 5.4 Nanostenciling of piezoelectric / ferroelectric materials

Our primary goal of assessing the nanostenciling approach as a new unconventional route for nanofabrication and patterning of various functional materials prompts to test it over more complex materials such as *oxide ceramics*. The experiments aimed in the first place to assess if nanostenciling can become a *general-purpose* nanoscale patterning technique offering both high resolution and unique flexibility for the combination *deposited material/substrate*. Unlike other processes reported for oxides nanostructuring, we do not process or modify the substrate, but *selectively* deposit material, directly, by interposing the *nanosieve* between the substrate and the deposition source. Simultaneously, there is an inherent control of the locations where the nucleation starts and where the structures’ growth will further take place, provided an accurate position of the stencil with respect to the substrate. A direct copy of the apertures opened in the stencil is realized on the substrate by “forcing” the material to pass through the former providing thus a *parallel* way to fabricate ordered arrays of islands.

We show that this selective deposition can be realized even with materials as complex as perovskite-oxides, both at room-temperature and at high-temperature. *3D functional structures* are directly generated, thus further etching steps usually employed in structuring of thin films, are eliminated. The patterned structures of ferroelectric materials are probed locally by scanning force microscopy in piezoresponse mode to check their individually functionality.

### 5.4.1 Patterning of barium titanate (BaTiO<sub>3</sub>)

Barium titanate (BaTiO<sub>3</sub>) is a typical example of an oxide that crystallizes in the perovskite structure (Fig.5.1). In the high-temperature limit (above  $T = 393\text{K}$ ) BaTiO<sub>3</sub> is paraelectric (non-polar) and possesses a cubic crystalline structure ( $a = 3.996 \text{ \AA}$ ). It has three ferroelectric phase transitions as the temperature decreases: cubic to tetragonal at 393 K, tetragonal to orthorhombic at 278 K, and orthorhombic to rhombohedral at 183 K. The most important properties of BaTiO<sub>3</sub> as a function of temperature are summarized in Appendix A.

As substrates onto which we patterned the structures, we used (100) oriented single crystals of strontium titanate (SrTiO<sub>3</sub>)<sup>6</sup>. SrTiO<sub>3</sub> has also a perovskite structure and is one of the few “*titanates*” with a cubic phase at room temperature. SrTiO<sub>3</sub> shows a structural phase transition from cubic to tetragonal at 110 K and to orthorhombic at 65 K. SrTiO<sub>3</sub> is an excellent substrate for the epitaxial growth of various oxide-based thin films. When doped with niobium (Nb:SrTiO<sub>3</sub>), it is electrically conductive and can be used also as a “bottom” electrode.

It is worth to mention that, the main advantage of PLD to transfer material congruently<sup>7</sup> from a bulk ceramic target (made out of several elements) onto the substrate of choice it is not always straightforward. Finding the optimal deposition parameters that result in films with highest crystallographic quality and best functional properties is yet an empirical process. Typically, complex oxide thin films are deposited at high substrate temperature, and in oxygen ambient, in order to facilitate the reorganization of the atomic

---

<sup>6</sup> Alternatively, (100)-oriented silicon and platinum-coated silicon were also used as substrates for several stenciling trials

<sup>7</sup> i.e. maintaining and transferring the ratio of the various elements composing the target onto the film

species into the desired crystal structure via increased surface mobility of the ad-atoms while preserving the stoichiometry [44]. The optimal substrate temperature usually falls in a narrow window of crucial importance, and governs both the nucleation and the growth of the deposited film.

The parameters used for epitaxial growth of ferroelectric *continuous* thin films provide a starting reference but do not necessarily correspond to the exact optimal conditions for the direct patterning of ordered islands of the same material, through stencils. For instance, an excessive O<sub>2</sub> background pressure in the deposition chamber (often required for the successful continuous film growth) may not be optimal for deposition through the nano-shadow-mask because of the scattering of the ablated species by the ambient gas before they reach and pass through the apertures thus hindering the accurate replication of the shape and pattern of the nano-apertures drawn in the stencil.

#### 5.4.1.1 Room-temperature patterning regime

To reduce the complexity of the growth process and in particular to “help” the stenciling process, first trials were carried out depositing BaTiO<sub>3</sub> through stencils at room temperature (RT) and in vacuum. To obtain the right crystal structure, the samples were then annealed in an O<sub>2</sub> atmosphere, either by a conventional process or by rapid thermal annealing (RTA).

In preliminary experiments we estimated the BaTiO<sub>3</sub> deposition rate, depositing continuous thin films with different thicknesses<sup>8</sup> by varying the number of laser ablation pulses, for a certain target-substrate distance. Their thickness was checked by profilometry (Fig. 5.6a). We observed that the as-deposited films are amorphous at room temperature and crystallize into the ferroelectric phase upon thermal treatment in an O<sub>2</sub> flow at temperatures above 600°C, leading to polycrystalline thin films (fig. 5.6b).

Later on, this approach (i.e. RT deposition followed by ex-situ annealing) was used in related studies focused on the preparation of separated BaTiO<sub>3</sub> structures.

---

<sup>8</sup> Assuming a linear dependence of the mass of the deposited films on the number of laser ablation pulses

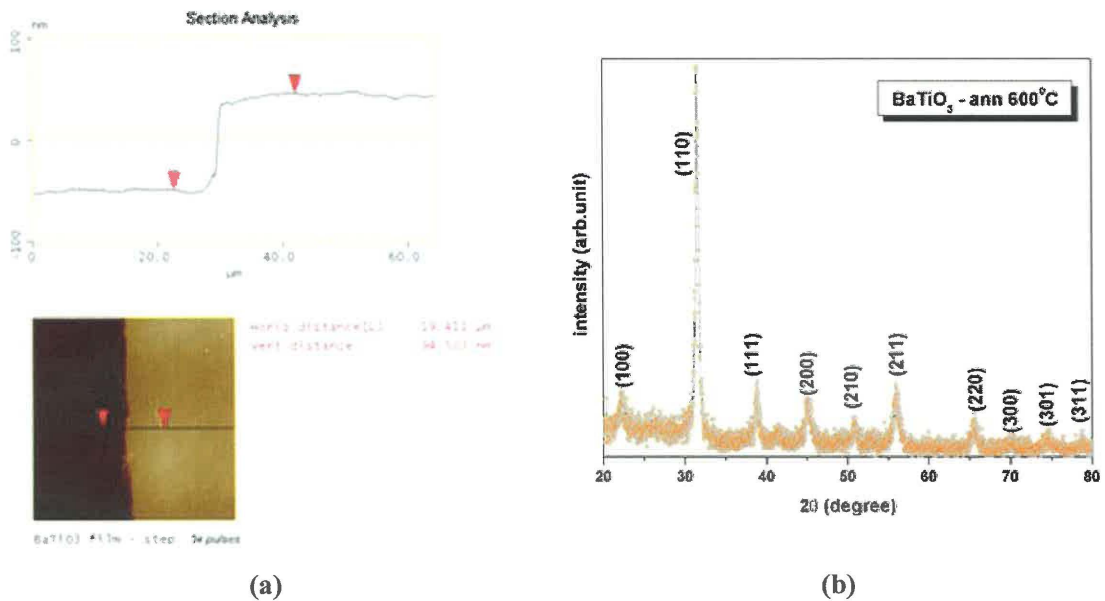


**Figure 5.6** BaTiO<sub>3</sub> film deposited at room temperature and in vacuum for 3000 laser pulses at a distance target-substrate of 7.5 cm. **(a)** AFM profilometry; deposition rate estimated to 0.3Å/pls. **(b)** XRD spectra recorded in grazing-incidence mode for a polycrystalline film of BaTiO<sub>3</sub> deposited at room temperature and annealed at 600°C, 1h in O<sub>2</sub> flow.

By depositing at room temperature continuous amorphous layers with thickness close to a certain threshold or critical thickness (~2 nm) and subsequently annealing, the BaTiO<sub>3</sub> continuous film breaks-up in islands and we obtained BaTiO<sub>3</sub> islands of 35-50 nm that were exhibiting ferroelectricity as proven via piezoresponse force microscopy [45]. Nevertheless, in this case, their position could not be controlled.

A first set of BaTiO<sub>3</sub> stenciling experiments was conducted using LIL-based stencil masks, with built-in 500 nm thick SiN nanosieves with circular apertures. These stencils have hexagonal arrays of pores (350 nm in diameter) with a periodicity of either 1.6µm or 700nm and are patterned on 12 to 14 free-standing, low-stress (LS-SiN) membranes (2 mm in length and 100 µm in width each, 100 µm apart). The SiN membranes are prepared on single crystal Si(100) wafers 380 µm thick and the stencil's dimension is 5×5 mm<sup>2</sup> with an active area of ~2×2.7 mm<sup>2</sup>. The stencils were mechanically clamped and temporarily fixed onto Nb-doped (100)-oriented SrTiO<sub>3</sub> substrates. The gap between stencil and substrate should be as small as possible (ideally 100 nm or less) and must be kept uniform over the whole shadowed area. Nevertheless, the stencil-substrate spacing usually varies due to substrate surface irregularities, dust

particles, roughness or bending of the membrane layer. Even with the contact fixture we used (stencil pressed against the substrate), a gap between stencil and substrate can not be avoided. The assembly substrate-stencil was mounted in the vacuum chamber of a PLD system, in front of a dense stoichiometric BaTiO<sub>3</sub> ceramic rotating target. A KrF Lumonics PM-800 excimer laser (radiation with  $\lambda = 248$  nm, pulse duration = 15.4 ns) was employed for ablation with a 45° incidence angle on the target and a laser fluence of 2 J/cm<sup>2</sup>. Depositions were carried out at room temperature, in vacuum at  $1 \times 10^{-5}$  mbar ( $7.5 \times 10^{-3}$  mTorr), with a laser repetition rate ranging from 5 to 10 Hz, and a target-substrate distance of 6.5-7 cm. Once the deposition was completed the stencils were unclamped and simply “lifted-off” (separated) from the substrate.

Rapid and parallel fabrication of ordered nanostructures of BaTiO<sub>3</sub> was achieved in a single deposition step, over the whole sieve areas. Fig. (5.7a) displays an SEM micrograph detail from a LS-SiN nanosieve with pores of 350 nm in diameter and a 700 nm pitch used during the depositions and fig. (5.7b) shows the well-ordered, dome-shaped, as-deposited structures, obtained via stenciling through the latter.

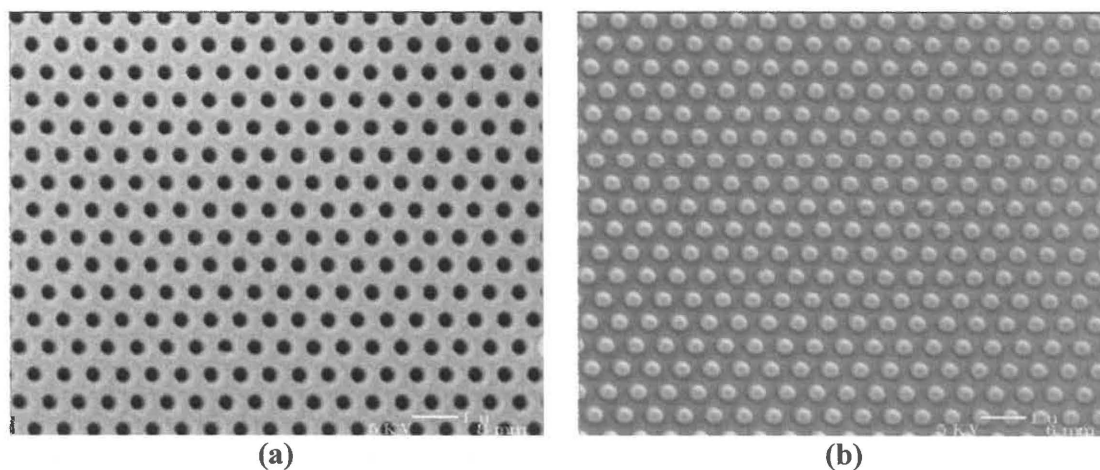


**Figure 5.7** SEM micrograph of a LS-SiN sieve (a) and ordered arrays of BaTiO<sub>3</sub> structures obtained by deposition through it (b); scale bar 1 micron

The broadening of the bottom width of the structures, caused by the shadow-effect of the mask, and visible in the AFM images is an indication that the stencil is not pressed tightly enough against the substrate. Besides this geometrical effect, the structures appear larger in the AFM image due to the tip-surface convolution (~ 400 - 425 nm, i.e. 15 - 20% larger than the nominal diameter of the stencil’s apertures). Thus a more accurate estimation of the “blurring” effect on the structures replication can be in

principle obtained using top-view scanning electron micrographs. The SEM micrograph from figure 5.8 reveals structures with basis enlarged to 385 – 390 nm and thus suggesting an overall base broadening of ~ 35 - 40nm, i.e. ~ 10% larger than the nominal value of the apertures.

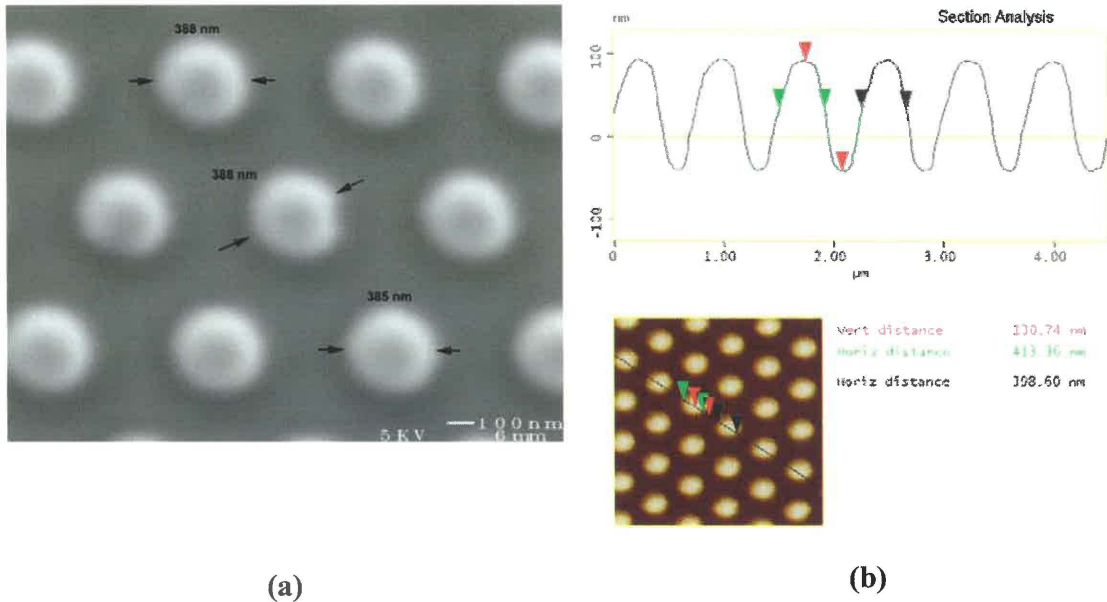
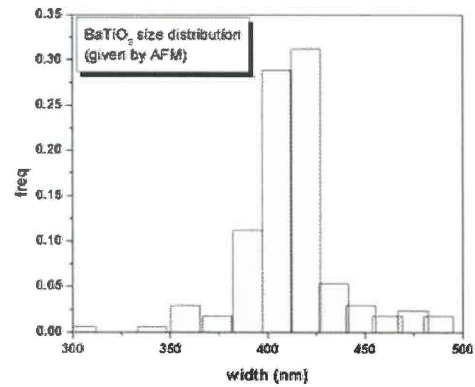


**Figure 5.8** (a) SEM micrograph detail of BaTiO<sub>3</sub> structures patterned directly through 350 nm wide apertures; and (b) AFM section profile revealing larger widths for the measured structures due to the tip-surface convolution during scanning; (c) BaTiO<sub>3</sub> size distribution given by AFM measurements



(c)

Using the formula that gives the broadening of a structure in function of the geometrical parameters used for deposition (eq. 3.1 chapter 3), including the target-substrate distance of 6.5 cm and the laser spot area on the target of 0.02 cm<sup>2</sup>, we can estimate the gap present during this experiment to be about 3.25 microns. Nevertheless this is just an approximate value which is not applicable to all other samples prepared, since the stencil attachment has been realized manually for each deposition trial.

In the particular case of PLD, the height of the as-deposited ( $\text{BaTiO}_3$ ) nanostructures can be controlled either by varying the number of laser ablation pulses on the target or by varying the target-substrate distance. Since the broadening of a structure replicated through an aperture decreases with the target-substrate distance, it is desirable to maintain a large distance substrate-target. Thus in this work we varied the number of ablation pulses in order to control the height of the structures (fig. 5.9) showing the versatility of stenciling in defining structures with different aspect ratios.

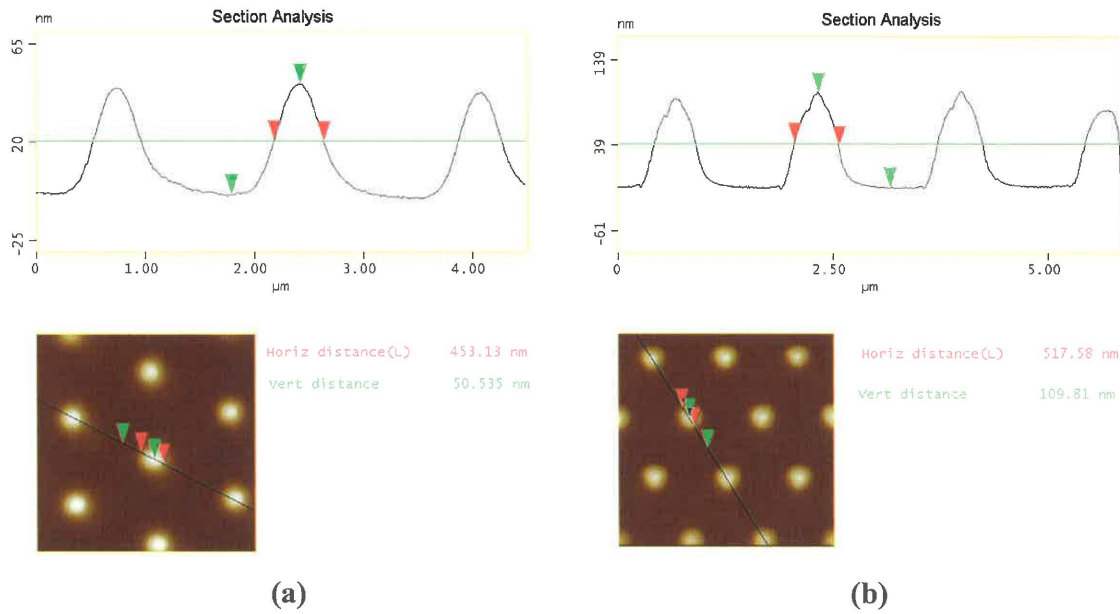


**Figure 5.9** AFM topography and typical section profiles for  $\text{BaTiO}_3$  arrays obtained for: **(a)** 1500 laser ablation pulses (50nm tall structures) and **(b)** respectively 3500 pulses (~100 nm tall structures) for the same distance target-substrate when deposited through 350 nm diameter apertures with a 1.6  $\mu\text{m}$  pitch.

For the sieves with 350 nm diameter circular holes, the transfer efficiency was found of being above 80% of the equivalent film thickness deposited for an equal number of pulses, in the same conditions. After consecutive depositions through the same stencil the structures are getting smaller in lateral size yet preserving their periodicity and registration (fig. 5.10), i.e. the clogging effect starts to manifest.

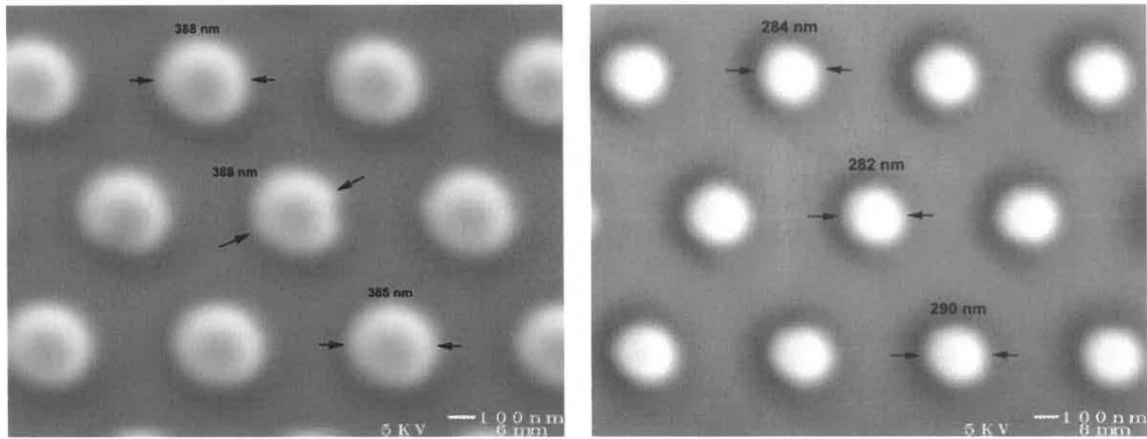


**Figure 5.10** SEM micrographs of BaTiO<sub>3</sub> patterned structures obtained with the same stencil used in consecutive depositions. 30% shrinkage in structures lateral size is observed after 8 depositions.

The progressive clogging (decrease of the hole size) of the mask's apertures during deposition represents one of the intrinsic drawbacks of nanostenciling. Previous studies, estimated that a circular hole will clog after *evaporating* a thickness equivalent to approximately 5 times its diameter [46]. However, practice shows that this strongly depends on the deposited material, on the mask material and on the beam collimation. For the particular case of BaTiO<sub>3</sub> we controlled the PLD process, reusing the stencils for a number of depositions giving a deposited thickness equivalent to 3.5 times the diameter of the apertures. At that point 30% shrinkage in lateral size is observed for the replicated structures (fig. 5.10).

For the experiments related to this work, we reused the same stencil with different target materials: e.g. metals such as Pt, Cr, CoNi or even other oxides such as lead zirconate-titanate (PZT). Gradually, the sieves suffered structural damages due to repeated mechanical clamping on the substrates and the stencil collapsed before we observed a complete clogging of the holes.

The choice of the physical vapor deposition technique used in combination with nanostenciling plays an important role and the control of the interaction of the material to be deposited, with the membrane apertures, remains a matter of further examination. Finding cleaning recipes for the stencils, such as selective etching of the material deposited on the sieves, constitute an issue of high interest as well, however, due to time considerations, this has not been investigated in this work.

The room-temperature as-deposited BaTiO<sub>3</sub> structures are amorphous and we used post-deposition annealing above 650 °C, in an O<sub>2</sub> flow, to crystallize them. After annealing, the individual structures loose their dome-like shapes and break into several grains of various crystallographic orientations. The shape change is attributed to the nucleation and growth of anisotropic BaTiO<sub>3</sub> crystallites during post deposition annealing<sup>9</sup>. The topography of the annealed structures, investigated by AFM in tapping mode is presented in (fig. 5.11).

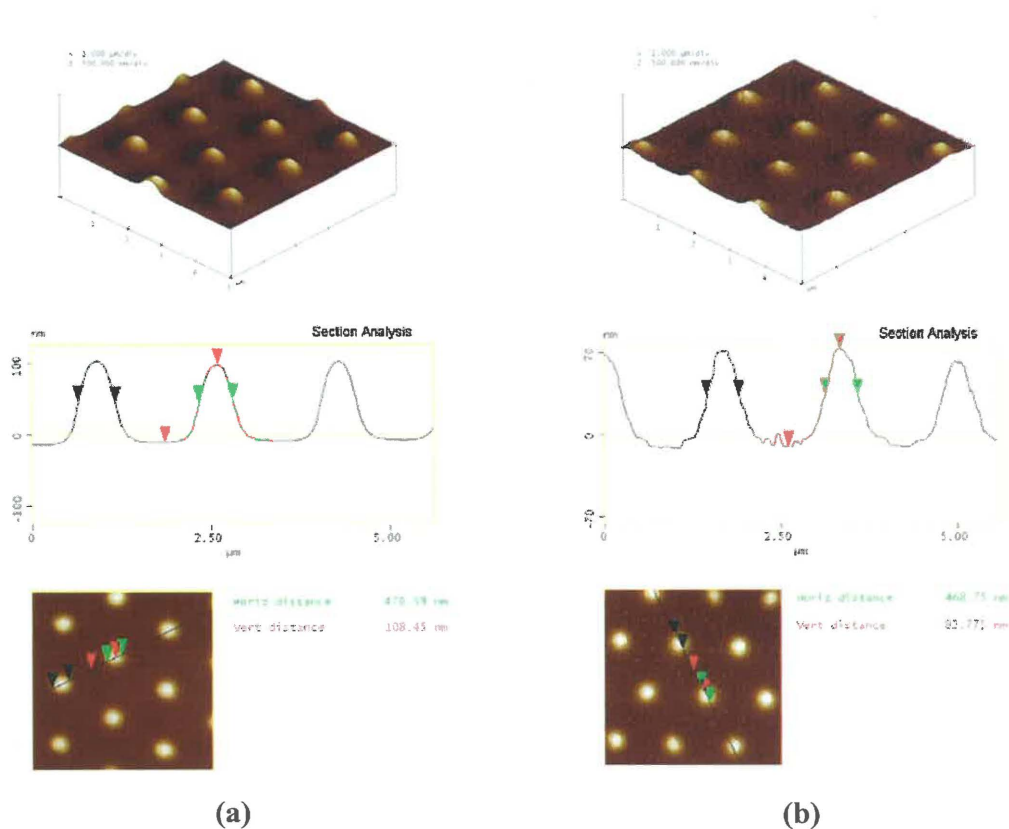


**Figure 5.11** 3-D AFM topography and section profiles for: (a) BaTiO<sub>3</sub> patterned at room temperature and (b) BaTiO<sub>3</sub> after annealing at 900°C in O<sub>2</sub> flow. From the section-profile analysis we noticed there is a vertical shrinkage of the structures of about 25% while the lateral shrinkage is less than 1% after annealing.

X-ray diffraction in grazing incidence (GIXRD) configuration was used to investigate the crystalline phases present in the patterned structures and their quality. The patterns recorded at an incidence of  $\omega = 1^\circ$  incidence (fig. 5.12), indicate the presence of

<sup>9</sup> In some cases, due to an elevated gap stencil-substrate, the deposited material diffused in between the aperture sites and was noticeable only after annealing (e.g. small structures in fig. 5.11)

a polycrystalline phase very similar to the perovskite cubic phase with grains  $\sim 30\text{-}35$  nm in size<sup>10</sup>.

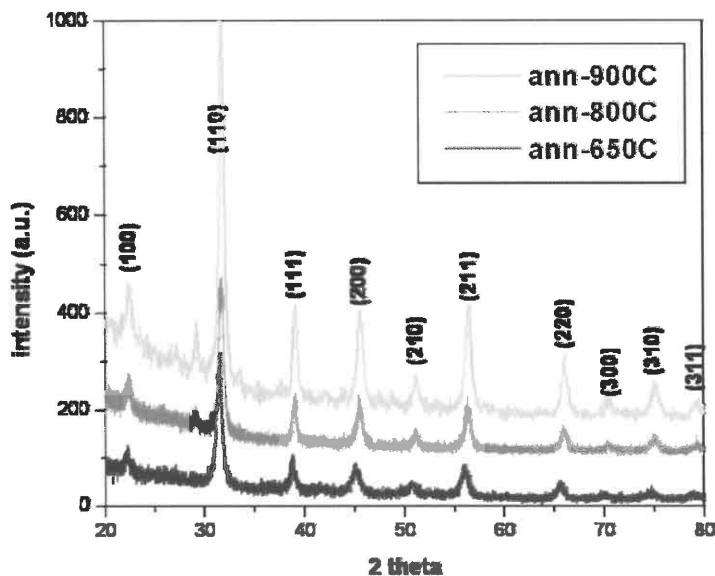


**Figure 5.12** Grazing incidence X-ray diffraction patterns for BaTiO<sub>3</sub> samples patterned at room temperature and annealed in O<sub>2</sub> at temperatures above 650°C; at higher annealing temperatures the narrow peaks indicate a better crystallization while foreign phases (e.g. barium oxide) start to appear.

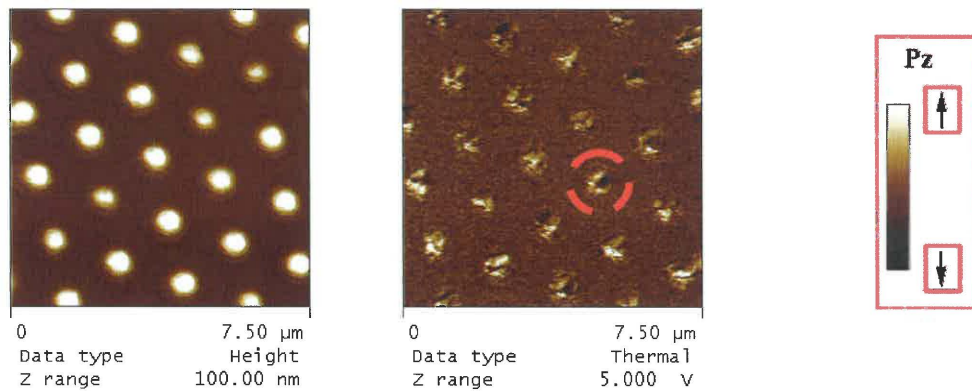
Polycrystalline fine grained BaTiO<sub>3</sub> thin films (sizes below 100 nm) were reported to exhibit weaker ferroelectric properties than larger grained films/ceramics or bulk single crystals [47] due to their reduced tetragonality. However, we succeeded in recording piezoelectric hysteresis loops from these individual structures, thus proving their ferroelectric nature.

Piezoelectric and ferroelectric properties of the obtained BaTiO<sub>3</sub> structures were probed locally by measuring the electric field induced converse piezoelectric effect. The basics of this experimental procedure were described in chapter 3 and a schematics of the setup employed is presented in Appendix B. Piezoresponse hysteresis loops were acquired by positioning PFM cantilever tip closer to the center of an individual nanostructure (i.e. closer to the highest topographical point observed in the AFM topography mode). The local piezoresponse signal was measured for DC bias voltages ranging from -10 V to +10 V superimposed on a small AC voltage (typical frequency 29

<sup>10</sup> The values were estimated using the Scherrer's formula and confirmed by AFM analysis.

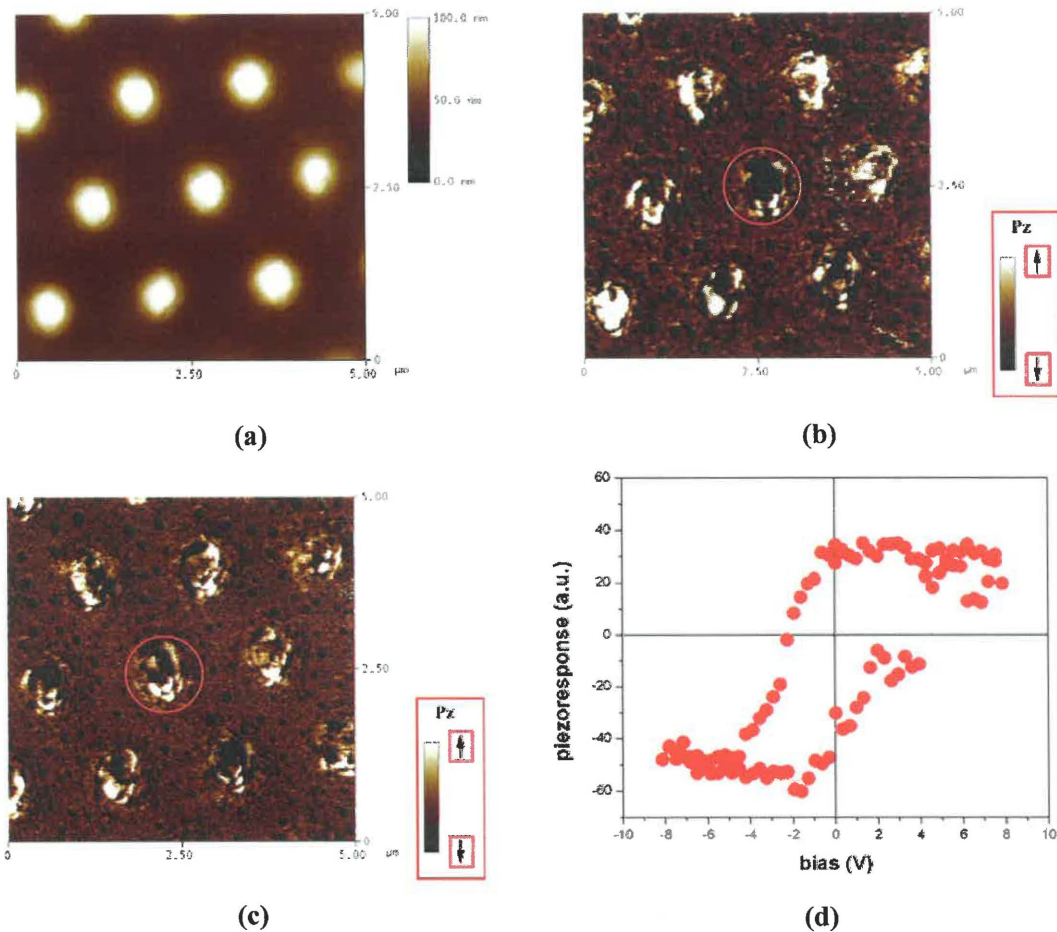
KHz; excitation amplitude 0.5 V) that practically should be smaller than the value of the coercive field necessary to switch the polarization of a structure. The local mechanical displacement generated was detected using the PFM tip and analyzed, using long integration times for the lock-in amplifier connected to the AFM via a Signal Access Module. The out-of-plane piezoelectric coefficient  $d_{33}$  was calculated according to the procedure given by Harnagea and Pignolet [48] and described in experimental chapter.

Figure 5.13 present the AFM topography (in contact mode) of BaTiO<sub>3</sub> patterned on a 0.1% Nb-doped SrTiO<sub>3</sub>(100) substrate with the *piezoresponse domain image* simultaneously recorded. The white regions in the *z-piezoresponse image* show that the dots have predominantly a *spontaneous polarization* oriented ‘upwards’ whereas the dark regions show a spontaneous ‘downwards’ polarization.



**Figure 5.13** AFM topography (left) and PFM domain image (right) of the BaTiO<sub>3</sub> arrays prepared at room-temperature and post deposition annealed at 900 °C [structures from fig 5.11]

The piezoresponse hysteresis loops recorded (see Fig. 5.14) reveals that the spontaneous polarization of the patterned BaTiO<sub>3</sub> structures can be switched and that they retain ferroelectricity despite the reduced tetragonality of their structure. The weak PFM signal – in this case the effective piezoelectric coefficient  $d_{33}$  was estimated to be 7 pm/V compared to  $d_{33} \sim 80\text{-}90$  pm/V in BaTiO<sub>3</sub> single crystal [49] - is attributed to the reduced tetragonality of the BaTiO<sub>3</sub> unit cell caused by the fine grain size of the nanostructures (~30-35 nm as detailed in footnote 10 on page 133). On the other hand, measurements of  $d_{33}$  coefficient reported for BaTiO<sub>3</sub> thin films, revealed values between 4pm/V and 50pm/V and were related with the orientation of the grains, strain or film thickness.



**Figure 5.14** (a)  $5 \times 5 \mu\text{m}^2$  AFM topography in contact mode, (b) and (c) PFM switching and (d) piezoresponse hysteresis loop recorded from individual structures

Being a non-invasive process, nanostenciling eliminates the doubts of extrinsic size effects i.e. due to damages occurred during the fabrication and patterning of the structures, thus the weak piezoelectric response is due to an intrinsic size effect induced by a reduced size of the  $\text{BaTiO}_3$  grains. Analyzing the domain structure, we noticed that in average, one domain extends over 2-3 grains. It is worth noticing here that our  $\text{BaTiO}_3$  structures were only slightly imprinted and the switched grains were stable for at least the time scale of several experiments (few days). The structures can be switched individually, exhibiting a clear piezoelectric hysteresis.

### 5.4.1.2 High-temperature patterning regime

A major goal pursued with nanostenciling of perovskite-type oxides has been to use this approach in order to achieve *epitaxially grown* complex oxide *nanostructures* (on appropriate substrates) in order to enable the study of the properties of this class of complex oxides at nanometer length scales. We therefore focused not only on achieving smaller structures but we investigate deposition parameters that will preserve their properties, namely that will both preserve the stoichiometry and will lead to a good quality crystalline structure. As mentioned previously, epitaxial thin films of complex oxides are usually obtained by the depositing materials at elevated temperatures and in an O<sub>2</sub> background atmosphere. Using stencils with the architectures presented in the previous section, we pursued the patterning of BaTiO<sub>3</sub> in various conditions according to the description provided in the table 5.1<sup>11</sup>. These experiments have been performed with the same stencils used during RT trials since solid-state SiN membranes are resistant to high temperature (up to 800°C).

**Table 5.1**

ID	Substrate	Temperature	Pressure [O <sub>2</sub> ] mTorr	Post-deposition annealing
BTO pattern I	Nb : STO (100)	620 °C	7.5 x 10 <sup>-3</sup>	N/A
BTO pattern II	Nb : STO (100)	620 °C	10	N/A
BTO pattern III	Nb : STO (100)	RT	7.5 x 10 <sup>-3</sup>	RTA – 700 °C
BTO film	Nb : STO (100)	615 °C	100	N/A

This time the stencil was kept at elevated temperature together with the substrate and the O<sub>2</sub> pressure was adjusted in the range 7.5 x 10<sup>-3</sup> mTorr - 10 mTorr. All the samples were prepared for the same number of laser ablation pulses (5000pls), using stencils with the same diameter of apertures (350 nm). Two samples were fabricated with stencils having periodic apertures spaced with 1.6 micron pitch (fig. 5.15 (a) and (b)). After deposition the samples were cooled down to room temperature, naturally, in a 150 mTorr O<sub>2</sub> background pressure.

<sup>11</sup> BTO film was prepared in optimal conditions reported in literature (i.e. high T and high O<sub>2</sub> atmosphere)

A comparison of the structural and functional (ferroelectric) properties of the high-temperature patterned structures with a third sample deposited *at room temperature* through a stencil with apertures with 700 nm pitch and annealed via a rapid-thermal process (RTA)<sup>12</sup> (fig 5.15 c and d) has been performed. The properties of a continuous epitaxial film (~100 nm thick) deposited in high O<sub>2</sub> atmosphere have been also investigated. In fig. 5.15 SEM micrographs show the characteristics of the ordered arrays of BaTiO<sub>3</sub> structures obtained in these particular conditions.

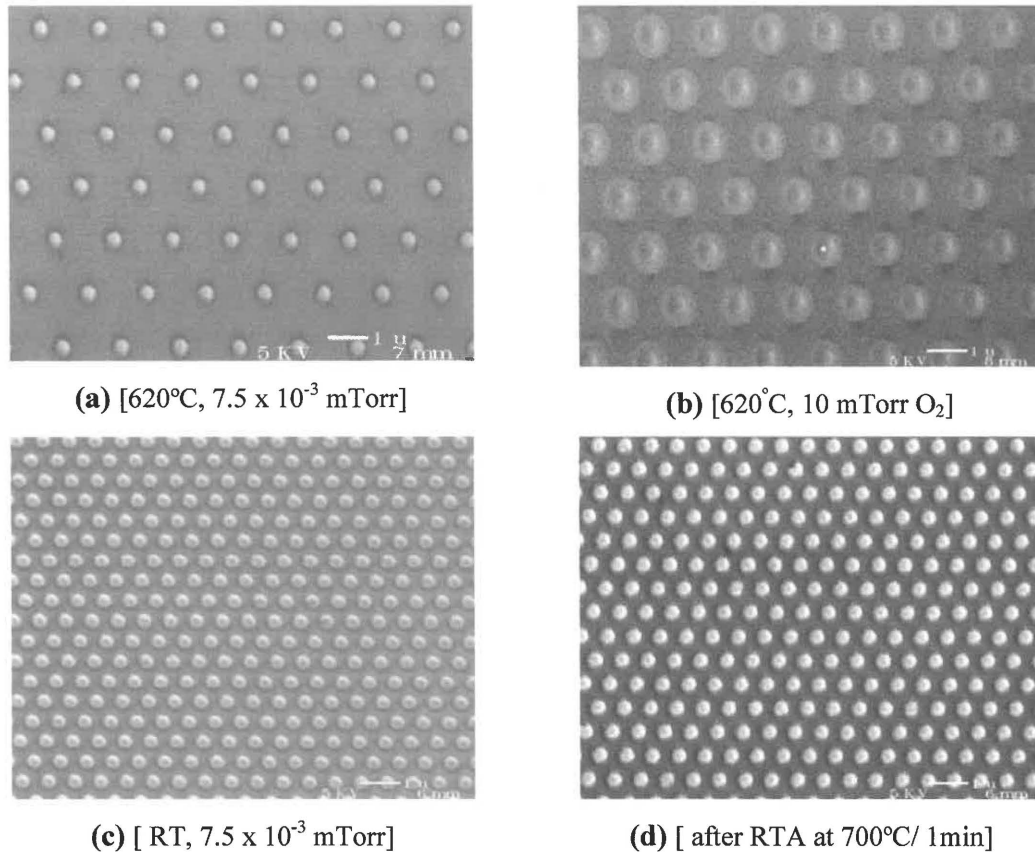


**Figure 5.15** SEM micrographs for the ordered BaTiO<sub>3</sub> arrays obtained in conditions described in table 5.1. (a) BTO pattern I; (b) BTO pattern II; (c) and (d) BTO pattern III before and after RTA annealing

The patterns obtained during the vacuum deposition exhibit the least broadening (issue discussed in the previous section). The ablated species, having the longest mean

<sup>12</sup> RTA process was performed in O<sub>2</sub> with the temperature ramped from 100 °C to 700 °C with 100 °C / sec and maintained at 700 ° for 60 sec.

free path, are not scattered by the time they reach the apertures of the membrane. A different situation is observed for the sample grown in 10 mTorr of O<sub>2</sub> in which case a rather large broadening of the structures bottom-width creates a distortion of the pattern and reduces the distance between the neighboring structures (Fig. 5.15b). For the case of the sample processed via RTA we see a shrinkage in lateral size similar to the one observed after a conventional thermal annealing process; however the crystallites are not very well defined indicating an incomplete crystallization (Fig. 5.15c and d).

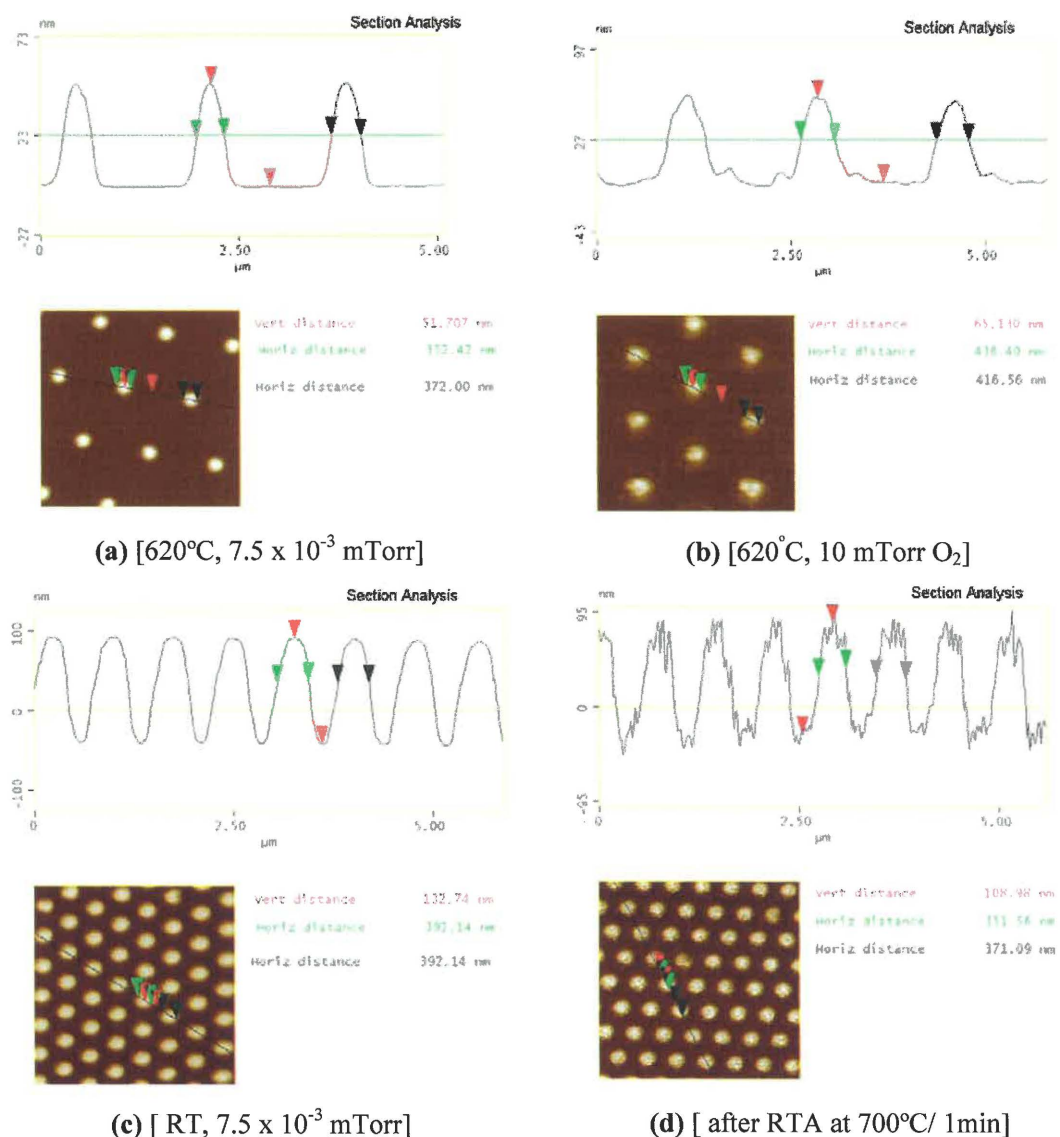


**Figure 5.16** AFM topography in tapping mode and section analysis for the structures showed in the SEM micrographs from fig. 5.15

To investigate the structural properties of these 3 samples deposited directly at high temperature, we performed X-ray diffraction in Bragg condition ( $\theta - 2\theta$ ) to probe the quality and epitaxial nature for the structures. Even though the amount of material in the islands is rather small to perform usual theta-2theta Bragg diffraction measurements, we succeeded in recording an XRD spectrum from the patterned areas using long time/step values for data acquisition. In figure 5.17, XRD spectra for the samples listed in table 5.1, along with a diffraction spectra from a bare Nb:SrTiO<sub>3</sub> substrate are represented together.

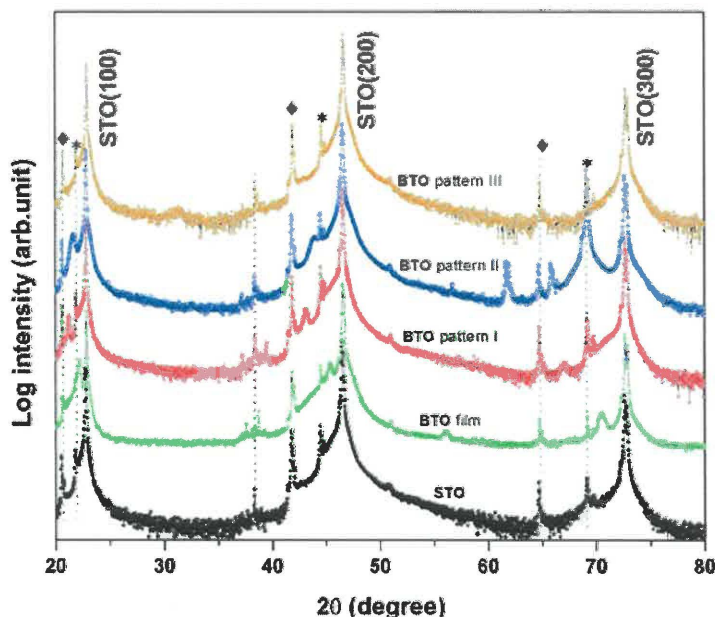


**Figure 5.17.** X-ray diffraction spectra ( $\theta$ - $2\theta$ ) recorded from bare SrTiO<sub>3</sub> substrate (black graph), BTO epitaxial film (green graph), and only from an area with BTO patterned arrays, denominated BTO pattern I, II, III realized with the fabrication conditions described in table 5.1

The parasitic peaks present in all recorded XRD patterns have been identified and attributed to the  $K_{\beta}$  line corresponding to the SrTiO<sub>3</sub> substrate peaks and to line corresponding to tungsten  $W_{\alpha}$  contamination from the X-ray tube. No foreign phases have been detected. The additional reflections visible at  $2\theta = 38^{\circ}$ , and  $52^{\circ}$  correspond to an unidentified contamination of the STO substrate (and therefore also present on the XRD spectra of the bare substrates). As “standard” in this sequence of measurements, we used the continuous film deposited in 100 mTorr O<sub>2</sub> for which the (00 $l$ ) peaks indicate an epitaxial BaTiO<sub>3</sub> film, corresponding to the values given by the library reference pattern (PDF card # 00-005-0626).

A detailed  $2\theta$  scan in the range  $20^\circ - 25^\circ$  displays the (001) peak of the  $\text{BaTiO}_3$  film at the expected position of  $22.26^\circ$ , while for the samples made at lower  $\text{O}_2$  pressure, a shift in the peak position towards lower angles is observed. This corresponds to a shift toward larger out-of-plane inter planar distances of the BTO films, giving a first indication that the patterned structures are strained by the substrate and try to accommodate the lattice in-plane parameter of tetragonal bulk  $\text{BaTiO}_3$  ( $3.994 \text{ \AA}$ ) with that of  $\text{SrTiO}_3$  ( $3.905 \text{ \AA}$ ).

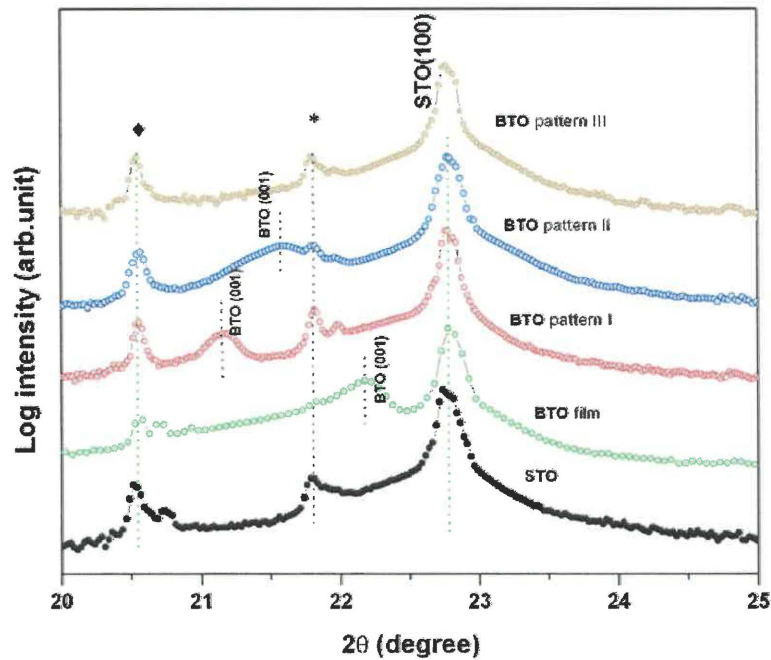


**Figure 5.18** X-ray diffraction spectra ( $\theta$ - $2\theta$ ) detail recorded in the range  $20 - 25^\circ$

For the samples annealed via RTA, no peaks are visible indicating a very weak crystallization and thus prompting longer times for RTA annealing (e.g. 2-3 min) or higher temperature ( $750-800^\circ\text{C}$ ). Moreover the granular aspect of the structures revealed by AFM and SEM observations, suggests that there is no apparent improvement brought by an RTA process in terms of delivering better quality crystalline structures compared with a conventional thermal annealing.

The lattice parameters of the epitaxial BTO patterned samples were investigated more in detail by X-ray Reciprocal Space Mapping (RSM), a technique typically used in epitaxial films to determine if the film is fully strained (pseudomorphic), partially strained (or relaxed), or fully relaxed.

Fig. 5.19 shows RSM graphs for the epitaxial BTO films used as standard and for BTO patterned nanostructures grown at high temperature around the peak (103).

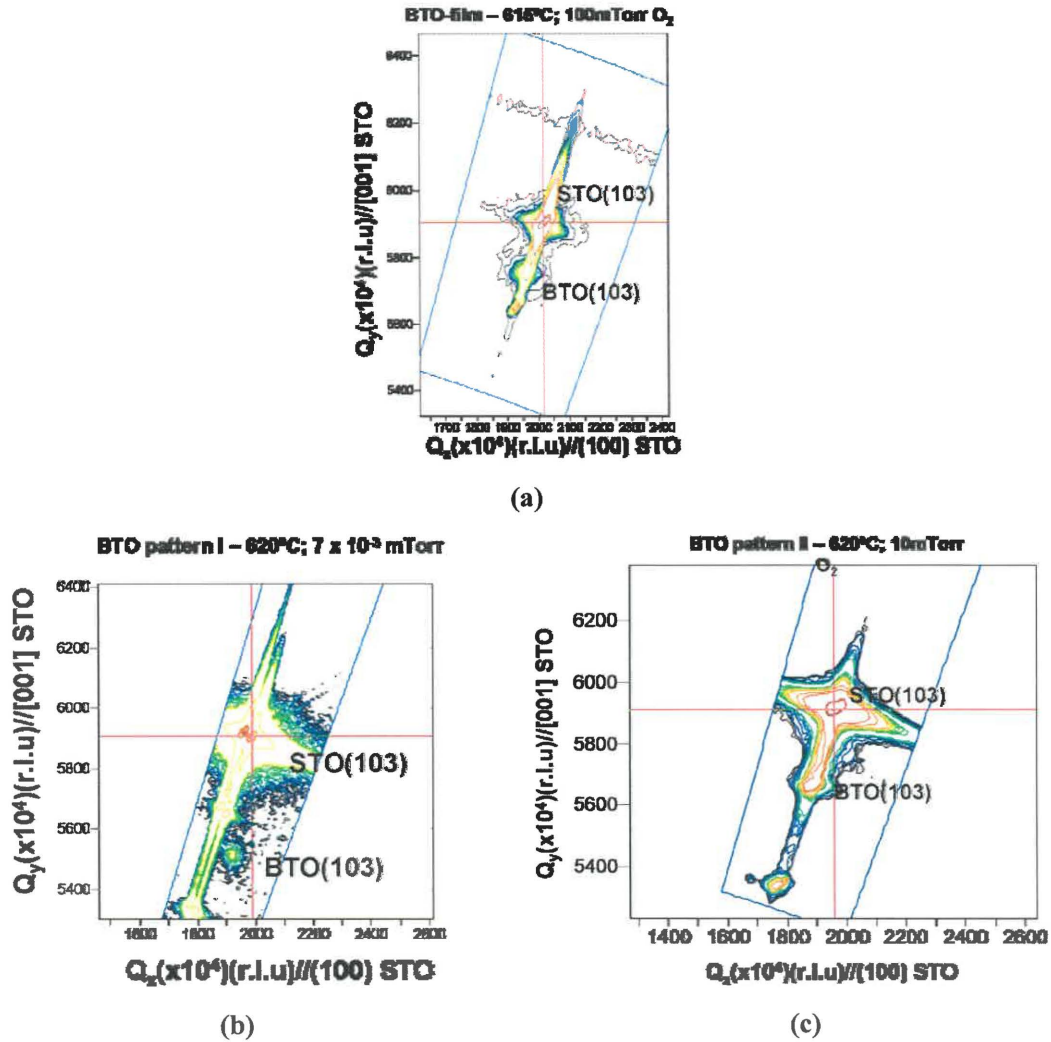


**Figure 5.19** X-ray reciprocal space mapping (RSM) performed for: BaTiO<sub>3</sub> film (a) and patterned samples (b) and (c), in order to calculate the in-plane and out-of plane lattice parameters

The out-of-plane and in-plane lattice parameter of BaTiO<sub>3</sub> structures are determined using in-plane reciprocal lattice parameter  $Q_x$  and out of plane reciprocal lattice parameter  $Q_y$  that are linked with the inter-planar distances by the following formulas:  $d_{in}=2\lambda/Q_x$  and  $d_{out}=2\lambda/Q_y$  with  $\lambda = 1.5406 \text{ \AA}$  the wavelength of the Cu K $\alpha$  X-ray radiation. For the film, the position of BaTiO<sub>3</sub> (103) reciprocal lattice point (r.l.p) with respect to that of STO(103) indicates a relaxed film and calculations for the exact lattice

parameters suggests a small distortion of the unit cell. When the deposition has been performed in a small amount of O<sub>2</sub> (BTO pattern II) the BaTiO<sub>3</sub> structures are almost completely relaxed, whereas strained structures appear when the deposition takes place in vacuum (BTO pattern I) and the (103) r.l.p of BTO is shifting towards that of STO (103).

The values measured from the RSM graphs are summarized in the table 5.2:

**Table 5.2**

Sample ID	In-plane lattice parameter a (Å)	Out-of-plane lattice parameter c (Å)
BTO film	4.00	4.02
BTO pattern I	3.974	4.191
BTO pattern II	4.00	4.067
BTO reference	3.994	4.038
STO reference	3.905	3.905

Analyzing the values obtained for the in-plane and out-of-plane lattice parameters we observed an increased c/a ratio for the sample deposited in vacuum, ratio that is decreasing towards the BTO bulk values once the O<sub>2</sub> pressure in the deposition chamber is increased (fig. 5.20).

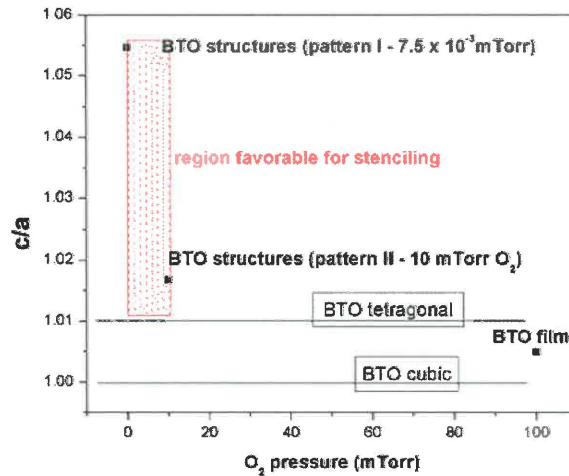


**Figure 5.20** BaTiO<sub>3</sub> (c/a) ratio versus O<sub>2</sub> pressure for the samples given in table 5.2

At lower pressure, due to the higher energy of the ablated particles, more vacancies are produced in the films (structures) leading to a higher in-plane compressive strain. This compressive strain results in the out-of-plane lattice parameter being elongated and thus an enhanced tetragonality of the structures.

During the BaTiO<sub>3</sub> growth at low O<sub>2</sub> pressure many oxygen vacancies are likely to occur. We observed that the volume of the BaTiO<sub>3</sub> unit cell for the patterned samples is larger than its bulk value (and decreases with the increase of oxygen pressure). This structural variation is associated with the oxygen vacancies existing in BaTiO<sub>3</sub> films deposited at low pressures [50] and was also reported for lead titanate (PbTiO<sub>3</sub>) films [51] i.e. our results on the structural characteristics of the patterned BaTiO<sub>3</sub> islands is in agreement with reports on ultra-thin epitaxial perovskite films.

We further tried to correlate these results with the ferroelectric properties of individual BaTiO<sub>3</sub> structures in order to observe the epitaxial strain's effect on the piezoresponse signal and in particular on the polarization switching at the nanometer-length scales. Local piezoresponse hysteresis loops were acquired from patterned BaTiO<sub>3</sub> islands (fig. 5.21) in a similar manner as described in section 5.4.1.1. As it was expected after the analysis of the XRD spectra, only the samples patterned at high-temperature exhibited a ferroelectric behavior.

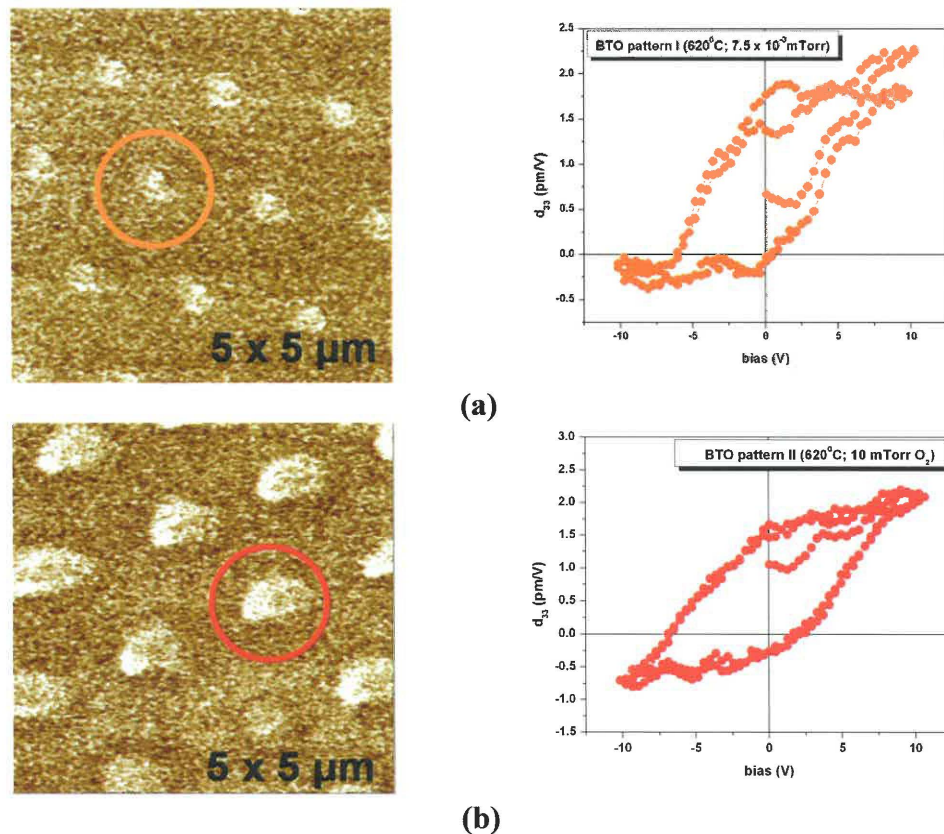


**Fig. 5.21** PFM domain images and local piezoresponse hysteresis loops recorded from samples BTO I and BTO II prepared at 620 °C and in vacuum (a) and 10 mTorr O<sub>2</sub> respectively (b).

The graphs presented in fig 5.21 were obtained from structures with heights of ~50 nm (a) and ~65 nm (b); in both cases, the piezoresponse hysteresis loops recorded clearly indicating that ferroelectricity is retained in the BaTiO<sub>3</sub> structures stenciled in a O<sub>2</sub> low-pressure regime.

The piezoresponse hysteresis loops were found to be shifted vertically (towards positive values) indicating a preferential polarization state known as imprint. It has been reported that oxygen vacancy-associated defect dipoles can enhance charge trapping near the substrate-ferroelectric interface thus aggravating the imprint problem. This pre-polarization phenomenon was reported for instance in as-processed epitaxial ((PbLa)(Zr,Ti)O<sub>3</sub>) thin-film capacitors and the imprint was linked with the oxygen pressure during the cooling [52]. Further on, the hysteresis loop from fig 5.21(a) shows a more square profile which evidence a better remnant polarization while the second loop (fig. 5.21 (b) shows at both edges (i.e. close to saturation) a more linear dependence of the piezoelectric coefficient with the applied field. Such linear dependence suggests a dielectric contribution to the hysteresis loop. Since we used Nb-doped STO substrates that are known to have weak conductivities (almost semiconducting type of transport behavior) we believe that this contribution is caused by the substrate.

A higher degree of tetragonality of the BaTiO<sub>3</sub> unit cell would suggest better piezoelectric and ferroelectric properties i.e. higher values for the piezoelectric coefficients in the case of the structures from the sample BTO pattern I. However the analysis of the piezoresponse loops in both cases are showing almost similar 2d<sub>33</sub> values of about 1.75 pm/V.

Since the usual synthesis of thin film perovskites are carried out in an oxygen background atmosphere, a vacuum-based deposition was thought to alter the functional properties of the films due to the appearance of oxygen vacancies. However, for the synthesis of stenciled BaTiO<sub>3</sub> structures a low pressure of oxygen is suitable for an accurate replication of the stencil's apertures and is leading to enhanced tetragonality of the unit cells thus allowing fabrication of structures with properties similar to those fabricated in a higher partial oxygen pressures.

## 5.5. Nanostenciling of multiferroics

The results obtained for the patterning of ferroelectric BaTiO<sub>3</sub> demonstrated the suitability of the nanostenciling approach to investigate the growth and properties of nanostructured complex materials, and to study possible size effects on their functional properties. This designates nanostenciling as the technique of choice for laboratory-environment nanoscale prototyping and as an invaluable tool for studying novel material-systems such as for instance *multiferroic complex oxides* for which suitable fabrication and patterning techniques have not yet been developed (e.g. post-patterning selective etching processes). We thus extended the application of nanostenciling to multiferroic materials, whose basic characteristics are introduced and outlined in the following.

Multiferroic materials are generally defined as materials that combine at least two “ferroic” properties such as ferromagnetic order (spontaneous magnetic polarization that can be reversed by a magnetic field), ferroelectricity (property discussed in section 5.2) or ferroelasticity (change in spontaneous strain induced by an applied mechanical stress) (fig. 5. 22)

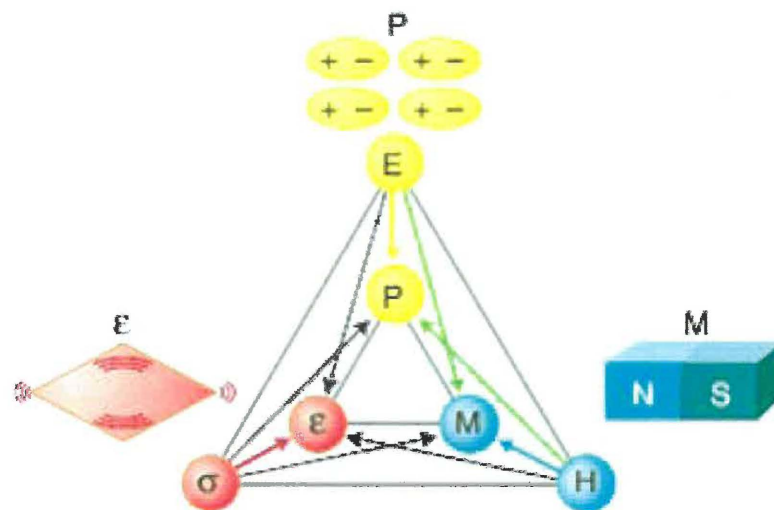


**Figure 5.22** The interplay between spontaneous electric polarization (**P**), spontaneous magnetization (**M**) and spontaneous strain (**ε**) that might be present in a multiferroic material. **P**, **M** and **ε** are controlled by the electric field **E**, magnetic field **H** and stress **σ**. [53]

A sub-family of multiferroics is formed by the *magnetoelectric materials* i.e. materials exhibiting simultaneously both ferroelectric and magnetic properties, which are coupled. The use of this magnetoelectric coupling is envisioned for promising applications in various areas where electric control and manipulation of magnetic field could be beneficial, such as in integrated miniaturized magnetic writing heads, sensors, smart devices as well as in the developing area of spintronics [54,55]. The magnetoelectric coupling could allow for magnetization reversal in a ferromagnetic material by applying an electric field instead of a magnetic field. However, multiferroics that combine ferromagnetism and ferroelectricity have proved quite rare in nature. Theoretical studies have shown that the atomic-level mechanisms driving ferromagnetism and ferroelectricity are basically exclusive in perovskite-oxides, since the ferromagnetism requires unpaired electrons on “d” orbitals while ferroelectricity requires empty “d” orbitals [56]. One of the fewest natural magnetoelectric materials is bismuth ferrite (BiFeO<sub>3</sub>) which is perhaps the most studied Bi-based perovskite within the family of BiXO<sub>3</sub> ones (with X = trivalent transition metal).

### 5.5.1. Patterning of Bismuth Ferrite (BiFeO<sub>3</sub>)

As stated previously, bismuth ferrite (BiFeO<sub>3</sub> or BFO) is a *multiferroic material*, exhibiting both electric and magnetic ordering at room temperature. In its bulk form, bismuth ferrite was reported as a *ferroelectric* perovskite with a high Curie temperature ( $T_C = 1103$  K) and *antiferromagnetic* properties below a Neel temperature of  $T_N = 643$  K [57]. Structural analysis of BFO indicates that it possesses a rhombohedrally distorted perovskite structure with R3c symmetry at room temperature ( $a = b = c = 3.962$  Å,  $\alpha = \beta = \gamma = 89.4^\circ$ ) [58]. Despite a high Curie temperature, suggesting a strong ferroelectric behavior, macroscopic measurement of ferroelectric and transport properties in BFO have been limited by leakage current problems, most likely due to defects and non-stoichiometry issues.

Recently, BFO in the thin film form has attracted attention because its ferroelectric properties were reported to be over an order of magnitude better (i.e.  $P_S \sim 60$   $\mu\text{C}/\text{cm}^2$ ) than in a bulk single crystal ( $P_S \sim 6.1$   $\mu\text{C}/\text{cm}^2$ ) [59]. The large ferroelectric

polarization of BFO epitaxial thin films, comparable for instance with PZT (e.g.  $P_S = 70 \mu\text{C}/\text{cm}^2$ ), would suggest the former as an alternative for lead-free ferroelectrics used for NV-FeRAMs. This enhanced ferroelectricity, together with the fact that BFO is antiferromagnetic with a weak ferromagnetism at room temperature, due to a canted spin structure, have opened perspectives for novel applications of BFO films [60]. The origin of the significant enhancement of BFO ferroelectric properties was mainly attributed to the decrease of oxygen vacancies when the material is prepared in thin film form [59]. Nevertheless, a change in crystal structure once a material has been patterned in structures of very small dimensions can not be ruled out. Fabrication of BFO nanostructures as well as investigating the influence of the reduced structure dimensions on the multiferroic material properties is therefore essential in view of their potential applications.

Intensive efforts have been made to prepare phase-pure BFO thin films by pulsed-PLD [61,62]. It was found that BFO thin films deposition is a great challenge, mostly due to the Bi evaporation, oxidation and precipitation in the form of  $\text{Bi}_2\text{O}_3$  or to film crystallization in other possible stable phases like  $\text{Fe}_2\text{O}_3$ ,  $\text{Fe}_3\text{O}_4$  and  $\text{Bi}_2\text{Fe}_4\text{O}_9$ . It has been shown to be quite hard to avoid generating impurity phases.

We encountered similar problems for the synthesis of patterned BFO when we tried the room-temperature (RT- PLD) stenciling approach that was successful in the case of  $\text{BaTiO}_3$ . Using same type of LIL-based stencils and a stoichiometric  $\text{BiFeO}_3$  target we prepared and patterned arrays of nanostructures with lateral dimension ranging from 350 to -100 nm and thickness from 50 to 10 nm. SEM and AFM analyses showed like in the case of barium titanate, totally separated and perfectly well-replicated (amorphous) structures at RT. However, after a conventional post-deposition annealing process (650-800 °C; for 30-60 min in oxygen), the *ferroelectric* character of the structures has not been proved by PFM measurements, fact attributed to extrinsic fabrication effects (Bi evaporation, non-stoichiometric deposition, etc) and not to the intrinsic reduced size-effects. Better and promising results were obtained for the BFO structures deposited at room-temperature and annealed by rapid-thermal annealing (RTA) at 900 °C, for 60 sec in oxygen.

After the RTA process, AFM topography shows two types of structures: small round-shaped (type 1), and larger size polygon-shaped (type 2) structures (fig. 5.23). PFM measurements revealed that only the type 1 structures have a piezoresponse contrast showing a complex ferroelectric domain structure and thus indicating a BiFeO<sub>3</sub> perovskite phase, whereas the type 2 structures exhibit uniform contrast. Yet the registration of the structures was not completely preserved and the presence of foreign phases is prompting further investigations to elucidate the nucleation / crystallization of nanometer-scale BiFeO<sub>3</sub> islands.

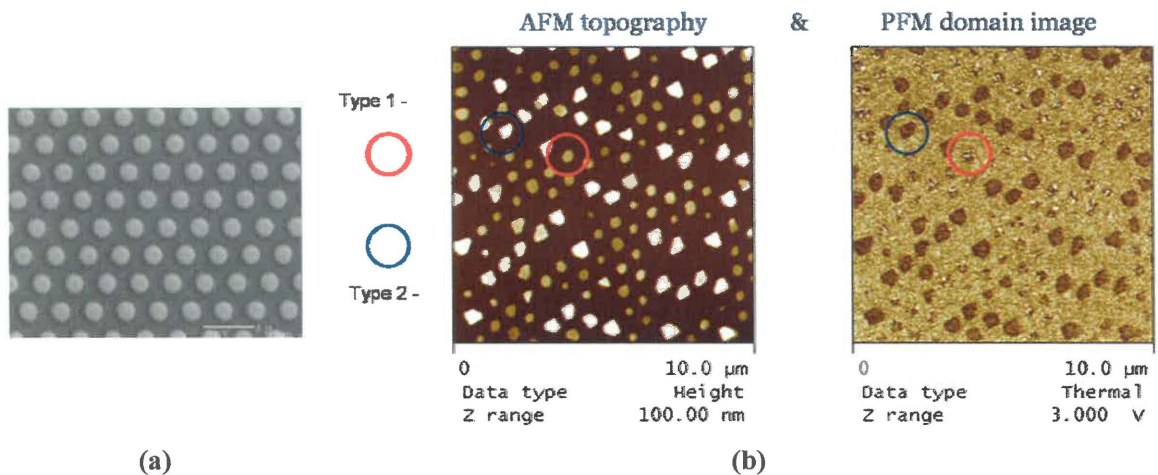


**Figure 5.23** (a) SEM micrograph of BiFeO<sub>3</sub> stenciled at room-temperature and (b) AFM topography and PFM domain image of the structures after RTA annealing

To integrate BFO films into functional heterostructures it is imperative to control its chemical composition and recent studies reported that stoichiometric BFO perovskites prepared by PLD could be stabilized only within a narrow range of temperatures and oxygen pressures [62]. It was further established that at lower temperature or higher pressure of oxygen, Bi<sub>2</sub>O<sub>3</sub> precipitates are most likely to form while at lower pressure or higher temperature, Fe<sub>2</sub>O<sub>3</sub> forms. Moreover, magnetization measurements revealed a high magnetic moment for films containing  $\gamma$ -Fe<sub>2</sub>O<sub>3</sub> (maghemite) impurities while single-phase films have a low magnetic moment ( $\sim 0.02 \mu_B/\text{f.u.}$ ) close to the bulk value<sup>13</sup>.

We further pursued the BiFeO<sub>3</sub> stenciling experiments keeping the assembly substrate-stencil at temperatures ranging from 580 to 625 °C and low-O<sub>2</sub> pressure ( $\sim 7 - 9$

<sup>13</sup> In fact the issue of the real value of the magnetic moment in pure BFO films is quite debated after controversial reports have been made by Wang et al. [59] who reported a strong enhancement of magnetic moment in the films they prepared.

mTorr O<sub>2</sub>) and depositing on (100) oriented STO-substrates, through stencils with circular apertures, like in the case of BaTiO<sub>3</sub> high-temperature deposition processes.

After SEM investigations (fig. 5.24) of a few samples deposited in the conditions described above, although the apertures in the stencils are circular, we noticed almost squared shapes for the patterned structures suggesting a tendency of “cubic” epitaxial growth for the patterned structures. However the structures obtained were not completely separated and deposited material can be noticed between the structures pointing to an enhanced surface diffusion at the deposition temperature and even to the possibility of a wetting layer formation on top of which the structures grow epitaxially. The enlargement of the BFO deposited structures with respect to the initial aperture size might be caused by the surface diffusion but also in part by the geometry setup (i.e. large gap stencil – substrate). At the same time the diffusion length depends primarily on the deposited material and on the substrate surface (temperature, preparation) or deposition rate.

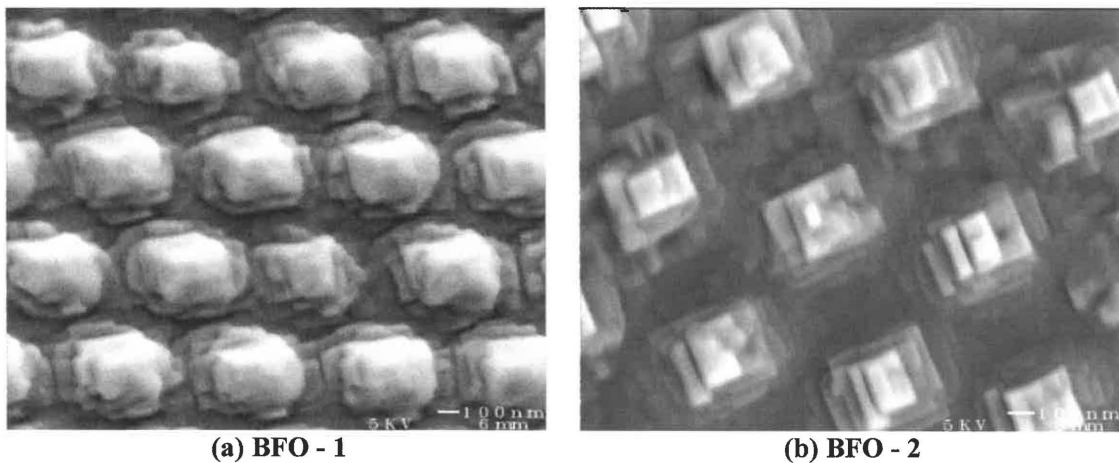


**Figure 5.24** SEM micrographs of BiFeO<sub>3</sub> stenciled patterns on (100) SrTiO<sub>3</sub> substrates: (a) BFO - 1 at 590 °C and (b) BFO - 2 at 625 °C in 9 mTorr O<sub>2</sub>. The substrate from (b) has been treated in a buffered HF solution prior to the BFO patterning.

XRD scans in  $\theta$ - $2\theta$  confirmed the presence of epitaxially grown BiFeO<sub>3</sub> and no foreign phases were detected. However since there is not a very clear separation between the structures (as for instance in the case of BaTiO<sub>3</sub> patterned islands) we can not exclude a continuous underlying BiFeO<sub>3</sub> layer which can bring its own contribution to the detected peaks as suggested in the inset of figure 5.25 a and by the RSM graphs from figure 5.25 (b) and (c).

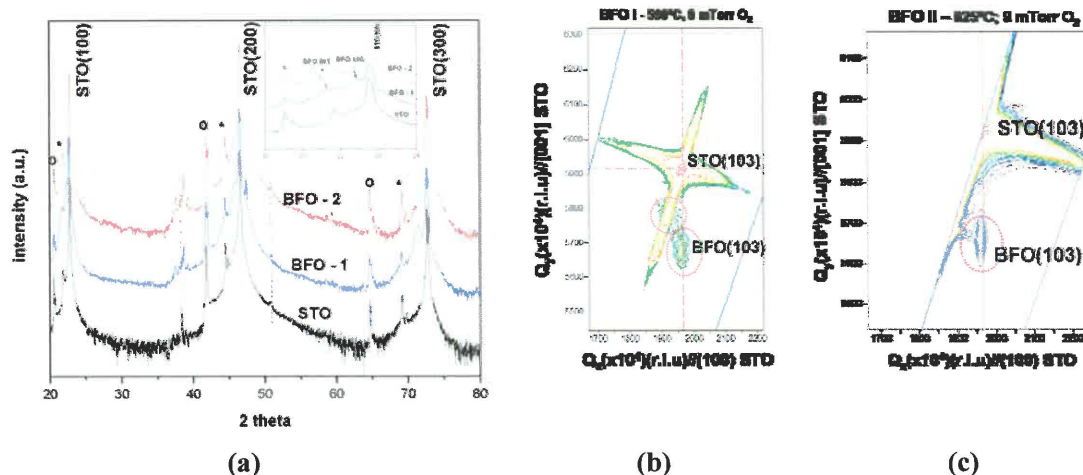


**Figure 5.25** (a) XRD spectra for the samples BFO-1 ( $T_{\text{dep}}=590$  °C) and BFO-2 ( $T_{\text{dep}}= 625$  °C) patterned at low-oxygen pressure; (b) and (c) X-ray reciprocal space maps recorded to estimate the lattice parameters

Assuming a tetragonal distortion of a pseudo-cubic symmetry for BFO, the calculations of the in-plane and out-of-plane lattice parameters are summarized below in table 5.3 showing a good tetragonality for the unit cell ( $c/a = 1.03$  and  $1.04$  respectively) and ferroelectric behavior tested by PFM.

**Table 5.3**

Sample ID	a (Å)	c (Å)
BFO 1	3.916	4.068
BFO 2	3.91	4.082
BFO (pseudo cubic)	3.96	3.96

While depositing BFO in the conditions described above we succeeded in controlling the synthesis of *epitaxial BFO films*, eliminating impurity phases like those present during the RT-PLD process. However we did not achieve the desired registration and control of the shapes of the patterned structures like in the case of BaTiO<sub>3</sub>, in the sense that a continuous wetting layer is possibly present and the BFO epitaxial structures observed are therefore not separated islands. It is, however, interesting to notice that the islands deposited through circular apertures, crystallize with the *cubic symmetry* of BFO and of the underlying substrate. Stencils with different architectures in terms of aperture size and pitches might enable further studies of direct patterning of BFO on STO substrates and possibly on the diffusion length of the species impinging on the substrate surface thus allowing to find the right parameters in order to obtain separated islands and an accurate replication of the motifs drawn in the membranes.

## 5.5.2 Patterning of $\text{Bi}_2\text{FeCrO}_6$

In the context of exploring novel multiferroic materials, Baettig et al. reported in 2005 the design and properties of a novel quaternary multiferroic, never observed in Nature, namely  $\text{Bi}_2\text{FeCrO}_6$  (BFCO) [63]. The authors predicted that BFCO would have a crystal structure similar to that of BFO (i.e. rhombohedral), except that every second iron cation in the (111) direction is replaced by a chromium cation. They also predicted that BFCO would be ferroelectric with a spontaneous polarization of  $80 \mu\text{C}/\text{cm}^2$  and ferromagnetic at 0 K, with a magnetic moment of  $2 \mu_B$  per formula unit.

Within the framework of investigating novel multiferroic materials undertaken in our group, Nechache et al. reported the first experimental synthesis of epitaxial BFCO films by PLD [64]. The BFCO films were deposited by laser ablation from a bulk ceramic target composed from a stoichiometric mixture of  $\text{BiFeO}_3$  and  $\text{BiCrO}_3$  on either  $\text{SrTiO}_3$  covered with an epitaxial  $\text{SrRuO}_3$  (SRO) buffer layer or directly on (100)-oriented  $\text{SrTiO}_3$  single crystalline substrates. The subsequent analysis of the films showed their higher stability compared to BFO films as well as good multiferroic properties at room-temperature [64].

As a natural continuation of the efforts undertaken to pattern multiferroic BFO structures, we turned our attention towards nanostenciling of BFCO. Initially, the BFCO films synthesized by Nechache et al. were deposited in oxygen ambient at a pressure of 20 mTorr and a substrate temperature of approximately  $750 \text{ }^\circ\text{C}$ . This background pressure is quite, close to the threshold at which accurate replication of the apertures can still take place for a certain target-substrate distance (e.g. 7 cm in our set-up).

As observed in previous experiments with BTO and BFO, an excessive  $\text{O}_2$  background pressure in the deposition chamber or the high temperature at which the substrate is kept during the growth is not optimal for deposition through the nano-shadow-mask and hinders the accurate replication of the nano-apertures drawn in the stencil<sup>14</sup>. Further refinement of the deposition conditions (based on earlier studies of BFO thin films) lead to the establishment of the precise conditions for the epitaxial growth, at

---

<sup>14</sup> In the case of BFO we have determined empirically a threshold pressure of about 30 mTorr  $\text{O}_2$  for a target-substrate distance of 7cm and a certain equivalent film thickness for the deposits above which the structures replication disappears.

rather low  $O_2$  background pressures, of stoichiometric BFCO thin films directly deposited on Nb-doped STO substrates of different crystallographic orientations [65,66]. These films exhibited good ferroelectric and magnetic properties at room temperature, the latter even exceeding the predicted ones.

We then combined the growth conditions described above with the stenciling procedure, and achieved the controlled-growth of epitaxial (oriented) nanoscale ordered arrays of multiferroic structures, in a quite spectacular fashion, as seen on (Fig. 5.26).

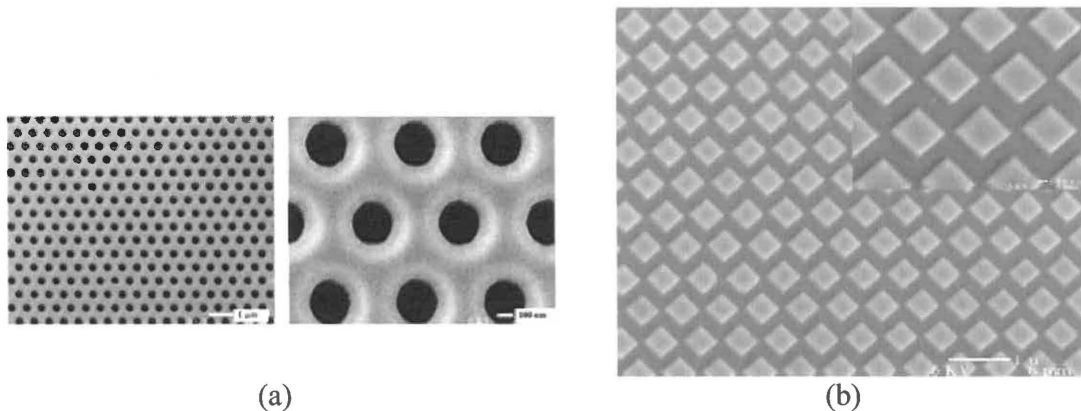


**Figure 5.26** Stenciling of multiferroic  $Bi_2FeCrO_6$ : **(a)** SEM micrographs of SiN membranes with apertures 350nm in diameter and 700nm pitch **(b)** arrays of square-based structures with an average lateral size of 400 nm and heights of 30 nm.

We used a nanostencil with hexagonal arrays of *circular apertures* (fig. 5.26(a)), in close proximity to the STO (100) substrate, ablate from the  $BiFeO_3 - BiCrO_3$  ceramic target, and the BFCO deposited islands resulted in ordered arrays of *square-based structures* (fig. 5.26(b)) that are following the 4-fold symmetry of the single crystalline STO(100) substrate. In contrast with the BFO structures discussed previously, in this case, the well-defined and completely separated structures not only retained perfectly the hexagonal architecture of the *circular* holes defined in the stencil i.e. a pitch of 700 nm, but also epitaxially grew in the form of *square-shaped* islands following thus both the cubic crystal symmetry of the underlying STO substrate and their own inclination to grow with a pseudo-cubic symmetry.

The resulting square-shape of the oriented grown islands is not entirely surprisingly in the light of the fact that most perovskite-type oxides exhibit lowest surface energies on the  $\{100\}$  facets thus leading to “cuboids” equilibrium-shapes dominated by six  $\{100\}$  facets [67]. Similar shapes of self-assembled  $BiFeO_3$  were reported by Zheng

et al. [68] who explored the growth of  $\text{BiFeO}_3\text{-CoFe}_2\text{O}_4$  nanostructures on STO substrates of different orientations. The authors explained the morphology of the BFO-CFO nanostructures using the Winterbottom construction [69], theory that determines the equilibrium shape of a crystalline nucleus on a substrate as a function of the surface energy terms (i.e. substrate surface energy  $\gamma_{\text{sub}}$ , interface energy  $\gamma_{\text{int}}$  and surface energy of the crystalline phase  $\gamma_{\text{str}}$ ).

According to the Winterbottom construction the possible substrate-solid particle configuration can be classified in the following categories: non wetting, partial wetting and complete wetting. On a (001) oriented substrate  $\text{BiFeO}_3$  completely wets the substrate and follows a layer-by layer growth. Since the crystal structure of BFCO is similar to that of BFO we can thus assume also in the case of BFCO the “cube on cube” epitaxial growth mode after a “wetting layer” is formed in the area defined by the stencil’s aperture<sup>15</sup>.

Elongated structures, along one of the main crystallographic directions of the substrate, have been observed in the areas where a slight tilting of the mask with respect to the substrate has been accentuated by an uneven pressure against the substrate. However all the structures follow the main crystallographic directions as shown in (figure.5.27). The inherent broadening of the structure’s sizes is given by the shadow-effect induced by the gap stencil-substrate always present due to surfaces irregularities or foreign particulates.

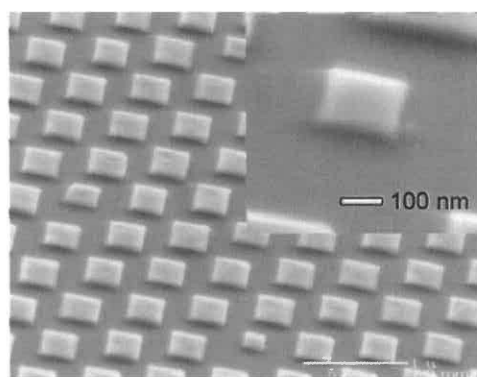


**Figure 5.27** SEM micrograph showing the elongation along one crystallographic axis and structures down to 150 nm (inset)

<sup>15</sup> For reasons that remain to be explained in details and are under investigation, the surface diffusion is not sufficient in the case of BFCO islands to form a continuous wetting layer between the structures.

Stencils have been used in several previous depositions of BFCO at RT and clogging of the apertures from their nominal diameter was already present. The SEM micrograph inset from (fig. 5.27) shows a detail of an island of about  $\sim 150$  nm in lateral size, apparently formed due to a premature clogging of some apertures – most probably caused by droplets retained on the top-side of the membrane. These so-called “accidents” revealed in fact that smaller initial apertures could lead to even smaller registered structures that could retain the symmetry of the substrate.

X-ray diffraction was performed in order to evaluate the crystallinity of the patterned arrays of structures that are covering a total area of  $2 \times 2.7$  mm<sup>2</sup>. As shown in the inset of Fig. 5.28, (00 $l$ ) peaks for the BFCO arrays are clearly observed along with the corresponding peaks of the (100) STO substrate revealing that the BFCO nanostructures are highly (001)-oriented. XRD analysis with extremely long counting times in the range  $2\theta = 91^\circ - 97^\circ$  were also performed (not shown here) in order to exclude the presence of magnetic parasite phases, as those reported by Bea et al.[70] No peaks corresponding to  $\alpha$ -  $\gamma$ -Fe<sub>2</sub>O<sub>3</sub> reflections were detected, even after these extra long scans.

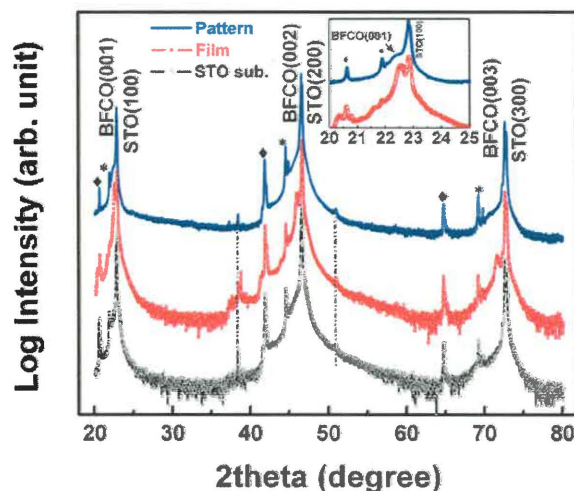


**Figure 5.28** X-ray diffraction spectra ( $\theta$ - $2\theta$ ) recorded from bare SrTiO<sub>3</sub> substrate (black graph), BFCO epitaxial film (red graph), and only from BFCO patterned arrays (blue graph); in the inset the position of the peak (001) for the BFCO arrays is indicated together with the peak (001) from the epitaxial film revealing the “oriented” nature of the former; Diamonds and Stars represent the K<sub>β</sub> peak of STO and W<sub>Lα</sub> contamination, respectively.

We further investigate the epitaxial nature of the BFCO nanostructures by high resolution cross-section transmission electron microscopy (HRTEM). The selected area electron diffraction pattern (SAED) (Fig 5.29), obtained from the (001)-oriented sample

along the [010] direction, confirms the epitaxial nature and the good single crystalline quality of the BFCO nanostructures.

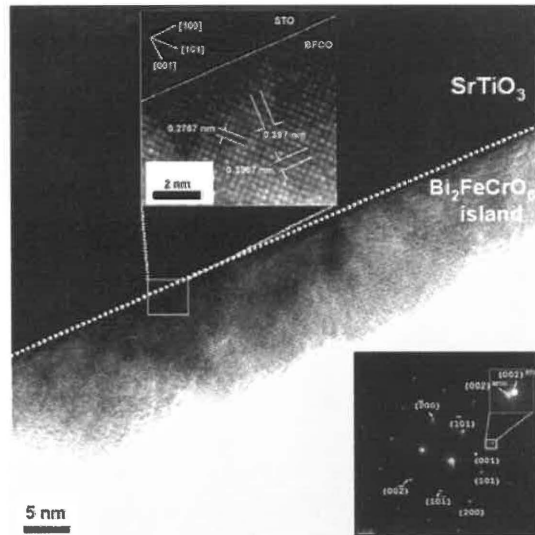
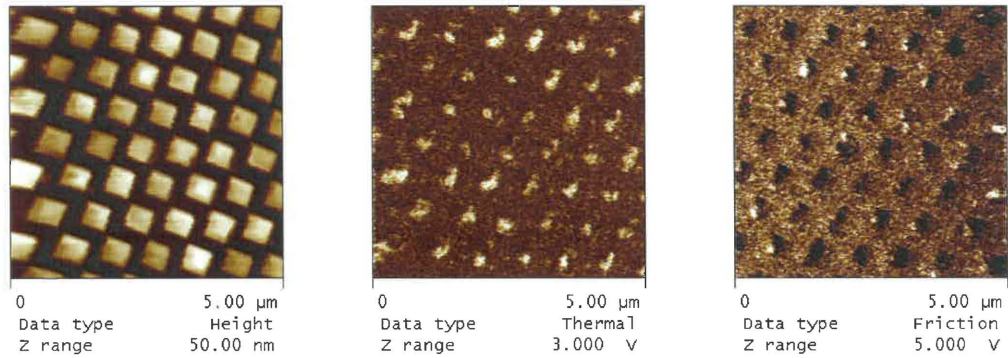


**Figure 5.29** High-resolution cross-section TEM image taken along the [010] direction and showing a part from a BFCO island. In inset selected area electron diffraction pattern from the (001) oriented sample along the [010] direction.

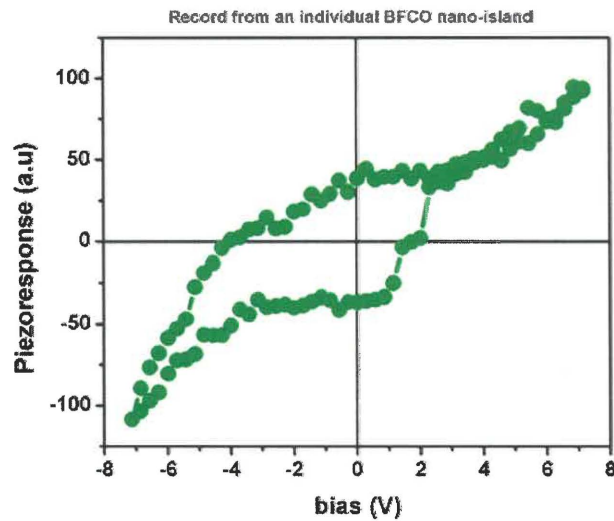
A zoom around (002) reflections suggests that the out-of-plane of BFCO is larger than that of the STO substrate, whereas the in-plane [(200) reflections] is very close to it. Detailed analysis of the SAED pattern from nanostructures reveals that the (200) and (002) reflections have different spacing, yielding a ratio of 1.0161. Indexing of this SAED pattern with pseudocubic indices yields an in-plane lattice parameter very close to that of STO substrate ( $\sim 3.91 \text{ \AA}$ ) and an out-of-plane parameter of  $3.97 \text{ \AA}$ .

To analyze the multiferroic character of the BFCO structures we probed individual islands by two scanning probe microscopy methods, namely piezoresponse force microscopy (PFM) and magnetic force microscopy (MFM) in randomly-chosen areas of the patterned substrate.

The characterization of the ferroelectric behavior is shown in Figure. 5.30 presenting a typical PFM experiment of BFCO patterned on a 0.5% Nb-doped SrTiO<sub>3</sub> (100) substrate with the PFM domain images. In the following, “z” and “x” stand for the out-of plane and in-plane components of the PFM signal or polarization, simultaneously recorded with topography (Fig. 5.30a). White contrast in the z-PFM image reveals regions with z component of spontaneous polarization oriented ‘upwards’ whereas the dark regions denote a ‘downwards’ component.



(a)



(b)

**Figure 5.30** (a) AFM/PFM measurements; contact AFM topography (left); z-PFM (middle) and x-PFM (right) recorded simultaneously; (b) piezoresponse hysteresis loop recorded from individual BFCO island in Z-PFM mode

For the x-PFM image white/dark contrast stands for “left”/“right” (in-plane) components of spontaneous polarization. The presence of both in- and out-of-plane components of polarization is consistent with the fact that  $P_s$  lies along one of the [111] directions due to the rhombohedral distortion of the BFCO unit cell. The structures present a rather complex domain configuration, with domain walls parallel to the [100] and [010] directions. A closer analysis determined that on average, one domain extends over several tens of nanometers, while near the edges the response is weaker. The pinning of ferroelectric domains at the free lateral surface of the structures and ferroelectric–

electrode interface, [71] as well as a particular strain configuration may explain such a behavior. Further investigations revealed that all probed structures are piezoelectric, can be switched individually and exhibit a clear piezoelectric hysteresis [similar to Fig. 5.30(b)], and therefore are clearly exhibiting ferroelectricity. The effective piezoelectric coefficient  $d_{33}$  was estimated to be 10 pm/V, which is 2 times larger than that of continuous BFCO films with similar thickness. A similar increase of the electromechanical response in finite size epitaxial structures when compared to the epitaxial film from which they were cut (using FIB-milling) has been reported for lead zirconate titanate, and the origin of this increased response for islands has been attributed to clamping on the substrate and the release of lateral clamping present in continuous films [72].

The magnetic character of the patterned structures has been investigated both at local and macroscopic levels.

Magnetic force microscopy (MFM) measurements (Fig. 5.31) have been performed in a magnetic field oriented perpendicular to the substrate. The chosen value of the magnetic field ( $\sim 250$  Oe) is higher than the coercive field of the structures, but lower than that of the magnetic tip. The structures exhibit a uniform contrast, clearly different from that of the substrate (Fig 5.31a).

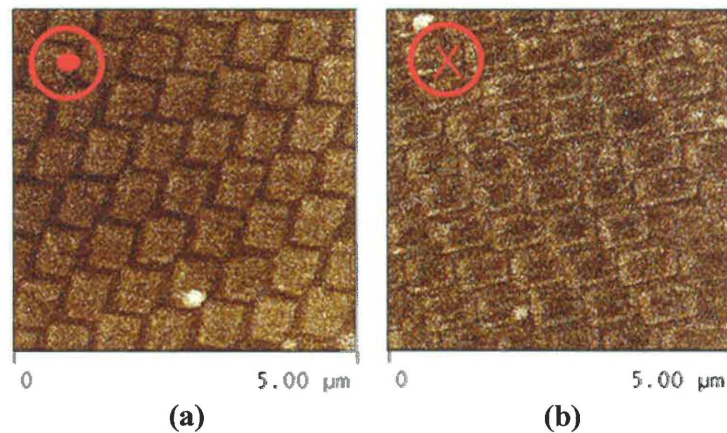


**Figure 5.31** MFM measurements (frequency shift) performed in magnetic field ( $\sim 250$  Oe) showing the magnetic switching of BFCO patterned structures: (a) magnetic field pointing out from the substrate, the frequency shift of the cantilever when the tip is above the structures is positive (the structures are brighter than the substrate). (b) change in the frequency shift (MFM contrast) of the BFCO islands upon reversing the direction of the magnetic field.

Since the MFM tips are also conductive, an electrostatic interaction is always present between the tip/cantilever and the sample and the latter is usually superimposed to the

magnetic interaction [73,74]. Electrostatic interaction has local variations, especially in the situation of non-conducting oxides/ferroelectrics such as BFCO, due to local variations in surface potential caused by surface charges/ferroelectric domains, therefore the recorded image shown in Fig. 5.31 rather reflects a convolution of both electrostatic and magnetic contributions between the tip and the probed media than the pure magnetic interaction. To prove that the structures are magnetically polarizable, and that the contrast has a magnetic origin, we reversed the direction of the external magnetic field.

The change in contrast upon reversing the magnetic field direction (Fig. 5.31b) proves that: first, the origin of contrast is the magnetic interaction, since only the magnetic field configuration has been changed between the two measurements, and second, there is an induced magnetic moment in each BFCO islands. Measurements performed in the absence of a magnetic field did not allow a clear estimation of the magnetic origin of the frequency shift contrast, due to the weak magnetization of BFCO. Attempts to increase the magnetic field above 300 Oe showed that then the moment of the tip switches as well, rendering the images unstable and inconclusive.

Finally, the local MFM investigations were supported with macroscopic measurements at room temperature using a vibrating sample magnetometer (VSM) with sensitivity better than  $10^{-6}$  emu. The room temperature magnetic hysteresis loops of the whole patterned area of BFCO structures is shown in (Fig 5.32), for both in-plane and out-of-plane measurement configurations.

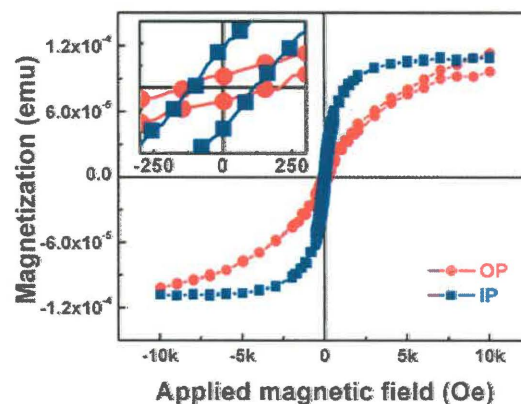


**Figure. 5.32** Magnetic hysteresis loops recorded from the BFCO patterned area via vibrating sample magnetometry showing an appreciable saturation magnetization and a coercive field of ~150 Oe. The in-plane loop is shown in blue, and the out-of-plane loop is in red. Inset shows a zoom around origin.

These macroscopic magnetic measurements show a clear hysteretic magnetic behavior of the BFCO structures with a coercive field of 150 Oe, about twice that of BFCO continuous films (80 Oe, [64]). The saturation magnetization along these two directions i.e. [001] and [100] coincide at higher field, indicating the existence of magnetic anisotropy in the BFCO nanostructures.

## 5.6 Summary

In this chapter, we presented and demonstrated the great potential of nanostenciling for the simultaneous fabrication and patterning of ordered arrays of nanoscale-sized structures of ferroelectric ( $\text{BaTiO}_3$ ) and multiferroic ( $\text{BiFeO}_3$  and  $\text{Bi}_2\text{FeCrO}_6$ ) multifunctional materials having a perovskite-type crystal structure.

We showed that the process can be carried out at both room and high temperature regimes and is highly compatible with the high-vacuum technology. Moreover being a resist free process, damages related to etching are avoided and nanostenciling conserves the desired functionality of the individual nanostructures, namely ferroelectricity and magnetic behavior (demonstrated by PFM, MFM and VSM measurements). It could be used for instance to study size effects and explore the detail of the functional properties in magnetoelectric (multi)ferroic structures, at the nanoscale.

The fabrication process described here is highly parallel and suitable for patterning complex multicomponent functional materials. In addition to its use to deliver patterns of mesoscopic structures, a more elaborate exploitation of shadow masks, (e.g. controlling their position, rotation, tilting angle with respect to the substrate) can be envisioned for use in a combinatorial approach. Such an approach would potentially lead to the fast synthesis of entire nanoscale libraries of nanostructured materials of different compositions and shapes that can further be investigated from their structural, compositional, or functional point of view.

## 5.7 References

- [1] N. Setter and R. Wasser, *Acta. Mater.* 48, 151 (2000)
- [2] M. E. Lines and A. M. Glass, “Principles and Applications of Ferroelectrics and Related Materials”, Clarendon Oxford, (1977)
- [3] R. E. Cohen, *Nature* 358, 136 (1992)
- [4] D. R. Askeland and P.P. Phulé, “The Science and Engineering of Materials”, 4th ed., Thomson (2002)
- [5] J. Baborowski, *J. of Electroceramics* 12, 33 (2004)
- [6] C.R. Martin and I.A. Aksay, *J. of Electroceramics* 12, 53 (2004)
- [7] M. Alexe, C. Harnagea and D. Hesse, *J. of Electroceramics* 12, 69 (2004)
- [8] D. Damjanovic, *Rep. Prog. Phys.* 61, 1267 (1998)
- [9] A. Gruverman and A. Kholkin, *Rep. Prog. Phys.* 69, 2443 (2006)
- [10] W.G. Cady, “Piezoelectricity”, Dover Publications, Inc., New York (1964)
- [11] M. Abplanalp, PhD thesis, Swiss Federal Institute of Technology, Zurich, Switzerland, (2001)
- [12] C. Harnagea, PhD thesis, Max Planck Institute, Halle, Germany, (2001)
- [13] C. Harnagea, A. Pignolet, M. Alexe, D. Hesse and U. Gösele, *Appl. Phys. A* 70, 261 (2000)
- [14] F. Jona and G. Shirane, “Ferroelectric Crystals”, New York, Dover Publications, (1993)
- [15] O. Auciello, J. F. Scott and R. Ramesh, *Phys. Today* 51, 22 (1998)
- [16] D. L. Polla and L.F. Francis, *Annu. Rev. Mater. Sci.* 28, 563 (1998)
- [17] K. Uchino, “Ferroelectric Devices”, New York, Decker, (2000)
- [18] J. Junquera and P. Ghosez, *Nature* 422, 506 (2003)
- [19] T. Tybell, C. H. Ahn and J. M. Triscone, *Appl. Phys. Lett.* 75, 856 (1999)
- [20] Y. S. Kim, D.H. Kim, J.D. Kim, Y.J. Chang, T.W. Noh, J.H. Kong, K. Char, Y.D. Park, S. D. Bu, J.-G. Yoon and J.-S. Chung, *Appl. Phys. Lett.* 86, 102907 (2005)
- [21] S. Li, J. A. Eastman, Z. Li, C.M. Foster, R. E. Newnham and L. E. Cross, *Phys. Lett. A* 212, 341 (1996)
- [22] D. D. Fong, G. B. Stephenson, S. K. Streiffer, J. A. Eastman, O. Auciello, P. H. Fuoss and C. Thompson, *Science* 304, 1650 (2004)

- [23] C. S. Ganpule, A. Stanishevsky, S. Aggarwal, J. Melngailis, E. Williams, R. Ramesh, V. Joshi and C. P.de Araujo, *Appl. Phys. Lett.* 75, 3874 (1999)
- [24] Y. Luo, I. Szafraniak, N. D. Zakharov, V. Nagarajan, M. Steinhart, R. B. Wehrspohn, J. H. Wendorff, R. Ramesh and M. Alexe, *Appl. Phys. Lett.* 83, 440 (2003)
- [25] W. S. Yun, J. J. Urban, Q. Gu and H. Park, *Nano Lett.* 2, 447 (2002)
- [26] A. Gruverman, O. Auciello and H. Tokumoto, *Ann. Rev. Mater. Sci.* 28, 101 (1998)
- [27] S. V. Kalinin, D.A. Bonnell, T. Alvarez, X. Lei, Z. Hu, J.H. Ferris, Q. Zhang and S. Dunn, *Nano Lett.* 2, 589 (2002)
- [28] K. Terabe, M. Nakamura, S. Takekawa, K. Kitamura, S. Higuchi, Y. Gotoh and Y. Cho, *Appl. Phys. Lett.* 82, 433 (2003)
- [29] P. Muralt, *IEEE Trans. on ultrasonics, ferroelectrics and frequency control*, 47, 903 (2000)
- [30] M. Alexe, C. Harnagea, D. Hesse and U. Gosele, *Appl. Phys. Lett* 75, 1793 (1999)
- [31] I. Szafraniak, C. Harnagea, R. Scholz, S. Bhattacharya, D. Hesse and M. Alexe, *Appl. Phys. Lett.* 83, 2211 (2003)
- [32] H. Nonomura, M. Nagata, H. Fujisawa, M. Shimizu, H. Niu and K. Honda, *Appl. Phys. Lett.* 86, 163106 (2005)
- [33] M. Dawber, I. Szafraniak, M. Alexe and J. F. Scott, *J. Phys.: Condens. Matter* 15, L667 (2003)
- [34] S. Clemens, T. Schneller, A. van der Hart, F. Peter and R. Waser, *Adv. Mater.* 17, 1357 (2005)
- [35] A. Stanishevsky, S. Aggarwal, A. S. Prakash, J. Melngailis and R. Ramesh, *J. Vac. Sci. Technol. B* 16, 3899 (1998)
- [36] C. S. Ganpule, A. Stanishevsky, Q. Su, S. Aggarwal, J. Melngailis, E. Williams and R. Ramesh, *Appl. Phys. Lett.* 75, 409 (1999)
- [37] V. Nagarajan, A. Roytburd, A. Stanishevsky, S. Prasertchoung, T. Zhao, L. Chen, J. Melngailis, O. Auciello and R. Ramesh, *Nat. Mat.* 2, 43 (2003)
- [38] S. Buhlmann, B. Dwir, J. Baborowski and P. Muralt, *Appl. Phys. Lett.* 80, 3195 (2002)

- [39] M. Alexe, C. Harnagea, W. Erfurth, D. Hesse and U. Gösele , Appl. Phys. A 70, 247 (2000)
- [40] C. Harnagea , M. Alexe, J. Schilling, J. Choi, R. B. Wehrspohn, D. Hesse and U. Gösele, Appl. Phys. Lett. 83, 1827 (2003)
- [41] W. Ma, C. Harnagea, D. Hesse and U. Gosele, Appl. Phys. Lett. 83, 3770 (2003)
- [42] S. K. Lee, W. Lee, M. Alexe, K. Nielsch, D. Hesse and U. Gosele, Appl. Phys. Lett. 86, 152906 (2005)
- [43] C.V. Cojocaru, C. Harnagea, F. Rosei, A. Pignolet, M.A.F. van den Boogaart and J. Brugger, Appl. Phys. Lett. 86, 183107 (2005)
- [44] M. Ohring, “The Materials Science of Thin Films”, Academic Press, Inc., ISBN 0-12-524990 (1992)
- [45] C. Harnagea, C. V. Cojocaru, O. Gautreau, F. Rosei and A. Pignolet, J. of Phys.: Conf. Series 59, 636 (2007)
- [46] S. Egger, A. Ilie, Y. Fu, J. Chongsathien, D-J. Kang, and M. Welland, Nano Lett., 5, 15 (2005)
- [47] K. M. Ring and K. L. Kavanagh, J. Appl. Phys. 94, 5982 (2003)
- [48] C. Harnagea and A. Pignolet, Chap.2, 47, in “Nanoscale Characterisation of Ferroelectric Materials-Scanning probe Microscopy Approach”; edited by M. Alexe and A. Gruverman Springer, Berlin, (2004)
- [49] X. Du, Q.-M. Wang, U. Belegundu, A. Bhalla and K. Uchino, Mat. Lett. 40, 109 (1999)
- [50] T. Zhao, F. Chen, H. Lu, G. Yang and Z. Chen, J. Appl. Phys. 87, 7442 (2000)
- [51] C. H. Park and D. J. Chadi, Phys. Rev. B 57, R13961 (1998)
- [52] J. Lee and R. Ramesh, Appl. Phys. Lett. 68, 484 (1996)
- [53] N. A. Spalding and M. Fiebig, Science 309, 391 (2005)
- [54] I. Zutic, J. Fabian and S. Das Sarma, Rev. Mod. Phys. 76, 323 (2004)
- [55] V. E. Wood and A. E. Austin, Int. J. Magn. 5, 303 (1974)
- [56] N. A. Hill, J. Phys. Chem. B. 104, 6694 (2000)
- [57] G. A. Smolenskii and I. Chupis, Sov. Phys. Usp. 25, 475 (1982)
- [58] F. Kubel and H. Schmid, Acta Crystallogr. Sect. B. 46, 698 (1990)

- [59] J. Wang, J. B. Neaton, H. Zheng, V. Nagarajan, S. B. Ogale, B. Liu, D. Viehland, V. Vaithyanathan, D. G. Schlom, U. V. Waghmare, N. A. Spaldin, K. M. Rabe, M. Wuttig and R. Ramesh, *Science* 299,1719 (2003)
- [60] K.Y. Yun, M. Noda, M. Okuyama, H. Saeki, H. Tabata, and K. Saito, *J. Appl. Phys.* 96, 3399 (2004)
- [61] J. Li, J. Wang, M. Wuttig, R. Ramesh, N. Wang, B. Ruetter, A. P. Pyatakov, A. K. Zvezdin and D. Viehland, *Appl. Phys. Lett.* 84, 5261 (2004)
- [62] H. Béa, M. Bibes, A. Barthélémy, K. Bouzehouane, E. Jacquet, A. Khodan, J-P. Contour, S. Fusil, F. Wyczisk, A. Forget, D. Lebeugle, D. Colson and M. Viret, *Appl. Phys. Lett* 87, 072508 (2005)
- [63] P. Baettig and N. A. Spaldin, *Appl. Phys. Lett.* 86, 012505 (2005)
- [64] R. Nechache, C. Harnagea, A. Pignolet, F. Normandin, T. Veres, L-P Carignan and D. Ménard, *Appl. Phys. Lett.* 89, 102902 (2006)
- [65] R. Nechache, C. Harnagea, L-P Carignan, D. Ménard and A. Pignolet, *Phil. Mag. Lett.* 87, 231-240 (2006)
- [66] R. Nechache, L-P Carignan, L. Gunawan, C. Harnagea, G. Botton, D. Ménard, and A. Pignolet, *J. Mater. Res.* 22, 2102 (2007)
- [67] B. Meyer, J. Padilla and David Vanderbilt, *Faraday Discuss.* 114, 395 (1999)
- [68] H. Zheng, F. Straub, Q. Zhan, P-L. Yang, W-K. Hsieh, F. Zavaliche, Y-H. Chu, U. Dahmen and R. Ramesh, *Adv. Mat.* 18, 2747 (2006)
- [69] W. L. Winterbottom, *Acta. Metall.* 15, 303 1967
- [70] H. Béa, M. Bibes, S. Fusil, K. Bouzehouane, E. Jacquet, K. Rode, P. Bencok and A. Barthélémy: *Phys. Rev. B.* 74, 020101 (2006)
- [71] M. Alexe, C. Harnagea, D. Hesse and U. Gosele, *Appl. Phys. Lett.* 79, 242 (2001)
- [72] A.L. Roytburd, S.P. Alpay, V. Nagarajan, C.S. Ganpule, S. Aggarwal, E.D. Williams and R. Ramesh, *Phys. Rev. Lett.* 85, 190 (2000)
- [73] R.D. Gomez, A.O. Pak, A.J. Anderson, E.R. Burke, A.J. Leyendecker and I.D. Mayergoyz, *J. Appl. Phys.* 83, 6226 (1998)
- [74] J. Yu, J. Ahner and D. Weller, *J. Appl. Phys.* 96, 494 (2004)

## **6. Conclusions and Outlook**

### **6.1 General**

Combining high resolution with high throughput at low costs is the main current challenge in Nanotechnology, due to the high demand for rapid and cost-effective fabrication of e.g. highly ordered arrays of nanosized structures from a broad range of materials. To alleviate the high costs and limitations of conventional lithography, various forms of parallel lithography such as molding, stamping, imprinting and stenciling have been revisited to investigate their potential as “unconventional” nanofabrication and patterning alternatives.

In this thesis, we focused on stenciling as it is an approach with considerable potential for overcoming many of the challenges faced by current conventional techniques and it is a valuable tool for pursuing fundamental research in academia. While offering a high degree of freedom in choosing the physical vapor deposition method, stenciling is in principle applicable to the deposition of various materials (e.g. metals, semiconductors, complex oxides) on a wide range of substrates. Without being a “patterning competitor” for CMOS technology, stenciling represents a fine solution for local nanometer scale patterning on “unconventional” surfaces (fragile, functionalized), non-planar surfaces such as MEMS or CMOS chips or mechanically unstable such as cantilevers and membranes [1-3].

Along with exploring new routes for fabricating nanostructures, the controlled growth of nanostructured materials with novel integrated functionality represents a stimulating challenge in fundamental research faced by the materials science community. Understanding growth processes and the relationship between the size/structure and properties of nanoscale multifunctional materials is necessary to provide essential

background knowledge needed to sustain the present pace of technological innovation and miniaturization in society today.

## 6.2 Summary of findings

A primary task within these studies was to assess the capability of stenciling, as a *general-purpose* nanoscale patterning method that combines high resolution, high purity and high flexibility with respect to the choice of deposited material and substrate. From the results obtained in this work, the main conclusions regarding the stencil's feasibility to pattern at the nanoscale can be outlined as follows:

(i) Nanostenciling is a process which is directly applicable to the deposition and positioning of a variety of materials (e.g. metals, semiconductors, oxides) onto a wide range of substrates [4-6]. It involves a reduced number of steps compared to any resist-based lithography process and generates 3-D nanoscale structures straightforwardly and accurately. There is almost unlimited freedom in the choice of vapor deposition technique, nevertheless the combination of pulsed laser deposition and stenciling offers the highest flexibility in exploring nanoscale fabrication of various material systems.

(ii) The method can be applied at RT or high temperature and is highly compatible with high or ultra-high vacuum technology, making it a reliable option for local deposition of functional materials on standard (flat, unprocessed) and non-standard (curved, functionalized) substrates. The most accurate replication of the apertures is obtained at low temperature and at low pressure or in vacuum.

(iii) The deposition through stencils suffers from two main drawbacks: gradual clogging of apertures and membrane deformation due to the deposition-induced stresses. These issues prompt the development of cleaning recipes such as selective etching of the material deposited on the sieves and finding fabrication solutions for improving the mechanical stability (i.e. reinforcement) of the stencil membrane.

### **Ge/Si nanostenciling**

Employing FIB-based stencils at RT, the minimum attainable Ge structure (~100 nm) was mainly limited by the ability to create small apertures in the stencil's membrane

rather than by deposition induced shadowing effects which usually accompany replication through the apertures of a mask. This prompts an optimization of the FIB milling process to realize apertures in the range of 10–50 nm, thus allowing the fabrication of smaller structures.

A 1:1 aspect ratio (width/depth) of the apertures in the membrane provides 90% material transfer efficiency while an aspect ratio of 1:2 results in a drop in efficiency to almost 50%. The smallest apertures (i.e. ~ 80-90 nm) clogged after the deposition of an equivalent film thickness of about 3 times the aperture diameter. At the same time, the material deposited on the the free-standing, large-opened membrane window (area over  $1 \times 1 \text{ mm}^2$ ) caused visible bending due to tensile stress.

LIL-based stencils (aperture sizes ~350nm) were particularly useful “tools” for organizing crystalline Ge islands and exploring their growth kinetics when deposition and patterning was performed at high temperature [7]. Ge islands nucleation sites were entirely preserved by the aperture pattern drawn in the nanostencil. We detected the formation of an anomalously thick “wetting layer” (up to 6nm thick) in each aperture location and observed that the morphological evolution of the structures with coverage follows a modified Stranski-Krastanov growth mode, due to the finite size of the wetting layer. We did not detected well defined facets for the dots but mostly rounded features which are attributed to the highly energetic character of PLD and a high growth rate. Micro-Raman spectroscopy indicated that the islands are crystalline Ge and that they followed the substrate’s crystallographic orientation.

We showed that the density and physical dimensions of the dots can be adjusted by varying the laser repetition rate. Furthermore, we observed that a high laser repetition rate (i.e. high growth rate) increased the QDs density per deposited site and the Si-Ge intermixing is kinetically limited. Future work might focus onto the correlation between other deposition parameters such as laser fluence and the Ge dots’ morphology and their density per deposited site.

Work is ongoing to investigate via X-ray photo-emission electron microscopy (XPEEM)<sup>1</sup> if Ge is diffusing between stencil sites (i.e. chemical mapping of the samples) since the XPEEM has been reported to provide high resolution and surface sensitivity [8].

---

<sup>1</sup> Measurements performed at Canadian Light Source Synchrotron facility, Saskatoon, Canada.

## **ABO<sub>3</sub> perovskites nanostenciling**

In the first phase of our experiments, we dealt with concurrent PLD-based nanostructuring and patterning of barium titanate (BaTiO<sub>3</sub>) on (100) Nb-doped strontium titanate (SrTiO<sub>3</sub>) and on Pt coated Si(100). We reported for the first time that we can obtain well-ordered nanostructures from complex materials by PLD and reusable stencils [4]. The crystal structure and chemical composition as well as the functionality (in this case ferroelectricity investigated by piezoresponse force microscopy) of the BaTiO<sub>3</sub> grown through the nanostencils were conserved.

When deposited at RT and in vacuum, the structures exhibit the least amount of broadening (~10% larger than the aperture nominal diameter). The patterned islands were amorphous and an annealing treatment was necessary to crystallize them in the perovskite tetragonal phase. After annealing the islands were polycrystalline and formed from grains with reduced size (~30 nm). The weak piezoelectric response we measured was due to an intrinsic size effect induced by a reduced size of the BaTiO<sub>3</sub> grains. Being a non-invasive process, nanostenciling eliminates the doubts about the extrinsic nature of size effects (i.e. damages occurring during fabrication and patterning as seen in FIB or EBL processes are avoided). Depositions carried out directly at high temperature and in a low O<sub>2</sub> atmosphere lead to epitaxially grown ordered structures that showed rather low values for the out-of-plane piezoelectric coefficients  $d_{zz}$ . In this case, the optimal pressure range for PLD stenciling was established to be between 0 and 10 mTorr O<sub>2</sub>, however oxygen vacancies occurring in the structures grown in the pressure range limited their ferroelectric response.

In the case of multiferroic complex oxides, stenciling proved to be a valuable patterning technique, however we encountered difficulties in synthesizing the stable multiferroic perovskite phase via PLD in the case of BiFeO<sub>3</sub>. Nevertheless, the patterning process was successfully employed for patterning Bi<sub>2</sub>FeCrO<sub>2</sub>, a newly predicted and recently synthesized quaternary multiferroic oxide. In this case we obtained epitaxial structures which we proved to be both ferroelectric and magnetic at RT.

The results obtained in this work strongly endorse the combination of nanostenciling with PLD as one of the most promising unconventional approaches for

parallel nanostructuring and surface patterning of complex functional materials. Furthermore, it has successfully demonstrated the functional properties in patterned magnetoelectric (multi)ferroic structures.

## 6.3 Outlook

### **2<sup>nd</sup> Generation stencils: improved design and “life-time”**

Two main directions can be followed for improving the accuracy and reliability of the process: (i) the optimization of stencils' design and fabrication and (ii) extending their life-time by developing cleaning recipes or protective coatings.

On one hand smaller apertures - if possible down to 10 nm - while maintaining the ability to vary shape and spacing are still sought after. On the other hand a higher mechanical stability of the membranes is desired while larger areas are perforated (opened) to increase the pattern size on the substrate of choice, thereby allowing for easier characterization of the patterns. Solutions to stabilize the membrane locally by introducing stabilization structures should be thought of (designed) before opening large membrane windows. We are currently testing the ability of nanostenciling at RT using FIB-prepared stencils having active SiN ultra-thin windows ( $1 \times 1 \text{ mm}^2$  wide and 50-100 nm thick) supported by 256  $\mu\text{m}$  thick Si frames. The main difficulty encountered during the milling of small apertures is ion beam drifting on the membrane surface resulting in the enlargement and sometimes distortion of the projected motif. Due to a better aspect ratio (width/depth) of the apertures and the larger active area of the membrane, the transfer efficiency is higher (approaching 100%) than in the case of LIL-based stencils (approx. 80%).

### **Nanostenciling for assisted self-organization**

A complementary path we investigated, although to a smaller extent, is that of assisted self-organization mechanisms on artificially nanostructured substrates by means of ion implantation (or ion sputtering) through nanostencils. The advantages of this combination of methods are the simultaneous control of the surface pattern's sizes and

locations (provided by the apertures realized in the stencils) and the ability to scale down the inter-feature distances of the deposited material. Precise control over characteristics of the patterned nanostructures (e.g. size, shape, pitch) allow for investigations into the influence of various experimental parameters (e.g. growth temperature, deposited thickness) on nanostructure formation.

Research can be directed towards understanding how concave and convex surfaces influence nanostructure formation as compared with planar surfaces and what factors govern the nucleation phenomenon in these particular situations.

### **Surfaces templating of growth catalysts via nanostenciling**

A nanostencil based patterning approach could be used in combination with a vapour-liquid-solid (VLS) growth technique, for the controlled positioning of vertical, single crystal semiconductor nanowires on appropriate substrates. Usually, before VLS is employed, site positions for growth and wiring are realized by photolithography patterning. To offer a higher degree of flexibility in choosing the combination of deposited material/substrate and to eliminate the inconvenience of resist-based processes, nanostencils could be used to control the deposition of a growth catalyst.

In a first step, specifically designed stencils could be used to deposit ordered arrays of metallic structures at specific locations. Once these templated surfaces are prepared they will serve as model catalysts for further material growth.

For example, gold (Au) particles can be selectively patterned on Si(100) or Si(111) substrates such as to act as “seeds” for VLS growth, of semiconductor (e.g. Si, C, SiC) nanowires or nanoprobes (tips). The VLS growth mechanism can be realized by means of chemical vapour deposition (CVD) techniques. Then, if needed, the obtained semiconductor structures can be plated with metal to offer the necessary electrical conductivity for specific purposes.

Currently there is an ongoing interest in finding reliable methods to grow such nanofabricated structures. A couple of examples of potential applications are the fabrication of atomically sharp nanoneedles or nanoprobes for the atomic scale imaging of materials, or conductive nanowires to be used as ultra-fine probes to contact biological components such as cells or even molecules.

## 6.4 References

- [1] J. Brugger, J. W. Berenschot, S. Kuiper, W. Nijdam, B. Otter and M. Elwenspoek, *Microelectron. Eng.* 53, 403 (2000)
- [2] A. R. Champagne, A. J. Couture, F. Kuemmeth and D. C. Ralph, *Appl. Phys. Lett.* 82, 111 (2003)
- [3] S. Egger, A. Ilie, Y. Fu, J. Chongsathien, D-J. Kang and M. Welland, *Nano Lett.* 5, 15 (2005)
- [4] C. V. Cojocaru, C. Harnagea, F. Rosei, A. Pignolet, M. A. F. van den Boogaart, and J. Brugger, *Appl. Phys. Lett.* 86, 183107 (2005)
- [5] C. V. Cojocaru, F. Ratto, C. Harnagea, A. Pignolet and F. Rosei, *Microelectron. Eng.* 80, 448 (2005)
- [6] C. V. Cojocaru, C. Harnagea, A. Pignolet and F. Rosei, *IEEE Trans. On Nanotechnology* 5, 470 (2006)
- [7] C. V. Cojocaru, A. Bernardi, J. S. Reparaz, M. I. Alonso, J. M. MacLeod, C. Harnagea and F. Rosei, *Appl. Phys. Lett.* 91, 113112 (2007)
- [8] F. Ratto, A. Locatelli, S. Fontana, S. Kharrazi, S. Ashtaputre, S. K. Kulkarni, S. Heun and F. Rosei, *Small* 2, 401 (2006)

# List of publications

## Articles published in refereed journals

**C.V. Cojocaru**, A. Bernardi, J.S. Reparaz, M.I. Alonso, J. MacLeod, C. Harnagea and F. Rosei, “*Site-controlled growth of Ge nanostructures on Si(100) via pulsed laser deposition nanostenciling*”, Applied Physics Letters 91, 113112, (2007)

C. Harnagea, **C.V. Cojocaru**, R. Nechache, O. Gautreau, F. Rosei and A. Pignolet, “*Towards ferroelectric and multiferroic nanostructures and their characterization*”, International Journal of Nanotechnology, in press (scheduled for 2008)

**C.V. Cojocaru**, C. Harnagea, A. Pignolet and F. Rosei, “*Nanostenciling of functional materials by room-temperature pulsed laser deposition*”, IEEE Transactions on Nanotechnology 5, 470-477, (2006)

C. Harnagea, **C.V. Cojocaru**, O. Gautreau, R. Nechache, F. Normandin, T. Veres and A. Pignolet, “*Piezoresponse force microscopy of PLD-grown multiferroic BiFeO<sub>3</sub> films and mesostructures*”, Integrated Ferroelectrics 83, 1-12, (2006)

**C.V. Cojocaru**, F. Ratto, C. Harnagea, A. Pignolet and F. Rosei, “*Semiconductor and insulator nanostructures: challenges and opportunities*”, Microelectronic Engineering 80, 448-456, (2005)

**C.V. Cojocaru**, C. Harnagea, M. Van den Boogaart, J. Brugger, F. Rosei and A. Pignolet, “*Complex oxide nanostructures by pulsed laser deposition through nanostencils*”, Applied Physics Letters 86, 183107, (2005)

## Conference proceedings

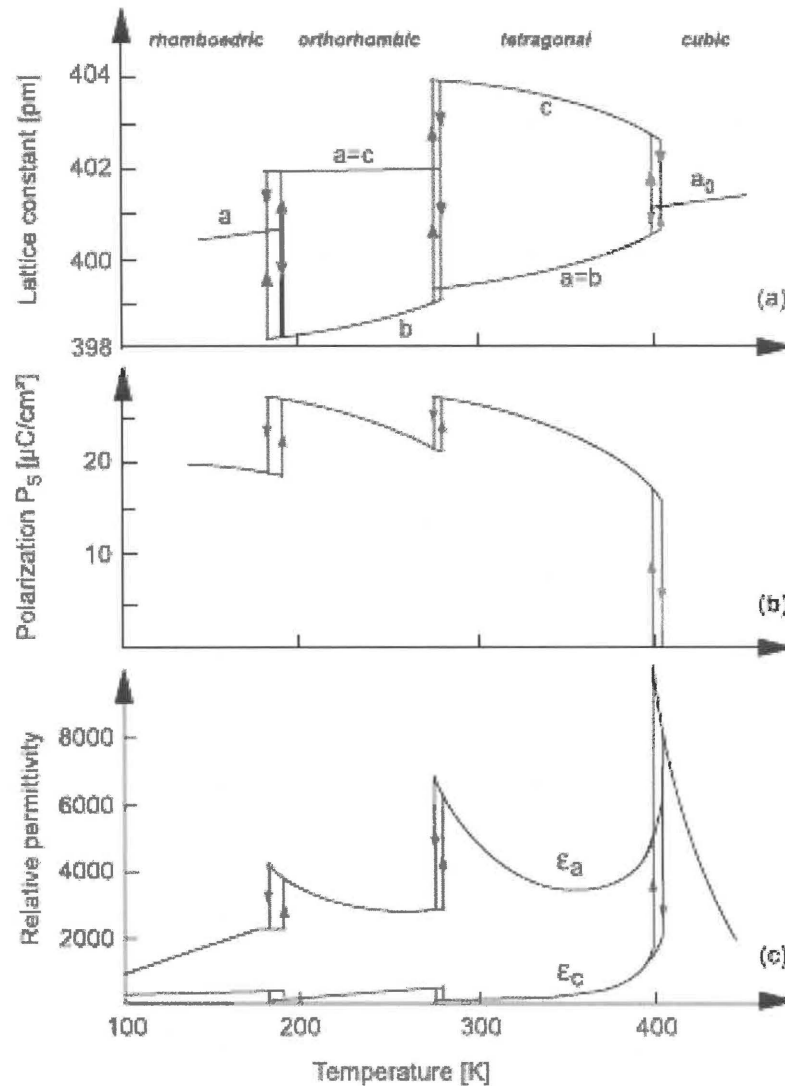
C. Harnagea, **C.V. Cojocaru**, O. Gautreau, F. Rosei and A. Pignolet, “*Ferroelectric mesoscopic structures by room-temperature PLD*”, Journal of Physics: Conference series 59, 636 - 639, (2007)

C. Harnagea, **C.V. Cojocaru** and A. Pignolet, “*Local ferroelectric switching properties in BiFeO<sub>3</sub> microstructures and their piezomagnetic response*”, Materials Research Society Symposium Proceedings, Vol. 902E, 0902-T10-57.1., (2006)

**Book chapter:** **C.V. Cojocaru**, F. Cicoira and F. Rosei “*Alternative nanofabrication techniques for non-CMOS applications*” in the Nanofabrication: Fundamentals and Applications, edited by Ampere A. Tseng, World Scientific Publishing Company, 5 Toh Tuck Link, Singapore 596224, (2007)

# Appendix A

Various properties of barium titanate ( $\text{BaTiO}_3$ ) as a function of temperature.

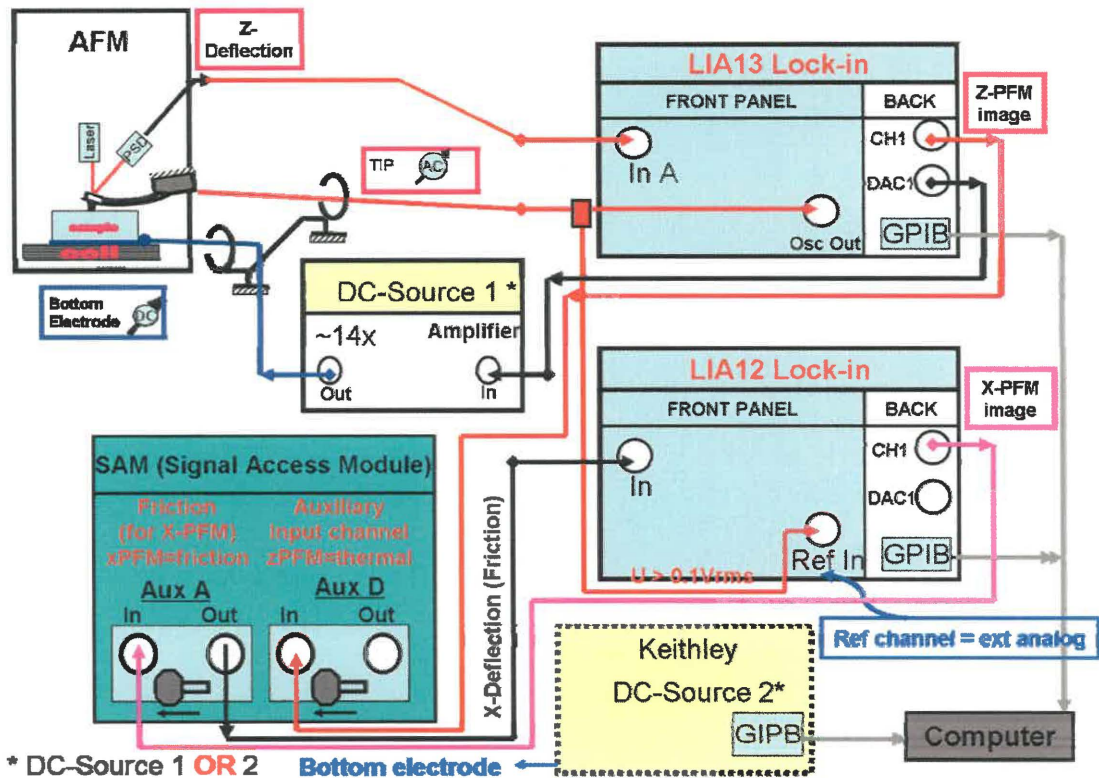


(a) Lattice constants, (b) spontaneous polarization  $P_s$  and (c) relative permittivity  $\epsilon_r$ , of barium titanate ( $\text{BaTiO}_3$ ) as a function of temperature. Anisotropic properties are shown with respect to the lattice direction.

[from U. Böttger, *Dielectric properties of polar oxides, Chapter 1*, in **Polar oxides: properties, Characterization and Imaging**, edited by R. Wasser, U. Böttger and S. Tiedke, Wiley VCH Berlin, 2004]

## Appendix B

### Piezoresponse force microscopy (PFM) – experimental set-up



We performed PFM measurements using a modified DI-EnviroScope (Veeco) AFM, and a computer-controlled lock-in amplifier (*Signal Recovery* Model 7265) connected to the AFM via a Signal Access Module. In a standard PFM experiment two lock-in amplifiers can be used to detect both components accessible together and simultaneously with the sample topography. Hysteresis measurements were obtained using an auxiliary digital to analog converter of the lock-in amplifier (or a Keithley 2400 DC sourcemeter), by applying a DC voltage that is swept between the chosen maximum and minimum values (e.g. -10 V to +10 V).

# Résumé

## 1. Introduction

### 1.1 Nanostructures fonctionnelles de matériaux fonctionnels

Les matériaux fonctionnels sont généralement décrits comme les matériaux avec des propriétés physiques et chimiques sensibles aux changements de différents paramètres extérieurs, tels que la température, la pression, les champs magnétiques et électriques, l'irradiation par de la lumière, etc. qui sont capables d'effectuer des fonctions spécifiques grâce à leurs propriétés de réponse intrinsèques. En voici quelques exemples: matériaux diélectriques, pyroélectriques, piezoélectriques, ferroélectriques, semi-conducteurs, conducteurs ioniques, supraconducteurs, matériaux magnéto- et électro-optiques, ainsi que matériaux magnétiques. Ces matériaux étant à la base des nouveaux systèmes intelligents permettent à ces derniers de sonder, détecter, analyser, et réagir (répondre) aux changements des différents paramètres extérieurs.

L'aspect clé du développement de nouveaux matériaux fonctionnels et de leur intégration dans des systèmes intelligents réside dans la possibilité de contrôler la relation entre leurs propriétés structurales et fonctionnelles. L'étude et le développement de ces matériaux permet ainsi d'améliorer leur réponse à la variation de certains paramètres du système (température, pression etc.) et d'optimiser leurs fonctionnalités. En particulier, à l'échelle nanométrique, avec l'amélioration de notre compréhension des propriétés physiques et de notre capacité de contrôler la morphologie des structures à cette échelle, il existe un réel potentiel de création d'un grand nombre de matériaux nouveaux avec de nouvelles propriétés, engendrant de nouvelles fonctions, permettant ainsi de nouvelles applications.

Pour le moment, nous sommes en mesure d'identifier un large spectre de matériaux nanocristallins ou nanostructurés: nanoparticules, nanofils, nanotubes, points quantiques, puits quantiques, etc. dont les propriétés fonctionnelles sont reliées aux effets surfaciques ou quantiques qui, à l'échelle du nanomètre, dominant par rapport à leurs

propriétés conventionnelles ce qui les rend très attrayants pour le développement de nouveaux matériaux fonctionnels. Dans ce contexte, la fabrication contrôlée de différents types de structures de taille nanométrique (nanostructures) devient nécessaire. Des méthodes de lithographie avancée utilisant une irradiation à une longueur d'onde inférieure à celle de la lumière visible (par ex. rayons X ou faisceaux d'électrons) mais qui sinon utilisent la technologie conventionnelle, est en constante évolution, ceci dans le but de diminuer la limite de résolution et de réaliser une structuration à l'échelle nanométrique.

Cependant, les points quantiques, les nanotubes ou les nanofils de haute qualité sont souvent les résultats d'un procédé de fabrication basée sur l'auto-assemblage (arrangement naturel des atomes sur des surfaces) et l'auto-organisation (sur des surfaces ayant un motif) à l'aide des techniques de croissance telles que dépôt par évaporation chimique (CVD), dépôt par évaporation physique (PVD), comme l'épitaxie par jet moléculaire (MBE), ou le dépôt électrolytique. De point de vue technologique, ces techniques de fabrication, simples et peu coûteuses, ont le grand désavantage de manquer de contrôle sur la taille et la forme de la structure produite ainsi que sur son positionnement exact.

Les techniques alternatives à la lithographie traditionnelle qui sont présentement développées démontrent un grand potentiel quant à leur flexibilité et à leur faible coût. Dans ce contexte, cette thèse servira à démontrer le potentiel offert par la technique de l'utilisation de nano-masques ou nano-pochoirs ou "*nanostenciling*" pour la production de nanostructures fonctionnelles organisées de haute qualité.

## **1.2 Organisation de la thèse**

Dans le cadre de cette thèse, nous allons nous concentrer sur *la croissance contrôlée, le positionnement et la caractérisation des matériaux fonctionnels nanostructurés* tels que les hétérostructures semi-conductrices (Ge/Si) et les oxydes fonctionnels complexes de type perovskite en utilisant des techniques de fabrication de patrons (*structuration*) *non-conventionnelles*. La principale approche étudiée et développée dans le cadre de ce projet se base sur le "*nanostenciling*", c'est à dire la croissance sélective des nanostructures par dépôt à travers des masques-miniatures.

L'utilisation de ces masques, avec des ouvertures nanométriques percées dans des membranes très fines auto-supportées, placés à une très faible distance du substrat, assure un dépôt direct, sélectif et bien défini de matériaux variés sur presque tous types de surface. Par conséquent, cette méthode convient parfaitement au prototypage parallèle sur des surfaces fragiles ou fonctionnalisées. C'est un procédé parallèle, qui ne nécessite pas de résine photosensible, qui est hautement compatible avec la technologie du haut et ultra-haut vide. Ces avantages définissent le nanostenciling comme une technique de choix pour le prototypage parallèle à l'échelle nanométrique et comme un outil extrêmement utile pour les études des systèmes de nouveaux matériaux originaux.

En utilisant l'ablation laser (PLD), nous avons concentré nos efforts sur le dépôt de nano-motifs "nano-structuration" des structures suivantes: (i) hétérostructures germanium – silicium, intéressantes pour la fabrication de dispositifs opto-électroniques à base de Si, et (ii) oxydes ferroélectriques de type perovskite, qui sont d'excellents candidats pour les applications à la fabrication de mémoires ferroélectriques intégrées (NV-FeRAM).

## **2. Structuration à l'échelle nanométrique: concepts et stratégies**

### **2.1. La grande quête de la structuration à l'échelle nanoscopique ou nanostructuration**

La demande pour la structuration ou structuration à l'échelle nanométrique des couches minces de matériaux fonctionnels provient des domaines de la fabrication des circuits intégrés en microélectronique, des supports pour le stockage et l'affichage de l'information de la fabrication des systèmes micro/nano-électromécaniques (MEMS/NEMS), des détecteurs et commandes miniaturisés, des dispositifs micro-fluidiques, des composants micro-optiques, des cristaux photoniques, des bio-puces et des surfaces biocompatibles nanostructurées. Pour tous ces domaines, l'avancement de la fabrication à l'échelle nanométrique et des techniques de structuration s'avère crucial afin d'assurer leur développement et leur commercialisation subséquente.

La lithographie à projection optique (OPL) a été une forme de lithographie utilisée dans la communauté industrielle de la microélectronique depuis plusieurs

décennies et sera sûrement utilisée au moins encore une dizaine d'années. La miniaturisation des transistors et des supports de stockage de données à l'aide des techniques de lithographie plus sophistiquées est un exemple remarquable de développement technologique continu. Ces techniques de fabrication sans cesse améliorées, développées et ré-inventées afin de pouvoir continuer à développer la microélectronique (par ex. UV lointain (DUV), UV extrême (EUV) ou lithographie par faisceau d'électrons (EBL)) sont dédiées au dessin des motifs dans des photorésines ou des résines sensibles à l'irradiation des électrons, appliquées au moyen de tournette (spin-coating) sur des surfaces semi-conductrices ultra-plates. L'adaptation de ces méthodes de lithographie aux autres domaines pouvant impliquer la structuration et le dessin des architectures atypiques sur des substrats non-conventionnels représente cependant un défi très important.

On retrouve des conditions moins restrictives dans des environnements de recherche où la productivité à grande échelle ne représente pas un objectif majeur. Dans un laboratoire universitaire, il est plus important d'utiliser des techniques de nanofabrication très flexibles qui permettent d'étudier de manière fondamentale un grand nombre de phénomènes physiques et d'explorer des nouveaux types d'ingénierie à l'échelle nanométrique dans des domaines telles que la science des matériaux, la microscopie, l'optique nanométrique et l'optoélectronique organique ou encore les sciences biologiques pour n'en nommer que quelques unes. Par exemple, la communauté de recherche en optique cherche à fabriquer des points et fils quantiques (QDs et QWs) avec des niveaux d'énergie très bien contrôlés, la communauté qui étudie la microscopie à champ proche met ses efforts sur le développement et l'utilisation d'outils de caractérisation à l'échelle atomique, tandis que les communautés des chimistes et des biologistes tentent d'utiliser l'auto-assemblage pour créer des molécules qui serviront de matériaux de construction à l'échelle nanométrique.

Pour atteindre ce but, il est important de développer des méthodes de structuration appropriées aussi bien pour la fabrication que pour le positionnement précis de nanostructures sur des surfaces non-lisses (par ex. pré-traitées, courbées ou rugueuses). Dans ce contexte, une variété d'autres formes de lithographie parallèle telles que le moulage, l'étampage, l'impression ou stencilling sont revisités et considérés quant à

leur potentiel pour la nanofabrication non-conventionnelle et le structuration alternatif, techniques qui pourrait repousser des limites de la lithographie conventionnelle.

## 2.2 Top-down versus Bottom-up

Deux approches principales de fabrication de micro- et nanostructures organisées ou aléatoires existent qui sont appelée "*top-down*" et "*bottom-up*". Le concept "*top-down*" peut être basé sur différentes méthodes de lithographie permettant de sculpter des structures à partir de matériau massif. Généralement, le matériau massif est un film mince continu déposé préalablement par une méthode de dépôt chimique ou physique sur un substrat approprié. Contrairement à l'approche "*top-down*", les techniques "*bottom-up*" utilisent des interactions intrinsèques inter-atomiques, moléculaires ou colloïdales dans le but d'assembler les blocs élémentaires en nanostructures séparées bi- ou tridimensionnelles. Le processus d'auto-assemblage, que l'on définit comme une organisation autonome des composantes en structures et motifs au-delà de l'intervention humaine, est un exemple-clé du processus parallèle de *bottom-up* qui génère des nanostructures organisées.

L'approche *top-down* peut utiliser les techniques de fabrication en série et en parallèle des structures nouvelles et/ou répliquées, typiquement bi-dimensionnelles (2D), sur les surfaces largement supérieures à la taille de ces structures. La problématique de fabrication des nanostructures organisées peut généralement être séparé en deux grandes parties: l'écriture et la réplication. Les deux procédés se réfèrent au concept de patron "maître" qui servira pour réplication de multiples copies. La réplication du patron-maître représente la façon la plus appropriée pour la production de plusieurs copies de nanostructures. Par conséquent, la création de patrons de haute précision combinée à des procédés de réplication à bas coût s'avère être l'approche la plus pratique et la plus utile pour l'avancement de la Nanotechnologie. L'approche du nanostenciling que nous étudions en détails fait partie de cette approche.

Outre les modèles mentionnés ci haut, de nombreux efforts ont été récemment faits pour élaborer d'autres techniques pour la fabrication de nanostructures via l'approche *bottom-up*. Comme on l'a vu plus haut, celles-ci utilisent la tendance naturelle

des atomes et des molécules à s'assembler et à former des structures régulières. Cet auto-assemblage "naturel" représente un excellent exemple de l'approche bottom-up qui est un procédé de fabrication parallèle.

Cependant, certains problèmes empêchent une utilisation de l'auto-assemblage naturel. Par exemple, le fonctionnement des dispositifs basés sur les points quantiques (QDs) repose sur la structure électronique des nanostructures confinées. Celle-ci, à son tour, dépend de la taille, de la forme, de la cristallinité ou de la composition chimique des points quantiques. Par conséquent, l'une des conditions requises pour l'exploitation de ces nanostructures est une distribution de taille et de forme très étroite. Cependant, l'auto-assemblage produit généralement des nanostructures ayant des distributions de tailles très larges, ce qui peut empêcher un fonctionnement correct du dispositif.

Le positionnement exact et parfaitement contrôlé des nanostructures en utilisant l'approche bottom-up est un défi extrêmement difficile. Dans la plupart des cas, le processus de nucléation des nanostructures se produit de façon aléatoire et leur croissance et coalescence subséquente ne modifient pas leur position de façon significative. Cependant, un positionnement ordonné à l'échelle nanométrique peut être parfois atteint à l'aide des caractéristiques intrinsèques des matériaux utilisés, par exemple en exploitant l'énergie des contraintes élastiques dans un système hétéroépitaxial. Ainsi, l'auto-assemblage des nanostructures devient dans certains cas une approche attrayante qui mérite une étude additionnelle afin de mieux comprendre et contrôler ces processus.

L'auto-organisation des nanostructures peut également être réalisée durant la croissance de celles-ci sur des surfaces sur lesquelles un patron a été réalisé artificiellement. Par exemple, pour un contrôle spatial de la croissance des nanostructures, les techniques top-down de haute résolution telles que lithographie optique, d'électrons ou de ions (par ex. LIL, EBL, FIB) ou les techniques d'impression ou d'étampage à l'échelle microscopique (par ex. NIL) sont utilisées pour la préparation des patrons, sur lesquels, par la suite, les nanostructures fonctionnelles réalisées par une technique bottom-up vont germer croître et seront finalement organisées (on parle alors d'aide à l'organisation ou d'organisation assistée).

## 2.3 Nanostenciling

Notre intérêt envers le développement et les applications de la technologie du nanostenciling à la fabrication de nanostructures fonctionnelles a été suscité par plusieurs caractéristiques attrayantes de cette méthode. Parmi celles-ci, notons:

(i) Le procédé est parallèle et peut être utilisé pour le dépôt direct de matériaux différents sur une grande gamme de substrats. Il implique un nombre réduit d'étapes à réaliser comparé aux techniques de lithographie à base des résines (polymères) et permet de fabriquer des structures tri-dimensionnelles.

(ii) Le procédé est compatible avec la technologie du haut et ultra-haut vide, ce qui la rend très intéressante pour le dépôt local de nanostructures de matériaux fonctionnels de grande pureté ayant une haute définition.

(iii) Cette méthode peut être utilisée à la température ambiante aussi bien qu'à haute température; elle permet de créer des systèmes multi-couches et s'avère d'être parfaitement adaptée pour le prototypage parallèle des surfaces fragiles ou fonctionnalisés.

(iv) Il y a une liberté illimitée quant au choix de la technique de dépôt par évaporation, lorsque la fabrication de nanostructures à l'aide des nanopochoirs n'interfère pas avec la dynamique de croissance des espèces déposées, absence d'interaction qui assure alors le contrôle précis du positionnement des nanostructures.

(v) Les patrons (pochoirs) – maîtres produits à l'aide des techniques de lithographie conventionnelles sont réutilisables et peuvent être nettoyés entre les utilisations, ce qui permet leur utilisation multiple.

Ces propriétés de la technique du nanostenciling la rendent extrêmement intéressante en tant qu'outil pour l'étude de nouveaux matériaux (par ex. des oxydes multiferroïques) et en tant que technique de choix pour le prototypage à l'échelle nanométriques dans des conditions de laboratoire.

### 3. Approche expérimentale et caractérisation

#### 3.1. Procédés de fabrication des nanostencils

Pour le design et la fabrication des masques pochoir, ceux-ci pouvant être représenté comme une membrane perforée sur un cadre-support, deux approches peuvent être appliquées: le Wafer Flow Process (WFP) et le Membrane Flow Process (MFP), figure 3.1 / p.44.

Selon le schéma WFP, tous les cycles du dessin du patron peuvent être réalisés à l'aide d'outils typiques de microfabrication utilisés dans la technologie du silicium (par ex. la lithographie avancée et la gravure par plasma d'ions réactifs (RIE)) sur des gaufres solides, résultant en la réalisation ultime d'une membrane perforée, ou l'ouverture de la membrane est la dernière opération effectuées. Plusieurs méthodes ont été conçues pour la fabrication efficace des membranes qui permettant de réaliser des masques de haute résolution et de forme bien définie. Parmi celles-ci, la lithographie à interférence laser (LIL) qui est une technique relativement peu coûteuse permettant de créer des structures périodiques de taille inférieure à un micron sur des surfaces très larges (par ex.  $\text{mm}^2$ ).

Dans cette thèse, nous avons largement utilisé des puces de Si avec des membranes de SiN, chaque membrane contenant des rangées de motifs hexagonaux d'ouvertures nanométriques fabriquées par la combinaison des techniques de LIL et RIE, figure 3.3 / p.46.

Selon le procédé MFP, la membrane est fabriquée en premier en utilisant les procédés de lithographie et de gravure classique. Par la suite, le procédé complet de définition de motif est appliqué (par ex. nano-perçage par lithographie au faisceau d'électron (EBL), ou par un faisceau d'ions focalisé (FIB)).

Pour minimiser le nombre d'étapes à réaliser lors de la préparation des pochoirs, nous avons profité des avantages de la technique du FIB, figure 3.4 / p.50. Ce dernier fonctionne selon un principe similaire à celui de microscope électronique à balayage mais au lieu d'électrons ce sont des ions (par ex. du  $\text{Ga}^+$ ) qui bombardent la surface de l'échantillon. La technique du FIB peut représenter une option de choix par rapport à la lithographie avancée ou EBL, car les étapes d'application du PMMA (résine), de

l'exposition et du développement de la résine ainsi que le transfert du motif par technique de gravure par plasma sont éliminés.

### 3.2. Dépôt par ablation laser

Dans cette thèse, la technique de dépôt par ablation laser (PLD) a été choisie comme méthode de croissance en phase gazeuse. La PLD représente plusieurs avantages incontestables, tels que la variation sur une large plage de l'énergie cinétique des espèces déposées, le transfert stœchiométrique du matériau de la cible au substrat sous certaines conditions expérimentales (incluant le contrôle de la température, de l'interaction entre les espèces ablatées et l'oxygène moléculaire introduit dans la chambre d'ablation) et la possibilité de fonctionnement dans une large gamme de pressions s'étendant du UHV à 100 Pa. La PLD, une technique extrêmement flexible de dépôt des films minces stœchiométriques sur une large variété de substrats, qui, lorsque combinée au stenciling, est tout à fait appropriée pour le prototypage des matériaux nanostructurés.

Le schéma du montage d'ablation laser utilisé dans cette thèse est montré sur la figure 3.6 / p.60. Ce montage contient un laser à gaz excimer KrF GSI Lumonics ( $\lambda = 248$  nm, la largeur à mi-hauteur de l'impulsion laser  $\tau = 15.4$  ns) et une chambre de dépôt. Le faisceau laser est dirigé sur la cible au moyen d'un système de lentilles. Le faisceau laser est focalisé sous angle de  $45^\circ$  sur une cible de poudre de céramique compressée (par ex. BaTiO<sub>3</sub>,) placée dans la chambre d'ablation.

Les pochoirs sont fixés mécaniquement de façon temporaire sur un substrat placé en face de la cible en rotation. La température du substrat lors du dépôt a été variée entre la température ambiante et 800 °C.

Les techniques de caractérisation de la morphologie, des propriétés structurales, ainsi que la composition et les propriétés fonctionnelles des nanostructures fabriquées dans ce travail englobent diverses microscopies, par ex. microscopie électronique à balayage (SEM), à force atomique, piezo-réponse, à force magnétique (AFM, PFM, MFM), ainsi que la diffraction des rayons X (XRD) et la spectroscopie micro-Raman.

### 3.3. Géométrie de dépôt

La géométrie la plus convenable pour le dépôt à travers un pochoir implique une source de dépôt "ponctuelle" (S), une distance source-substrat relativement large (D) et une distance minimale entre le substrat et le masque (G). Ce sont des conditions de base qui vont minimiser l'effet d'ombrage (élargissement de taille des structures déposées) qui est toujours présent lors de la croissance directe à travers un masque. La PLD est une technique qui satisfait largement ces conditions. Dans nos expériences de dépôt par PLD, le faisceau laser a été focalisé sur une cible à l'aide d'un système de lentilles de façon à minimiser la taille de la tache laser à un diamètre de 1 mm en respectant ainsi la condition d'une source quasi-ponctuelle. Cependant, nous n'avons pas beaucoup de contrôle sur la distance entre le masque et le substrat car les pochoirs ont toujours été fixés manuellement.

Dans l'approximation de l'absence de diffusion de surface, nous pouvons estimer la largeur ( $w_B$  – largeur de la base et  $w_T$  – largeur de la partie supérieure d'une structure) des structures déposées à l'aide de l'équation suivante:

$$w_{B,T} = w_A \pm S \cdot \frac{G}{D} \quad (1)$$

où  $w_A$  est la taille de l'ouverture dans la membrane, figure 3.7 / p.61.

Généralement, la distance entre le masque et le substrat devrait être minimisée (idéalement 100 nm ou moins) et le masque devrait être parallèle à la surface de l'échantillon. Cependant, cet espacement n'est pas uniforme à cause des irrégularités de la surface du substrat, de la présence de particules étrangères, de la rugosité ou encore du fléchissement de la membrane. L'analyse de nombreuses micrographies SEM de différents types de structures déposées donne un élargissement moyen des structures déposées d'environ 10 à 15 % qui peut éventuellement être minimisé par une fixation plus robuste du pochoir sur le substrat. Cependant, si le pochoir est trop proche du substrat, la membrane peut alors se déformer et se briser.

L'élargissement  $w_B$  des structures déposées par rapport à la taille initiale de l'ouverture  $w_A$  peut également être due à la diffusion des espèces déposées à la surface de l'échantillon. La longueur de diffusion dépend premièrement du matériau déposé et

de la surface du substrat (température, préparation, taux de dépôt). La diminution de la température du substrat (par ex. les expériences à température ambiante) permet de diminuer considérablement la longueur de diffusion.

Une des limitations importantes de l'utilisation de la technique de nanostenciling est l'obstruction graduelle des ouvertures du masque (la diminution de la taille des trous) durant le dépôt. L'occlusion se produit lorsque le matériau déposé sur la membrane commence à s'accumuler à l'intérieur des ouvertures. Ce phénomène modifie la forme géométrique de l'ouverture et peut éventuellement causer la fermeture complète de celle-ci.

Une autre limitation de la membrane pochoir est sa déformation ou son fléchissement dû aux contraintes mécaniques. Les membranes sont très mince (env. 100-200 nm), sont très fragiles mécaniquement et se déforment sous la pression du matériau déposé dû à son coefficient d'expansion thermique différent de celui de la membrane, ainsi qu'aux contraintes internes présentes dans la couches durant le dépôt. Des efforts importants ont été récemment faits en ce qui concerne la stabilisation locale de la membrane à l'aide de structures rigides de support intégrées dans celle-ci.

#### **4. Nanostenciling d'hétérostructures semi-conductrices Ge/Si par PLD**

Nous avons étudié, pour la première fois, la nanostructuration d'hétérostructures de Ge/Si par déposition par ablation laser à travers les nanostencils réutilisables à température ambiante ou à haute température. Deux aspects de la présente étude sont à souligner : premièrement, nous démontrons une approche extrêmement flexible et sans résine (donc beaucoup plus propre) qui assure le contrôle de l'organisation des nanostructures cristallines de Ge à travers le positionnement spatial précis imposé par les pochoir, avec des applications possibles en ingénierie. Deuxièmement, de par l'utilisation de nanostencils en tant qu'outil de fabrication et de structuration, nous avons découvert de nouveaux aspects des phénomènes cinétiques lors de la croissance du Ge cristallin par ablation laser.

#### **4.1 Nanostructures de Ge/Si auto-assemblées et auto-organisées**

Le concept de la fabrication bottom-up basé sur l'auto-assemblage de type Stranski-Krastanov (SK) est une approche viable pour la fabrication parallèle et à bas coût des structures de type "point quantique". Cependant, dans un procédé SK conventionnel, le positionnement des sites de nucléation des îlots 3D est aléatoire. De plus, l'évolution de la taille des îlots dépend généralement de leur environnement immédiat, c'est à dire. de leur position relative par rapport aux îlots avoisinants et de leurs interactions. Le positionnement de nanostructures obtenues par croissance SK conventionnelle est pratiquement impossible à contrôler.

Plusieurs méthodes ont été proposées pour l'organisation des points quantiques de Ge lors de leur croissance SK et ces méthodes se basent soit sur l'influence des champs de contraintes sur les îlots lors de leur nucléation, soit sur la cinétique du processus de croissance. Les surfaces prétraitées sont utilisées pour influencer (minimiser) les processus de diffusion dans le but de prédéfinir un arrangement de sites de nucléation, prédéterminant ainsi (jusqu'à un certain point) la taille des îlots et leur organisation. Malgré ces progrès, l'auto-organisation du Ge/Si sur les surfaces prétraitées n'est pas encore une méthode suffisamment mature pour la réalisation d'architectures complexes et bien définies.

L'approche du nanostenciling que nous utilisons dans ce travail, basée sur le dépôt contrôlé à travers des nano-masques, repose sur un concept innovant qui est très différent de toutes les approches précédentes. Nous ne traitons pas le substrat de Si mais nous déposons le Ge de manière sélective sur les sites de nucléation prédéterminés (par la position des ouvertures), dans le régime de croissance de SK. Cette méthode est supposée permettre la formation de structures individuelles de qualité cristalline optimale et de performance électronique appropriée.

#### **4.2 Nanostenciling du Ge par PLD à température ambiante**

En premier lieu, nous avons évalué la possibilité du nanostenciling du Ge à température ambiante (TA). Les films et les structures de germanium ont été déposés sous vide ( $\sim 10^{-5}$  mbar), à l'aide du laser excimer KrF décrit dans le chapitre 3. Les

pochoirs ont été légèrement appuyés contre les substrats à l'aide d'attaches métalliques et cet assemblage a été placé en face d'une cible solide de Ge (pureté 99%) en rotation. Ces expériences à température ambiante ont servi pour l'ajustement des paramètres géométriques (distance cible-substrat, fixation du pochoir sur le substrat) et des paramètres de dépôt (fluence du laser, taux de répétition du laser); elles peuvent être considérées comme un procédé de référence pour le dépôt PLD des matériaux variés (par ex. des métaux, des oxydes, etc.) sur des substrats variés.

La figure 4.3 / p.89, montre un fragment du pochoir<sup>1</sup> utilisé en contact proche avec un substrat de Si pour la réplique de structures de Ge. Le positionnement exact des structures déposées a été contrôlé par le motif périodique de la membrane et est uniforme sur toute la surface de celle-ci. L'efficacité de transport (figure 4.4 / p.91) et le temps de vie du pochoir à température ambiante ont été également estimés lors de ces expériences préliminaires. Les îlots de Ge déposés à température ambiante sont amorphes et un traitement thermique est nécessaire pour la cristallisation de ces structures.

### **4.3 Structuration du Ge/Si(100) par PLD à haute température et analyse micro-Raman**

Pour l'étude de la structuration du Ge sur des substrats de Si(100)<sup>2</sup> à haute température, nous avons utilisé la technique PLD décrite dans la section précédente et les pochoirs-LIL avec des rangées de motifs d'ouvertures hexagonales (350 nm de diamètre et une périodicité de 700 nm). Pour passiver la surface de l'échantillon, la couche d'oxyde natif a été enlevée à l'aide d'une solution de HF (5%). Le dépôt de Ge a été effectué sous vide ( $\sim 10^{-5}$  mbar) à un taux de répétition de 10 Hz et à une fluence laser de  $4 \text{ J/cm}^2$ . La température du substrat a été maintenue à  $600^\circ\text{C}$ ; elle a été contrôlée à l'aide d'un thermocouple de type K installé sur le support du substrat-pochoir. Le même pochoir a été utilisé pour plusieurs dépôts consécutifs. Plusieurs échantillons d'îlots de Ge sur Si(100) ont été obtenus en variant le nombre d'impulsions laser entre 250 et 1500

---

<sup>1</sup> Les membranes SiN ( $1 \times 1 \text{ mm}^2$ ) disponibles commercialement ont été percées par FIB sur plusieurs régions de  $32 \times 32 \text{ }\mu\text{m}^2$

<sup>2</sup> Si(100) – (type n, dopé Sb, résistivité  $0.015 \text{ }\Omega\text{cm}$ )

(avec un taux de dépôt estimé à  $\sim 0.28 \text{ \AA/pulse}$  pour une distance cible-substrat de 6.5 cm).

Les images SEM, figure 4.8 / p.95, montrent que la forme des îlots évolue avec l'augmentation de l'épaisseur du Ge, et les îlots plats (2D) deviennent des agglomérations nanocristallines 3D placées au dessus des îlots plats 2D. Lors de la croissance continue, ces agglomérations se transforment en structures de "grains de café" et finalement coalescent en monocristaux.

Les îlots 2D ont des ressemblances avec une "couche de mouillage" (WL) qui précède généralement la croissance des îlots lors de la croissance SK classique. D'après les images AFM, nous pouvons conclure que les îlots peuvent croître jusqu'à 6 nm en hauteur (figure 4.7 / p.95) ce qui est environ 10 fois plus épais que la valeur critique pour la couche de mouillage conventionnelle. Cette épaisseur critique anormale pourrait être expliquée par la taille limitée des îlots 2D (WL) où les contraintes en périphérie des îlots disparaissent retardant ainsi la formation des îlots 3D. Un phénomène semblable a été observé dans le cas de l'auto-assemblage des îlots de Ge dans les ouvertures de couches ultra-fines d'oxyde de silicium. L'évolution morphologique des îlots de Ge par PLD peut être intuitivement expliquée par la croissance et la transition de forme due à la relaxation des contraintes mécaniques, un phénomène couramment observé lors de dépôts par des techniques telles que la MBE ou la CVD.

La caractérisation structurelle des agrégats de Ge a été effectuée par spectroscopie micro-Raman, une technique permettant d'extraire l'information sur la composition et les contraintes à l'intérieur des nanostructures de Ge. Les mesures optiques ont été effectuées à l'aide d'un laser  $\text{Ar}^+$  (raie à 514.5 nm) avec une dimension de la tache laser d'environ 1  $\mu\text{m}$ . Par conséquent, chaque spectre Raman, (figure 4.10 / p.98) est mesuré pour plusieurs sites de Ge à la fois.

La position spectrale et la forme du pic phononique Ge-Ge démontrent la cristallinité des structures de Ge et l'absence du pic Si-Ge autour de  $\sim 400 \text{ cm}^{-1}$  (encart de la figure 4.10 / p.98) suggère clairement qu'il n'y a pas d'interdiffusion de Si dans des structures de Ge. Ceci démontre que le phénomène d'interdiffusion est limité par le haut taux de croissance des îlots lors du dépôt par ablation laser à 10 Hz de taux de répétition. De plus, le pic phononique de Ge-Ge augmente en intensité avec l'augmentation de

l'épaisseur du matériau déposé (augmentation du nombre d'impulsions). Les spectres mesurés aux premiers stades de croissance montrent un déplacement du pic phononique Ge-Ge vers les plus hautes énergies ( $\sim 303 \text{ cm}^{-1}$ ) relié aux contraintes en compression à l'interface substrat-îlot. Les contraintes sont graduellement réduites pour les îlots plus hauts (c'est-à-dire avec un plus grand nombre d'impulsions laser), et la fréquence du pic approche la valeur conventionnelle du Ge massif ( $\sim 300.8 \text{ cm}^{-1}$ ), figure 4.10 / p.98. La présence des contraintes indique que la croissance du Ge sur le Si est effectivement basée sur les contraintes provoqués par le désaccord de maille entre ces deux matériaux et que l'orientation des cristaux de Ge est reliée à celle de la structure cristalline du substrat.

#### **4.4 Structuration du Ge/Si(111) par PLD à haute température et analyse micro-Raman**

Nous avons poursuivi l'étude de l'influence de l'orientation du substrat sur les îlots de Ge organisés en préparant une série d'échantillons déposés par pochoir du Ge sur les substrats de Si(111)<sup>3</sup>. Nous avons utilisé le même pochoir que dans la première série d'expériences sur le Si(100), en vérifiant ainsi la durabilité et la limite d'obturation des ouvertures du pochoir. Trois échantillons ont été préparés avec un taux de répétition du laser de 10 Hz, une fluence laser de  $4 \text{ J/cm}^2$  et une température de substrat de  $600^\circ\text{C}$ , la longueur de dépôt étant 250, 500 et 1000 impulsions laser. L'échantillon obtenu avec 250 impulsions laser a démontré des structures similaires à celles observées sur le Si(100) en suggérant ainsi l'absence d'influence de l'orientation cristalline du substrat, figure 4.12a / p.100). En augmentant l'épaisseur de la couche de Ge, les îlots 2D jouent de nouveau le rôle d'une couche de mouillage très épaisse (5-6 nm tel qu'observé par AFM) et des points ronds sont de nouveau formés sur le dessus de ces îlots, figure 4.12b / p.100.

La forme circulaire des îlots de Ge obtenue dans les deux cas est reliée à une combinaison de deux effets: (i) confinement fort et rapide d'un flux des espèces frappant la surface à travers des ouvertures de pochoir et (ii) la "diffusion d'angle" observée quand les espèces de haute énergie arrivent sur le substrat.

---

<sup>3</sup> Si(111) – (type n, dopé As,  $0.001\text{-}0.005 \Omega\text{cm}$ )

Le positionnement des sites reproduit très bien le patron du pochoir et les images SEM montrent que les points quantiques ont tendance à rester sur le dessus des îlots de Ge, sans diffuser vers les sites avoisinants. Nous n'avons pas observé de facettes bien définies à la surface des points mais plutôt les structures arrondies ce qui est probablement dû au caractère hautement énergétique de la PLD ainsi qu'au taux de dépôt élevé.

Les propriétés structurelles, les contraintes et la composition des îlots de Ge organisés sur le Si(111) ont été étudiée par spectroscopie micro-Raman en utilisant le montage décrit dans la section précédente. La forme spectrale et la position du pic phononique du Ge-Ge ( $\sim 300 \text{ cm}^{-1}$ ) indique une bonne cristallinité des structures de Ge. Nous avons également observé un pic de Si-Ge ( $\sim 400 \text{ cm}^{-1}$ ) pour les échantillons déposés à bas taux de répétition (1 Hz). La présence de ce pic indique l'interdiffusion du Si dans les échantillons déposés à bas taux de répétition, tandis qu'à haut taux de répétition de 10 Hz l'interdiffusion est cinétiquement limitée (figure 4.16 / p.105). Les spectres Raman des échantillons de 1000 impulsions montrent un déplacement du pic Ge-Ge vers le bleu ce qui correspond à une plus petite taille des points quantiques ayant des contraintes plus importantes. Par ailleurs, les spectres de l'échantillon de 2000 impulsions montrent un pic convolué qui correspond à la distribution de taille des points quantiques (c'est-à-dire petits et gros points), et met ainsi en évidence la présence des petits points avec des contraintes en compression (pic à  $305 \text{ cm}^{-1}$ ) et des gros points relaxés (pic à  $300 \text{ cm}^{-1}$ ), voir figure 4.17 / p.106.

#### **4.5 L'influence de taux de répétition du laser sur la densité des QDs du Ge**

Nous nous sommes posés la question de savoir si la densité et la taille des points quantiques de Ge sur le dessus des îlots 2D peuvent être contrôlées par les paramètres de dépôt (paramètres laser). Nous avons choisi de faire croître une série d'échantillons à bas taux de répétition de 1 Hz (au lieu de 10 Hz) en gardant la température des substrats de Si à  $600^\circ\text{C}$ . La distribution statistique du nombre des points quantiques par site déposé a été évaluée à l'aide de nombreuses images SEM représentant différentes parties des échantillons. Tel que montré à la figure 4.13 / p.102, pour le taux de répétition laser de

1 Hz, la densité des points quantiques du Ge est égale à environ 10-12 points par site, ce qui représente environ la moitié de la densité obtenue pour le taux de répétition de 10 Hz (20-30 points par site). Lorsqu'aucune structure de Ge n'a été observée entre les sites déposés, la réduction de la densité de points quantiques est principalement due à la désorption du Ge puisque la surface a été maintenue plus longtemps à 600°C (16 min et 40 sec pour 1 Hz et 1 min et 40 sec pour 10 Hz). Dans les deux cas, la fluence laser a été fixée à 4 J/cm<sup>2</sup> en assurant ainsi la distribution de taille des points quantiques similaire.

La densité et les dimensions des points peuvent être ajustées en variant le taux de répétition du laser. Le travail futur pourrait éventuellement être concentré sur la corrélation entre d'autres paramètres de dépôt tels que la fluence laser et la morphologie des points de Ge ainsi que leur densité.

## **5. Fabrication d'oxydes complexes fonctionnels de type perovskite par PLD et nanostencil**

Dans ce chapitre nous présentons des études sur la nanostructuration, le modelage et la caractérisation des propriétés structurales et fonctionnelles d'oxydes ferroïques, principalement des piézoélectriques et ferroélectriques, ainsi que d'oxydes multiferroïques par dépôt à travers un nanopochoir (*nanostencil*). Nous montrons que ce dépôt sélectif peut être réalisé même avec des matériaux aussi complexes que des oxydes de type perovskite, à température ambiante ou à haute température. Des structures fonctionnelles tridimensionnelles (3D) sont directement générées, ce qui élimine le besoin de recourir à des étapes susequentes de gravure généralement employées pour la structuration de couches minces. Leur fonctionnalité est étudiée par microscopie à force atomique (en mode "piezoresponse") et à force magnétique (pour les propriétés magnétiques). Les expériences présentées ici ont pour but de prouver que la technique de dépôt à travers un nanopochoir (ou nanostencil) peut devenir une technique de nanostructuration d'intérêt général qui offre à la fois une haute résolution et une flexibilité unique pour le choix de la combinaison matériaux déposés / substrat.

## 5.1 Nanostructures ferroélectriques et effets d'échelle

L'effet de taille dans les ferroélectriques, induit par la réduction des dimensions géométriques de l'échantillon, peut produire, par exemple, une diminution de la polarisation rémanente, de la permittivité diélectrique ou de la température de transition de phase, ainsi qu'une augmentation du champ coercitif, des changements dans la structure des domaines, ou d'autres phénomènes encore. Diverses méthodes incluant les approches top-down et bottom-up ont été testées et utilisées pour produire des structures ferroélectriques nanométriques de taille contrôlées. Le but de toutes ces nouvelles méthodes et procédés de fabrication est de fournir à grande échelle des réseaux de structures fonctionnelles de haute qualité, positionnés précisément sur un substrat donné, et avec des performances et à un coût comparables (voire meilleurs) que ce qui est obtenu en utilisant les procédés de photolithographie standards utilisés de nos jours.

Dans les prochaines sections nous décrivons le travail entrepris dans notre groupe pour fabriquer des nanostructures d'oxydes complexes ferroélectriques et multiferroïques par dépôt par PLD à travers des nanopochoirs, tant à température ambiante que pour des régimes à haute température. Les défis liés à la caractérisation des réseaux ordonnés de nanostructures d'oxydes fonctionnels obtenus seront également traités.

## 5.2 Nanostenciling de matériaux ferroélectrique de type perovskite

Le titanate de baryum ( $\text{BaTiO}_3$ ) est un exemple typique d'un oxyde qui cristallise dans une structure de type perovskite (figure 5.1 / p.113). Dans la limite des hautes températures (au dessus de  $T = 393\text{K}$ ),  $\text{BaTiO}_3$  est paraélectrique (non polaire) et possède une structure cristalline cubique ( $a = 3.996 \text{ \AA}$ ). Il passe par trois transitions de phase ferroélectriques lorsque la température décroît: Il passe de paraélectrique cubique à tétragonal à  $393\text{K}$ , puis de tétragonal à orthorhombique à  $278\text{K}$ , et enfin d'orthorhombique à rhomboédrique à  $183\text{K}$ , les trois dernières phases étant ferroélectrique. Comme substrat sur lequel les structures sont fabriqués nous utilisons des monocristaux de titanate de strontium ( $\text{SrTiO}_3$ )<sup>4</sup>orientés (100). Le  $\text{SrTiO}_3$  a aussi une

---

<sup>4</sup> Alternativement nous avons aussi utilisé pour quelques essais du silicium orienté (100) ainsi que du silicium recouvert de platine.

structure perovskite et est l'un des rares "*titanates*" qui soit cubique à température ambiante. Le SrTiO<sub>3</sub> est un excellent substrat pour la croissance épitaxiale de couches minces à base d'oxydes. Lorsqu'il est dopé au niobium (Nb:SrTiO<sub>3</sub>), il est conducteur électrique et peut être utilisé comme électrode pour des mesures électriques.

### 5.2.1 Structuration du titanate de baryum (BaTiO<sub>3</sub>) – température ambiante

Les premiers essais ont été faits en déposant du BaTiO<sub>3</sub> par pochoir à température ambiante (TA) et sous vide, puis les échantillons ont été recuits sous atmosphère d'O<sub>2</sub>, par procédé conventionnel ou par recuit thermique rapide, de manière à obtenir la structure cristallographique voulue.

Une première série d'expériences avec BaTiO<sub>3</sub> par pochoir a été réalisée en utilisant des masques LIL (lithographie par interférence laser) avec un tamis incorporé de SiN de 500 nm d'épaisseur possédant des ouvertures circulaires. Ces pochoirs ont un réseau de pores (de diamètre 350 nm) avec une périodicité de 1.6µm ou 700nm, qui sont ouverts sur 12 à 14 membranes libres, faiblement contraintes (LS - SiN) de 2mm de long et 100 µm de large chacune et distantes les unes des autres de 100 µm. L'assemblage substrat-pochoir est monté dans le bâti à vide d'un système d'ablation laser, en face d'une cible tournante de céramique stoechiométrique dense de BaTiO<sub>3</sub>. Un laser à excimère à KrF (Lumonics PM-800,  $\lambda = 248$  nm, durée de pulse = 15.4 ns) est employé pour l'ablation avec un angle d'incidence de 45° sur la cible et une fluence de 2 J/cm<sup>2</sup>. Les dépôts sont faits à température ambiante, sous un vide de  $1 \times 10^{-5}$  mbar ( $7.5 \times 10^{-3}$  mTorr), avec une fréquence de répétition du pulse du laser de 5 à 10 Hz, et une distance cible – substrat de 6.5-7 cm.

La figure 5.7a / p.128, montre le détail d'une image par microscopie électronique à balayage (MEB) d'un nanopochoir LS-SiN avec des pores de 350 nm de diamètre et un pas de 700 nm utilisé pour les dépôts, et la figure 5.7b / p.128, montre les structures ordonnées en forme de dôme obtenues grâce à ce nanopochoir. L'élargissement de la largeur du bas des structures, causée par un effet d'ombrage du masque et visible dans les images AFM, et indique que le pochoir n'est pas pressée suffisamment contre le substrat. En dehors de cet effet géométrique, les structures apparaissent plus grandes dans l'image

AFM en raison de la convolution entre la pointe et la surface (qui donne une FWHM de  $\sim 400 - 425$  nm, c'est-à-dire 15 - 20% plus large que le diamètre nominal des ouvertures du pochoir). Ainsi une estimation plus exacte de l'effet d'élargissement sur la réplification des structures peut être obtenu en principe en utilisant la vue de dessus d'un MEB. L'image MEB de la figure 5.8 / p.129, montre des structures avec une base élargie de 385 – 390 nm, ce qui suggère un élargissement global de  $\sim 35 - 40$  nm, c'est-à-dire  $\sim 10\%$  plus large que la valeur nominale des ouvertures.

Les structures BaTiO<sub>3</sub> telles que déposées à température ambiante sont amorphes, et nous avons appliqué un recuit à 650 °C sous flux d'O<sub>2</sub> pour les cristalliser. Après recuit, les structures individuelles perdent leur forme en dôme et se séparent en plusieurs grains de diverses orientations cristallographiques. Ce changement de forme est attribué à la nucléation et croissance de nanocristaux BaTiO<sub>3</sub> anisotropes pendant le recuit après dépôt.

Les propriétés piézo-électriques et ferroélectriques des structures de BaTiO<sub>3</sub> ainsi obtenues ont été testées localement en mesurant l'effet piézoélectrique induit par un champ électrique. Des boucles d'hystérèse sont mesurées en positionnant la pointe d'un microscope PFM le plus proche possible du centre d'une structure individuelle (le point topographique le plus haut tel que mesuré par AFM en mode topographique).

La réponse piézoélectrique locale est mesurée pour des tensions DC entre -10V et +10V superposées à une petite tension AC (fréquence typique 29 kHz ; amplitude d'excitation 0.5V) qui doit être plus petite que la valeur du champ coercitif nécessaire pour inverser la polarisation de la structure. La figure 5.13 / p.134, montre pour du BaTiO<sub>3</sub> déposé sur un substrat de SrTiO<sub>3</sub>(100) dopé 0.1% Nb, l'image AFM (en mode contact) avec l'image des domaines de réponse piézoélectrique acquises simultanément. Les régions blanches dans l'image de la réponse piézoélectrique en z indiquent des structures ayant une *polarisation spontanée* principalement orientée vers le haut, alors que les régions sombres indiquent une polarisation spontanée orientée vers le bas. La boucle d'hystérèse piézoélectrique enregistrée (voir figure 5.14 / p.135) montre que la polarisation spontanée des structures de BaTiO<sub>3</sub> peut être commutée et inversée et que les structures gardent leur ferroélectricité en dépit de la tétragonalité réduite de leur

structure cristalline. Le faible signal PFM est attribué à la tétragonalité réduite de la cellule unitaire de BaTiO<sub>3</sub> causée par la fine taille des grains des nanostructures (~30nm).

En étant propre et sans résine le procédé par nanopochoir élimine les doutes quant à de possible effets d'échelle extrinsèques, c'est-à-dire qui seraient dus à des dégâts qui seraient causés pendant la fabrication des structures. Ainsi la faible réponse piézoélectrique est due à un effet d'échelle intrinsèque induit par la taille réduite des grains de BaTiO<sub>3</sub>. En analysant la structure de domaines, nous avons remarqué qu'un domaine s'étend en moyenne sur 2-3 grains. Il est intéressant de noter ici que nos structures de BaTiO<sub>3</sub> étaient presque symétriques et que les grains inversé par le champ électrique appliqué étaient ensuite stables en champ nul pour au moins la durée de plusieurs expériences (quelques jours).

### 5.2.2 Structuration de BaTiO<sub>3</sub> - le régime haute température

Un des défis majeurs parmi les études sur le dépôt d'oxydes perovskite par PLD à travers des nanopochoirs a été d'utiliser cette approche pour obtenir des nanostructures d'oxydes complexes épitaxiés (sur des substrats appropriés) et ainsi de permettre l'étude d'autres classes d'oxydes complexes à des échelles nanométriques. En utilisant des pochoirs avec les architectures présentées dans la section précédente nous avons créé des structures de BaTiO<sub>3</sub> sous les conditions rapportées dans le tableau 5.1. Ces expériences ont pu être effectuées avec le même pochoir que eux utilisés pour des dépôts à température ambiante car les membranes solides en SiN sont résistantes à haute température (jusqu'à 800°C).

Afin de vérifier les propriétés structurelles des ces trois échantillons nous avons effectué des mesures de diffraction de rayons X en condition de Bragg ( $\theta - 2\theta$ ) pour tester la qualité et la nature épitaxiale des structures déposées à haute température. Les paramètres de maille du BTO épitaxié ont été étudiés plus en détails par RSM (*X-ray Reciprocal Space Mapping*), une technique utilisée typiquement pour déterminer si un film épitaxié est complètement contraint (pseudomorphe), partiellement contraint ou complètement relaxé.

La figure 5.19 / p.141, montre des graphiques RSM dans ce cas autour du pic (103). Les valeurs mesurées dans les graphiques RSM sont résumées dans le tableau 5.2.

A faibles pressions de  $O_2$  dans la chambre de dépôt, un nombre important de lacunes sont créées en raison de l'énergie élevée des particules déposées, ce qui produit une grande contrainte de compression dans le plan. Cette dernière induit une elongation du paramètre de maille hors du plan et ainsi une tétragonalité plus prononcée des structures. Nous avons essayé de corrélérer ces résultats avec les propriétés ferroélectriques des structures individuelles de  $BaTiO_3$  pour observer l'effet de la contrainte épitaxiale sur la réponse piézoélectrique, en particulier sur la commutation de la polarisation à des échelles nanométriques. Les graphiques présentés dans la figure 5.21 / p.143, ont été obtenus à partir de structures de hauteurs  $\sim 50\text{nm}$  (a) et  $\sim 65\text{nm}$  (b). Dans les deux cas, la boucle d'hystérèse piézoélectrique enregistrée montre clairement que la ferroélectricité est maintenue dans les structures déposées à basse pression d' $O_2$ . Les boucles d'hystérèse mesurées sont décalées verticalement (vers les valeurs positives), ce qui montre un état de polarisation préférentielle connu sous la dénomination d'empreinte. La synthèse de structures  $BaTiO_3$  par nanostencil à faible pression d'oxygène convient pour une reproduction précise des motifs d'ouvertures du pochoir, et produit également une tétragonalité plus prononcée de la cellule cristalline unitaire, ce qui permet la fabrication de structures aux propriétés similaires à celles fabriquées avec une pression d'oxygène moyenne.

### 5.3 Nanostenciling de multiferroïques

Nous avons ensuite étendu l'application du nanostencil aux multiferroïques, des matériaux dont nous allons préciser les caractéristiques ci-dessous. Les multiferroïques sont généralement définis comme des matériaux qui combinent au moins deux propriétés "ferroïques" telles que l'ordre ferromagnétique (une polarisation magnétique spontanée qui peut être inversée par l'application d'un champ magnétique antiparallèle), la ferroélectricité (une polarisation électrique spontanée qui peut être inversée par l'application d'un champ électrique antiparallèle) ou la ferroélasticité (un changement de la contrainte spontanée induit par une contrainte mécanique appliquée). Une sous-famille des multiferroïques est formée par les *matériaux magnétoélectriques*, des matériaux qui présentent simultanément des propriétés ferroélectriques et magnétiques et qui sont couplées.

### 5.3.1 Structuration de ferrite de bismuth BiFeO<sub>3</sub>

Un des rares matériaux magnétoélectriques naturels est le ferrite de bismuth (BiFeO<sub>3</sub>) qui est probablement la perovskite à base de Bi la plus étudiée dans la famille des BiXO<sub>3</sub> (X = le métal de transition trivalent). Des efforts importants ont été fournis pour préparer des couches minces de phase pure de BFO par PLD. Les films de BFO sont très difficiles à synthétiser, principalement à cause de l'évaporation, de l'oxydation et de la précipitation de Bi sous la forme de Bi<sub>2</sub>O<sub>3</sub>, ou à la cristallisation du film dans d'autres phases stables possibles telles que Fe<sub>2</sub>O<sub>3</sub>, Fe<sub>3</sub>O<sub>4</sub> et Bi<sub>2</sub>Fe<sub>4</sub>O<sub>9</sub>. Il est donc difficile d'éviter la formation de phases d'impuretés. Nous avons eu des problèmes similaires pour la synthèse de structures de BFO quand nous avons utilisé l'approche par pochoir à température ambiante (RT-PLD) qui avait réussi pour le BaTiO<sub>3</sub>. Les analyses par MEB et AFM ont montré, comme dans le cas du titanate de baryum, des structures à température ambiante complètement séparées et parfaitement formées (amorphes). Mais après un recuit conventionnel (650-800 °C; pour 30 - 60min sous oxygène), le caractère ferroélectrique des structures ne pouvait pas être extrait des mesures par PFM, ce que l'on attribuait à des effets de fabrication extrinsèques (l'évaporation de Bi, la non-stoechiométrie des dépôts, etc) et non à des effets d'échelle intrinsèques des structures. De meilleurs résultats plus prometteurs ont été obtenus pour des structures de BFO déposées à température ambiante et traitées par recuit thermique rapide (RTA) à 900 °C, pour 60 s sous oxygène. Après le traitement RTA, la topographie par AFM montre deux types de structures : des petites structures circulaires (type 1) et des structures polygonales plus larges (type 2), figure 5.23 / p.148. Les mesures par PFM indiquent que seules les structures de type 1 ont un contraste piézoélectrique qui montre alors une structure complexe de domaines ferroélectriques et prouve donc que c'est vraisemblablement une phase perovskite de BiFeO<sub>3</sub>, alors que les structures de type 2 ont un contraste uniforme et ne sont pas du BFO. L'arrangement parfaitement périodique des structures après déposition à température ambiante n'était plus complètement préservé après le recuit et la présence de phases étrangères apparues lors du traitement thermique nous pousse à des études plus avancées pour élucider la nucléation et la cristallisation des îlots nanométriques de BiFeO<sub>3</sub>.

### 5.3.2 Structuration de $\text{Bi}_2\text{FeCrO}_6$

Dans le contexte d'exploration de nouveaux matériaux multiferroïques un nouveau composé quaternaire, le  $\text{Bi}_2\text{FeCrO}_6$  (BFCO) a été proposé. En poursuivant naturellement les efforts entrepris pour créer des structures BFO, nos efforts se sont tournés vers l'utilisation du nanopochoir avec du BFCO. Des améliorations des conditions de dépôts (basées sur les études antérieures sur les couches minces de BFO) ont permis d'établir précisément les conditions pour une croissance épitaxiale des couches minces de BFCO stoechiométriques déposées directement sur des substrats de STO dopés au Nb et avec différentes orientations cristallographiques, et ceci à des pressions d' $\text{O}_2$  plutôt basses. Nous avons ensuite combiné ces conditions de croissance PLD avec le procédé par pochoir, et pu obtenir une croissance contrôlée de réseaux de structures multiferroïques ordonnées, épitaxiées et orientées. La forme carrée résultant des îlots orientés (figure 5.26 / p.152) n'est pas complètement surprenante compte tenu du fait que la plupart des oxydes de type perovskite possèdent des énergies de surface moindres sur les facettes  $\{100\}$ , ce qui engendre des structures d'équilibre de type cubique dominées par six facettes  $\{100\}$ . Nous pouvons expliquer la morphologie des nanostructures de BFCO par une analogie avec les nanostructures BFO et la construction de Winterbottom, une théorie qui permet de déterminer la forme d'équilibre d'un noyau cristallin sur un substrat en fonction des termes d'énergie de surface.

Afin d'évaluer la cristallinité des réseaux de structures recouvrant un surface totale de  $2 \times 2.7 \text{ mm}^2$  nous avons eu recours à la diffraction de rayons X, et nous avons aussi étudié la nature épitaxiale des nanostructures de BFCO grâce à des images en coupe transversale par microscopie électronique à transmission à haute résolution (HRTEM) figure (5.29 / p.155). Pour analyser le caractère multiferroïque des structures BFCO nous avons testé des îlots individuels par microscopie à force atomique en mode piézoréponse (PFM) et microscopie à force magnétique (MFM) dans des endroits choisis aléatoirement sur le substrat.

La PFM a pu révéler que les structures sont piézoélectriques, peuvent être individuellement commutées et présentent une nette hystérèse piézoélectrique, elles sont donc bien ferroélectriques (figure 5.30 / p.156).

Les mesures MFM ont été établies avec un champ magnétique orienté perpendiculairement au substrat. Les structures ont un contraste uniforme, clairement différent de celui du substrat. Puisque les pointes MFM sont aussi conductrices, il y a toujours une interaction électrostatique entre la pointe et l'échantillon qui se superpose à l'interaction magnétique. Afin de démontrer que les structures sont polarisables magnétiquement et que le contraste a une origine magnétique, nous avons retourné la direction du champ externe. Le changement de contraste observé (figure 5.31 / p.157), prouve: premièrement, que l'origine du contraste est l'interaction magnétique, puisque seule la configuration du champ magnétique a changé, et deuxièmement qu'il y a un moment magnétique induit dans chaque îlot de BFCO.

Les études locales par MFM ont été confirmées par des mesures à température ambiante avec un magnétomètre de type "vibrating sample" (VSM). Ces mesures macroscopiques montrent un comportement d'hystérèse des propriétés magnétiques des structures avec un champ coercitif de 150 Oe (figure 5.32 / p.158) environ le double de celui des couches continues de BFCO (80 Oe).

Ce travail a clairement démontré la versatilité et la flexibilité du *nanostenciling* en tant qu'excellente approche alternative pour la nanofabrication et la structuration, lorsque les différents matériaux, des métaux et semi-conducteurs aux oxydes complexes, peuvent être manipulés aisément.